UNIL | Université de Lausanne

Unicentre
CH-1015 Lausanne
http://serval.unil.ch

Year : 2023

Bedload transport in Alpine streams: Lessons from newly-emerging monitoring systems

Gilles Antoniazza

Gilles Antoniazza, 2023, Bedload transport in Alpine streams: Lessons from newly-emerging monitoring systems

Originally published at : Thesis, University of Lausanne

Posted at the University of Lausanne Open Archive http://serval.unil.ch
Document URN : urn:nbn:ch:serval-BIB_CE66484075955

Droits d’auteur
L'Université de Lausanne attire expressément l'attention des utilisateurs sur le fait que tous les documents publiés dans l'Archive SERVAL sont protégés par le droit d'auteur, conformément à la loi fédérale sur le droit d'auteur et les droits voisins (LDA). A ce titre, il est indispensable d'obtenir le consentement préalable de l'auteur et/ou de l’éditeur avant toute utilisation d'une oeuvre ou d'une partie d'une oeuvre ne relevant pas d'une utilisation à des fins personnelles au sens de la LDA (art. 19, al. 1 lettre a). A défaut, tout contrevenant s'expose aux sanctions prévues par cette loi. Nous déclinons toute responsabilité en la matière.

Copyright
The University of Lausanne expressly draws the attention of users to the fact that all documents published in the SERVAL Archive are protected by copyright in accordance with federal law on copyright and similar rights (LDA). Accordingly it is indispensable to obtain prior consent from the author and/or publisher before any use of a work or part of a work for purposes other than personal use within the meaning of LDA (art. 19, para. 1 letter a). Failure to do so will expose offenders to the sanctions laid down by this law. We accept no liability in this respect.

Bedload transport in Alpine streams
Lessons from newly-emerging monitoring systems

PhD thesis in Environmental Science

presented at the

Faculté des Géosciences et de l'Environnement de l'Université de Lausanne,

Institute of Earth Surface Dynamics

by

Gilles Antoniazza

B.Sc., M.Sc., University of Lausanne, Switzerland

Committee

Thesis director:	Prof. Dr. Stuart N. Lane (University of Lausanne)
Thesis co-director:	Dr. Dieter Rickenmann (Swiss Federal Research Institute WSL)
Internal expert:	Prof. Dr. Virginia Ruiz-Villanueva (University of Lausanne)
External expert:	Dr. Jens M. Turowski (GFZ Potsdam)
External expert:	Prof. Dr. Francesco Comiti (University of Bolzano)
Jury president:	Prof. Dr. Marie-Elodie Perga (University of Lausanne)

Lausanne, March 2023

UNIL | Université de Lausanne
Faculté des géosciences et de l'environnement
bâtiment Géopolis bureau 4631

IMPRIMATUR

Vu le rapport présenté par le jury d'examen, composé de

Présidente de la séance publique :	Mme la Docteure Stéphanie Grand
Présidente du colloque :	Mme la Professeure Marie-Elodie Perga
Directeur de thèse :	M. le Professeur Stuart Lane
Co-directeur de thèse :	M. le Docteur Dieter Rickenmann
Experte interne :	Mme la Professeure Virginia Ruiz-Villanueva
Expert externe :	M. le Professeur Francesco Comiti
Expert externe :	M. le Docteur Jens Turowski

Le Doyen de la Faculté des géosciences et de l'environnement autorise l'impression de la thèse de

Monsieur Gilles ANTONIAZZA

Titulaire d'un
Master ès Sciences en Géographie
de l'Université de Lausanne

intitulée

BEDLOAD TRANSPORT IN ALPINE STREAMS: LESSONS FROM NEWLY-EMERGING MONITORING SYSTEMS

Lausanne, le 10 mars 2023

Pour le Doyen de la Faculté des géosciences et de l'environnement

Docteure Stéphanie Grand

« Eventually, all things merge into one, and a river runs through it. The river was cut by the world's great flood and runs over rocks from the basement of time. On some of those rocks are timeless raindrops. Under the rocks are the words, and some of the words are theirs. I am haunted by waters. »

Norman Maclean – A river runs through it (1976)

« C’est que la montagne a ses idées à elle, c’est que la montagne a ses volontés. »

Charles-Ferdinand Ramuz – La Grande Peur dans la Montagne (1926)

À mon père, Michel Antoniazza (1952 – 2021)

Remerciements

Cette thèse est le fruit d’un vaste travail d’équipe. Je tiens à remercier ici du fond du coeur les personnes m’ayant aidé de près ou de plus loin à son élaboration.

À Stuart Lane, mon directeur de thèse, pour avoir partagé ta passion et ta connaissance des cours d’eau, et pour la confiance que tu m’as témoignée dès ton arrivée à l’UNIL en 2011, en dirigeant mes travaux de Bachelor et de Master, en m’engageant comme assistant-étudiant à de multiples reprises, et en dirigeant finalement ma thèse de doctorat. Ta motivation sans faille et ton enthousiasme débordant m’ont apporté confiance et sérénité pour l’élaboration de nombreux travaux. Tu as toujours su trouver le juste équilibre dans la supervision, me laissant la liberté de développer mes idées tout en offrant ton soutien, tes conseils et ton expertise dès que j’en avais besoin. Tes qualités scientifiques et humaines m’ont beaucoup apporté et m’ont permis de m’épanouir pendant ces années d’université riches et stimulantes. Tu as mon éternelle reconnaissance !

À Dieter Rickenmann, mon co-directeur de thèse, pour la fructueuse et stimulante collaboration que nous avons eue dès 2015 au WSL, d’abord en tant que civiliste, puis en tant que stagiaire, et finalement en tant que co-superviseur de thèse. Ton expertise du monde du charriage m’a apporté énormément et j’ai beaucoup appris en te côtoyant. Un grand merci pour ton soutien et ton excellence au cours de ces années.

À toutes les personnes qui m’ont apporté une aide essentielle pour les nombreux travaux de terrain : Tobias Nicollier, Magalí Matteodo, Thomas Antoniazza, Mehi Mattou, Aurélien Ballu, Micha Dietze, Pascal Egli, Floreana Miesen, Davide Mancini, Matteo Roncoroni, Matt Jenkins, Boris Ouvry, François Mettra, Valentin Pipoz, Jonas Walker, Nicolas Steeb, Maxime Capt, Christoph Heim, Dilan Reich, Nora Krebs, Sabrina Henning, Laurianne Heym, Guillaume Mayoraz, Florian Schläfli, Konrad Eppel, Micaela Faria, Andreas Schmucki, Werner Gerber, Eduardo Viegas, Maarten Bakker, Chrystelle Gabbud. Un merci tout particulier à Stefan Boss pour avoir mis en service cette merveilleuse station de mesure du Vallon de Nant, qui a fonctionné parfaitement durant toutes mes années de thèse, et sur laquelle repose une grande partie des données qui ont été collectées et analysées dans le cadre de ce doctorat.

À toute l’équipe du Vallon de Nant, pour votre accueil, votre soutien et les intéressantes discussions que nous avons eues sur la dynamique du bassin versant : Aurélien, Cédric et toute l’équipe de l’Auberge de Pont de Nant, François Bonnet du Jardin botanique la Thomasia, Valentin Quartenoud et famille, Sylvain Bernard et famille.

À mes collègues de groupe et d’institut, à l’IDYST et au WSL, pour les riches échanges (pas toujours scientifiques) et les bons moments passés ensemble. Merci à Alexandre Badoux et Manfred Stähli pour m’avoir toujours accueilli à bras ouverts au WSL. Merci à Antoine Guisan, Rémy Freymond et aux membres du Conseil de Coordination scientifique du Vallon de Nant pour votre soutien. Merci à Mike James de l’Université de Lancaster pour la riche collaboration autour des questions de photogrammétrie. Merci à toute la section Géomorphologie du GFZ Potsdam pour m’avoir accueilli durant mon projet Doc.Mobility, et pour tout ce que j’y ai appris. Merci à Urs Fischer et Angela Landgraf de la Nagra. Merci à François Cruchod, Emmanuel Reynard et Christophe Lambiel pour m’avoir transmis votre passion pour cette magnifique discipline qu’est la géomorphologie.

Aux membres du Comité de thèse et du Comité de suivi, pour leur intérêt, leur temps et leurs conseils avisés: Jens Turowski, Francesco Comiti, Virginia Ruiz-Villanueva, Grégoire Mariéthoz, Georgina King, Marie-Elodie Perga et Stéphanie Grand.

À mes potes de toujours, sans qui la vie serait beaucoup moins belle, en particulier Petric, Gerbolli, Biopane, Cambrax, Keke, Cid, Jean, Fly, Adima, Johnny, Fauquex, Paulette, Armelle, Jérémie, Nax, Quim, Smiling.

À ma famille, pour votre présence réconfortante. Un merci tout particulier à mes parents pour votre soutien durant mes (interminables) années d'étude. À ma mère Brigitte, pour m'avoir transmis ta passion pour la marche et les montagnes. À mon père Michel, pour m'avoir inculqué ton insatiable curiosité pour le monde qui nous entoure.

À Magalí, pour ton amour, ton soutien, ton énergie, ta joie de vivre, ton intelligence, ta curiosité, ta force, qui rendent beau chaque jour passé à tes côtés.

Et à Rémi !

Corcelettes, mars 2023.

Gilles

Financial support

This thesis received financial support from the University of Lausanne, from the Swiss Federal Research Institute WSL, and from the Swiss National Science Foundation, notably via a 6-months Doc.Mobility grant awarded to Gilles Antoniazza. The University of Lausanne, the Swiss Federal Research Institute WSL and the ETH-Zürich funded the building of the monitoring station at the Vallon de Nant. The National Cooperative for the Disposal of Radioactive Waste (Nagra) also funded part of the research activities. The Agassiz Foundation and the Faculty of Geosciences and Environment have supported the acquisition of field equipment. The Geophysical Instrument Pool Potsdam (GIPP) of the GFZ provided seismic instrumentation. Those different supports were essential to the realization of this PhD, and all contributors are warmly thanked. I am also grateful to the Institute of Earth Surface Dynamics of the University of Lausanne, which provided with the necessary conditions for sane and stimulating research.

Summary

Despite a critical importance for current and future Alpine watershed management, bedload transport remains a difficult process to measure and to predict accurately. It is extremely complex to describe physically, and the lack of reliable and cost-effective field monitoring systems has limited progress in this field. Recent methodological advances in acoustic and seismic techniques have permitted major developments in the continuous monitoring of bedload transport in steep Alpine streams. The aim of this PhD thesis is to develop further and to apply those emerging techniques to gain a new understanding of coarse material mobilization, transfer and storage throughout Alpine watersheds.

The first objective of this thesis was to improve the calibration of the widely-used Swiss Plate Geophone (SPG) acoustic bedload monitoring system, because variability in calibration coefficients were observed within and between different SPG sites, which limits their universal transferability. An impact experiment was performed at four SPG stations and positively showed that individual plates within and across sites present in general comparable signal response, but signal propagation due to poor insulation was identified as an important reason for calibration coefficient variability. This aspect needs to be accounted so as to obtain transferable calibration coefficients for the SPG system, which will save substantial sensor-specific field calibration effort.

The second objective was to use five-years of SPG-acquired bedload transport time-series to understand how hydrological variability drove bedload transport in a nival-dominated Alpine watershed (Vallon de Nant), and to assess implications for how climate change might impact bedload transport in the future in such environments through its effect on Alpine hydrology. Results of the analysis emphasized the importance of combined rain and snow-melt events for yearly transported bedload volumes (77% on average), the non-negligible contribution of snowmelt-only events (14% on average), and the non-negligible but smaller contribution of late-summer and autumn rainfall events (9% on average). In terms of climate change, this implies that lower snowfall amounts and seasonal shift in both precipitation and melt periods may lead to enhanced bedload transport in winter and spring, and reduced bedload transport in summer and autumn, although the timing and magnitude of extreme rainfall events is likely to be key. Results of the study allow development of climate-sensitive Alpine watershed management strategies.

The third objective was to improve understanding of the spatial structure of bedload sediment supply and transport that lead to the kinds of temporal variations we observe at the watershed outlets. The difficulty of measuring distributed bedload transport reliably means that there are no data and very little understanding of this spatial structure. Environmental seismology has great potential in this context; sensors are cheap, easily deployable, and previous research has shown that reliable bedload transport time-series could be extracted from the seismic signal emitted by a stream. A network of 24 seismic sensors was deployed across the Vallon de Nant Alpine watershed during a high-magnitude bedload transport event, providing with a unique distributed dataset. Comparison of the seismic inversion procedure with the calibrated SPG time-series was encouraging. Results of the analysis emphasized the relative inefficiency of steep Alpine watersheds in conveying coarse material even during a high-magnitude event. Bedload moved slowly, and over short distances. Multiple periods of competent flow would be required to evacuate coarse material mobilized in the watershed during individual-sourcing events. This understanding has major implications for constraining the present and future of coarse material fluxes throughout steep Alpine watersheds. Seismic networks have the potential to capture the time-space variability in bedload transport; a necessary condition towards obtaining more accurate predictions of the process.

Résumé

Malgré son importance pour la gestion actuelle et future des bassins versants alpins, le charriage reste un processus difficile à mesurer et à prédire. La physique du processus est complexe, et le manque de techniques de mesure de terrain fiables et abordables a également limité les progrès dans la discipline. Les développements récents, notamment dans les techniques acoustiques et sismiques, ont permis des avancées majeures dans la mesure continue du charriage dans les rivières alpines. Le but de cette thèse de doctorat est d'affiner les connaissances sur ces nouvelles technologies, et d'en tirer profit afin d'étendre notre compréhension sur les flux sédimentaires dans les bassins versants de montagne.

Le premier objectif de cette thèse était d'améliorer la calibration du système acoustique de mesure du charriage Swiss Plate Geophone (SPG), car une variabilité conséquente des coefficients de calibration a été observée au sein et entre différentes stations SPG, ce qui limite leur transférabilité universelle. Un test d'impact a été effectué à quatre stations SPG, et a démontré avec succès que les capteurs individuels au sein et entre les différentes stations présentaient des réponses similaires, mais la propagation du signal à cause de problèmes d'isolation a été identifiée comme un facteur de contrôle important de la variabilité des coefficients de calibration. Cet aspect doit être pris en compte afin d'obtenir une calibration universelle du système SPG, ce qui va économiser un effort de terrain substantiel.

Le deuxième objectif était d'utiliser une série temporelle de charriage de cinq ans mesurée avec le système SPG afin de comprendre comment la variabilité hydrologique contrôle le charriage dans un bassin versant alpin dominé par la fonte de neige (le Vallon de Nant), et d'évaluer comment les changements climatiques pourraient affecter le charriage dans cet environnement via leurs effets sur l'hydrologie alpine. Les résultats de l'analyse montrent l'importance des événements mixtes (pluie et fonte de neige combinées) dans les masses annuelles de charriage mesurées (77% en moyenne), la contribution non-négligeable des événements de fonte (14% en moyenne), et la contribution non-négligeable mais plus faible des événements pluvieux à la fin de l'été et en automne (9% en moyenne). En termes de changements climatiques, cela signifie que la diminution des volumes de neige, et le décalage saisonnier des précipitations et de la fonte, pourraient résulter en des volumes charriés plus importants en hiver et au printemps, et plus faibles en été et en automne, bien que la temporalité et la magnitude des événements de pluie extrêmes vont être déterminantes. Les résultats de l'étude aident à développer des stratégies de gestion des bassins versants adaptées aux changements climatiques.

Le troisième objectif était d'améliorer la compréhension des flux sédimentaires au sein des bassins versants alpins qui conduisent à la variabilité que l'on observe aux exutoires. La difficulté à mesurer le charriage en des points multiples de manière fiable fait que peu de données existent et les connaissances sont très limitées. La sismique environnementale a un grand potentiel dans ce contexte : les capteurs sont bon marché, facilement déployable, et il a été démontré que des données de charriage fiables peuvent être extraites à partir du signal sismique émis par une rivière. Un réseau de 24 capteurs sismiques a été déployé au Vallon de Nant durant une forte crue, mettant à disposition un jeu de données unique. Après validation du modèle d'inversion sismique, les résultats de l'analyse montrent l'inefficacité relative des bassins versants alpins pour le transport par charriage, même pendant une crue importante, et soulignent le besoin de multiples périodes de hautes eaux pour évacuer le matériel grossier mobilisé durant des événements individuels. Ces résultats ont des implications importantes pour mieux cerner les flux sédimentaires actuels et futurs dans les bassins versants alpins, et les réseaux sismiques présentent un grand potentiel pour couvrir la variabilité spatiale et temporelle du charriage : une condition nécessaire pour améliorer la prédiction du processus.

Zusammenfassung

Obwohl der Geschiebetransport für die Beurteilung von alpinen Einzugsgebieten heute und in Zukunft von großer Bedeutung ist, ist er schwierig zu messen und vorherzusagen. Seine physikalische Beschreibung ist äußerst komplex, und der Mangel an zuverlässigen und kosteneffizienten Monitoringsystemen hat den Fortschritt auf diesem Gebiet eingeschränkt. Neueste methodische Fortschritte bei akustischen und seismischen Verfahren haben wichtige Entwicklungen für die kontinuierliche Überwachung des Geschiebetransports in alpinen Flüssen ermöglicht. Das Ziel dieser Doktorarbeit ist es, diese neuen Techniken weiterzuentwickeln, um ein neues Verständnis der Mobilisierung, des Transfers und der Lagerung von grobem Geschiebe in alpinen Einzugsgebieten zu gewinnen.

Das erste Ziel dieser Arbeit war es, die Kalibrierung des akustischen Geschiebeüberwachungssystems Swiss Plate Geophone (SPG) zu verbessern, da Schwankungen der Kalibrierungskoeffizienten innerhalb und zwischen verschiedenen SPG-Standorten beobachtet wurden, was ihre universelle Übertragbarkeit einschränkt. Ein Schlagexperiment wurde an vier SPG-Stationen durchgeführt und zeigte, dass die einzelnen Sensoren innerhalb und zwischen den Standorten im Allgemeinen eine vergleichbare Signalantwort aufweisen, aber die Signalausbreitung aufgrund limitierter Isolierung wurde als wichtiger Grund für die Variabilität der Kalibrierungskoeffizienten ermittelt. Dieser Aspekt muss berücksichtigt werden, um übertragbare Kalibrierkoeffizienten für das SPG-System zu erhalten, wodurch ein erheblicher Aufwand für die sensorspezifische Feldkalibrierung eingespart werden kann.

Das zweite Ziel war es, eine mit dem SPG gemessene fünfjährige Geschiebezeitreihe zu verwenden, um zu verstehen, wie die hydrologische Variabilität das Geschiebe in einem von der alpinen Schneeschmelze dominierten Einzugsgebiet (Vallon de Nant) beeinflusst, und um zu beurteilen, wie sich Klimaänderungen auf das Geschiebe in dieser Umgebung über ihre Auswirkungen auf die alpine Hydrologie auswirken könnten. Die Ergebnisse der Analyse zeigen die Bedeutung gemischter hydrologischer Ereignisse für die gemessenen jährlichen Geschiebemassen (im Durchschnitt 77%), den wichtigen Beitrag von Schmelzereignissen (im Durchschnitt 14%) und den wichtigen, aber geringeren Beitrag von Regenereignissen im Spätsommer und Herbst (im Durchschnitt 9%). In Bezug auf den Klimawandel bedeutet dies, dass die geringeren Schneemengen und die saisonale Verschiebung von Niederschlag und Schmelze dazu führen könnten, dass im Winter und Frühling größere und im Sommer und Herbst kleinere Mengen transportiert werden, obwohl das Timing und die Größe der extremen Regenereignisse entscheidend sein werden.

Das dritte Ziel bestand darin, das Verständnis der Sedimentflüsse innerhalb der alpinen Einzugsgebiete zu verbessern. Da es schwierig ist, das Geschiebe an mehreren Punkten zuverlässig zu messen, gibt es nur wenige Daten und das Wissen ist sehr begrenzt. Die Umweltseismik hat in diesem Zusammenhang ein großes Potenzial: die Sensoren sind billig, leicht einsetzbar und es wurde nachgewiesen, dass zuverlässige Geschiebedaten aus dem seismischen Signal eines Flusses extrahiert werden können. Ein Netzwerk von 24 seismischen Sensoren wurde während eines starken Abflussereignisses im Vallon de Nant eingesetzt. Die Ergebnisse der Analyse zeigen die relative Ineffizienz der alpinen Einzugsgebiete für den Geschiebetransport selbst während eines großen Hochwassers und unterstreichen die Notwendigkeit mehrfacher Hochwasserperioden, um das während einzelner Ereignisse mobilisierte grobe Material weiterzutransportieren. Diese Ergebnisse haben wichtige Implikationen für ein besseres Verständnis der aktuellen und zukünftigen Sedimentflüsse in alpinen Einzugsgebieten, was für eine bessere Vorhersage des Prozesses notwendig ist.

Riassunto

Nonostante l'importanza critica per la gestione attuale e futura dei bacini idrografici alpini, il trasporto di fondo rimane un processo difficile da misurare e da prevedere con precisione. È estremamente complesso da descrivere fisicamente e la mancanza di sistemi di monitoraggio sul campo affidabili ed economici ha limitato i progressi in quest’aera. I recenti progressi metodologici nelle tecniche acustiche e sismiche hanno consentito importanti sviluppi nel monitoraggio continuo del trasporto di fondo nei fiumi alpini. L'obiettivo di questa tesi di dottorato è quello di sviluppare ulteriormente e applicare queste tecniche emergenti per ottenere una nuova comprensione della mobilizzazione, del trasferimento e dello stoccaggio di materiale grossolano nei bacini idrografici alpini.

Il primo obiettivo di questa tesi è stato quello di migliorare la calibrazione del sistema di misurazione acustica del trasporto di fondo della Swiss Plate Geophone (SPG), in quanto è stata osservata una significativa variabilità dei coefficienti di calibrazione all'interno e tra le diverse stazioni SPG, che ne limita la trasferibilità universale. Un test d'impatto è stato effettuato su quattro stazioni SPG e ha dimostrato con successo che i singoli sensori all'interno e tra le diverse stazioni mostrano risposte simili, sebbene la propagazione del segnale dovuta a problemi di isolamento sia stata identificata come un importante fattore di controllo per la variabilità dei coefficienti di calibrazione. Questo aspetto deve essere preso in considerazione per ottenere una calibrazione universale del sistema SPG, la quale consentirà di risparmiare un notevole sforzo sul campo.

Il secondo obiettivo è stato quello di utilizzare una serie temporale di cinque anni di misura del trasporto di fondo con il sistema SPG per capire come la variabilità idrologica controlla il trasporto di fondo in un bacino alpino dominato dal disgelo della neve (il Vallon de Nant) e per valutare come il cambiamento climatico potrebbe influenzare il trasporto di fondo in questo ambiente attraverso i suoi effetti sull'idrologia alpina. I risultati dell'analisi mostrano la grande importanza degli eventi misti (pioggia associata a scioglimento della neve) nelle masse di carico annue misurate (77% in media), il contributo notevole degli eventi di fusione (14% in media) e il contributo rilevante, ma minore, delle precipitazioni di fine estate e autunno (9% in media). In termini di cambiamento climatico, ciò significa che la diminuzione dei volumi di neve e lo spostamento stagionale delle precipitazioni e dello scioglimento potrebbero portare a volumi di carico di fondo più elevati in inverno e in primavera e più bassi in estate e in autunno, anche se la tempistica e l'entità degli eventi pluviometrici estremi saranno fondamentali. I risultati dello studio aiutano a sviluppare strategie di gestione dei bacini idrografici adattate ai cambiamenti climatici.

Il terzo obiettivo è stato quello di migliorare la comprensione dei flussi di sedimenti all'interno dei bacini idrografici alpini. La difficoltà di misurarli in modo affidabile mostra che esistono pochi dati e le conoscenze sono ancora molto limitate. La sismica ambientale ha un grande potenziale in questo contesto: i sensori sono economici, facilmente dispiegabili ed è stato dimostrato che è possibile estrarre dati affidabili sul trasporto di fondo dal segnale sismico emesso da un fiume. Una rete di 24 sensori sismici è stata dispiegata nel Vallon de Nant durante una grande alluvione, fornendo un set di dati unico. Dopo la validazione del modello di inversione sismica, i risultati dell'analisi mostrano la relativa inefficienza dei bacini idrografici alpini per il trasporto di fondo, anche durante una grande alluvione, ed evidenziano la necessità di più periodi di acqua alta per evacuare il materiale grossolano mobilitato durante i singoli eventi. Questi risultati hanno importanti implicazioni per una migliore comprensione dei flussi di sedimenti attuali e futuri nei bacini idrografici alpini. Inoltre, mostrano quanto le reti sismiche abbiano un grande potenziale per coprire la variabilità spaziale e temporale del trasporto di fondo: una condizione necessaria per migliorare la previsione del processo.

Table of contents

List of Figures

List of Tables

Nomenclature

Roman symbols

1D	One-dimensional.
2D	Two-dimensional.
A	Ampere.
A_{max}	Signal maximum positive amplitude.
c	Equation coefficient.
b	Channel width.
CI	Confidence Interval.
D	Diameter.
dB	Decibel.
D_{50}	Median diameter of the grain-size distribution.
D_{84}	84th percentile of the grain-size distribution.
D_{90}	90th percentile of the grain-size distribution.
e	Residuals of regression.
E_k	Kinetic Energy.
E_r	Erosion rate.
f	Frequency.
g	Gravitational acceleration.
h	Hour.
h	Water depth.
Hz	Hertz.
$IMPT$	SPG impulse rate.
K	Dimensionless quality factor.
k	Different variables.
K_0	Dimensionless quality factor at frequency of 1 Hz.
kg	Kilograms.
M	Mass.
M_{tot}	Mass of bedload transport samples.
m	Meter.
min	Minute.
n	Number of

N_{imp}	Number of impulses in the SPG signal exceeding a defined amplitude threshold.
P	Precipitation.
Q	Streamflow.
q^{**}	Dimensionless streamflow.
Q_{amp}	Amplitude of daily streamflow hydrograph.
Q_b	Bedload transport rate.
q_b	Unit bedload transport rate.
Q_{det}	Detrended streamflow hydrograph.
R^2	Coefficient of determination.
R	Relative sediment density.
r_0	Distance between the channel centerline and a seismic sensor.
r_h	Hydraulic radius.
S	Channel gradient.
s	Second.
S_xA_{max}	Standard deviation of the SPG signal maximum positive amplitude.
T	Time.
t	Tons.
t	t-value of Student test.
T_m	Mean temperature.
U	Depth-averaged flow velocity.
U^{**}	Dimensionless mean flow velocity.
V	Volts.
v	Velocity.
v_{g}	Wave group velocity.
v_{p}	Phase velocity of Raleigh waves.
v_{p0}	Phase velocity of Raleigh waves at frequency of 1 Hz.
W	Channel width.
W^*	Dimensionless bedload transport rate.
x	Different variables.
y	Year.
y	Different variables.

Greek symbols

η	Dimensionless exponent that expresses the change in the quality factor with frequency.
θ	Channel gradient.
ξ	Dimensionless exponent used to scale a frequency-dependent decay in seismic signal.
ρ	Water density.
ρ_s	Sediment density.
σ_g	Standard deviation of a parametric log-raised cosine function.
σ_{mass}	Mass uncertainty in bedload transport samples.
τ^*_{D50}	Dimensionless bed shear stress.
τ^*_{rD50}	Dimensionless reference bed shear stress.

Acronyms

ADCP	Acoustic Doppler Current Profiler.
AdN	Avançon de Nant.
a.s.l	Above sea level.
C	Stream transport capacity.
CA	Contributing Area.
CH1903	Swiss geographic coordinate system.
CH1903+	Swiss geographic coordinate system.
DAS	Distributed acoustic sensing.
DEM	Digital Elevation Model.
dGPS	Differential Global Positioning System.
DJF	December-January-February.
ECOL	Ecological Engineering Laboratory, EPFL.
EPFL	Swiss Federal Institute of Technology, Lausanne.
ETH	Swiss Federal Institute of Technology, Zürich.
FGSE	Faculty of Geosciences and Environment, University of Lausanne.
FMI	Fluvial Model Inversion.
G	Channel gradient.
GIUB	Geography Institute of the University of Bern.
GIPP	Geophysical Instrument Pool, GFZ Potsdam.

GP-Acc	Geophone Plate Accelerometer.
GPS	Global Positioning System
GSD	Grain-Size Distribution.
GFZ	German Research Center for Geosciences, Potsdam.
IDYST	Institute of Earth Surface Dynamics, University of Lausanne.
JJA	June-July-August.
JPM	Japanese Pipe Microphone.
LIDAR	Light Detection and Ranging.
LoD	Limit of Detection.
MAM	March-April-May.
MeteoSwiss	Swiss Federal Office of Meteorology.
MPA	Miniplate Accelerometer.
MVS	Multi-View Stereo.
Nagra	National Cooperative for the Disposal of Radioactive Waste.
OCCR	Oeschger Center for Climate Change Research, University of Bern.
PC	Personal Computer.
PhD	Doctor of Philosopy.
PIT	Passive Integrated Transponder.
PSD	Power Spectral Density.
PVC	Polyvinyl Chloride.
RCP	Representative Concentration Pathway.
RFID	Radio Frequency Identification.
RhiresD	Daily precipitation data.
ROS	Rain On Snow.
RTK	Real Time Kinematics.
S	Upstream coarse material supply.
SCA	Sediment Contributing Area.
SCR	Sediment Capacity Ratio.
SDR	Sediment Delivery Ratio.
SfM	Structure-from-Motion.
SNSF	Swiss National Science Foundation.
SON	September-October-November.

SPG	Swiss Plate Geophone system.
SPS	Squared Pipe System.
Swisstopo	Swiss Federal Office of Topography.
TabsD	Daily temperature data.
UAV	Uncrewed Aerial Vehicle.
UNIL	University of Lausanne.
VAW	Laboratory of Hydraulics, Hydrology and Glaciology, ETH Zürich.
VdN	Vallon de Nant.
WSL	Swiss Federal Research Institute for Forest, Snow and Landscape research.

I - Introduction

This thesis is concerned with improving our ability to measure bedload transport in steep Alpine streams (gradient > 5%), and with our understanding of coarse material fluxes throughout steep Alpine watersheds. This introductive Chapter sets out the basic state of knowledge of research in this field via a general review of the literature, so as to justify the core foci of the thesis (I-1). It then states the primary three research objectives of the thesis, which correspond to the three main thesis Chapters, and introduces the approach applied to answer each of them individually (I-2). The thesis structure is presented in (I-3). A set of complementary contributions, realized in the frame of this PhD but not part of the main core of the thesis are presented in (I-4).

I-1 The status of bedload transport knowledge and research in Alpine environments

This section begins by defining bedload transport and addressing its importance for Alpine watershed management (I-1.1). It then provides a conceptual model of steep Alpine stream dynamics (I-1.2), and describes the bedload transport process, emphasizing why accurate predictions are so challenging to obtain (I-1.3). Evolution and limits of earlier bedload transport monitoring systems are presented in (I-1.4). Recent developments and applications of acoustic bedload transport monitoring techniques, as well as two of the primary contributions of this thesis, are contextualized in (I-1.5). Recent developments and applications of seismic bedload transport monitoring techniques, as well as the third primary contribution of this thesis, are contextualized in (I-1.6).

I-1.1 Bedload transport in steep Alpine streams: its importance

Bedload comprises the transport by streams of sediment particles by sliding, rolling and saltation, generally near the river-bed (Einstein, 1950; Gomez, 1991). It is differentiated from suspended sediment transport, as suspension occurs when turbulence maintains sediment particles higher in the water column, without contact with the bed over long distances (Vanoni, 2006; Turowski et al., 2010). If bedload typically relates to the transport of the coarsest fraction of the sediment, it is the combination between stream power and turbulence rate that ultimately determines whether a given particle size is transported as bedload or in suspension at a given time (Abbott and Francis, 1977; Gomez, 1991; Turowski et al., 2010). As such, the relative importance of bedload transport as compared with suspended sediment transport increases from lower energy settings (e.g. continental margins) towards higher energy settings (e.g. mountain ranges; Vanoni, 2006; Turowski et al., 2010). Bedload transport is commonly a consequence of hillslope supply and fluvial erosion. As a major contributor to fluvial deposition, it is central in determining channel patterns (Schumm, 1985; Church and Ferguson, 2015) and is a critical driver of river morphological changes, notably inducing bed incision, bank erosion, channel lateral migration, bed aggradation and channel avulsion (Ashworth and Ferguson, 1986; Leopold et al., 2012; Knighton, 2014; Church and Ferguson, 2015).

Through its effects on river morphology, bedload transport is therefore an important aspect of watershed management for Alpine countries such as Switzerland. It is a serious natural hazard, costly in economical terms. Badoux et al. (2014a) estimated an average cost related to the bedload transport process of ~120 millions CHF per year over four decades (1970-2010) in Switzerland, with four individual years alone producing more than 500 millions CHF of damage. Bedload transport can also be costly in terms of loss of human lives. Badoux et al. (2016) reported that more than 120 people died during bedload-exacerbated flooding events in Switzerland over the period 1946 to 2015. Bedload transport is also a major challenge for hydropower production in Alpine environments. High rates of erosion from upstream watersheds (Hinderer et al., 2013; Li et al., 2022; Zhang et al., 2022) lead to high rates of sediment supply to water intakes and retention basins, and abrade infrastructures. Their mitigation can represent up to 20-30% of power plant annual operational costs (Schleiss et al., 2010; Pralong et al., 2015; Schleiss et al., 2016). By providing support to riverine ecosystems (e.g. salmonids spawing, fluvial and alluvial habitats), bedload transport is also an important and positive feature of stream ecology, and needs to be integrated into Alpine river management (Wohl, 2006, 2013). As an example, alluvial areas in Switzerland house over 50% of national plant diversity, while representing only 0.05% of the territory (FOEN, 2005).

I-1.2 Bedload transport in steep Alpine streams: a conceptual model

The dynamics of steep Alpine streams in terms of erosion and deposition depends on the sediment balance between the river transport capacity (C) and the coarse material supply (S), in turn defining the sediment capacity ratio (SCR) (Lane, 1955). During times where C > S SCR < 1 and the river erodes. During times where C < S, SCR > 1 the river aggrades.

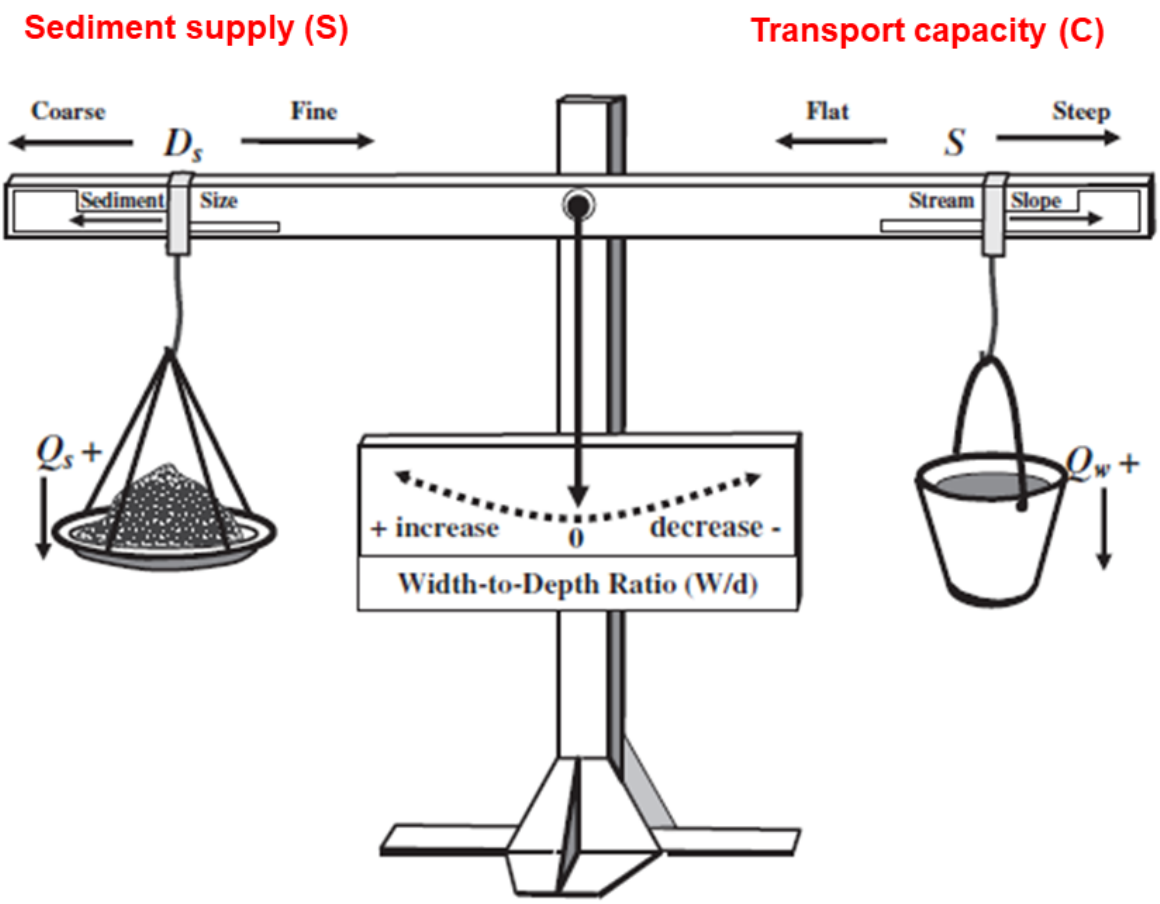

Figure I-1. The Lane balance (Lane, 1955) conceptual model, reproduced from Dust and Wohl (2012).

In the ‘graded channel’ theory of Mackin (1948), both erosion and aggradation may be self-limiting over the longer term (i.e. multiple years) due to feedbacks that occur as a result of sediment transport, until the stream profile and its sedimentology are adjusted to the imposed transport capacity (C) and material supply (S), and reach a relative ‘equilibrium’ of SCR = 1. In any situation where a river has less supply than capacity (SCR < 1), erosion should lead to slope reduction and via size-selective transport, to an increase of the critical shear stress required for material mobilization. In any situation where a river has more supply than capacity (SCR > 1), aggradation should increase the slope and reduce the critical shear stress, provided the supplied material is poorly sorted (Mackin, 1948; Lane, 1955; Lane et al., 2021). Yet, steep Alpine streams are forced by varying discharge and hence varying transport capacity (related to Alpine watershed hydrology) and by varying sediment supply (related to coarse material mobilization, transfer and storage throughout Alpine watersheds), which means that “out-of-equilibrium” or “unadjusted” state, with SCR < 1 (erosion) or SCR > 1 (deposition) are often the norm over the shorter term (i.e. less than multiple years). In this context, the ‘graded channel’ conceptual model (Mackin, 1948; Lane, 1955) sets a theoretical framework to constrain the dynamics of bedload transport in steep Alpine streams at both shorter and longer time-scales, but the latters are in reality rarely “graded” at any one point in time.

I-1.3 Bedload transport in steep Alpine streams: the challenge of prediction

Despite its importance for watershed management, bedload transport remains an elusive variable to predict accurately, in particular for steep Alpine streams (gradient > 5%; Bathurst, 1987; Piton and Recking, 2017; Ancey, 2020a, 2020b; Gomez and Soar, 2022). Part of the uncertainty derives from a process that is complex to describe physically (Parker and Klingeman, 1982; Kirchner et al., 1990; Gomez, 1991; Buffington and Montgomery, 1997; Yager et al., 2012a; Ancey, 2020a, 2020b).

The capacity of a stream to transport sediment as bedload (C) results in the balance between two competing forces: the drag and lift forces of the flowing water, and the resisting force of the bed to mobilization (Leopold et al., 2012; Knighton, 2014; Church and Ferguson, 2015; Ancey, 2020a). On the one hand, the typical steepness of Alpine streams gives the flowing water a high energy, which is partly and variably dissipated through turbulence (Nitsche et al., 2011; Rickenmann and Recking, 2011), particularly linked to roughness elements in the bed (e.g. cascades, steps, boulders, woody debris, bedfroms). On the other hand, Alpine stream beds typically comprise mixed grain-size, where the resisting force to mobilization depend on the way particles of different size interact (i.e. rate of imbrication, armoring, packing, infiltration, ‘hiding’ and/or protrusion), and the frequent presence in the bed of large immobile or poorly-mobile particles issuing from hillslope processes (e.g. landslides, debris flow), from deglaciation deposits, or from bedrock outcrops (Kirchner et al., 1990; Buffington and Montgomery, 1997; Yager et al., 2012a, 2012b). While partial size-selective transport of bedload particle has been reported (Ashworth and Ferguson, 1989; Wilcock and McArdell, 1993; Mao, 2012), resistance to motion due to particle interactions at the bed (often called “hiding effects”) can lead to near equal-mobility in gravel-bed streams; i.e. particles of different size been transported suddenly and simultaneously within a narrow range of shear stress once the resisting force of the bed matrix is exceeded (Parker et al., 1982; Andrews, 1983; Parker and Toro Escobar, 2002; Ancey, 2020a). Note that this effect is particularly relevant for the finer half of the grain-size distribution (Parker, 2008). These processes taken together mean that the boundary conditions that drive bedload transport are highly variable in space and time, are rarely known *a priori*, and yet produce transport rates that are extremely variable, across multiple orders of magnitude even under steady streamflow and sediment supply conditions (Gomez, 1983; Bathurst, 1987; Gomez et al., 1989; Aigner et al., 2017; Rickenmann, 2020). Consequently, accurately determining the local transport capacity (C) in such settings, as a function of changing streamflow and changing particle mobility, is a very challenging task (Bathurst, 1987; Buffington and Montgomery, 1997; Yager et al., 2012b; Ancey, 2020a, 2020b).

However complex is the estimation of the local transport capacity (C), bedload transport predictive equations developed to date have used it to derive bedload transport rates, assuming that capacity is fulfilled (SCR = 1) by sufficient upstream sediment supply (S) (Bathurst, 1987; Parker, 1990; Yager et al., 2012a; Recking, 2012; Rickenmann, 2018) at the moment of transport. A second set of uncertainties thus derives from the fact that supply limitation conditions (SCR < 1) are commonly observed in steep Alpine streams (Yager et al., 2012b; Recking, 2012; Piton and Recking, 2017; Gomez and Soar, 2022). Upstream sediment supply (S) depends on the way steep Alpine streams transiently mobilize, convey and store coarse material through the different morphological sections they are typically composed of (Piton and Recking, 2017; Gomez and Soar, 2022). The morphology of steep Alpine streams largely derives from their glacier legacy, with a typical 'staircase' long-profile made of a succession of steep rockwalls and hillslopes, flatter and wider glacier troughs, and steeper glacier riegls (Hooke, 1991; Egholm et al., 2012; Cook and Swift, 2012; Dell'Agnese et al., 2015). Alpine rivers tend to develop different morphologies along sections that present contrasting topographic and hydraulic properties. In the flatter sections, usually covered with deposits of Quaternary material, Alpine rivers are typically alluvial with plane-bed or braided morphologies, where the bed is mainly composed of the river's own deposits (Church and Ferguson, 2015; Lane et al., 2017; Mao et al., 2017; Piton and Recking, 2017; Comiti et al., 2019). Alluvial reaches may alternatively act as both sources and sinks of sediment, but may not be always hydraulically efficient to convey coarse material (Dell'Agnese et al., 2015; Lane et al., 2017; Mao et al., 2017). In the steeper and sometimes more confined sections, semi-alluvial reaches tend to develop cascade or step-pool morphologies (Recking, 2012; Rickenmann, 2012; Turowski, 2012; Yager et al., 2012b). Along these reaches, the streambed is typically armored, resulting in potentially limited sediment availability at the bed (Recking, 2012; Yager et al., 2012b; Piton and Recking, 2017), except for extreme events that may destabilize its structure (Turowski et al., 2009; Rainato et al., 2017). Alpine rivers may also be colluvial, which means that intermittent material inputs from tributaries may be supplied to the main channel (Piton and Recking, 2017; Rainato et al., 2017), as long as their (diffusive) alluvial fans are not disconnecting the main river from the steep gullies draining the hillslopes (Cavalli et al., 2013; Lane et al., 2017; Rainato et al., 2017; Mancini and Lane, 2020). As such, coarse material may be produced intermittently and conveyed with different efficiencies through the contrasting morphological sections of Alpine streams (Dell'Agnese et al., 2015; Lane et al., 2017; Comiti et al., 2019), which matters to determine the local upstream material supply (S) and how it varies through time (Piton and Recking, 2017; Gomez and Soar, 2022).

In periods of supply-limitation (SCR < 1), the actual transport rate is expected to be temporarily lower than suggested by capacity (C), which means that the application of capacity-based (C) equations will result in substantial over-estimate of bedload transport rates (Recking, 2012; Yager et al., 2012a; Gomez and Soar, 2022). They are also evidence that throughout heavily armored sections of Alpine streams (e.g. step-pool reaches), finer bedload particles than the ones composing the bed may 'travel' and be conveyed without inducing major remobilization of the streambed (Yager et al., 2012b; Recking, 2012). Estimation of local transport capacity (C) from a coarsely-packed bed, whilst observed bedload transport is finer, may under-estimate the actual bedload transport rate (Piton and Recking, 2017; Gomez and Soar, 2022). As a consequence, uncertainties in determining both local transport capacity (C) and upstream material supply (S) result in large errors in bedload transport predictions for steep Alpine streams, typically between one and multiple orders of magnitude when compared to independent field data (Bathurst, 1987; Yager et al., 2012a; Piton and Recking, 2017; Rickenmann, 2018). Meyer-Peter and Müller (Meyer-Peter and Müller, 1948) published some 70 years ago one of the first predictive bedload transport equation for steep Alpine gravel-bed streams (Ancey, 2020a, 2020b). Despite decades of subsequent research to improve the performance of bedload transport predictive equations (Parker, 1990; Wilcock and Crowe, 2003; Rickenmann, 2001; Yager et al., 2012b), uncertainty in transport rate prediction remains extremely high (Nitsche et al., 2011; Yager et al., 2012a; Schneider et al., 2015; Rickenmann, 2018).

Not only is bedload transport difficult to predict, it is also extremely difficult to measure and progress in monitoring has been slow (Gomez, 1991; Church and Ferguson, 2015; Ancey, 2020a, 2020b). Early measurements of bedload transport used direct sampling devices such as baskets or pressure-difference samplers (Helley and Smith, 1971; Bunte et al., 2004). Discrete-in-time and at-a-point in space, they failed to quantify time-space variability in bedload transport (Parker et al., 1982; Gomez, 1983; Hoey and Sutherland, 1991; Aigner et al., 2017). Measurement of the rate of filling of traps across streams provided cross-sectional integrated estimates of bedload transport rates (Leopold and Emmett, 1976; Lenzi et al., 1999). However, such traps are often rapidly filled, they modify hydraulic conditions and require heavy stream engineering, while still providing no detail on the temporal (within events) and spatial (across section or watershed) variations of bedload transport rates (Gomez, 1991, 1983; Hicks and Gomez, 2003). The deployment of slot samplers with a pressure-sensor continuously measuring the rate of filling of reservoirs has provided with more information on ‘within event’ and ‘across section’ (i.e. when multiple samplers are deployed aside) bedload transport rate variability (Reid et al., 1995; Reid and Laronne, 1995; Laronne et al., 2003). Yet, they are still limited by the sampler capacity (i.e. in terms of both transport volume and maximal grain-size) and the need for frequent manual emptying.

Following a slightly different approach, particle tracking experiments have also provided insights regarding bedload transport dynamics, notably with regards to thresholds of particle motion (May and Pryor, 2014; Chapuis et al., 2015; Mao et al., 2017), travel distance and resting duration of individual particles (Habersack et al., 2001; Liébault et al., 2012; Hassan et al., 2013; Vázquez-Tarrío et al., 2019), active layer depth (Houbrechts et al., 2012; Schneider et al., 2014), particle velocity and the effect of channel morphology on particle displacement (MacVicar and Roy, 2011; Dell’Agnese et al., 2015). Yet, the low proportion of tagged particles as compared to the total bulk bedload transport and the time required to survey lengths of channel typically limit the benefits of such approaches to determine the total bulk bedload volume and its temporal variability (Hassan and Ergenzinger, 2003; Mao et al., 2017). But, these methods have delivered valuable insights on the motion of individual particles in space (Liébault et al., 2012; Hassan et al., 2013; Dell’Agnese et al., 2015; Vázquez-Tarrío et al., 2019). Repeated topographic surveys of Alpine rivers have also brought interesting information on the spatial dynamics of coarse material and on erosion and deposition patterns (Lane et al., 1995, 2017; Comiti et al., 2019), but such techniques also provided very little temporal resolution, notably within-event.

As a consequence, existing field techniques to monitor bedload transport in steep Alpine streams have long failed to simultaneously capture bedload transport temporal and spatial variability (Piton and Recking, 2017; Ancey, 2020a, 2020b; Gomez and Soar, 2022). This has limited our understanding on the way coarse material is alternatively produced, conveyed and or stored within Alpine watersheds (Cavalli et al., 2013; Comiti et al., 2019; Coviello et al., 2022), as well as its drivers (Micheletti and Lane, 2016; Lane et al., 2017). It has not fully resolved the key balance between local transport capacity (C) and upstream sediment supply (S): a necessary step towards the improvement of predictive bedload transport equations (Yager et al., 2012a; Piton and Recking, 2017; Gomez and Soar, 2022). It is for this reason that the primary focus in this thesis is developing new understanding of bedload transport in steep Alpine streams, based on recent progress in two monitoring techniques: acoustic and seismic sensing of bedload transport.

I-1.5 Development and application of acoustic bedload transport monitoring systems

The last three decades has witnessed major steps forward in the continuous monitoring of bedload transport in steep Alpine streams. As a first set of methods, indirect acoustic sensors deployed in the riverbed were shown to scale with bedload transport magnitude (Downing, 2010; Mizuyama et al., 2010a; Aigner et al., 2017; Rickenmann, 2017). The sound produced by bedload in transport can be captured with hydrophones (Barton et al., 2010; Geay et al., 2020), and the vibration of embedded structures (e.g. plate, pipe, column) induced by impacting bedload particles can be measured with piezoelectric, geophone, microphone or accelerometer sensors (Rickenmann and McArdell, 2007; Mizuyama et al., 2010a; Rickenmann et al., 2012, 2014b; Kreisler et al., 2017). Provided that the sensors are calibrated against concurrent direct bedload samples, absolute continuous time-series of bedload transport are obtained (Rickenmann et al., 2012, 2014b; Geay et al., 2020). In turn, such series should allow new understanding on how environmental variability in steep Alpine watersheds influences bedload transport, especially as understanding to date is limited by the lack of reliable measurements.

I-1.5.1 Swiss Plate Geophone monitoring of bedload transport: development

Amongst acoustic sensors, the Swiss Plate Geophone (SPG) system developed by the Swiss Federal Research Institute WSL has proved to be particularly effective for monitoring bedload transport in steep Alpine streams (Rickenmann et al., 2012, 2014b; Kreisler et al., 2017; Habersack et al., 2017; Rickenmann, 2018, 2020). It has now been deployed at more than 20 sites in Switzerland, Austria, Italy, Israel and the United States (Rickenmann, 2017). The SPG system is made of a series of steel plates embodied in a concrete structure flush with the riverbed to not affect surrounding flow hydraulic conditions. Particles sliding, rolling and saltating over the bed impact the steel plates, and a geophone mounted below each plate continuously records the induced vibration. SPG are typically mounted in a line across the stream to cover the entire channel width (Rickenmann et al., 2014b; Habersack et al., 2017; Rickenmann et al., 2017; Kreisler et al., 2017; Rickenmann and Fritschi, 2017). Like any other indirect acoustic monitoring system, the SPG requires a robust calibration to transform the recorded signal into the actual mass of bedload in transport, typically by relating it to concurrent direct bedload samples (Mizuyama et al., 2010a; Rickenmann et al., 2012, 2014b; Rickenmann and Fritschi, 2017; Geay et al., 2020). Such sampling is typically difficult to undertake in steep Alpine streams, notably during high flows (Rickenmann et al., 2012; Kreisler et al., 2017; Habersack et al., 2017). It has been achieved so far through four main approaches. First, by measuring the rate of filling of retention basins located directly downstream of the sensors (Rickenmann and McArdell, 2007, 2008). Second, it is possible to use mobile sediment baskets mounted on a rail, which is built along a concrete sill. The baskets can be placed below a plate targeted for calibration, and all the particles impacting it are collected into a basket (Rickenmann et al., 2012, 2014b). Third, it can be based upon sediment baskets or net samplers mounted on a crane and operated from a truck on the riverbank, which collects bedload samples downstream of a plate targeted for calibration (Rickenmann and Fritschi, 2017; Kreisler et al., 2017; Nicollier et al., 2019, 2020; Coviello et al., 2022). Fourth, it can use embedded automatic slot samplers that continuously measures the reservoir rate of filling by bedload particles directly downstream of a plate targeted for calibration (Habersack et al., 2017; Kreisler et al., 2017; Halfi et al., 2020).

These approaches have resulted in successful calibration of the SPG system in multiple steep Alpine streams (Rickenmann et al., 2012, 2014b; Wyss et al., 2016a, 2016b; Kreisler et al., 2017; Habersack et al., 2017), with site-specific coefficients of determination R^2 typically ranging between 0.85 and 0.99 (Rickenmann, 2017). Yet, it is not yet well constrained between different streams, with calibration coefficients varying by about a factor of 20 between individual samples from different sites and a factor 6 between mean calibration values of different sites (Rickenmann et al., 2014b; Rickenmann and Fritschi, 2017; Kreisler et al., 2017; Habersack et al., 2017). Given the intensive field effort required to calibrate SPG systems, the community would benefit from transferable calibration coefficients, through a better understanding of what causes this variability. Wyss et al. (2016b) identified flow velocity as an important driver of variability in SPG calibration coefficients, higher flow velocities inducing a weaker SPG signal response for the same transported bedload mass. Wyss et al. (2016c) and Nicollier et al., (2021) also found that the bedload grain-size distribution drives variability, coarser material inducing a stronger signal response than finer one for a same transported bedload mass. Finally, Chen et al. (2021) showed that the mode of particle transport was also an important factor, the signal per unit mass increasing as particle move from sliding to rolling to saltation. Given the above, the first primary contribution of this thesis addresses the search for general calibration coefficients for SPG systems. It is made through an impact experiment that systematically tested the response of individual SPG at four different field sites. While the experiment positively confirmed that sensors within and across SPG sites presented comparable responses, it also permitted the identification and quantification of another relevant factor of variability in the SPG response; the rate of signal propagation from impacted plates towards non-impacted plates due to insulation issues.

I-1.5.2 Swiss Plate Geophone monitoring of bedload transport: application

Despite calibration challenges, absolute time-series of bedload transport obtained with the SPG system or other calibrated acoustic devices are of great value for studying the temporal variability in bedload transport rates. They have notably been used to quantify transported bedload mass and its variability over shorter (floods, seasons; Dell'Agnese et al., 2014; Rickenmann et al., 2014b) and longer (e.g. years, decades; Rainato et al., 2017; Rickenmann, 2018, 2020) timescales, as well as its spatial variability (i.e. across a river section; Habersack et al., 2017). They have also been employed to estimate bedload transport grain-size distributions (Barrière et al., 2015; Mao et al., 2016; Nicollier et al., 2021, 2022a) and to determine the start and end of bedload transport (Turowski et al., 2011; Rickenmann, 2020). For stations where streamflow is also measured, time-series of bedload transport have been related to transport capacity (C) (Rickenmann and Fritschi, 2017; Habersack et al., 2017; Geay et al., 2017; Kreisler et al., 2017; Rickenmann, 2018; Perolo et al., 2019; Rickenmann, 2020). Although these studies confirmed a considerable scatter in the relationship between transport capacity and transport rates, especially at shorter time-scales (i.e. typically up to a few hours), stronger correlations emerged over longer-time periods, confirming streamflow variation as an important driver of bedload transport. Within Alpine streams, there are a range of hydrological processes that can lead to streamflow variations, and through it drive bedload transport. These hydrological processes notably include ice and snowmelt, rainfall, and the co-occurrence of rainfall and melt events (Mutzner et al., 2015; Corripio and López-Moreno, 2017; Musselman et al., 2018). To date, the contributions of these different hydrological drivers to annual bedload bugets is unknown. This matters not only for improving our understanding of bedload transport dynamics under current climatic conditions, but also for predicting how bedload transport may evolve with climate change impacts on the hydrology of Alpine watersheds (Rainato et al., 2017; Comiti et al., 2019; Coviello et al., 2022). The aim of the second primary contribution of this thesis is to investigate this question by quantifying in a nival-dominated Alpine watershed – the Vallon de Nant in the Swiss Alps – the contribution of different hydrological drivers (i.e. snowmelt events, rainfall events, mixed snowmelt and rainfall events) in the total amount of bedload transported over a 5-year period, using continuously-measured time-series of both streamflow and bedload transport.

I-1.6 Development and application of seismic bedload transport monitoring systems

Although continuous time-series of bedload transport rates obtained with calibrated acoustic sensors have a great potential to study the temporal variability in bedload transport rates, how it scales with streamflow and the transport capacity (C), and the hydrological drivers of bedload transport (Habersack et al., 2017; Kreisler et al., 2017; Rickenmann, 2018, 2020; Coviello et al., 2022); they may not represent the most suitable approach to address the issue of upstream sediment supply (S). In fact, the deployment of acoustic sensors such as the SPG requires stable cross-sections (e.g. weirs) to be mounted efficiently, which may represent substantial installation costs and ecological impacts (Rickenmann, 2017). Acoustic sensors are in best cases deployed at single locations, and they are limited to quantify coarse material production, transfer and storage across steep Alpine watersheds, which is necessary to better constrain upstream sediment supply (S), and a condition towards the improvement of bedload transport predictions (Recking, 2012; Piton and Recking, 2017; Gomez and Soar, 2022).

Spatially-distributed datasets of bedload transport are scarce, and our understanding of how steep Alpine watersheds mobilize, convey and store coarse material is very limited. We do not know, during high-magnitude streamflow events, where and how much material is mobilized and stored, and the proportion of it that is finally exported at the watershed outlet. Neither do we know precisely the rate at which coarse material is conveyed. In this context, there is an ongoing debate on the respective contribution of small to intermediate streamflow events, as compared to the high magnitude ones, in the production, transfer and storage of coarse material within steep Alpine watersheds (Turowski et al., 2009; Yager et al., 2012b; Rainato et al., 2017; Comiti et al., 2019; Coviello et al., 2022). High-magnitude streamflow events are assumed to be important to supply material from less-connected areas of Alpine watersheds (Cavalli et al., 2013; Lane et al., 2017; Mancini and Lane, 2020), and to substantially rework the bed (including possibly more stable bed structures like steps; Turowski et al., 2009; Rainato et al., 2017). In contrast, low to intermediate flow events could be responsible for the progressive evacuation of the material made available in the main channel network by antecedent high-magnitude flow events (Turowski et al., 2009; Yager et al., 2012b; Turowski et al., 2013a; Lane et al., 2017; Rainato et al., 2017), in line with the 'graded channel' theory (Mackin, 1948; Lane, 1955). Yet, this premise has not yet been effectively tested, due to the difficulty of obtaining spatially-distributed bedload transport datasets.

For about a decade, environmental seismology (Cook and Dietze, 2022) has provided an alternative. Out-of-bank seismometers have shown that the energy released by bedload transport is manifest in a specific frequency band (Burtin et al., 2011; Tsai et al., 2012; Roth et al., 2016; Bakker et al., 2020). As this frequency is normally different to that associated with other fluvial processes, such as turbulence, absolute time-series of bedload transport may also be inferred (Gimbert et al., 2019; Bakker et al., 2020; Lagarde et al., 2021) through the application of appropriate physical inversion models (Tsai et al., 2012; Gimbert et al., 2014). Seismometers are cheap, easily deployable and require little maintenance such that they can be deployed as networks to investigate bedload transport at multiple locations of steep Alpine watersheds (Schmandt et al., 2017; Cook et al., 2018; Coviello et al., 2019; Piantini et al., 2022). Networks of seismic sensors have notably been deployed to investigate the dynamics of floods (Schmandt et al., 2017; Chmiel et al., 2022; Piantini et al., 2022), debris flows (Walter et al., 2017; Coviello et al., 2019; Chmiel et al., 2021) and glacier lake outburst floods (Cook et al., 2018; Maurer et al., 2020). To date, dense networks of seismic sensors have not been deployed at the watershed scale to study the mobilization, transfer and storage of coarse material during a high-magnitude streamflow event. Thus, the aim of the third primary contribution of this thesis was to investigate the spatial structure of coarse material fluxes at the watershed scale during a high-magnitude bedload transport event by deploying a network of 24 seismic sensors in the Vallon de Nant Alpine watershed in the Swiss Alps. The anatomy of the bedload transport event in terms of coarse material mobilization, transfer and storage was revealed, and fed the understanding of the respective contribution of low to intermediate streamflow events versus larger ones in the dynamics of coarse material fluxes throughout steep Alpine watersheds.

I-2 Thesis aim, objectives and approaches

Following from (I-1), the main aim of this thesis is to improve our ability to measure bedload transport in steep Alpine streams in time and space by further developing and applying acoustic and seismic monitoring techniques, to gain a new understanding of coarse material mobilization, transfer and storage throughout steep Alpine watersheds. This general aim leads to three specific objectives:

(1) To improve the calibration of the widely-used Swiss Plate Geophone (SPG) acoustic bedload monitoring system, because variability in calibration coefficients were observed within and between different SPG sites, which limits their universal transferability. An impact experiment is performed at four Alpine SPG stations to assess the response of individual sensors within and across SPG sites, and to identify potential drivers of variability in SPG calibration coefficients.

(2) To assess the implications for how climate change might impact bedload transport in the future through its effect on Alpine watershed hydrology by using five years of SPG-acquired bedload transport time-series in the Vallon de Nant. Following a calibration of the SPG bedload sensors, and a quantification of the hydraulic forcing of streamflow upon bedload, a hydrological analysis is performed to identify periods where the flow is driven by different hydrological drivers: rainfall, snowmelt, and combined rain and snowmelt events. We then quantify their respective contribution to bedload transport, and discuss how bedload transport may evolve under a changing climate through its effect on the identified hydrological drivers.

(3) To provide the first spatially-distributed, time-dependent quantification of how coarse material is mobilized, transported and stored throughout steep Alpine watersheds, using a network of 24 seismic sensors installed during a high-magnitude event upstream of the SPG monitoring station considered under (2). Following the application of the relevant seismic inversion model to obtain absolute time-series of bedload transport, and a comparison of the seismic inversion procedure with the calibrated SPG dataset, distributed bedload time-series for all 24 sites are used to reveal the anatomy of the bedload transport event at the watershed scale in terms of coarse material mobilization, transfer and storage. Combined with a morphological change analysis through DEM differencing, we discuss the contribution of low to intermediate flow events versus high-magnitude ones as drivers of coarse material fluxes throughout steep Alpine watersheds.

Common to objectives (2) and (3), and also included as one of the sites in objective (1) is the Vallon de Nant watershed in south-west Switzerland. This is a 13.4 km^2 steep Alpine watershed with elevation ranging from ~1’200 to ~3’050 m a.s.l., located at the north-western margin of the European Alps (Figure I-1). It has a local high relief (notably on its eastern side) forming a natural barrier to westerly and north-westerly air streams (Vittoz and Gmür, 2009; Lane et al., 2016) and so receiving considerable precipitation (~ 1850 mm·y-1) (Dutoit, 1983; Vittoz and Gmür, 2009; Lane et al., 2016; Antoniazza et al., 2022). A significant proportion (~45 % in the year 2020) of annual precipitation occurs as snowfall (Thornton et al., 2021, 2022; Antoniazza et al., 2022) with snow cover persisting until late spring-early summer in more-shaded, higher-altitude areas of the watershed (Dutoit, 1983; Vittoz and Gmür, 2009; Lane et al., 2016; Thornton et al., 2021, 2022; Antoniazza et al., 2022). A small debris-covered glacier (Glacier des Martinets) occupies ~3% of the watershed, supplying only negligible amounts of ice melt. Thus, the hydrological regime of the watershed is dominated by snowmelt and rainfall (Ceperley et al., 2020; Mächler et al., 2021; Michelon et al., 2021, 2022; Thornton et al., 2021, 2022; Antoniazza et al., 2022). Land cover in the watershed is composed at 48 % of bare sediment and scree slopes, at 33 % of Alpine grasslands, at 16 % of forests and the remaining 3 % by the Glacier des Martinets (Ceperley et al., 2020).

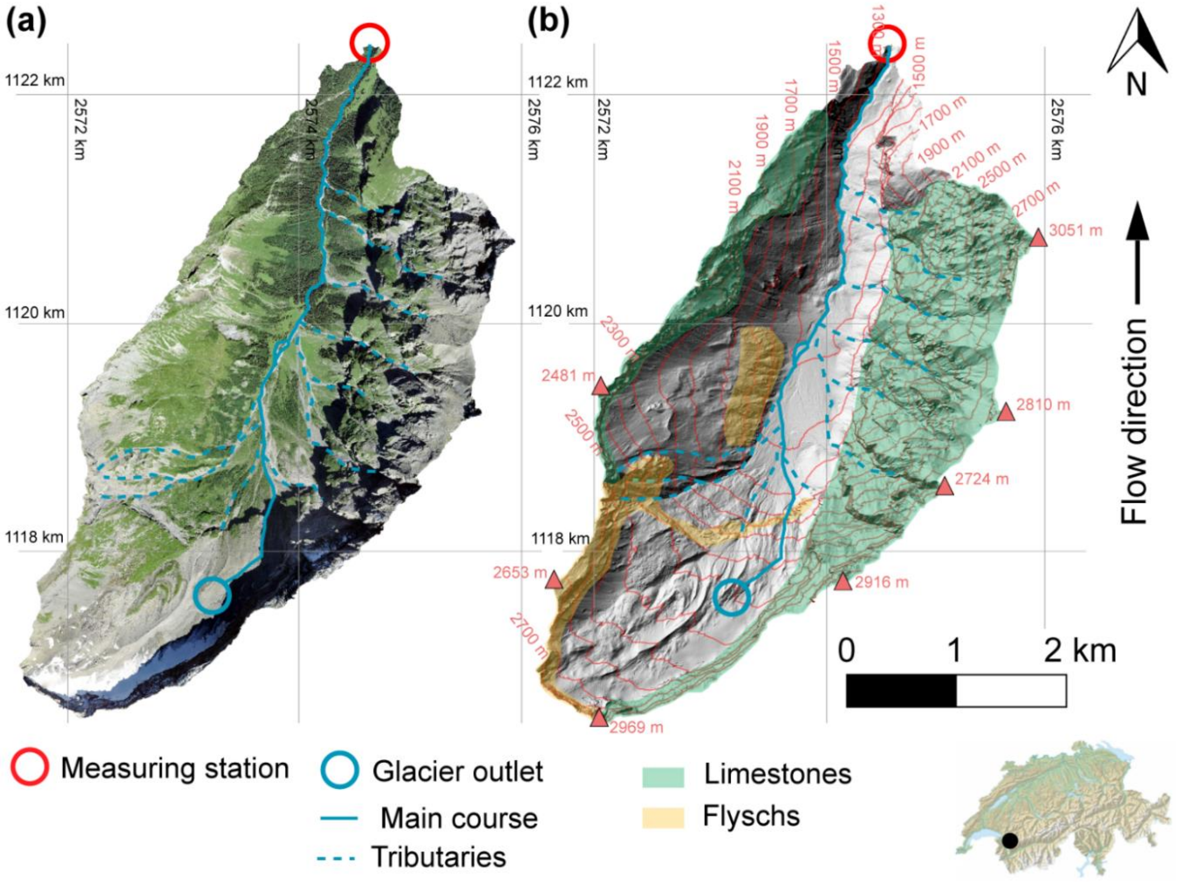

Figure I-2. The Vallon de Nant Alpine watershed in (a) a 0.1-m orthophoto (2020) and in (b) a hillshade (2020) based on the the 0.5-m resolution LIDAR-based SwissAlti3d digital elevation model (Acknowledgments ©Swisstopo). Coordinates are provided in the CH1903+ Swiss system. The streamflow and SPG monitoring station at the outlet is labelled with a red circle. The Glacier des Martinets outlet and the Avançon de Nant (AdN) main course are labelled with a blue circle and blue line, respectively. The main temporarily-flowing tributaries are labelled with a dashed blue line. In (b), the main bedrock outcrops are delineated in green (limestones of the 'Nappe de Morcles-Doldenhorn') and in yellow (flyschs of the Northern Helvetic), the rest of the surface in gray being covered by Quaternary sediment. Modified from Antoniazza et al. (under review).

Geologically, the watershed comprises rocks from the calcareous sedimentary series (limestones of Secondary age) belonging to the Helvetic domain (inverse flank of the 'Nappes de Morcles – Doldenhorn'). There are also softer North-Helvetic Tertiary flyschs outcropping locally in the southern part of the watershed (Figure I-2; Badoux, 1971; Thornton et al., 2018). Whilst limestones are subject to karstification at different rates (i.e. depending on their composition), flyschs are expected to be much less permeable, which gives the Vallon de Nant complex hydro-geological properties (Thornton et al., 2018, 2022). The geomorphology of the Vallon de Nant largely derives from its glacial legacy (Hooke, 1991; Cook and Swift, 2012;

Egholm et al., 2012; Antoniazza and Lane, 2021), with a typical 'staircase' profile made of a succession of steep rockwalls and hillslopes, flatter glacier troughs, and steeper glacier riegls (Figure I-2). Bedrock only outcrops in the steeper sections (i.e. rockwalls, riegls), while the flatter sections (i.e. rockwall feet, glacier troughs) are covered by substantial depths (up to 80 m) of Quaternary till, which forms important aquifers (Thornton et al., 2022). The Avançon de Nant – the stream that drains the Vallon de Nant – tends to develop different morphologies along sections that present contrasting topographic and hydraulic properties. In the flatter sections, usually covered by Quaternary material, the river is typically alluvial with plane-bed or braided morphologies. In the steeper and sometimes more confined sections, semi-alluvial reachs tend to develop cascades or step-pool morphologies.

The Vallon de Nant thus provides an ideal and representative focus for the thesis. Hydrologically, it is representative of many steep Alpine watersheds of the front range of the western and northern facing Alps. Its basin is nival-dominated, setting it apart from non-Alpine and low-Alpine basins where warming climate is making snow accumulation much less frequent. This transfer of "hydrological memory" (winter snow accumulation to summer runoff) is characteristic of nival watersheds and has only rarely been considered in relation to continuous measurement of bedload transport. Geomorphologically, it is representative of many Alpine watersheds shaped by glaciations, with 'staircase' long profile made of a succession steeper and flatter reaches. In addition to these scientific reasons for choosing the basin, the Vallon de Nant has an SPG that has given reliable data since 2016. The spatial scale of and access to the basin made a spatially-distributed acquisition of time-series of bedload transport feasible.

I-3 Thesis structure

Following this Chapter, this thesis is subdivided into three research Chapters, corresponding to the three primary objectives identified in (I-2). Each Chapter comprises a scientific article that details the research context and needs, the applied methodology and the scientific outcomes. Supporting Information is also provided for each Chapter, furnishing additional information to the research. I am the lead author of each Chapter and my contribution to each research article with respect to those of the co-authors is also highlighted at the start of each Chapter. The first two research articles of Chapter II and III, corresponding to the first two primary objectives identified in (I-2), have been published into international scientific journals after complete peer-review process. The third research article composing Chapter IV is currently under peer-review process in an International scientific journal.

The first research article composing Chapter II focuses on the general calibration of the SPG system through an impact experiment conducted at four Alpine SPG sites:

- **Antoniazza, G.**, Nicollier, T., Wyss, C. R., Boss, S., & Rickenmann, D. (2020). Bedload transport monitoring in Alpine rivers: variability in Swiss Plate Geophone response. *Sensors*, *20*(15), 4089.

The second research article composing Chapter III focuses on the hydrological drivers of bedload transport in the nival-dominated Vallon de Nant Alpine watershed:

- **Antoniazza, G.**, Nicollier, T., Boss, S., Mettra, F., Badoux, A., Schaefli, B., Rickenmann, D. & Lane, S. N. (2022). Hydrological drivers of bedload transport in an Alpine watershed. *Water resources research*, *58*(3), e2021WR030663.

The third research article composing Chapter IV deals with the anatomy of a high-magnitude bedload transport event captured with a network of 24 seismic sensors in the Vallon de Nant Alpine watershed:

- **Antoniazza, G.**, Dietze, M., Mancini, D. Turowski, J. M., Rickenmann, D., Nicollier, T., Boss, S. & Lane, S. N. (under review). Anatomy of an Alpine bedload transport event: a watershed-scale seismic network perspective. *Submitted to Journal of Geophysical Research: Earth Surface.*

In Chapter V, a synthesis of the thesis main research outcomes in the prism of recent published research is performed to assess the state of scientific knowledge following from realization of the three primary objectives of the thesis, and identifies where future research should now focus. Chapter VI concludes the thesis.

I-4 Additional contributions to research

In addition to the three primary contributions of this thesis, ten first-authored and co-authored peer-viewed journal articles individually published (or under review); one peer-reviewed co-authored article resulting from a conference proceedings, and one scientific report resulting from an executed mandate hired by the Nagra (Swiss National Cooperative for the Disposal of Radioactive Waste); were completed as part of collaborations or following from research that began before the thesis. The related abstracts are reported below, and the outcomes of the different main and complementary contributions are mentioned where appropriate in the 'Synthesis and perspectives' Chapter V.

These contributions relate to the thesis objectives as follows:

(1) Some of the complementary contributions [1-4] (see numbering below) deal with the continuous monitoring of bedload transport using the SPG system and other acoustic devices, and their calibration, and are as such closely related to the first primary contribution of Chapter II.

(2) Some of the complementary contributions deal with sediment yield within Alpine watersheds at longer time-scales, both considering (a) the past and the effects of Ice Ages on Alpine valley development, landforms and how they affect contemporaneous coarse material fluxes [5-6]; and (b) the future with the effects of rapid climate change on coarse material dynamics and Alpine watershed management [7]. As such, they provide with relevant context for the two primary contributions of Chapter III and Chapter IV.

(3) Contributions [8-12] address recent progress in high-resolution topographic data acquisition, and how they can be used to quantify spatially coarse material fluxes within Alpine rivers. In this context, they are complementary to the third primary contribution of Chapter IV.

The thesis complementary contributions, and individual abstracts, are reported below:

[1] Nicollier, T., **Antoniazza, G.**, Rickenmann, D., Hartlieb, A., & Kirchner, J. W. (2022b). Improving the calibration of the Swiss plate geophone bedload monitoring system by filtering out seismic signals from extraneous particle impacts. *Earth and Space Science*, e2021EA001962.

Abstract: The spatio-temporal variability of bedload transport processes poses considerable challenges for bedload monitoring systems. One such system, the Swiss plate geophone (SPG), has been calibrated in several gravel-bed streams using direct sampling techniques. The linear calibration coefficients linking the signal recorded by the SPG system to the transported bedload can vary between different monitoring stations by about a factor of six, for reasons that remain unclear. Recent controlled flume experiments allowed us to identify the grain-size distribution of the transported bedload as a further site-specific factor influencing the signal response of the SPG system, along with the flow velocity and the bed roughness. Additionally, impact tests performed at various field sites suggested that seismic waves generated by impacting particles can propagate over several plates of an SPG array, and thus potentially bias the bedload estimates. To gain an understanding of this phenomenon, we adapted a test flume by installing a partition wall to shield individual sensor plates from impacting particles. We show that the SPG system is sensitive to seismic waves that propagate from particle impacts on neighboring plates or on the concrete bed close to the sensors despite isolating elements. Based on this knowledge, we designed a filter method that uses time-frequency information to identify and eliminate these “apparent” impacts. Finally, we apply the filter to four field calibration datasets and show that it significantly reduces site-to-site differences between calibration coefficients and enables the derivation of a single calibration curve for total bedload at all four sites.

[2] Nicollier, T., **Antoniazza, G.**, Ammann, L., Rickenmann, D., & Kirchner, J. W. (2022a). Toward a general calibration of the Swiss plate geophone system for fractional bedload transport. *Earth Surface Dynamics Discussions*, 1-29.

Abstract: Substantial uncertainties in bedload transport predictions in steep streams have encouraged intensive efforts towards the development of surrogate monitoring technologies. One such system, the Swiss plate geophone (SPG), has been deployed and calibrated in numerous steep channels, mainly in the Alps. Calibration relationships linking the signal recorded by the SPG system to the intensity and characteristics of transported bedload can vary substantially between different monitoring stations, likely due to site-specific factors such as flow velocity and bed roughness. Furthermore, recent flume experiments on the SPG system have shown that site-specific calibration relationships can be biased by elastic waves resulting from impacts occurring outside the plate boundaries. Motivated by these findings, we present a hybrid calibration procedure derived from flume experiments and an extensive dataset of 308 direct field measurements at four different SPG monitoring stations. Our main goal is to investigate the feasibility of a general, site-independent calibration procedure for inferring fractional bedload transport from the SPG signal. First, we use flume experiments to show that sediment size classes can be distinguished more accurately using a combination of vibrational frequency and amplitude information than by using amplitude information alone. Second, we apply this amplitude–frequency method to field measurements to derive general calibration coefficients for 10 different grain-size fractions. The amplitude–frequency method results in more homogeneous signal responses across all sites and significantly improves the accuracy of fractional sediment flux and grain-size estimates. We attribute the remaining site-to-site discrepancies to large differences in flow velocity and discuss further factors that may influence the accuracy of these bedload estimates.

[3] Rickenmann, D., **Antoniazza, G.**, Wyss, C. R., Fritschi, B., & Boss, S. (2017). Bedload transport monitoring with acoustic sensors in the Swiss Albula mountain river. *Proceedings of the International Association of Hydrological Sciences*, *375*, 5-10.

Abstract: Bedload transport measurements with acoustic sensors were obtained during summer 2015 in the Albula River in Switzerland. An impact plate measuring system was used with geophone and accelerometer sensors. This system provides indirect estimations of bedload transport in watercourses. In April 2015, 30 impact sensors were installed in a new permanent measuring station to monitor continuously bedload transport in a mountain river with a large annual rate of sediment transport (around 90'000 $m^3 \cdot yr^{-1}$). Records of the first year of measurement showed that (i) the signal response in terms of geophone and accelerometer impulses is comparable for both types of sensors; (ii) there is a good correlation between discharge data and impulses recorded by both types of sensors; (iii) the critical discharge at the start of bedload transport is around 5 $m^3 \cdot s^{-1}$; (iv) a mean calibration factor for the geophone impulses can be estimated which is in a similar range as values determined from other sites with field calibration measurements.

[4] Rickenmann, D., Amman, L., Nicollier, T., Boss, S., Frischti, B**., Antoniazza, G.**, Steeb, N., Chen, Z., Wyss, C. R. & Badoux, A. (2022). Comparison of calibration characteristics of different acoustic impact systems for measuring bedload transport in mountain streams. *Earth Suface Dynamics 10* (6), 1165-1183.

Abstract: The Swiss plate geophone (SPG) system has been installed and tested in more than 20 steep gravel-bed streams and rivers, and related studies generally resulted in rather robust calibration relations between signal impulse counts and transported bedload mass. Here, we compare this system with three alternative surrogate measuring systems. A variant of the SPG system uses the same frame (housing) set-up but with an accelerometer instead of a geophone sensor to measure the vibrations of the plate (GP-Acc, for geophone plate accelerometer). The miniplate accelerometer (MPA) system has a smaller dimension of the impact plate and is embedded in more elastomer material than the SPG system. The Japanese pipe microphone (JPM) is a 1 m long version of the system that has been installed in many streams in Japan. To compare the performance of the four systems, we used calibration measurements with direct bedload samples from three field sites and an outdoor flume facility with controlled sediment feed. At our field sites, the systems with an accelerometer and a microphone showed partly large temporal variations in the background noise level, which may have impaired the calibration measurements obtained during certain time periods. Excluding these periods, the SPG, GP-Acc and JPM all resulted in robust calibration relations, whereas the calibration of the MPA system showed a poorer performance at all sites.

[5] **Antoniazza, G.** and Lane, S. N. (2019). Geomorphological processes in proglacial areas and their implications for landforms evolution at the scale of Ice Ages [Scientific report]. Swiss National Cooperative for the Disposal of Radioactive Waste (Nagra). Wettingen, Switzerland, 207 pp.

Abstract: Considering both the glacial history of Switzerland and a safety period of 1 Ma, long-term storage of radioactive waste in deep geological repositories must consider glacial overdeepening and the potential for excavation of radioactive waste repositories. In such cases, eroded sediment at the glacier bed may absorb radioactive contaminants, and the contaminated sediment may be re-mobilized and dispersed into the environment together with the rest of the eroded waste. Therefore, the following questions are of importance in the context of this review: (1) will the eroded and contaminated material be transported from below the glacier to the glacier portal? And (2) will the eroded and contaminated material be further transported, sorted, mixed, diluted, buried and/or transferred in/through the glacial forefield? The following literature study deepens those two questions, focusing notably on piedmont glacier dynamics and analogues. Both questions are mainly related to the processes of sediment erosion, transport and deposition in different river settings.

Chapter 2 addresses the theory of fluvial sediment transport in rivers, looking at conceptual understanding of the relationships between streamflow, slope, channel geometry, grain size, erosion and deposition. The Chapter addresses the basic mechanics of flow and thresholds of motion. It discusses the different modes of sediment transport (diluted load, suspended load, bedload), and gives particular attention to the main characteristics of sediment transport (relationships between streamflow and load, selective transport and development of bed pavements, bed forms, cycles of erosion and deposition). The Chapter finishes by presenting the main channel patterns and the dynamic evolution of river floodplains and deposits to contextualize sediment transport in the specific settings reviewed in the following Chapters of the report.

Chapter 3 focuses on sediment transport under glaciers. It describes the different modes of sediment transport under glaciers (e.g. integration of sediment from the bed into the ice, glacio-tectonic deformation and transport by meltwater). It then gives special attention to transport by meltwater, with an overview of subglacial channel theory. The chapter discusses water pathways and solutes/sediment export over daily and seasonal cycles of melt, such as during high-magnitude flow events (e.g. high-melt rate, rainfall-induced floods, outburst flood events, megafloods). The Chapter closes by looking at sediment transport under glaciers within overdeepenings.

Chapter 4 describes the main sediment-related glacio-fluvial features in glacial environments in terms of genesis, grain size distribution and morphological characteristics. This includes notably eskers, kames, kame terraces, drumlins and kettle holes. The chapter discusses the conditions required for their formation during Ice Ages, which can be of use for reconstructing the paleo-dynamics of former glaciers and ice sheets (e.g. water pore pressure at the bed, loose versus hard substrate).

Chapter 5 focuses on fluvial reworking of sediment in glacier forefields. Starting from a definition, the Chapter describes the main characteristics of the geomorphological processes responsible for the transport, sorting, mixing, dilution, enrichment and burying of sediment, and associated landforms, linking into Chapter 1. The Chapter first discusses the morphological response of glacial forefield as a function of glacially shaped topography and varying water and sediment inputs from the glacier (i.e. Chapter 3). It gives particular attention to the morphodynamics of braided rivers, which are the most common morphological expression of meltwater, and so high stream power, and high rates of sediment supply. Typical erosion rates in glacial forefields are reported, and the effects of hillslopes supply, ground ice, ground water, biogeomorphic succession and proglacial lakes on the morphodynamics and sediment continuity of glacier forefield are discussed.

Chapter 6 synthetizes the chain of processes described in Chapters 3, 4 and 5 and provides a conceptual model of sediment yield from glaciated catchments during phases of glacier advance and retreat. Starting from a situation where a glacier retreats, it describes the paraglacial adjustment of sediment as conditioned by glaciation, whose duration depends on the rate of glacier decay, sediment source exhaustion and/or sediment stabilization. It also describes the remobilization of stabilized or disconnected sedimentary sources during phases of glacier advance.

Chapter 7 focuses on the piedmont area of Northern Switzerland and draws from the first five Chapters to reconstruct the paleo-dynamics of the glacier lobe and the erosion and deposition of sediment over the course of multiple Ice Ages. The Chapter describes sediment cores and dating measurements to identify key processes and their relative timing. It uses current and paleo analogues to better constrain the dynamics of the former ice sheets over the course of Pleistocene Ice Ages in order to understand glacier and sediment transfer dynamics, and the required conditions for sediment to be stored in glacier forelands over the course of multiple Ice Ages.

The conclusions of the report in Chapter 8 provide scenarios of radioactive waste dispersion following glacier advance and retreat and identify further questions that need to be addressed.

[6] **Antoniazza, G**., & Lane, S. N. (2021). Sediment yield over glacial cycles: A conceptual model. *Progress in Physical Geography: Earth and Environment*, *45*(6), 842-865.

Abstract: The temporal variability in sediment export yield from glaciers over a timescale of multiple glacial cycles (e.g. 1×10^2 - 1×10^6 years) is of interest for a wide range of applications in glaciology, sedimentology, geomorphology, climatology and environmental engineering. However, the time required for the products of glacial erosion to be transferred through glaciated catchments and the extent to which glacially-conditioned sediment can be transiently stored within them are still poorly constrained and a matter of debate within the community. We propose a conceptual model of the variability in sediment exported from glaciers over multiple glacial cycles based on a literature review. Sediment yield is likely to be highly variable through a glacial cycle, notably between phases of glacier advance, retreat and re-advance due to changes in ice velocity and erosion rates, ice and meltwater transport capacity, and in glacially-conditioned sediment accessibility at the bed. Typically, early phases of glacier retreat and re-advance are expected to lead to the highest increase in sediment yield due to the ease with which the products of bedrock erosion can be accessed and reworked. In contrast, later phases of glacial (re)advance, once glacially-conditioned sedimentary sources become exhausted, may be characterized by intermediate rates of sediment export yield maintained through bedrock erosion. The latest phases of deglaciation, once glacially-conditioned sedimentary sources are either exhausted, stabilized or disconnected from active processes of sediment transfer, are likely to have the lowest rate of export. The conceptual model proposed in this paper fills a gap in the literature by developing a continuous pattern of sediment yield rate variability over the course of multiple glacial cycles, with wider implications for future research. However, its systematic applicability to various glacier settings and glaciations needs more field and modeling data to validate it.

[7] Lane, S. N., **Antoniazza, G.**, Dietze, M., & Mancini, D. (2021). Bedload transport: Are we doing restoration right in the face of alpine climate change. In *Proceedings of the International Symposium on Bedload Management* (pp. 8-10).

Abstract: Alpine landscapes are undergoing climate warming at a higher rate than other regions of the world. The current and future impacts of this warming on the cryosphere (snow and ice) and their implications for stream flows are now well known and there exist predictions of how snow, ice and river flows are likely to evolve in Alpine environments over the 21st century. There is no doubt that such changes will also impact bedload transport in Alpine streams. Bedload transport in many Alpine streams is, however, also impacted significantly by the direct effects of human activities such as hydropower and gravel extraction. These direct effect have dominated the concerns of bedload management or river restoration over the last decade or more. It is therefore a logical question to ask whether or not river restoration and the bedload management policies thought necessary to support them needs to adapt in the face of climate change. The lead in time to many policy solutions for bedload management, especially those involving new infrastructure, is not negligible. Given the current rate of warming in Alpine environments, higher than many non-Alpine regions, climate change sensitive bedload management may already be needed. However, the target of river restoration should not be bedload transport itself but rather the societal ecosystem services that are sustained by the consequences of bedload transport. This may be in terms of the right level of sediment evacuation to stop bed level rise during a flood that can lead to catastrophic loss of property and even life; or the gravel sized sediment that spawning salmonids need during the late autumn of each year; as examples of a wider set of services that rivers provide. Simply developing a bedload management policy to be climate sensitive is not enough; the focus has to be on the consequences of such policy for erosion, deposition, grainsize, river morphodynamics etc. These need to be evaluated at the scale of a river basin and so also need to recognize the basic challenges posed by sediment continuity; a policy decision to increase or to decrease bedload transport locally will have downstream consequences that may be either positive or negative. Communities and ecosystems downstream, may have already become accustomed to a certain bedload transport regime and this further complicates the problem. In this paper, we seek to answer six broad questions that should be part of a sustainable bedload management policy in Alpine environments in the light of climate change: (1) What must we be capable of predicting? (2) Is there a bedload transport "hockey stick" in Alpine streams? (3) Can we predict bedload transport rates now with sufficient precision and accuracy for them to be usable in predictions of the future? (4) How might bedload transport capacity change in the future in Alpine basins? (5) How might sediment supply change in the future in Alpine basins? (6) So, are we doing restoration right in the light of Alpine climate change?

[8] James, M. R., **Antoniazza, G.**, Robson, S., & Lane, S. N. (2020). Mitigating systematic error in topographic models for geomorphic change detection: accuracy, precision and considerations beyond off-nadir imagery. *Earth Surface Processes and Landforms*, *45*(10), 2251-2271.

Abstract: Uncrewed aerial vehicles (UAVs) and structure-from-motion photogrammetry enable detailed quantification of geomorphic change. However, rigorous precision-based change detection can be compromised by survey accuracy problems producing systematic topographic error (e.g. 'doming'), with error magnitudes greatly exceeding precision estimates. Here, we assess survey sensitivity to systematic error, directly correcting topographic data so that error magnitudes align more closely with precision estimates. By simulating conventional grid-style photogrammetric aerial surveys, we quantify the underlying relationships between survey accuracy, camera model parameters, camera inclination, tie point matching precision and topographic relief, and demonstrate a relative insensitivity to image overlap. We show that a current doming-mitigation strategy of using a gently inclined (<15°) camera can reduce accuracy by promoting a previously unconsidered correlation between decentring camera lens distortion parameters and the radial terms known to be responsible for systematic topographic error. This issue is particularly relevant for the wide-angle cameras often integrated into current-generation, accessible UAV systems, frequently used in geomorphic research. Such systems usually perform on-board image pre-processing, including applying generic lens distortion corrections, that subsequently alter parameter interrelationships in photogrammetric processing (e.g. partially correcting radial distortion, which increases the relative importance of decentring distortion in output images). Surveys from two proglacial forefields (Arolla region, Switzerland) showed that results from lower-relief topography with a 10°-inclined camera developed vertical systematic doming errors > 0·3 m, representing accuracy issues an order of magnitude greater than precision-based error estimates. For higher-relief topography, and for nadir-imaging surveys of the lower-relief topography, systematic error was < 0·09 m. Modelling and subtracting the systematic error directly from the topographic data successfully reduced error magnitudes to values consistent with twice the estimated precision. Thus, topographic correction can provide a more robust approach to uncertainty-based detection of event-scale geomorphic change than designing surveys with small off-nadir camera inclinations and, furthermore, can substantially reduce ground control requirements.

[9] Dai, W., Guanghui, Z., **Antoniazza, G.**, Zhao, F., Chen, K., Lu, W. And Lane, S. N. (under review). Improving UAV-SfM photogrammetry for measurement of high-relief terrain: image collection strategies and ground control quantity. Submitted to *Earth Surface Processes and Landforms.*

Abstract: Image collection strategies and ground control are of particular importance for UAV–SfM photogrammetry, and the generalization of their effects has proved elusive. This study designed various photogrammetric scenarios to investigate the effects of image collection strategies, ground control quantity, and their interaction on digital elevation model (DEM) errors and their spatial structure in high-relief terrain. The results of 10^5 UAV–SfM scenarios provide insights for improving UAV-SfM practices. A high image capture angle (＞20°) enhances camera calibration quality for high-relief terrain decreasing the magnitude of errors (mean error and standard error) and also their spatial correlation. A high camera inclination also reduces the sensitivity of mean error and standard error to flying height, but does not reduce the sensitivity of the error's spatial correlation to flying height. Including additional data (e.g., supplemented convergent images and images captured at multiple flying heights) has only a minor effect if imageries are highly inclined. GCPs provide more effective constraints for successful bundle adjustment than image collection strategies. The mean error and standard error decline quickly with a small number of GCPs and then become stable in all scenarios, but the spatial correlation of error can be further improved with increasing GCPs. However, the effects of GCP quantity also interact with image collection strategies. High camera inclination seems to reduce requirements for GCPs, while the flying height and combination dataset strategies have little effect on necessary GCP quantity. Finally, the distribution of GCPs still affects the errors, but the effect of GCP distribution becomes less important with the increase in the number of GCPs.

[10] **Antoniazza, G.**, Bakker, M., & Lane, S. N. (2019). Revisiting the morphological method in two-dimensions to quantify bed-material transport in braided rivers. *Earth Surface Processes and Landforms*, *44*(11), 2251-2267.

Abstract: Research in the 1990s showed that bed-material transport rates could be estimated at the reach scale in both one-dimension and, over small spatial scales (10s of m), in two-dimensions. The limit on the latter was the spatial scale over which it was possible to obtain distributed data on morphological change. Here, we revisit the morphological method given progress in both topographical data acquisition and hydraulic modelling. The bed-material transport needed to conserve mass is calculated in both one and two dimensions for a 1600m× 300m Alpine braided river "laboratory". High-resolution topographical data were acquired by laser scanning to quantify Digital Elevation Models (DEMs), and morphological changes caused by the flushing of the water intake were derived from repeated surveys. Based on DEMs of differences, 1D bed-material transport rates were calculated using the morphological method. Then, a 2D hydraulic model was combined with a topographic correction to route sediment through the network of braided channels and to obtain a spatially variable estimate of transport in both downstream and cross-stream directions. Monte Carlo simulation was applied to the routing model parameters, allowing identification of the most probable parameter values needed to minimize negative transport. The results show that within-section spatial compensation of erosion and deposition using the 1D treatment leads to substantial local errors in transport rate estimates, to a degree related to braiding intensity. Even though the 2D application showed that a large proportion of the total transport was actually concentrated into one main channel during the studied low flow event, the proportion of transport in secondary anabranches is substantial when the river starts braiding. Investigations of the effects of DEM resolution, competent flow duration and survey frequency related to 'travelling bedload' and sequential erosion-deposition emphasized the critical importance of careful data collection in the application of the morphological method.

[11] Bakker, M., **Antoniazza, G.**, Odermatt, E., & Lane, S. N. (2019). Morphological response of an alpine braided reach to sediment-laden flow events. *Journal of Geophysical Research: Earth Surface*, *124*(5), 1310-1328.

Abstract: Braided gravel-bed rivers show characteristic temporal and spatial variability in morphological change and bedload transport under steady flow and sediment supply rates. Their morphodynamic behavior and long-term evolution in response to nonstationary external forcing is less well known. We studied daily morphological changes in a well-constrained reach of an Alpine braided river that is subject to regulated sediment-laden flows, associated with hydroelectric power exploitation, as well as occasional floods. We found that net reach erosion and deposition were forced by upstream sediment supply, albeit in a nonlinear fashion. The spatial distribution of morphological change and inferred spatially-distributed sediment transport rates varied strongly along the braided reach and between successive sequences of flushing. Local morphological change was driven by two factors: (1) local relief, leading to the preferential filling of topographic lows and erosion of highs, particularly during longer duration floods, which allow braided dynamics to be maintained; and (2) system memory, leading to a negative autocorrelation in bed level changes where erosion was followed by deposition of similar magnitude and vice versa. This effect was associated with the temporary storage of high sediment loads from flushing due to the abrupt on-off nature of these flows and reveals the relatively efficient transport of sediment in a river that is heavily impacted upon by flow abstraction. In general, the internal morphodynamics of the braided river condition their own response to external forcing events and thus sediment transfer.

[12] Dai, W., Xiong, L., **Antoniazza, G.**, Tang, G., & Lane, S. N. (2021). Quantifying the spatial distribution of sediment transport in an experimental gully system using the morphological method. *Earth Surface Processes and Landforms*, *46*(6), 1188-1208.

Abstract: Whilst time-series of sediment transport in gullies in both laboratory experimental and field settings can be determined through instrumentation, quantifying the spatial distribution of transport rates remains challenging. The morphological method, which was proposed for estimating bed-material transport in both one- and two-dimensions in rivers, provides an alternative. Here, we developed this method for gully systems. A laboratory catchment was used to simulate gully erosion. High-resolution topographical data were acquired by close-range digital photogrammetry. Morphological changes were determined using high-resolution topographic data and an associated level of detection. Based on measured morphological changes, one-dimensional (1D) and two-dimensional (2D) sediment transport rates were calculated by cross-section routing (1D) and cell by cell routing (2D). The 1D application provided a general trend of longitudinal variation of sediment transport for the whole gully system, increased gradually from zones of headward extension to a zone downstream where erosion and deposition were in balance, and sediment transport rates less variable in space. For the 2D application, hydrological and blended hydrological-hydraulic routing solutions were compared. We found that the level of negative transport was insensitive to whether or not a blended hydrological-hydraulic routing was used and that results from applying the hydrological routing throughout were not significantly degraded. We also found that consideration should be given to spatial and temporal resolution of the topographic data. The 2D application provided spatial patterns of sediment transport that vary with gully evolution. The main gully remained a high transport corridor but branch transport became more important through time. The framework we report provides an additional tool for both experimental and field quantification of the spatial patterns of sediment transport in gullies; and quantification of how these patterns change under different forcing factors.

II - Bedload transport monitoring in Alpine rivers: variability in Swiss Plate Geophone response

Personal contribution to the research article

I designed the impact experiment with Dieter Rickenmann (DR), Carlos Wyss (CW) and Stefan Boss (SB), I tested it in the laboratory, before performing it at the four investigated measuring stations. I performed the data curation, data investigation and all the analysis under the supervision of DR, with the help of CW and Tobias Nicollier (TN). I wrote the original draft of the manuscript, which was revised by all the other co-authors. Following the review process at the journal *Sensors*, I revised the manuscript until final publication.

Bedload transport monitoring in Alpine rivers: variability in Swiss Plate Geophone response

Gilles Antoniazza[1,2], Tobias Nicollier[1], Carlos R. Wyss[1], Stefan Boss[1] and Dieter Rickenmann[1]

[1] Swiss Federal Institute for Forest, Snow and Landscape Research (WSL), Mountain hydrology and mass movements, Zürcherstrasse 111, CH-8903 Birmensdorf.

[2] University of Lausanne (Switzerland), Institute of Earth Surface Dynamics (IDYST), Géopolis, CH-1015 Lausanne

Reference: Antoniazza, G., Nicollier, T., Wyss, C. R., Boss, S., & Rickenmann, D. (2020). Bedload transport monitoring in Alpine rivers: variability in Swiss Plate Geophone response. *Sensors*, *20*(15), 4089.

Abstract: Acoustic sensors are increasingly used to measure bedload transport in Alpine streams, notably the Swiss Plate Geophone (SPG) system. An impact experiment using artificial weights is developed in this paper to assess the variability in individual plate response and to evaluate the extent to which calibration coefficients can be transferred from calibrated plates to non-calibrated plates at a given measuring site and/or to other measuring sites. Results of the experiment over 43 plates at four measuring sites have notably shown : (a) that the maximum amplitude [V] recorded by individual plates tends to evolve as a power law function of the impact energy [J], with an exponent slightly larger than 1, for all the plates at all measuring sites; (b) that there is a substantial propagation of energy across plates that should be taken into account for a better understanding of the signal response; and (c) that the response of individual plates is in most cases consistent, which suggests that calibration coefficients are comparable within and in between measuring sites, but site-specific and plate-specific variabilities in signal response have to be considered for a detailed comparison.

Keywords: bedload transport, acoustic sensors, Alpine stream, Swiss Plate Geophone system (SPG), impact experiment, sensor sensitivity, sensor calibration.

II-1 Introduction

Bedload transport in rivers represents the motion of coarse particles of the bed by rolling, sliding and saltation when the shear force of the water flow exceeds the resistance force of the bed matrix (Richards, 2004; Bridge, 2009; Knighton, 2014). As such, bedload is both a consequence of fluvial erosion and a driver for fluvial deposition (Ashworth and Ferguson, 1986; Richards, 2004; Leopold et al., 2012). Bedload has therefore a critical impact on flooding risk (Stover and Montgomery, 2001; Lane et al., 2007; Rickenmann et al., 2016), can induce bank erosion and in turn impact infrastructures (Ruiz-Villanueva et al., 2014; Mikuś et al., 2016). It can also reduce the efficiency of hydropower facilities (Annandale, 2016; Gabbud and Lane, 2016; Schleiss et al., 2016) and impact fluvial ecosystems both negatively and positively (Harrison et al., 2011; Wang et al., 2014). Bedload transport therefore matters for many ecosystems and human activities in the vicinity of rivers, notably in Alpine environments where the rate of climate warming is accelerated and lead to rapid glacier recession and/or an increase in the frequency of extreme hydrological events, which both tend to enhance bedload activity (Lane et al., 2017; Lane and Nienow, 2019).

At the same time, bedload transport remains one of the most elusive phenomenon to measure and predict. This is notably due to the complex interactions between the flowing water, the heterogeneous nature of river bed sediments, the unsteady hydraulics (themselves being a product of mobile channel boundaries) and the sediment transport (Parker et al., 1982;

Ashworth and Ferguson, 1986; Gomez, 1991; Buffington and Montgomery, 1997). These elements particularly matter in Alpine environments where high and spatially-variable gradients in energy are observed, associated to the complex effects of coarse roughness elements on the stream bed, the turbulent and unsteady hydraulics that result, and the frequent reworking of stream bed by erosion and deposition (Nitsche et al., 2011; Rickenmann and Recking, 2011; Schneider et al., 2015; Lamb et al., 2017; Bakker et al., 2019).

Early measurements of bedload have used direct sampling with baskets or pressure-difference samplers (Helley and Smith, 1971; Bunte et al., 2004). Discrete in time and at-a-point in space, they however failed to quantify the spatio-temporal variability in bedload transport (Parker et al., 1982; Gomez, 1991). Meanwhile, measurements of the filling rate of traps dug across streams have provided cross-section integrated estimates of bedload transport rate (Milhous, 1973; Hayward and Sutherland, 1974; Lenzi et al., 1999). However, such traps are often rapidly filled, they affect the hydraulic conditions and provide no detail on the temporal (within events) and spatial (across the section) variations of bedload transport (Gomez, 1991; Hicks and Gomez, 2003). Progress with passive acoustic sensors over the past 20 years opened new perspectives for the continuous monitoring of bedload transport (Barton et al., 2010; Rickenmann, 2017; Koshiba et al., 2018; Goodwiller et al., 2019). Bedload produces acoustic (in the water column) and elastic (in media such as the riverbed) waves that are measurable with acoustic sensors. The magnitude of these waves tends to be proportional to bedload transport rates. Therefore, acoustic sensors deployed in a river and measuring the sounds (e.g. hydrophones, microphones) or the vibrations of structures impacted by particles in transport (e.g. geophones, accelerometers, piezoelectric sensors) are able to monitor continuously the bedload transport intensity, without modifying the surrounding hydraulic conditions. When a network of acoustic sensors is deployed (along and/or across a channel), both spatial and temporal variations of bedload transport intensity can be monitored. This approach has been successfully used in many environments, including steep and highly-energetic Alpine streams (Rickenmann et al., 2012, 2014b; Wyss et al., 2016a, 2016b, 2016c), for both theoretical (Kuhnle et al., 2017; Mizuyama et al., 2010a; Rickenmann et al., 2012; Wyss et al., 2016a, 2016b) and applied (Badoux et al., 2009; Rickenmann et al., 2014b, 2017; Rickenmann and Fritschi, 2017) purposes. By providing an indirect signal of bedload transport intensity, acoustic sensors however require calibration and validation to transform the signal recorded by the sensors into an actual mass of bedload in transport (Rickenmann et al., 2012, 2014b; Wyss et al., 2016b; Rickenmann, 2017).

Among acoustic sensors, the Swiss Plate Geophone (SPG) system developed by the Swiss federal Institute WSL is one of the acoustic measuring systems with the most widespread experience to monitor bedload transport in Alpine streams (Rickenmann et al., 2012, 2014b; Rickenmann, 2017). Over the past 20 years, more than 20 measuring stations have been equipped with such a measuring system in Switzerland, Austria, Italy, Israel and in the United States (Rickenmann, 2017). The SPG system is made of a series of steel plates embodied in a concrete structure flush with the river bed to not affect surrounding hydraulic conditions. Particles rolling, sliding, and saltating over the bed impact the steel plates, and a geophone sensor mounted from below each plate continuously records the induced vibration. SPGs are typically mounted in a line across the stream to cover with sensors the entire channel width (Rickenmann et al., 2017; Rickenmann and Fritschi, 2017). But like any other acoustic measuring system, the SPG requires calibration and validation to transform the recorded signal into an actual mass of bedload in transport. This is typically performed by collecting direct bedload samples that can be related to the signal measured by the sensors (Rickenmann et al., 2012; Rickenmann and Fritschi, 2017; Rickenmann et al., 2014b). Such calibration and validation samples are typically difficult to obtain and require the design of robust sediment baskets that can be deployed in Alpine streams during high flows. This has been achieved so far through two main approaches. First, by using mobile sediment baskets mounted on a rail, which is built along a concrete sill and allows to move the sediment basket across the section to collect bedload particles that have impacted the plates (Rickenmann et al., 2012, 2014b). Second, by using sediment baskets or net samplers mounted on a crane and operated from a truck on the river bank, which can collect bedload samples downstream of the impacted plates (Rickenmann et al., 2014b; Kreisler et al., 2017; Rickenmann and Fritschi, 2017; Nicollier et al., 2019, 2020).

However, the collection of sufficient bedload samples for each plate at a given measuring site is highly demanding in terms of field effort, infrastructure, cost and time. Therefore, it is important to assess the variability in signal response in space, between different plates and different sites. In doing so, the extent to which calibration coefficients can be transferred from calibrated plates to uncalibrated ones can be evaluated. The general objective of this paper is to assess the variability in signal response of SPGs to impacts of similar magnitude. For this purpose, we performed an experiment using synthetic weights that are employed to artificially generate an impact on the plate, which is recorded by the geophone sensor. The impact experiment was conducted on each plate at four measuring stations in the Swiss Alps equipped with the SPG system. In particular, we were interested to examine (i) how variable the signal response is between individual plates within and in between the measuring stations, and (ii) how much energy propagates from an impacted plate towards non-impacted plates. These two elements matter because ultimately they both influence the calibration relation obtained for a given site and plate, and the potential transferability of calibration relations to other (uncalibrated) plates.

II-2 Materials and Methods

The aim of the experiment developed in this paper is to study the response variability of Swiss Plate Geophones. To do so, an impact test using artificial weights is performed on 43 plates spread over four sites. First, we describe the design of both the weights and the impact experiment. Then, we report on the experiment using a laboratory SPG. Finally, we describe the application of the impact experiment at the four field sites.

II-2.1 Material

The impact experiment developed in this paper was performed as follows. Impacts were produced by using a generic steel pedologist hammer (Figure II-1a), whose usual purpose is to pack down soils by letting fall down a weight along a stake on its base, which lies on the soil surface. The weight (Figure II-1b) hits the hammer base and energy is transmitted through it to the ground (Figure II-1c). During the experiment, the apparatus was set at the exact center (uncertainty ± 0.01 m) of each tested plate (Figure II-1d), and a minimum support pressure was given to the stake to not add any unnecessary random tension to the plate beside the mass of the device itself (2.272 kg + mass of the released weight [kg]; Table II-1). The SPGs are made from stainless steel and have standard dimensions of 492 mm width, 358 mm length (in flow direction), and 15 mm thickness (Rickenmann, 2017; Rickenmann et al., 2012; Wyss et al., 2016b), resulting in a mass of 21 kg. The weights used in the impact experiment are composed of PVC cylinders with the same diameter as the hammer base (0.05 m). Central holes of 0.02 m diameter were drilled trough the PVC weights to make them fall down along the metal stake. The diameter of the central hole is slightly larger than the diameter of the stake (0.015 m) to reduce the risk of friction when falling. Then, each PVC cylinder was cut at the height matching the wanted mass (Table II-1). Because most of the tested plates were underwater during the experiment (up to 0.1 m), it was necessary to add a PVC cylinder of 0.1 m height above the base (so-called ‘heightening cylinder’) and seal them together to make sure the weight would hit the base above water level. Striking the plates from above the water surface represents a limit as it is not likely to mimic how sediment actually impact the plates in natural flow conditions. Yet, the field tests were performed at varying low-flow conditions (from no-water to flowing water up to ~ 0.1 m), and thus there is a partial similarity to natural transport conditions.

(a) The pedologist hammer used during the experiment

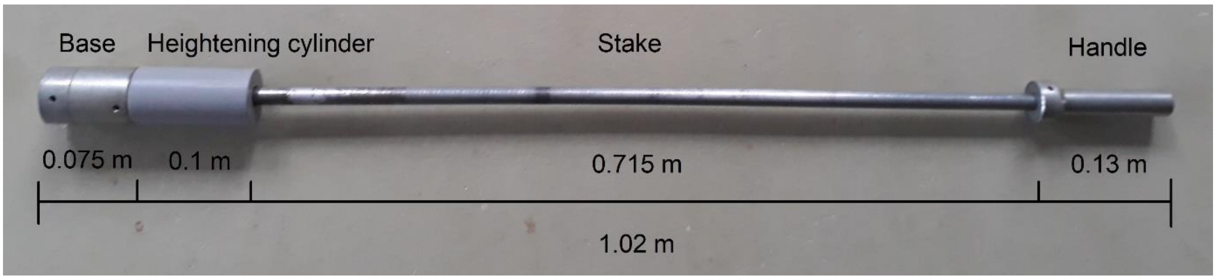

(b) The different weights used during the experiment

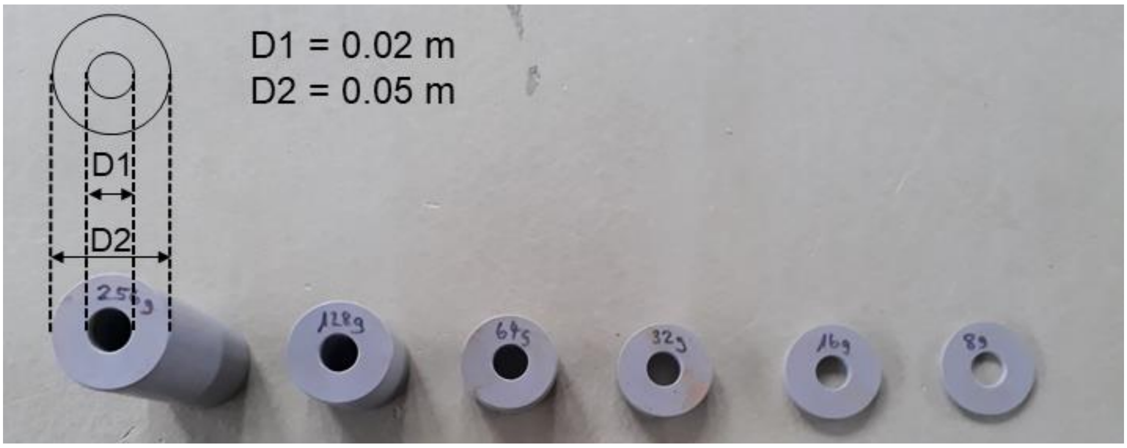

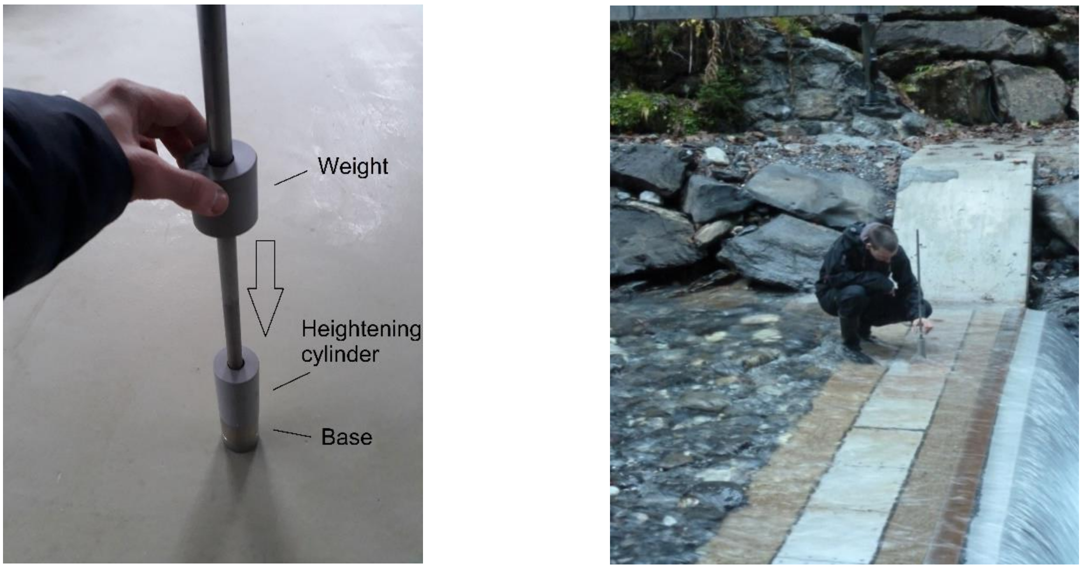

(c) Illustration from the laboratory

(d) Illustration from the field

Figure II-1. Set up of (a) the pedologist hammer, (b) the weights used for the experiment, (c) illustration of the experiment in the laboratory and (d) in the field.

The setting of the impact experiment developed in this paper also includes some sources of uncertainty. Both the surrounding air and the potential friction of the weight along the stake on the way down can affect the delivered energy. In addition, the propagation of the energy from the weight to the plate through the base can increase the variability in the transmitted energy for an impact assumed to be of same magnitude. Therefore, an initial laboratory experiment was performed to better constrain the experiment and make sure it was reproducible. In addition, video recordings of the falling weights were taken using a high-speed camera in order to quantify the velocity of the weight at the impact and the associated kinetic energy delivered for each weight-height drop category.

Table II-1. Characteristics of the devices used for the experiment

Element	Mass [kg]	Length [m]	Diameter [m]	Remarks
Hammer (without handle)	2.386	0.89	0.05 / 0.015	base / stake
Hammer (with handle)	2.948	1.02	0.05 / 0.015	base / stake
Heightening cylinder	0.250	0.1	0.05 / 0.02	cylinder / hole
Hammer set up for experiments (without handle + heightening cylinder)	2.272	0.89	0.05 / 0.015 / 0.05	base / stake / height cylinder
Weights	0.256	0.104	0.05 / 0.02	cylinder / hole
	0.128	0.051	0.05 / 0.02	cylinder / hole
	0.064	0.021	0.05 / 0.02	cylinder / hole
	0.032	0.013	0.05 / 0.02	cylinder / hole
	0.016	0.007	0.05 / 0.02	cylinder / hole
	0.008	0.003	0.05 / 0.02	cylinder / hole

II-2.2 Laboratory experiment

II-2.2.1 Reproducibility test

The initial laboratory experiment was performed on a single plate installed at the Laboratory of Hydraulics, Hydrology and Glaciology of the ETH Zürich (Wyss et al., 2016a, 2016b) in a similar configuration as the SPGs installed in the field.

In a first phase of the experiment, a reproducibility test was conducted by impacting the laboratory plate with a medium weight mass – 0.064 kg – dropped from a 0.1 m falling height, and repeating the same procedure 25 times. The maximum positive amplitude of the signal A_{max} [V] as defined by Wyss et al. (2016b) was recorded for each impact. The mean, standard deviation, 5th and 95th centile of the experiment after k= 5, 10, 15, 20 and 25 impacts were calculated out of 5 million random combinations (k tests out of the total 25 tests). Results (Figure II-2a) show that the standard deviation of the impacts stabilizes when the amount of impacts reaches ~ 10. Based on this knowledge, we decided to repeat a same impact 10 times per category of weight-height to take into account the variability in energy transmission from the impacting weight to the plate through the hammer base when conducting the field experiment. An example of a given category of impact (in terms of weight and height) repeated 10 times, such as performed in the field, is presented in Figure II-2b (here for a 0.064 kg weight dropped from a 0.1 m height).

(a) Reproducibility test with a 0.064 kg weight dropped 25 times from 0.1 m height.

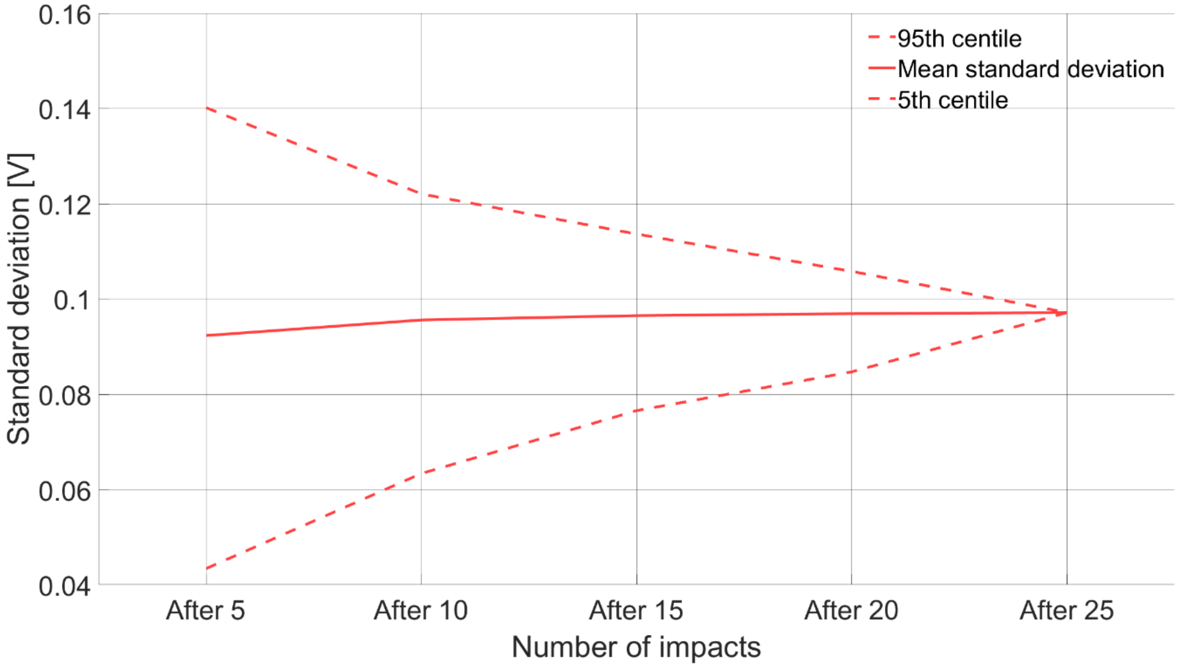

(b) Example of a serie of 10 impacts with a 0.064 kg weight dropped from 0.1 m height.

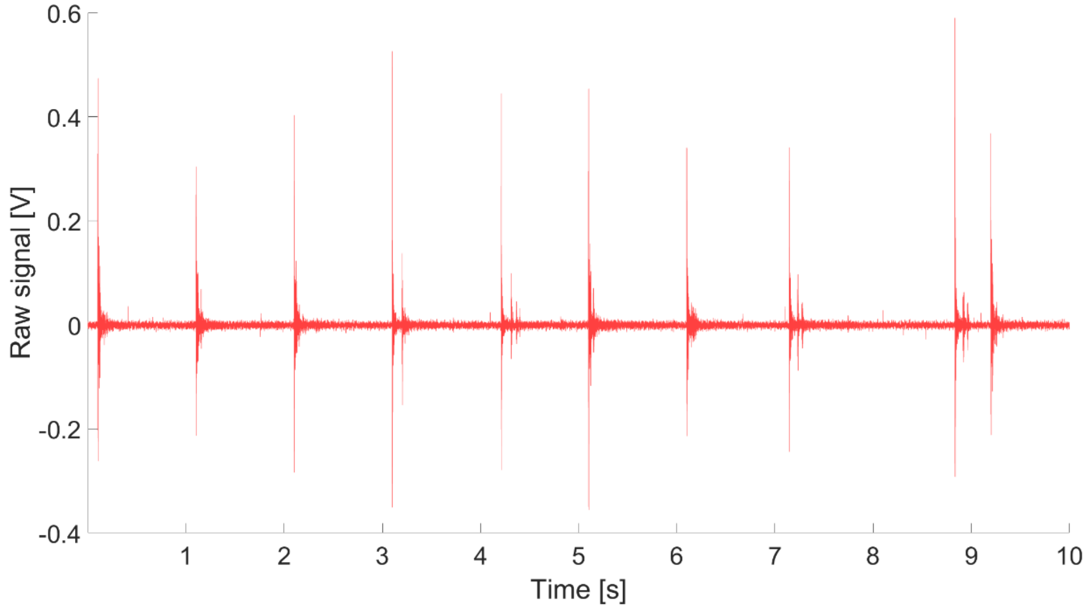

Figure II-2. (a) Reproducibility test conducted in the VAW laboratory with a weight of 0.064 kg dropped 25 times from a 0.1 m height, the graph shows the standard deviation of maximum amplitudes as function of cumulative number of tests calculated in 5 million random combinations; (b) voltage associated to 10 impacts induced by a 0.064 kg weight dropped from a 0.1 m height. The maximum positive amplitude [V] is recorded for each impact.

II-2.2.2. Experiment design

Although the shape of the weights is unlikely to closely mimic the impact of natural bedload particles, we wanted the impacts of the experiment to cover a range of voltage that is close to the one recorded by the SPG for natural bedload events. Earlier works showed they were typically ranging between 0.02 V and 10 V in Alpine rivers equipped with the SPG system (Rickenmann et al., 2012; Wyss et al., 2016b). To fulfill this condition, initial tests in the laboratory were carried out with 9 different categories of weight-height according to Table II-2. Both the maximal amplitude of the impacts $\overline{A_{max}}$ [V] (mean of 10 impacts) and their standard deviation $S_x\, A_{max}$ [V] (standard deviation of 10 impacts) tend to increase with the energy released by a given combination of weight-height (Table II-2). The variability between the impacts of a given drop category tends however to remain relatively low, between 6-26 % of the mean maximum amplitude $\overline{A_{max}}$. Given the uncertainty related to the energy transmitted by the impacting weight to the plate through the hammer base, the variability in the recorded A_{max} between impacts of same theoretical magnitude appears to be acceptable.

Table II-2. Mean and standard deviation (10 impacts) for each of the 9 categories of drop weight-height that were retained from the laboratory experiment to be conducted in the field.

Category	**Mass [kg]**	**Height [m]**	$\overline{A_{max}}$ [V]	σ_{Amax} [V]	$\sigma_{Amax}/\overline{A_{max}}$ [%]
1	0.008	0.1	0.042	0.011	26
2	0.016	0.1	0.069	0.012	17
3	0.032	0.1	0.165	0.034	21
4	0.064	0.1	0.353	0.038	11
5	0.128	0.1	1.267	0.201	16
6	0.256	0.1	3.661	0.491	13
7	0.256	0.2	4.93	0.581	12
8	0.256	0.4	7.341	0.877	12
9	0.256	0.6	9.442	0.651	7

II-2.2.3 Kinetic energy of the impacts

Because the likeliness of having friction along the stake is greater for longer fall distance (i.e. falling height of 0.6 m as compared to 0.1 m), we investigated the actual kinetic energy produced on average for each category of weight-height drops. To do so, we performed videos in the laboratory using a high-resolution AOS X-PRI high-speed camera and filmed the speed at which the different categories of weight-height impacted the base of the pedologist hammer. We considered the last 5 ms before the impact, and repeated each fall 3 times. The kinetic energy was derived from the falling speed before the impact, as:

$$E_k = 0.5 * m * \ v^2 \qquad \text{[II-1]}$$

where E_k is the kinetic energy of the impact [J], m is the mass of the weight [kg] and v [m/s] is the speed of the weight during the last 5 ms before the impact. Table II-3 summarizes the falling speed and kinetic energy for each category of weight-height (mean of 3 drops). As expected, the fall velocity and the kinetic energy of the weights increase together with the weight mass and the height of the drop. The calculation of the kinetic energy allows to investigate the relationship with the A_{max} recorded for each category of impact, which seems to be best expressed by a power law function, with an exponent slightly above 1 (Figure II-3). In the laboratory, the experiment covers an energy field between 0.006 and 1 J, and A_{max} ranges between 0.04 and 10 V, which fits well the targeted range of amplitudes that is observed for natural bedload transport events in Alpine rivers equipped with the SPG system (Rickenmann et al., 2012; Wyss et al., 2016b).

Table II-3. Average fall velocity and kinetic energy for each category of weight-height calculated based on high-speed camera video recordings.

Category	**Mass [kg]**	**Height [m]**	$\overline{v}$ **[m/s]**	$\overline{E_k}$ **[J]**
1	0.008	0.1	1.27	0.006
2	0.016	0.1	1.32	0.014
3	0.032	0.1	1.311	0.027
4	0.064	0.1	1.234	0.049
5	0.128	0.1	1.317	0.111
6	0.256	0.1	1.347	0.232
7	0.256	0.2	1.89	0.457
8	0.256	0.4	2.636	0.891
9	0.256	0.6	2.883	1.064

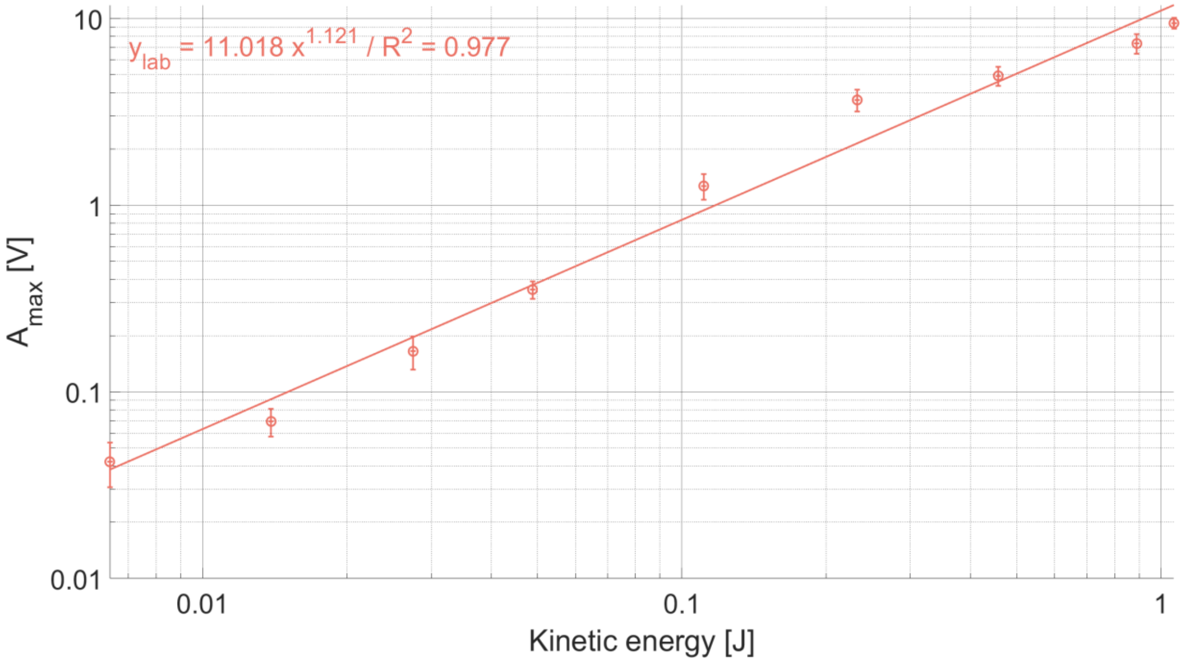

Figure II-3. The maximum amplitude A_{max} recorded by the laboratory plate is best expressed by a power law function of the kinetic energy released by the impact, with an exponent slightly above 1.

II-2.3 Field experiment

After testing the applicability of the method in the laboratory, each plate at four Swiss field measuring stations was impacted 10 times for each of the 9 categories of weight-height drop presented in Table II-3, which means that each plate was impacted 90 times. Each of those measuring stations was constructed in a similar way: a concrete sill across the channel width was built flush with the riverbed, and a steel frame is embedded into the sill. The plates are then mounted within the steel frame, and 20DX geophone sensors from Geospace technologies (Houston, Texas, USA) are mounted from below the plate in a PC801 LPC Landcase set in an aluminum box (Rickenmann et al., 2017). During sediment transport events, bedload particles sliding, rolling or saltating over a given steel plate produces an impact shock that induces a change of the electrical voltage measured by the geophone, which is assumed to be proportional to the amount of bedload in transport (Rickenmann et al., 2012, 2014b; Wyss et al., 2016b). Each plate is acoustically isolated from each other by elastometer elements, and the geophone sensors are connected to an industrial PC that records the signal at a frequency of 10 kHz. The amount of plates per measuring station is set so that the greatest portion of the cross-section is covered by sensors.

In the frame of this paper, we aim to quantify the variability in plate response on the one hand, but also the extent to which there may be some energy that propagates from impacted plates towards non-impacted plates. Indeed, earlier analyses of the SPG system (Rickenmann et al., 2012, 2014b; Wyss et al., 2016a) have suggested that there may be some energy that propagates across plates despite the isolating elastomer elements. This needs to be quantified properly to know how it influences the relationship between the signal recorded by the plate and the actual bedload mass in transport on the one hand, and the extent to which calibration coefficients could be used more broadly within bedload measuring stations equipped with the SPG system on the other hand. At each measuring station, SPGs are grouped together into steel frame segments holding 5-6 plates with sensors. The specific setting of each measuring station in terms of number of plates and segments is presented in Table II-4 and Figure II-4.

Table II-4. Number of tested plates at four measuring stations where the impact experiment was conducted. The four measuring stations are all located within the Swiss Alps, at Alpine rivers that give their name to the measuring site.

Measuring station	Location	Coordinates (WGS 84)	Number of plates	Total number of impacts
Avançon de Nant	Western Swiss Alps	46° 15’ 12’’ N / 7° 06’ 35’’ E	10	90
Ablula	Eastern Swiss Alps	46° 39’ 41’’ N / 9° 34’ 48’’ E	14	1260
Naviscence	Southern Swiss Alps	46° 07’ 52’’ N / 7° 37’ 38’’ E	12	1080
Riedbach	Southern Swiss Alps	46° 15’ 44’’ N / 7° 55’ 17’’ E	07	630
Total	Total		43	3060

The operation of the measuring station at the Avançon de Nant (Western Swiss Alps) started in 2014 and results from a collaboration between the University of Lausanne (UNIL), the Swiss Federal Institute for Forest, Snow and Landscape Research (WSL) and the ETH-Zürich. The station is equipped with 10 SPGs (Figure II-4a), installed in two different segments. When the experiment was performed in October 2015, the flow discharge was very low and there was only ~ 0.02 m of water flowing over the concrete weir. Therefore, no additional random tension was added to the pedologist hammer by the need of holding it, and the experiment could be conducted with a minimal disturbance of the measuring system, close to laboratory conditions.

The measuring station at the Albula Alpine river (Eastern Swiss Alps) was built in 2015. Over the 15 meters width of the channel at the location of the station (Figure II-4b), 30 impact plates were installed, below which 15 geophones and 15 accelerometers were alternatively set up. The impact plates at the Albula are connected into 5 segments, gathering 6 sensors each (3 geophones and 3 accelerometers). In the frame of this project, the experiment was only conducted on the SPGs to make the results comparable to the datasets from other stations where only SPGs are mounted. The experiment was conducted on every SPG but n°1 (omission). When we performed the experiment in November 2015, the discharge was fairly low, but there was still about ~ 0.1 m of water depth over the sensors flowing at ~ 0.3-0.4 m/s, which forced us to slightly support the pedologist hammer by holding the stake during the experiment. However little the support was, it may have added some additional tension to the plates.

(a) Avançon de Nant **(b)** Albula

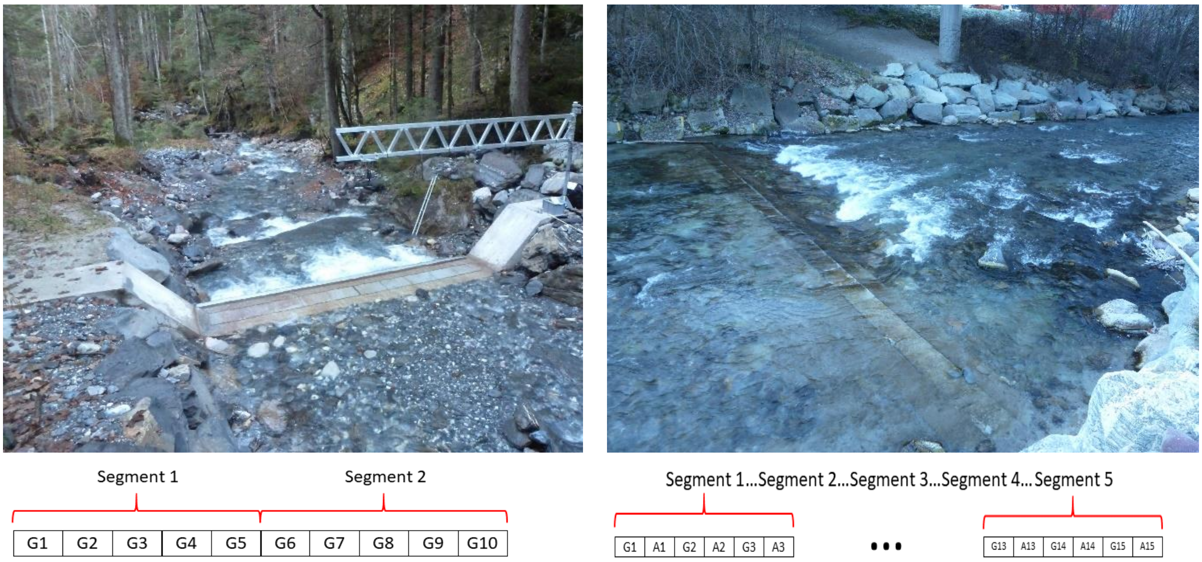

(c) Naviscence **(d)** Riedbach

Figure II-4. The four measuring stations where the impact experiment was conducted and the setup of the plates and segments: (a) at the Avançon de Nant (Western Swiss Alps), (b) at the Albula (Eastern Swiss Alps), (c) at the Naviscence (Southern Swiss Alps) and (d) at the Riedbach (Southern Swiss Alps). The numbers on the plates give the SPG number. At the Albula, plates ‘A’ are accelerometer sensors, the others labelled G are SPGs. The numbering is made with view in downstream flow direction at the Avançon de Nant and Riedbach measuring stations, and upstream flow direction at the Albula and Naviscence measuring stations.

The measuring station at the Naviscence (Southern Swiss Alps) was set in operation in 2011. Twelve SPG sensors are mounted flush with the riverbed within the concrete sill (Figure II-4c). On the day the experiment was conducted in October 2015, conditions were similar to the ones we encountered at the Albula, which means that some support was required for the pedologist hammer during the experiment, which may have also added some additional tension to some of the plates. SPGs at the Naviscence are mounted into two segments gathering 6 sensors each.

The measuring station at the Riedbach (Southern Swiss Alps) was set in operation in 2009 and is equipped with 7 SPG sensors, which are slightly inclined (i.e. 5-10°) towards the slope (Figure II-4d). This means that even if there was no flowing water over the sensors at the day of the experiment in October 2015, the inclination of the plates may have influenced the way the weights were falling and impacting the plates. This may also have consequences on the comparability of the Riedbach measuring station with the results coming from the other measuring stations where the SPGs are mounted over a flat sill. The 7 SPG sensors at the Riedbach are connected to a single segment.

II-2.4 Metric calculation

Datasets of the impact experiment are used to calculate three main elements. First, the maximum positive amplitude A_{max} [V] that each impact produces on a given plate (Rickenmann et al., 2012, 2014b; Wyss et al., 2016b; Rickenmann, 2018). Second, the amount of energy from a given impact that propagates in space to neighboring non-impacted plates, also measured as the maximum positive amplitude A_{max}. Third, the number of impulses N_{imp} [-], which is the number of times the raw signal exceeds a predefined threshold. This threshold is set at 0.1 V at the four SPG measuring stations, because it was estimated to be greater of at least one order of magnitude as compared to the noise level for conditions without bedload transport (Wyss et al., 2016a, 2016b). Data are then used to quantify (a) the response of each individual plate at the four measuring stations and (b) the main characteristics of the energy that propagates from impacted plates towards non-impacted plates. We then draw from (a) and (b) to generalize findings about the response variability of SPGs, and its implications regarding the necessary calibration effort.

II-3 Results

II-3.1 Direct maximum amplitude

The relationship between E_k and the recorded A_{max} is plotted in Figure II-5 for each individual plate at (a) the Avançon de Nant, (b) the Albula, (c) the Naviscence and (d) the Riedbach. The kinetic energy values were taken from the laboratory experiment, and the A_{max} values correspond to the energy recorded directly on a given impacted plate. In Figure II-5, each dot represents the mean of a given drop category (in terms of impact energy) repeated 10 times. The intercept, slope and R^2 of the regressions for all the plates from all tests at one measuring station taken together are given in Table II-5. The regression coefficients for every individual plate are reported in the Supporting Information II-S1. Such as observed in the laboratory experiment (Figure II-3), the energy resulting from the different categories of drops resulted in A_{max} ranging from ~ 0.01 V to ~ 10 V. A_{max} tends to increase as a power law function of the kinetic energy delivered by the impact for all the plates at all four measuring stations, the exponent of the power law relationship being on average slightly larger than 1, such as observed for the laboratory experiment. However, some signal variability is visible between plates of a given measuring station. The variability is more pronounced at the Albula and Naviscence measuring stations (factor 3-5 of difference), while it is smaller at the Avançon de Nant and Riedbach measuring stations (factor 1-2 of difference).

(a) Avançon de Nant **(b) Albula**

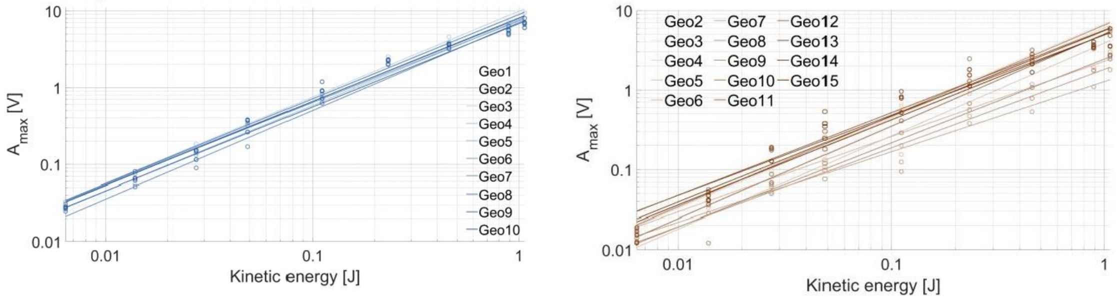

(c) Naviscence **(d) Riedbach**

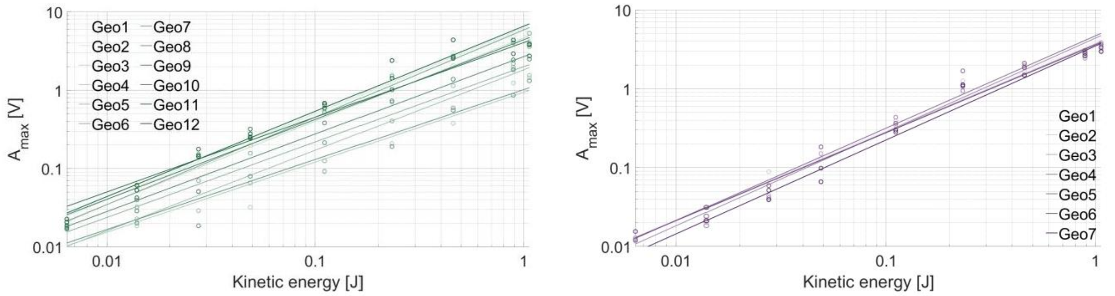

Figure II-5. Relationship between the kinetic energy [J] of the impact and the associated A_{max} at (a) the Avançon de Nant, (b) the Albula, (c) the Naviscence and (d) the Riedbach. Each point represents the $\overline{A_{max}}$ [V] of the given drop category repeated 10 times.

Table II-5. Regression coefficients of the relationship between the impact kinetic energy derived from laboratory experiments, and the recorded direct A_{max} , for all the impact tests over all the plates (taken together) at the Avançon de Nant, Albula, Naviscence and Riedbach measuring stations respectively, and the results for the corresponding laboratory experiment.

	Intercept	**Slope**	**R^2**
Avançon de Nant	8.183	1.107	0.991
Albula	4.528	1.077	0.988
Naviscence	3.867	1.030	0.99
Riedbach	3.963	1.144	0.984
Laboratory	11.018	1.121	0.977

II-3.2. Energy propagation across plates

We also quantified the extent to which some energy propagates in space from impacted plates towards non-impacted plates. Because the Riedbach measuring station is setup with an older electronic measuring system that does not allow for recording the signal over all the plates simultaneously, this analysis could only be performed for the other three measuring sites.

Results from Figure II-6 illustrate that the energy tends to propagate to some extent from impacted plates towards non-impacted plates within a given segment, but poorly across different segments. This is notably true at the Avançon de Nant and Albula measuring stations (Figure II-4a,b). For these two stations, the propagation of the signal was therefore quantified for the plates placed within the same segment. Depending on the position of an impacted plate within a segment (in the middle or at an edge), the A_{max} on the neighboring plates at 1, 2, 3 and 4 plates of distance was measured from a single plate, or as a mean between two plates. For instance, when impacting SPG 4 at the Avançon de Nant measuring station, there are two plates located at one plate of distance (SPGs 3 and 5), but only one located at two plates of distance (SPG 2) when considering the propagation of the energy within the same segment. In the first case, the A_{max} recorded at one plate of distance is calculated as the mean between the A_{max} of SPG 3 and SPG 5, while at two plates of distance it is computed as the A_{max} from SPG 2 only. At the Naviscence, the energy seems to also propagate across the different segments (Figure II-6c), and only at this site the energy propagation was therefore also assessed across the two neighboring segments. For instance, the amount of propagated energy when impacting SPG 6 at the Naviscence was taken as the mean of SPG 5 and SPG 7, even if SPG 7 is installed into another segment.

(a) Avançon de Nant

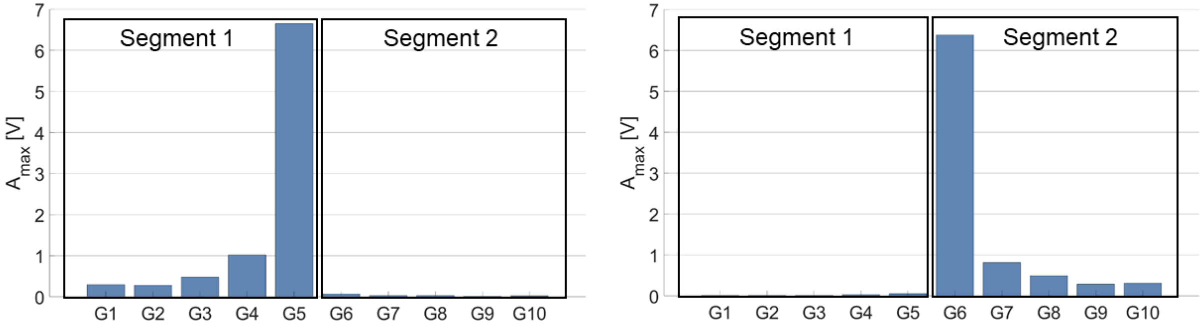

(b) Albula

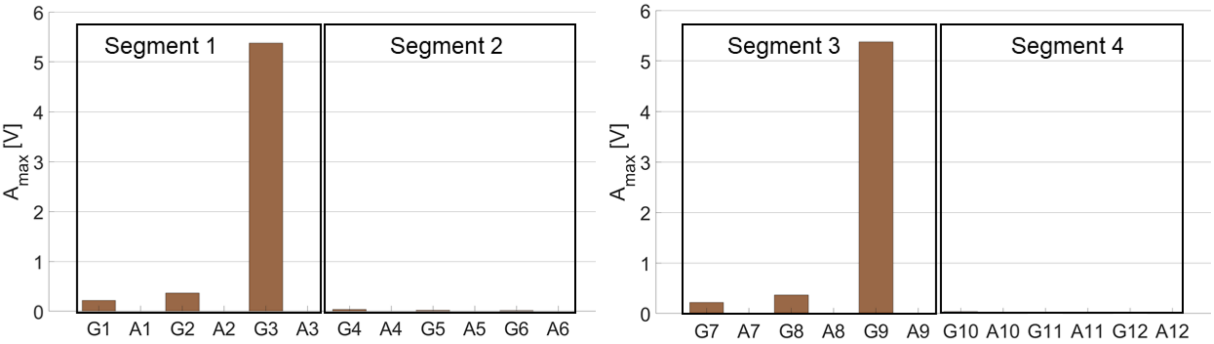

(c) Naviscence

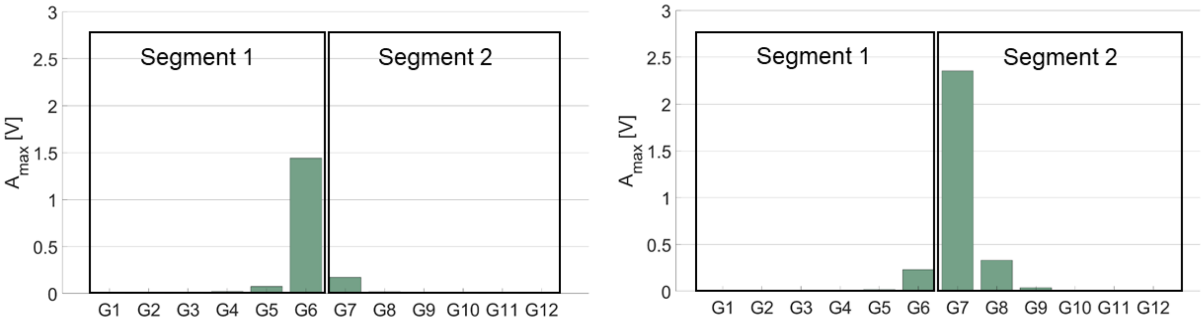

Figure II-6. Energy propagation from impacted plates towards non-impacted plates, and across segment limits, at (a) the Avançon de Nant, (b) the Albula and (c) the Naviscence. Plates located at the margin of different segments have been impacted in this example to illustrate how the energy propagates at the different measuring sites. In this example, one plate per scheme was impacted 10 times (average value) with a weight of 0.256 kg dropped from 0.6 m height (category 9).

(a) 1st plate, absolute

(b) 1st plate, percentage

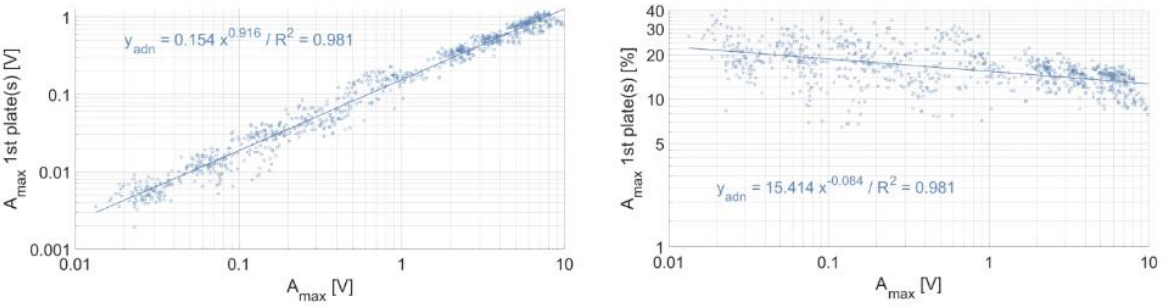

(c) 2nd plate, absolute

(d) 2nd plate, percentage

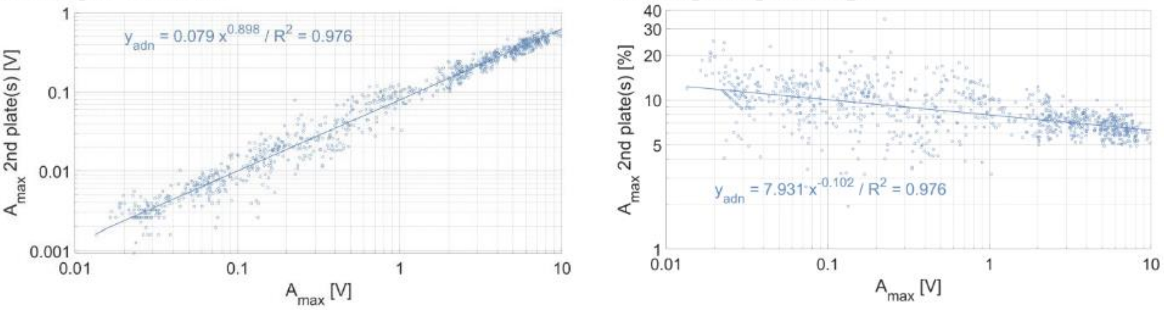

(e) 3rd plate, absolute

(f) 3rd plate, percentage

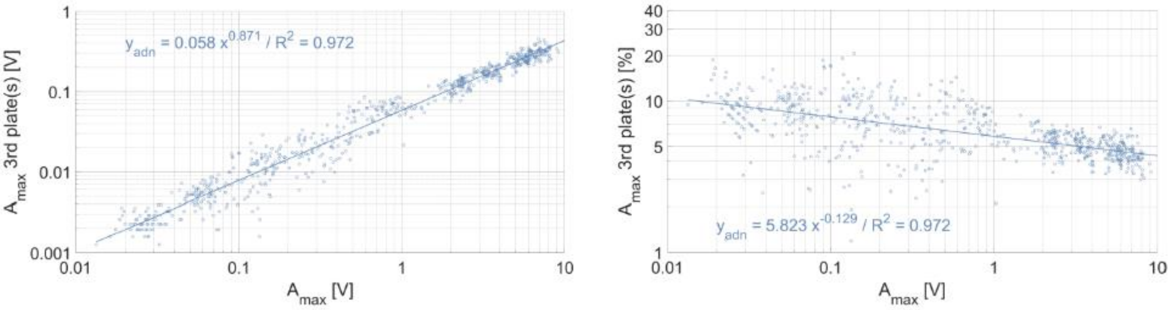

(g) 4th plate, absolute

(h) 4th plate, percentage

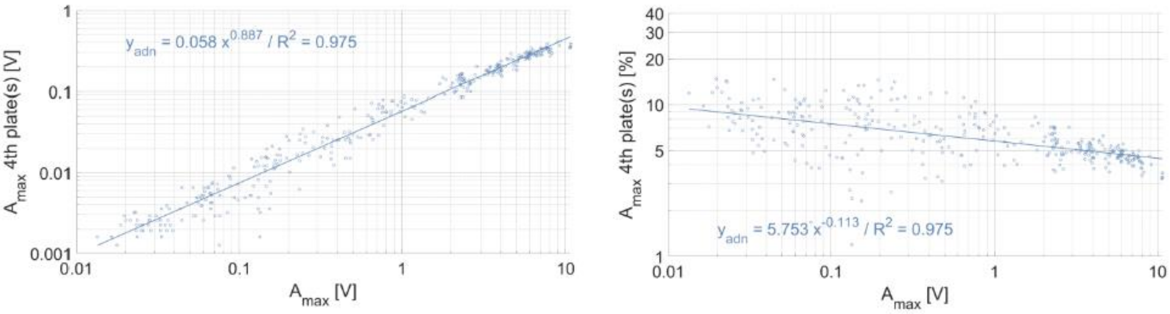

Figure II-7. Energy propagation across plates at the Avançon de Nant measuring station (a-b) at one plate of distance, (c-d) at two plates of distance, (e-f) at three plates of distance and (g-h) at four plates of distance, in absolute (left column) and relative (right column) numbers. Each dot represents the voltage associated to an individual impact.

In Figure II-7 to Figure II-9, the energy propagation towards neighboring plates is expressed in terms of A_{max} and as a relative reduction of A_{max}. Because there are accelerometers mounted below each second plate at the Albula measuring station, the energy propagation from impacted plates towards non-impacted plates in this station could only be computed at two and four plates of distance respectively, when considering each segment separately (Figure II-6, Figure II-8). As can be expected, the amount of energy that propagates from impacted plates toward non-impacted plates at all three sites increases with the magnitude of the impact. The energy propagation across plates can be expressed by a power law function, with an exponent slightly lower than 1, which decreases progressively as the energy propagates further away from the impacted plate. Exponents are steadily slightly greater at the Avançon de Nant (Figure II-7) as compared to the Albula (Figure II-8) at both two and four plates of distance, and the rate of attenuation is much faster at the Naviscence as compared to the other two sites (Figure II-9) from two plates of distance on. At the Albula and Naviscence measuring sites, the propagated energy across plates does not increase significantly for low magnitude A_{max}. It only does so when a threshold of 0.02 V is exceeded at the Albula, and thresholds of 0.08 V, 0.5 V, and 1 V are exceeded at the Naviscence at one, two and 3-4 plates of distance, respectively. In relative terms, the proportion of the energy that propagates from impacted plates towards non-impacted plates is however greater for small magnitude impacts at all three sites. In summary, in terms of Amax, a similar level of propagation is observed at the Avançon de Nant and Albula sites, whereas the propagated values are clearly smaller at the Naviscence site .

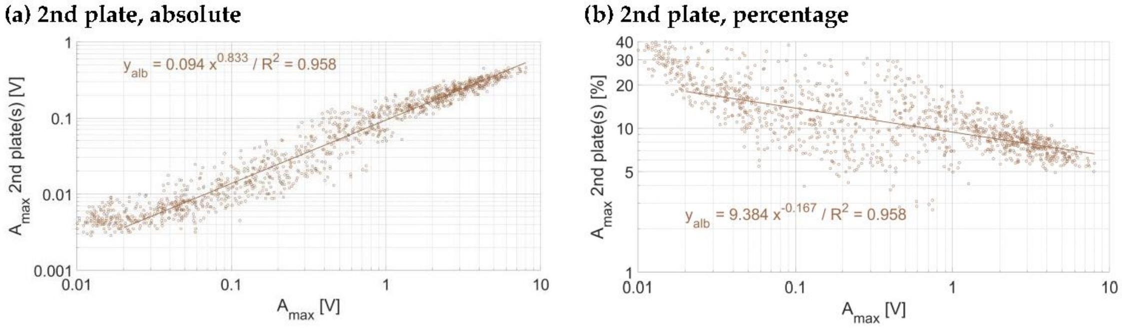
(a) 2nd plate, absolute

(b) 2nd plate, percentage

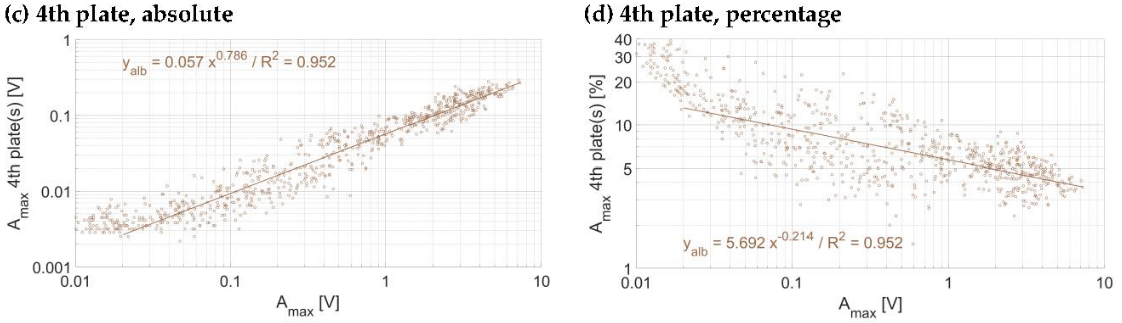
(c) 4th plate, absolute

(d) 4th plate, percentage

Figure II-8. Energy propagation across plates at the Albula measuring station (a-b) at two plates of distance and (c-d) at four plates of distance, in absolute (left column) and relative (right column) numbers. Each dot represents the voltage associated to a single impact. The regression is fitted only for A_{max} greater than 0.02 V.

Considering the threshold of impulse counting of 0.1 V, which is the reference at many measuring stations equipped with the SPG system (Rickenmann et al., 2012; Wyss et al., 2016b), impacts greater than 0.6 V are required to exceed the 0.1 V threshold at one plate of distance at the Avançon de Nant measuring station. Impacts greater than 1 V and 2 V are required to exceed it at two and 3-4 plates of distance, respectively (Figure II-7, Table II-6). At the Albula, impacts greater than 1 V are required to exceed the 0.1 V threshold at two plates of distance, and greater than 2 V at four plates of distance (Figure II-8, Table II-6). At the Naviscence, only impacts greater than 1 V produce a signal that exceeds the 0.1 V threshold at one plate of distance. At two, three and four plates of distance, even the strongest impacts do not produce a signal that exceeds 0.1 V, at least in the investigated domain (impacts up to 10 V) (Figure II-9, Table II-6).

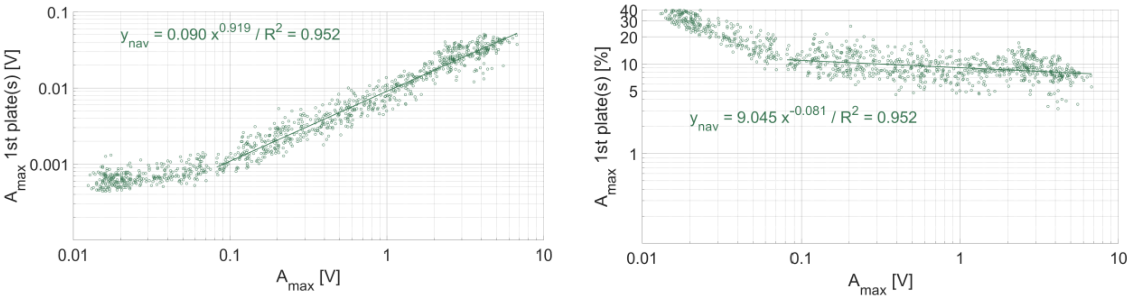

(a) 1st plate, absolute

(b) 1st plate, percentage

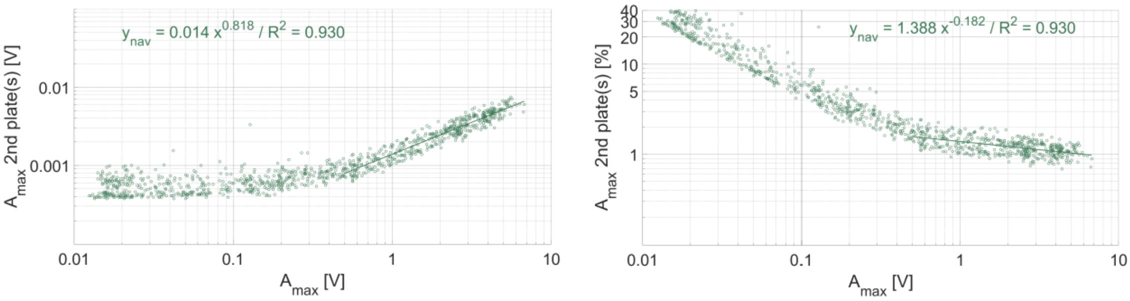

(c) 2nd plate, absolute

(d) 2nd plate, percentage

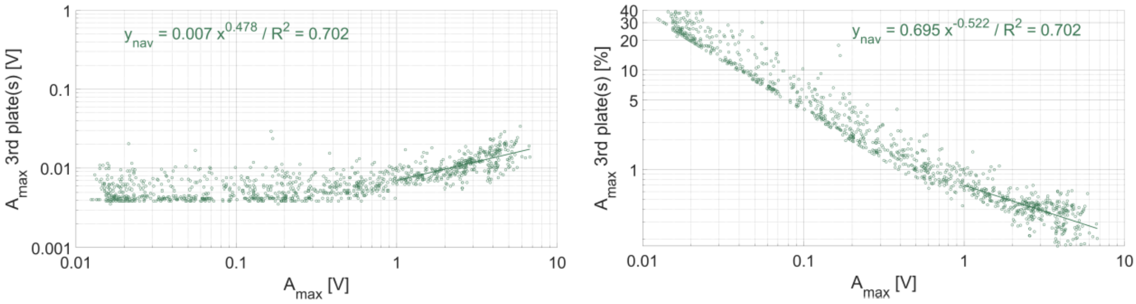

(e) 3rd plate, absolute

(f) 3rd plate, percentage

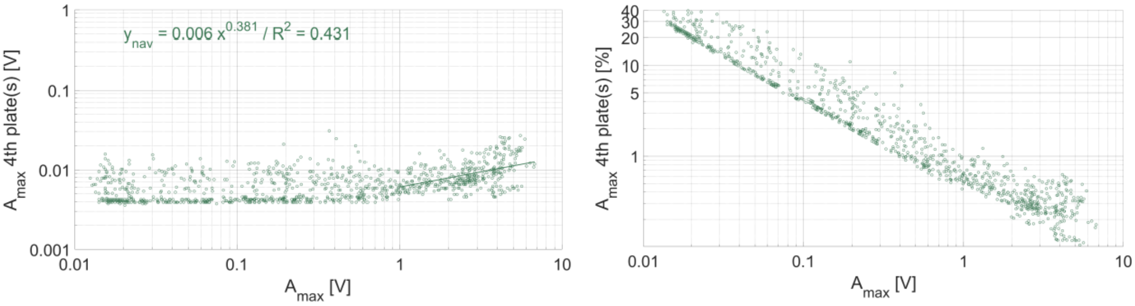

(g) 4th plate, absolute

(h) 4th plate, percentage

Figure II-9. Energy propagation across plates at the Naviscence measuring station (a-b) at one plate of distance, (c-d) at two plates of distance, (e-f) at three plates of distance, and (g-h) at four plates of distance, in absolute (left column) and relative (right column) numbers. Each dot represents the voltage associated to a single impact. The regression is fitted only for maximum impact amplitudes greater than 0.08 V, 0.5 V, 1 V at one, two and 3-4 plates of distance, respectively.

(a) A_{max}

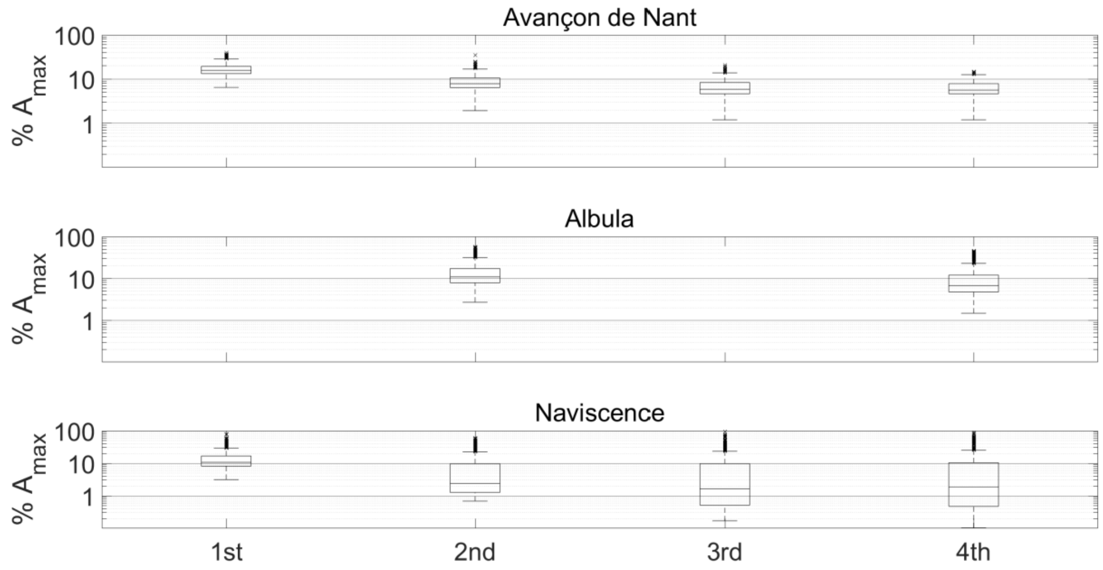

(b) N_{imp}

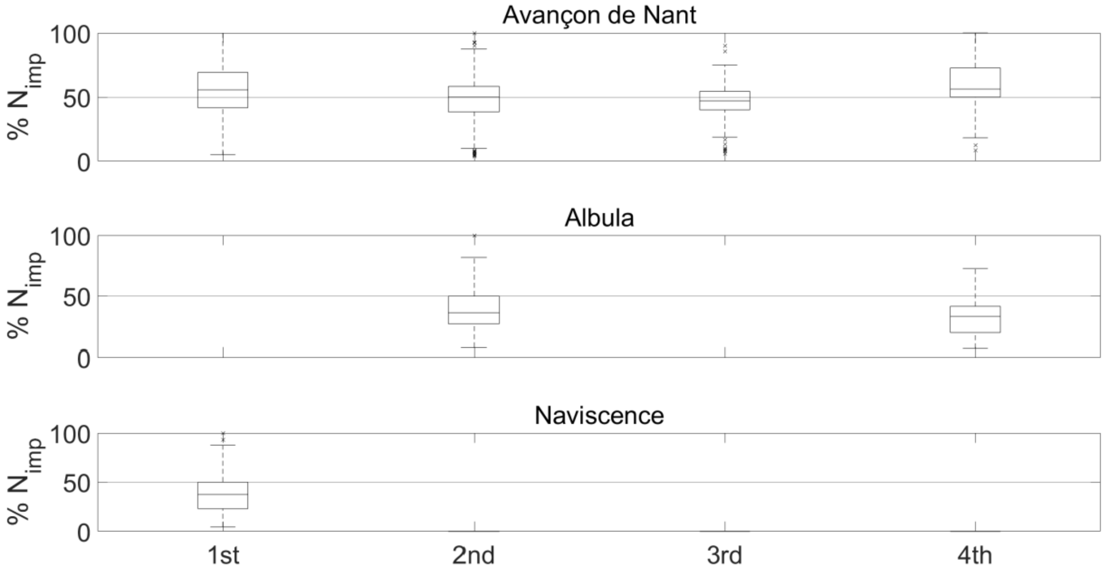

Figure II-10. Percentage of (a) the impact A_{max} (note the logarithmic scale on the y-axis) and (b) N_{imp} (> 0.1 V) recorded at one, two, three and four plates of distance in all three investigated measuring stations. Boxplots show the 5th, 25th, 50th, 75th and 95th centiles of the distribution, outliers are marked with crosses. Note that A_{max} covers a range of impacts between 0.01 V and 10 V, while N_{imp} [-] only considers the impacts greater than 0.1 V. At the Albula, there is no data available at 1 and 3 plates of distance, because there are accelerometers mounted below each second plate. At the Navisence, no impulses are detected further than one plate of distance.

Table II-6. A_{max} required for the 0.1 V threshold to be exceeded at one, two, three and four plates of distance in all three investigated measuring stations.

	1st	2nd	3rd	4th
Avançon de Nant	0.6 V	1 V	2 V	2 V
Albula		1 V		2 V
Naviscence	1 V	-	-	-

Once the 0.1 V threshold is exceeded, the proportion of the impulse count N_{imp} that is accounted for on the first, second, third and fourth neighboring plates remains however steadily higher than the proportion of A_{max}. At the Avançon de Nant, it represents in average 55 %, 49 %, 46 % and 55 % at one, two, three and four plates of distance, respectively (Figure II-10b). At the Albula, it represents in average 39 % and 32 % of the impulses counted on the impacted SPG at two and four plates of distance (Figure II-10b). At the Naviscence at one plate of distance, 37 % of the impulses remain in average accounted for (Figure II-10b). The relationship between the A_{max} and the impulse count N_{imp} (> 0.1 V) at the Avançon de Nant, Albula and Naviscence measuring stations are presented in a Supporting Information II-S2.

As observed in Figure II-7 to Figure II-9, there is an attenuation of the propagated energy across plates with distance from the impacted plate when considering the A_{max}. In Figure II-11, the regression equations between the impact A_{max} and the propagated A_{max} across plates were fitted for all the impacts on every plates taken together for a given impact distance (i.e. one, two, three or four plates of distance) and at a given site. At the Avançon de Nant, there is a significant attenuation of energy propagation between one and two plates of distance (factor 2), then smoother between two and three plates of distance (factor 0.5), then there is no more attenuation between three and four plates of distance. At the Albula, the attenuation between two and four plates of distance is moderate (factor 1/3-2/3). At the Naviscence, the attenuation is substantial between one and two plates of distance, about a factor 2.5 for impacts of 0.5 V to a factor 8.5 for impacts close to 10 V. Then the attenuation decays between two, three and four plates of distance (to a factor 2-3), but the remaining propagated energy is anyway very low.

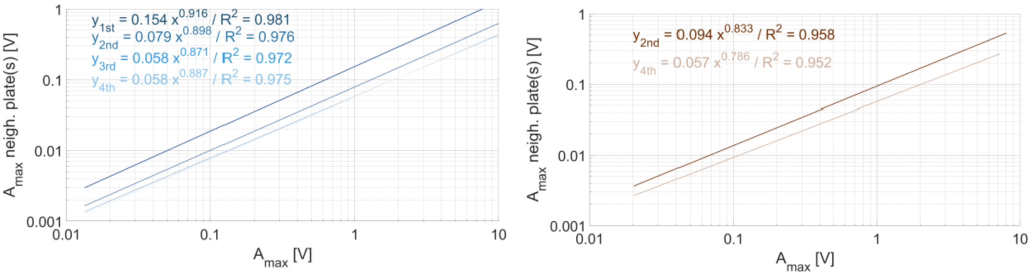

(a) Avançon de Nant

(b) Albula

(c) Naviscence

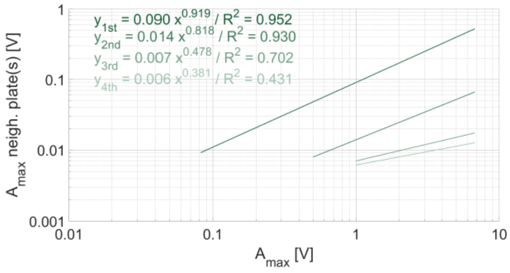

Figure II-11. Attenuation of the propagated energy across plates at (a) the Avançon de Nant, (b) the Albula and (c) the Naviscence measuring stations. Regressions are calculated from all impacts on every plates taken together at each given site.

II-3.3 Sensor sensitivity

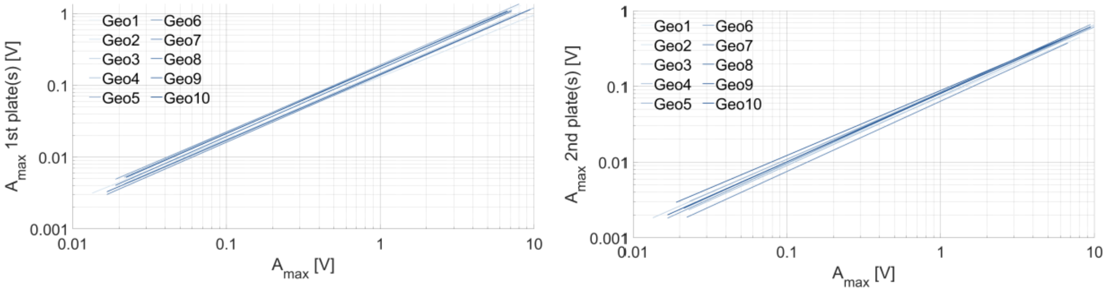

(a) Avançon de Nant, 1st plate

(b) Avançon de Nant, 2nd plate

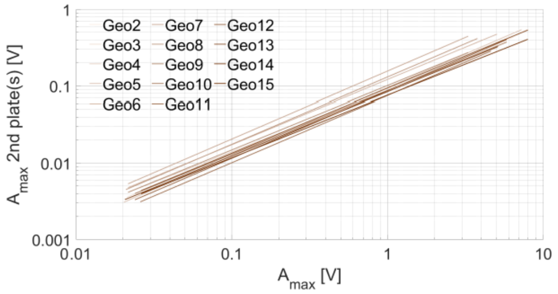

(c) Albula, 2nd plate

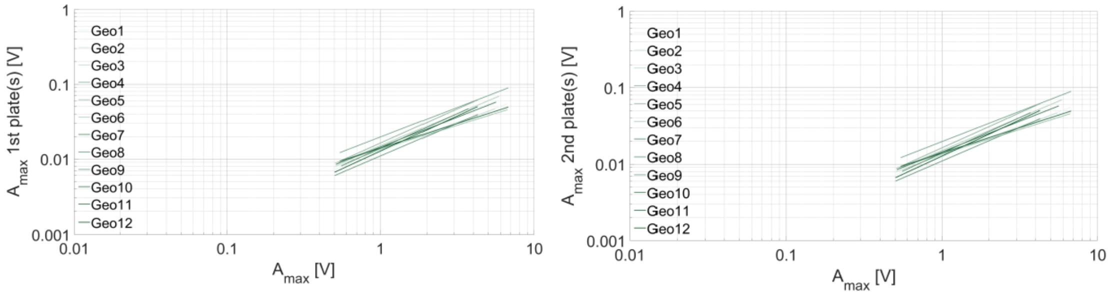

(d) Naviscence, 1st plate

(e) Naviscence, 2nd plate

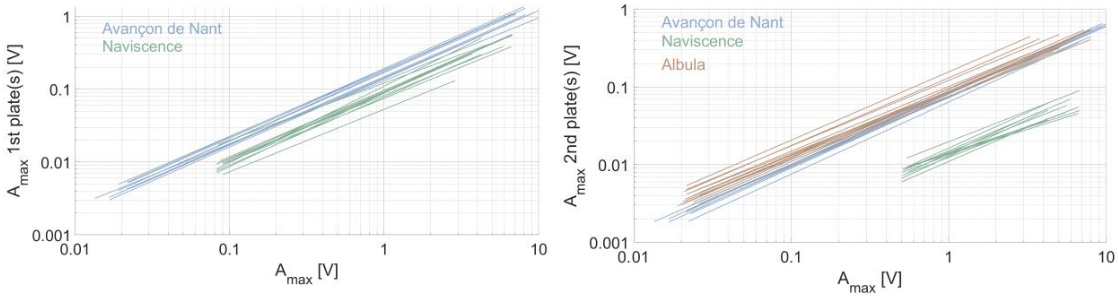

(f) All, 1st plate

(g) All, 2nd plate

Figure II-12. Energy propagation across plates computed for individual plates (a-b) at the Avançon de Nant, (b) at the Albula, (c-d) at the Naviscence and (f-g) for all three measuring stations together.

Comparing the regression lines of the relationship between the impact A_{max} and the propagated A_{max} across plates (here plotted for one and two plates of distance), also allows to investigate whether the different plates have a similar sensitivity, or whether there is a significant response variability (a) between different plates of a given measuring station and (b) between plates at different measuring sites (Figure II-12), to energy propagation across plates. To estimate the individual sensor sensitivity in Figure II-12, the propagation of energy for one plate has been calculated slightly differently as compared to section 3.2. Here, instead of taking the mean value of the propagated energy of a given impact (measured as a A_{max}) on the neighbouring plate(s), we have taken the mean of the propagated energy (measured as a A_{max}) from the neighbouring plate(s) onto a given plate. This explains the small differences that can be observed in power law coefficients between section 3.2. (e.g. Figure II-7 to Figure II-11) and section 3.3. (e.g. Table 7). The power law coefficients of all impacts on every plates at a given site are given in Table II-7. The power law coefficients of every individual plate at the three measuring sites are reported in the Supporting Information II-S3.

In terms of (a), it appears that the 10 plates at the Avançon de Nant measuring station have a comparable response at both one and two plates of distance (Figure II-12a), with exponents of the power law relationship slightly below 1 (Table II-7). At the Albula, the variability between the different plates is slightly larger, while the exponent of the power law function is of a comparable magnitude with the Avançon de Nant (Table II-7). At the Naviscence, the variability between the different plates is the largest, both considering the coefficient (factor 2-3) and the exponent of the power law functions (between 0.786 and 1.05 at one plate of distance, and between 0.661 and 0.946 at two plates of distance, Supporting Information II-S3).

Table II-7. Regression coefficients between the impact A_{max} and the associated energy propagation at one and two plates of distance recorded for all the impacts on every plates taken together at a given measuring site.

	1st plate			**2nd plate**		
	Intercept	**Slope**	**R^2**	**Intercept**	**Slope**	**R^2**
Avançon de Nant	0.153	0.919	0.978	0.079	0.899	0.976
Albula				0.094	0.832	0.958
Naviscence	0.091	0.919	0.932	0.014	0.813	0.903

In terms of (b), the plates at the Avançon de Nant seem to be overall more sensitive to energy propagation across plates, than at the Naviscence (about a factor 2) at one plate of distance. The between-plates variability at a given measuring station is smaller than the between-site variability for the Avançon de Nant and Naviscence measuring stations at one plate of distance. At two plates of distance, the Avançon de Nant and the Albula have a comparable response, and the between-plates variability cannot be clearly distinguished from the between-site variability. The pattern at the Naviscence is clearly different due to the greater rate of signal attenuation, and the between-plates variability is lower than the between-site variability.

II-4 Discussion

II-4.1 Comparability in SPG response and energy propagation across plates

The impact experiment presented in this paper allowed to determine the response of 43 SPGs at four measuring sites to impacts of comparable magnitude, and to quantify the amount of energy that propagates in space from impacted plates towards non-impacted plates. Results from the field were similar to the initial laboratory experiment. The relation between A_{max} and E_k is best expressed by a power law with an exponent on average slightly larger than 1 for all the sensors at all measuring sites (Figure II-3, Figure II-5, Table II-5, Supporting Information II-S1). This result is encouraging because it indicates that all sensors respond in a similar way to impacts of increasing magnitude.

Regarding energy propagation across plates, the proportion of A_{max} that is recorded on neighboring non-impacted plates is substantial, and should notably be accounted for at one and two plates of distance, whereas the propagated energy attenuates much more at larger distance away from the impact location. When considering the impulse count N_{imp} (> 0.1 V), the propagated impulses from impacted to non-impacted plates is even greater and does not attenuate with distance to the same extent as A_{max}. Therefore, the spatial propagation of energy from impacted plates towards non-impacted plates should be considered for an entire segment when using the impulse count as an indicator of bedload transport intensity.

The energy propagation across plates can be reasonably well expressed by a power law function between A_{max} at the impacted plate and the propagated A_{max} for all the plates and at all three investigated sites. Exponents of the power law relationship at one plate of distance were slightly smaller than 1, and decreased with distance from the impacted plate due to attenuation effects. Considering the sensitivity of individual SPGs to energy propagation across plates, every non-impacted plates at the Avançon de Nant and Albula measuring sites seem to record a comparable amount of energy for a given impact A_{max} on a neighboring plate, which suggest that the plates at these two sites have a comparable sensitivity to energy propagation across plates (Figure II-11, Supporting Information II-S3). At the Naviscence, the rate of attenuation is greater but the slope of the relationship remain comparable in between the three sites (Figure II-11, Supporting Information II-S3).

II-4.2 Variability in SPG response and energy propagation across plates

Although the SPG response and the energy propagation across plates showed general similarities between the investigated sites, a non-negligible variability in the signal response was observed among individual plates at a given site, and in between sites. This was notable (a) from a comparison of the power law coefficients of the relations between A_{max} and E_k between individual plates and (b) in the propagation of energy across plates. As compared to the Avançon de Nant and Albula plates, the SPGs at the Naviscence notably presented a lower level of sensitivity to energy propagation across plates, higher A_{max} needed to exceed the impulse count threshold of 0.1 V on non-impacted plates, so as a greater rate of attenuation with distance from the impact. Meanwhile, the propagation of energy across SPG segments was shown (c) to be negligible at the Avançon de Nant and Albula sites, while it is non-negligible at the Naviscence. Finally (d), energy propagation across plates was observable for the entire range of A_{max} (~ 0.01 V and ~ 10 V) at the Avançon de Nant site, while it was only detectable for the upper range A_{max} at the Albula and Naviscence sites. A range of reasons can be invoked to explain the variability in plate response across the investigated sites.

A first set of reasons for such differences are related to the design of the experiment itself, and to its operation in the field. While the initial laboratory test showed that the standard deviation of the recorded A_{max} stabilized at a relatively low level when repeating a given impact ~ 10 times (Figure II-2, Table II-2), the different flow conditions surrounding the apparatus during the field experiment may have influenced the energy propagation from the impacting weight to the plate through the hammer base, and thus the E_k estimated from the laboratory experiment. Also, the slight support on the hammer stake that was necessary in some instances where flow conditions were too strong, may have affected the signal recording. These aspects notably influence point (a) – the relationship between E_k and the direct A_{max} recorded – and may be related to the greater variability between individual plates that has been observed at the Albula and Naviscence sites (Figure II-5, Table II-5, Supporting Information II-S1). When considering points (b), (c) and (d), — the surrounding flow conditions are less likely to generate variability in the propagation of energy across plates, because the energy propagation is presumably less affected by the detailed impact conditions at the impact location then by the elastic properties of the SPG structure.

A second set of reasons are related to the SPG system, and how it is mounted at a given site. First, there is an intrinsic variability in the sensitivity of the individual geophone sensors mounted within the SPG system, with an open-circuit sensitivity of 27.6 V/m/s that can vary by about 10 % (Geospace technologies, personal communication). This may account for a part of the variability in signal response observed in our experiments. Second, it has been shown that different torque moments applied to the screws fixing a steel plate to the steel frame may also affect the response of each individual plate. For example, when varying the torque moment applied to the screws from 7 Nm to 30 Nm, the signal response for an impact in the center of the plate remained almost constant in terms of A_{max} but the impulse count increased from 7 to 10, or by about 43 % (Morach, 2011). Third, the way the steel frame has been embedded during civil engineering works may also influence the response of plates between different segments, and/or at different sites, to an unknown extent (Rickenmann et al., 2012; Rickenmann, 2017). Finally, some disturbance of the measuring system after construction, notably due to flood events, may also change the sensitivity of individual plates, to an unknown extent. The elements cited above can influence all (a), (b), (c) and (d), and, at this stage, it is difficult to give a hierarchical importance between them to explain the observed variability between plates.

II-4.3 Consequences for SPG calibration

Even though the SPG system is exposed to multiple sources of variability, results of the impact experiment have shown that the signal response variability of individual plates remains relatively low within and in between sites. This is notably observable at the Avançon de Nant and Albula measuring sites, where individual SPG responses to energy propagation across plates were shown to be comparable within a given site, and also in between the two sites (Figure II-12, Table II-7, Supporting Information II-S3). For these two stations, the transfer of calibration coefficient in between SPGs at a given site, or even in between sites, may be considered. At the Naviscence however, clearly less energy propagated across plates as compared to the Avançon de Nant and Albula measuring sites, and may therefore require the use of different calibration coefficients than at the other two sites.

The transferability of calibration coefficients between plates within and in between sites, as well as the systematic correction of the propagated energy across plates, is challenged by different elements. First, the signal recorded by a given plate for a given bedload particle can differ depending on the particle's trajectory, which notably depends on surrounding flow conditions, as for example water discharge, flow velocity and bed roughness (Downing et al., 2003; Downing, 2010; Wyss et al., 2016a, 2016b, 2016c). For example, Kuhnle et al. (2017) experimentally tested an acoustic sensor very similar to the SPG system, using a steel plate with similar dimensions but an accelerometer sensor instead of a geophone sensor (Kuhnle et al., 2017). They found that the mass of a grain impacting the plate is related with a power law to the maximum amplitude A_{max} of the signal. The scatter of A_{max} of the experimental data for a given particle mass was up to about a factor of five, and thus in a similar range as for a comparable experimental data set between A_{max} and particle size for the SPG system (Wyss et al., 2016a). Second, there are temporal changes in bedload transport rates across the section, which may change the proportion of signal that propagates across plates at a given time (Rickenmann et al., 2012, 2014b). This also applies to calibration samples collected during natural bedload events, because these are usually gathered downstream of a single plate, which could also record part of the signal that is generated by impacts on neighboring plates (Rickenmann et al., 2012; Nicollier et al., 2019, 2020). Third, it was shown that the location of the impact on a given plate affects the signal response for a given impact (Turowski et al., 2013b). This point is also true for example for the Japanese pipe microphone system (Mizuyama et al., 2010a, 2010b), an alternative surrogate bedload transport measuring technique. Fourth, the shape of a particle also influences the signal response for given flow conditions (Turowski and Rickenmann, 2009). For all these reasons, the transferability of calibration coefficients from calibrated plates to non-calibrated ones should be performed with care.

II-4.4 Future research along this topic

When considering natural bedload events, it is unlikely that free-falling cylindrical weights used in this experiment are closely mimicking the way particles impact the plates during natural bedload transporting flows. Also, the shape of the weights used in this experiment may influence the signal pattern recorded by the plates for each specific impact. Therefore, there may likely be some differences in the signal recorded by the plates between natural bedload events and the patterns determined from the impact experiment presented in this paper. This aspect could for instance affect the relationship between impact A_{max} and the impulse count (> 0.1 V) N_{imp} that was established from our experiments (Supporting Information III-S3), due to different trajectories and particle shape impacting the plates. Further developments in similar experimental systems could therefore consist of impact experiments where weights of spherical shape impact the plates underwater, ideally in a setting that is not affected by the surrounding flow but still in conditions that are closer to natural bedload transport events than the impact experiments of this study. Assessing individual sensor response with varying hydraulic conditions (e.g. discharge, flow velocity, turbulence rate, suspended sediment concentration) would also be insightful.

Since the SPG system records bedload particles impacts at high temporal resolution (10 kHz) and the propagation of energy across plates appears to be comparable to some extent between individual SPGs, it may also be possible to distinguish the signal from direct impacts and the propagated signal, and to systematically correct for it. This could result in a better understanding of the relationship between the signal recorded by the plate and the actual mass of bedload in transport, and may reduce the need for collection of large calibration samples. Finally, recent research aimed at identifying bedload particle size classes using acoustic sensors, based on the maximum amplitude of the signal (Kuhnle et al., 2017; Wyss et al., 2016b). By developing an impact experiment that covers the range of maximum amplitude produced by mixed-size particles during natural bedload transport events, the results presented in this paper contribute to the effort made towards a grain-size identification of bedload transport using the SPG system. Further studies are nevertheless needed in this domain to improve the conversion of the SPG signal in grain-size fractions of bedload, which would help to reduce the field calibration effort that is needed.

II-5 Conclusion

The indirect measurements of bedload transport using acoustic or seismic sensors offer new perspectives for the continuous monitoring of coarse sediment transport, notably in steep stream environments, where such dataset are typically difficult to acquire.

Impact sensors such as with the Swiss Plate Geophone (SPG) system rely on calibration and validation data to convert a relative signal of bedload transport intensity into an actual mass flux of coarse sediment in transport. An impact experiment was conducted in this study using artificial weights to test the variability in signal response of 43 individual SPGs located at four field measuring sites in the Swiss Alps. In a second step, the propagation of energy (measured in terms of the recorded maximum signal amplitude) in space from impacted plates towards non-impacted neighboring plates at each site was also quantified. The impact experiment was first tested and developed in the laboratory, and was then applied to the 43 plates in the field.

The experiments showed that the multiple impacted plates have a comparable signal response in general. The maximum amplitude A_{max} recorded by the SPGs was related to the impact energy E_k by a power law function, with an exponent slightly larger than 1. The propagation of energy across plates could also be expressed by a power law relationship between A_{max} and the propagated A_{max}, with an exponent slightly lower than 1. The proportion of energy that propagates across plates appeared to be non-negligible, notably when considering the impulse counts N_{imp} greater than 0.1 V. Energy propagation across plates is therefore an aspect that must be taken into account for a better understanding of the SPG system. Differences in the energy propagation across plates were identified between the Naviscence and the other two sites (rate of attenuation, SPG sensitivity), which means that different calibration coefficients may be required for different sites. There are several aspects related to the SPG system and field installation properties that may be responsible for the observed variability in the signal response of individual SPGs, which need to be further investigated.

II-S Supplementary material

II-S1 Relationship between kinetic energy and associated maximum amplitude

Table II-S.1. Regression coefficients between the kinetic energy of the impacts E_k [J] and the associated maximum amplitude A_{max} [V] recorded for each SPG at the laboratory experiment and at the four investigated measuring stations. The line 'All' gives the regression coefficient for all the impacts on every sensors taken together at a given measuring station.

	Intercept	Slope	R^2
Avançon de Nant			
Geo1	10.312	1.198	0.986
Geo2	7.895	1.082	0.992
Geo3	9.910	1.121	0.994
Geo4	7.565	1.112	0.992
Geo5	7.820	1.074	0.992
Geo6	7.411	1.067	0.984
Geo7	7.052	1.149	0.985
Geo8	8.979	1.101	0.986
Geo9	6.823	1.088	0.990
Geo10	8.094	1.091	0.987
All	8.183	1.107	0.991
Albula			
Geo2	5.508	1.178	0.986
Geo3	6.844	1.145	0.987
Geo4	6.041	1.133	0.988
Geo5	3.878	1.166	0.972
Geo6	2.290	0.945	0.982
Geo7	1.271	0.881	0.989
Geo8	1.814	0.987	0.963
Geo9	2.439	1.052	0.965
Geo10	6.542	1.142	0.958
Geo11	5.047	1.159	0.989
Geo12	5.659	1.039	0.925
Geo13	4.913	1.009	0.953

Geo14	5.566	1.077	0.966
Geo15	4.944	1.070	0.948
All	4.528	1.077	0.988
Naviscence			
Geo1	5.643	1.050	0.976
Geo2	6.247	1.095	0.983
Geo3	4.676	1.064	0.992
Geo4	0.943	0.894	0.950
Geo5	1.821	1.027	0.941
Geo6	2.003	0.963	0.957
Geo7	5.900	1.115	0.985
Geo8	1.019	0.893	0.953
Geo9	2.690	0.989	0.969
Geo10	4.417	1.019	0.964
Geo11	4.067	0.954	0.973
Geo12	6.582	1.088	0.958
All	3.867	1.030	0.99
Riedbach			
Geo1	3.991	1.129	0.977
Geo2	3.733	1.120	0.970
Geo3	3.705	1.119	0.979
Geo4	4.394	1.190	0.972
Geo5	4.700	1.171	0.968
Geo6	3.615	1.116	0.985
Geo7	3.491	1.192	0.975
All	3.963	1.144	0.984
Laboratory	11.018	1.121	0.977

II-S2 Maximum amplitude A_{max} [V] versus impulse count (> 0.1 V) N_{imp} [-]

The maximum amplitude A_{max} and the impulse count N_{imp} are linked by a power law function with exponents close to 0.3 for the impact experiment developed in this paper, at all three measuring sites (Figure II-S.1). The relations are not directly comparable to previously reported similar relations in the literature because of difference in the conditions of the experiment (Rickenmann et al., 2014b). The above relationships are important to understand the link between A_{max} and N_{imp}, notably the way the energy propagates across plates (Figure II-10 in the main document). Results in Figure II-S.1 show that the Avançon de Nant measuring station records about 30% more impulses for a given magnitude (energy) impact than the other two stations, potentially due to the lower rate of attenuation of the propagated energy across plates at this site, which leads to a greater number of impulses counted on non-impacted plates.

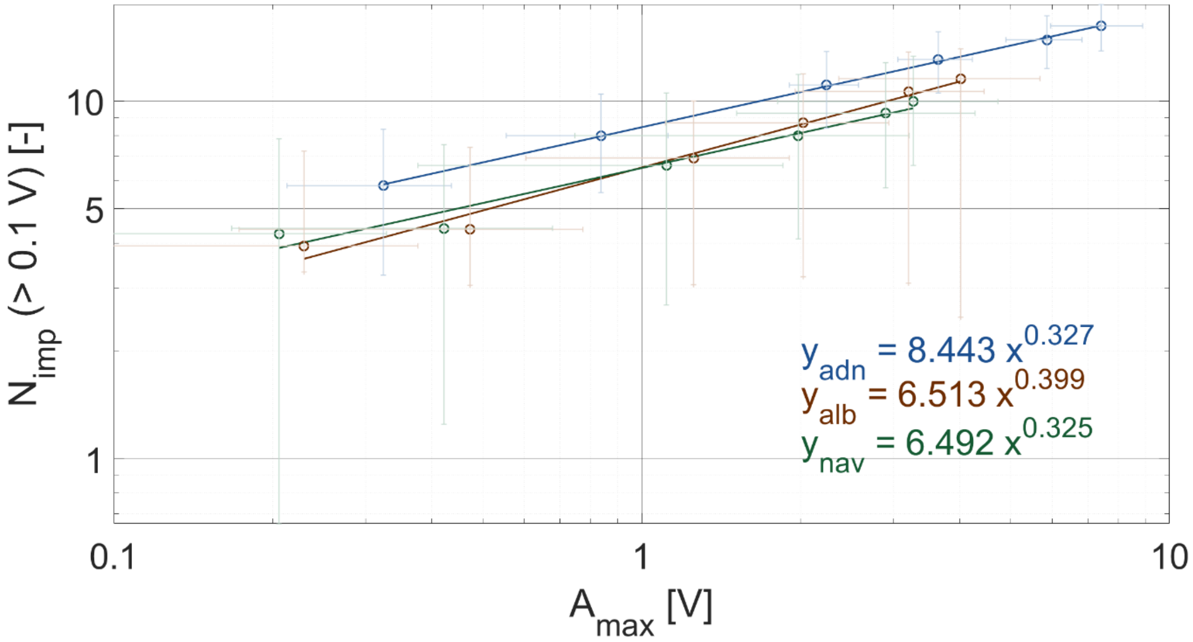

Figure II-S.1. Relationship between A_{max} and N_{imp} for the experiment developed in this paper at the Avançon de Nant, Albula and Naviscence measuring stations.

II-S3 Relationship between impact maximum and associated propagated energy towards non-impacted plate(s)

Table II-S.2. Regression coefficients between the impact maximum amplitude A_{max} [V] and the associated energy propagation at one and two plates of distance recorded for each SPG at the Avançon de Nant, the Albula and the Naviscence measuring sites. The line 'All' gives the regression coefficients for all impacts on each plate taken together for a given measuring station, which are also reported in Table II-7 in the main document.

	1st plate			**2nd plate**		
	Intercept	**Slope**	**R^2**	**Intercept**	**Slope**	**R^2**
(a) Avançon de Nant						
Geo1	0.175	0.950	0.980	0.075	0.905	0.985
Geo2	0.130	0.863	0.987	0.073	0.871	0.987
Geo3	0.149	0.927	0.987	0.084	0.888	0.977
Geo4	0.143	0.924	0.980	0.074	0.917	0.978

Geo5	0.192	0.939	0.986	0.082	0.876	0.987
Geo6	0.184	0.914	0.987	0.082	0.930	0.956
Geo7	0.139	0.935	0.979	0.064	0.929	0.979
Geo8	0.168	0.941	0.985	0.083	0.917	0.976
Geo9	0.143	0.923	0.976	0.089	0.859	0.989
Geo10	0.183	0.935	0.979	0.081	0.903	0.969
All	0.153	0.919	0.978	0.079	0.899	0.976
(b) Albula						
Geo2				0.088	0.856	0.984
Geo3				0.094	0.847	0.988
Geo4				0.088	0.795	0.978
Geo5				0.095	0.880	0.962
Geo6				0.122	0.843	0.985
Geo7				0.156	0.879	0.961
Geo8				0.131	0.871	0.926
Geo9				0.101	0.833	0.974
Geo10				0.087	0.826	0.978
Geo11				0.075	0.871	0.954
Geo12				0.087	0.874	0.982
Geo13				0.094	0.842	0.965
Geo14				0.084	0.832	0.972
Geo15				0.076	0.810	0.976
All				0.094	0.832	0.958
(c) Naviscence						
Geo1	0.096	0.912	0.989	0.012	0.786	0.973
Geo2	0.075	0.863	0.972	0.014	0.673	0.947
Geo3	0.082	0.870	0.975	0.013	0.742	0.948
Geo4	0.091	0.950	0.936	0.015	0.860	0.922
Geo5	0.078	0.935	0.882	0.014	0.636	0.979
Geo6	0.053	0.858	0.901	0.016	0.917	0.987
Geo7	0.088	1.009	0.942	0.020	0.792	0.968
Geo8	0.096	0.930	0.957	0.011	0.879	0.949

Geo9	0.110	1.050	0.896	0.014	0.930	0.905
Geo10	0.121	0.786	0.938	0.014	0.801	0.967
Geo11	0.092	0.940	0.967	0.014	0.661	0.961
Geo12	0.089	0.942	0.909	0.013	0.946	0.928
All	0.091	0.919	0.932	0.014	0.813	0.903

III – Hydrological drivers of bedload transport in an Alpine watershed

Personal contribution to the research article

I conceptualized the study with the help of Stuart Lane (SL) and Dieter Rickenmann (DR). I designed the SPG calibration campaign under the supervision of DR, and with the help of Tobias Nicollier (TN), Alexandre Badoux (AB) and Stefan Boss (SB). I collected the bedload samples needed for SPG calibration with TN. I performed the curation of the SPG and streamflow time-series, and the data investigation with the help of the other co-authors. I performed the transport capacity analysis with the help of DR, and the hydrological analysis with the support of SL, Bettina Schaefli (BS) and François Mettra (FM). I wrote the initial draft of the manuscript with the support of SL, DR, BS and the other co-authors. Following the review process at the journal *Water Ressources Research*, I revised the manuscript until final publication.

Hydrological drivers of bedload transport in an Alpine watershed

Gilles Antoniazza[1,2], Tobias Nicollier[2], Stefan Boss[2], François Mettra[3], Alexandre Badoux[2], Bettina Schaefli[4], Dieter Rickenmann[2] and Stuart. N. Lane[1]

[1] Institute of Earth Surface Dynamics (IDYST), University of Lausanne, Lausanne, Switzerland.
[2] Mountain Hydrology and Mass Movements, Swiss Federal Research Institute WSL, Birmensdorf, Switzerland.
[3] Ecological Engineering Laboratory (ECOL), Ecole Polytechnique Fédérale de Lausanne (EPFL), Lausanne, Switzerland.
[4] Institute of Geography (GIUB) and Oeschger Center for Climate Change Research (OCCR), University of Bern, Switzerland.

Reference: Antoniazza, G., Nicollier, T., Boss, S., Mettra, F., Badoux, A., Schaefli, B., Rickenmann, D. & Lane, S. N. (2022). Hydrological drivers of bedload transport in an Alpine watershed. *Water resources research*, *58*(3), e2021WR030663.

Abstract: Understanding and predicting bedload transport is an important element of watershed management. Yet, predictions of bedload remain uncertain by up to several order(s) of magnitude. In this contribution, we use a 5-year continuous time series of streamflow and bedload transport monitoring in a 13.4-km^2 snow-dominated Alpine watershed in the Western Swiss Alps to investigate hydrological drivers of bedload transport. Following a calibration of the bedload sensors, and a quantification of the hydraulic forcing of streamflow upon bedload, a hydrological analysis is performed to identify daily flow hydrographs influenced by different hydrological drivers: rainfall, snowmelt, and combined rain and snowmelt events. We then quantify their respective contribution to bedload transport. Results emphasize the importance of combined rain and snowmelt events, for both annual bedload volumes (77% on average) and peaks in bedload transport rate. A non-negligible, but smaller, amount of bedload transport may occur during late summer and autumn storms, once the snowmelt contribution and baseflow have significantly decreased (9% of the annual volume on average). Although rainfall-driven changes in flow hydrographs are responsible for a large majority of the annual bedload volumes (86% on average), the identified melt-only events also represent a substantial contribution (14% on average). The results of this study help to improve current predictions of bedload transport through a better understanding of the bedload magnitude-frequency relationship under different hydrological conditions. We further discuss how bedload transport could evolve under a changing climate through its effects on Alpine watershed hydrology.

Key-points:

- The co-occurrence of rainfall in a watershed where the snowmelt signal is strong was the largely dominant driver of bedload transport.
- Melt-only events and rainfall events occurring once the melt signal has become smaller were drivers of secondary importance.
- Combined rain and snowmelt, and melt-only drivers of bedload transport, may decrease due to climate change impacts on Alpine hydrology.

Key-words: Bedload transport; Alpine watershed; Hydrological drivers; Rainfall; Snowmelt; Climate change.

III-1 Introduction

Bedload transport in Alpine watersheds is a serious natural hazard, which can be costly in economic terms and potential loss of life (Badoux et al., 2014a, 2016). It often requires river engineering and represents a challenge for land-use planning (Sims and Rutherfurd, 2017; Heritage et al., 2019) and hydropower production (Pralong et al., 2015; Speerli et al., 2020; FOEN, 2021). It also has a direct impact on the ecology of river systems (Badoux et al., 2014b; Wang et al., 2014; Hauer et al., 2018; Gabbud et al., 2019; Lane et al., 2020; FOEN, 2021). These aspects are of particular concern for the current management of river systems, but also for their future with regards to the evolution of bedload dynamics under a rapidly changing climate.

Despite decades of development of bedload transport models, best estimates of bedload transport rates still suffer from at least one order of magnitude of error (Recking, 2013; Schneider et al., 2015; Yager et al., 2015; Ancey, 2020a, 2020b). The challenge of bedload transport prediction derives partly from the fact that it is a complex process to express physically (Parker et al., 1982; Ashworth and Ferguson, 1986; Gomez and Church, 1989; Gomez, 1991; Buffington and Montgomery, 1997; Ancey, 2020a), bedload being the balance between changing sediment transport capacity (as a function of changing streamflow; e.g. (Rickenmann, 2018, 2020), but also changing sediment availability (both at the streambed and as supply from the drainage network ((Kammerlander et al., 2017; Piton and Recking, 2017; Comiti et al., 2019). In addition, it is also extremely challenging to measure in natural settings, and so to obtain the data needed to determine the level of complexity in bedload transport models. Direct sampling devices (Helley and Smith, 1971; Bunte et al., 2004) may be hazardous to deploy and only provide at-a-point data in time and space. They also commonly require the signal (or at least its variance) to be known in order to determine a reliable sampling frequency (Parker et al., 1982; Gomez et al., 1989; Gomez, 1991; Bunte and Abt, 2005; Singh et al., 2009). Measurements of the rate of filling of traps or reservoirs dug across streams provided cross-sectional integrated estimates of sediment loads, including during high flows (Lenzi et al., 1999; Gray et al., 2010; Hinderer et al., 2013; Lane et al., 2017). Yet, their resolution depends on the rate at which trap-filling is measured, leading to time-series of low temporal resolution (e.g. load per event in the best case, but more common are annual loads; e.g. Hinderer et al., 2013).

Indirect passive sensors have allowed new perspectives for bedload transport monitoring (Rickenmann, 2017). The noise produced by bedload particles in motion can be captured by underwater microphones (Barton et al., 2010; Rigby et al., 2016; Geay et al., 2017, 2020), by out-of-bank seismometers (Burtin et al., 2008; Roth et al., 2016; Dietze et al., 2019) or by measuring the vibration of a structure (e.g. plate, pipe) impacted by bedload particles in motion (Downing, 2010; Mizuyama et al., 2010a; Rickenmann et al., 2012, 2014b; Dell'Agnese et al., 2014; Mao et al., 2016; Perolo et al., 2019). Such approaches may provide continuous time-series of bedload transport at high temporal resolution (i.e. down to 1 second), covering both high and low flow conditions (Rickenmann, 2017); and also absolute fluxes if the sensors can be calibrated (Dell'Agnese et al., 2014; Mao et al., 2016; Rickenmann et al., 2012, 2014b; Nicollier et al., 2021).

Continuous, high-resolution records allow quantification of relationships between bedload transport and discharge (Rickenmann, 2018) as well as evaluation and development of bedload transport models (Rickenmann, 2020). Such studies have confirmed in field settings the inherent autogenic variability of bedload transport observed in laboratory flumes (Gomez et al., 1989; Hoey and Sutherland, 1991) over short time-periods (i.e. less than a couple of hours; Rickenmann, 2018). Over longer time-periods, stronger correlations between streamflow and bedload transport rate emerge (Rickenmann, 2018, 2020). They suggest at such time-scales some forcing of bedload transport by exogenic controls such as watershed hydrology, and associated hydraulic transport capacity. In the meantime, the relationship remains dependent on sediment supply conditions, both from the streambed and from the surrounding drainage network (Buffington and Montgomery, 1997; Mao, 2012, 2018; Mao et al., 2014; Masteller et al., 2019; Rickenmann, 2020).

Within Alpine watersheds, a range of hydrological processes can lead to streamflow variations, and so trigger bedload transport if the transport capacity is sufficient, and sediment is available. These hydrological processes notably include ice and snowmelt, rainfall, and the co- occurrence of rainfall and snowmelt events, which include “rain-on-snow” (ROS) events (Corripio and López-Moreno, 2017; Musselman et al., 2018; Li et al., 2019). Despite the increasing number of bedload transport time-series measured within Alpine watersheds, there are very few studies (Mao, 2012; Dell’Agnese et al., 2015; Rainato et al., 2017; Comiti et al., 2019) that have related temporal variations in bedload transport to possible hydrological drivers, and their respective contribution to annual bedload budgets. This matters not only for improving our ability to predict bedload transport under current climatic conditions, but also for predicting how bedload transport may evolve with climate change impacts on the hydrology of Alpine watersheds.

The goal of this paper is to relate bedload volumes exported from an Alpine watershed to hydrological drivers (e.g. snowmelt, rainfall, combined rainfall and snowmelt events). The analysis is based on a five-year (2016-2020) bedload time-series recorded with passive acoustic sensing using a Swiss Plate Geophone system (Rickenmann, 2017). The system is installed in the stream that drains the Vallon de Nant, a snowmelt-dominated Alpine watershed in the Western Swiss Alps. After calibration, the time-series of bedload transport were associated with streamflow and classified into the different hydrological categories (i.e. snowmelt, rainfall, co-occurrence of rain and snowmelt) likely dominant at different time-periods throughout the year. This allows us to tease out the contribution of different hydrological drivers to bedload transport and, using knowledge of likely future changes in watershed hydrology under a warming climate, assess possible evolution in bedload transport.

III-2 Material and methods

III-2.1 The Vallon de Nant watershed

The Vallon de Nant (VdN) is a 13.4 km^2 watershed located in the western Swiss Alps (Figure III-1), with elevations ranging from c. 1200 to 3050 m a.s.l. Although ~ 3 % of the watershed surface is occupied by the debris-covered Glacier des Martinets, it provides only small amounts of ice melt and the hydrological regime of the Avançon de Nant (AdN), the Alpine stream that drains the VdN, is dominated by snowmelt (Ceperley et al., 2020; Mächler et al., 2021; Michelon et al., 2021; Thornton et al., 2021). The AdN flows from the glacier snout (2313 m a.s.l) over a length of ~ 6.5 km to a hydrological and bedload monitoring station (1200 m a.s.l) installed at the watershed outlet. The average gradient of the AdN is c. 17 %, but varies (8-29 %) over its course, including braided reaches with lower slopes and steeper step-pool and semi-alluvial reaches (Figure III-1). It is fed by ~10 intermittent, steep (40-60%), torrential tributaries that mainly flow during the snowmelt season or briefly during storm events, and which form large coalescent fans at the hillslope base (Figure III-1; Lane et al., 2016). Most of the exported sediment is expected to come from the large capacity-limited braided areas along the AdN main course, notably found in the upper half of the watershed, and which are well connected down to the outlet. These are fed by torrential tributaries. In addition, between the braided zones and the measurement station there are additional torrential tributaries, which may only be well connected during low-frequency high-magnitude events. The steeper step-pool and semi-alluvial channels in the lower half of the watershed are expected to convey sediment and may be dominated by supply-limited conditions (Figure III-1).

During the period 2014-2015, a hydrological and bedload monitoring station was built at the outlet of the watershed (1200 m a.s.l), through a collaboration between the University of Lausanne (FGSE), the Swiss Federal Institute for Forest, Snow and Landscape Research WSL and the ETH Zürich (Physics of Environmental Systems). Details of the monitoring station are given in the sections below.

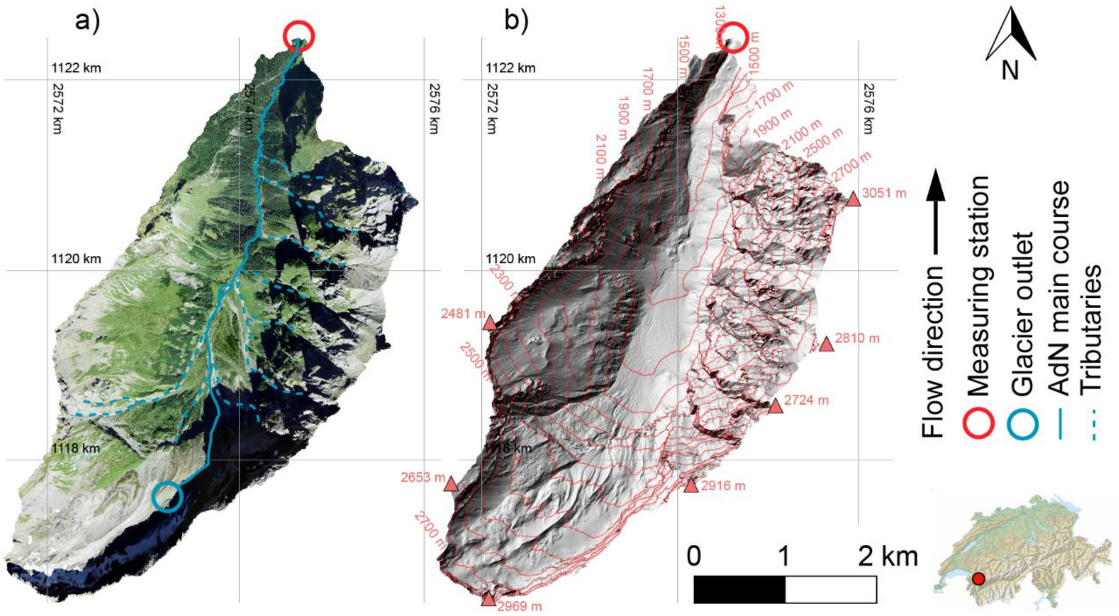

Figure III-1. The 13.4-km^2 VdN watershed with the Glacier des Martinets outlet (blue circle), and the monitoring station at the outlet (red circle). In a) aerial image from 2013. In b) hillshade of the Swiss Alti3d digital elevation model (Acknowledgments © Swisstopo). Coordinates are in the CH1903 Swiss system.

III-2.2 Streamflow monitoring

Streamflow data were derived from a radar-based stage sensor (Vegapuls WL 61). The sensor was mounted on a steel arm extended (Figure III-2b), over a trapezoidal concrete cross-section installed in the stream and where neither erosion nor deposition could occur. The transit time of the radar pulses from emission to reception allows estimation of the distance to the water surface. Knowing the height of the sensor above the streambed (1.83 m), absolute water depths can be derived. The sensor records at a sampling rate of ~ 0.5 s, and data were averaged over 1 minute. Globally, the water depth measurement has been reliable throughout the period of interest (2016-2020), with the exception of discrete periods of time where the measurement failed and the data are missing. Missing streamflow data are notably found in the winter period, during which the AdN channel is sometimes covered by ice and snow, biasing the water height sensing. Thus, an equivalent of 80 full days are missing over the 1827 days of the period of observation, and 72 % of the missing data occur in the winter period (December to March), where bedload activity is typically very low (i.e. 98.8 % of the total bedload occurred outside the missing discharge data window).

A calibration is required to transform the measured water depths [m] into a streamflow per unit time [$l \cdot s^{-1}$]. Salt gauging was performed at the VdN monitoring station to build a rating curve between measured water depths and streamflow (Ceperley et al., 2018). During the years 2016 and 2017, 56 salt gauging samples were collected for water depths varying between 0.05 and 0.3 m. The relationship between water depth and streamflow was best expressed by a power law rating curve (Ceperley et al., 2018):

$$Q = 19998 * d^{1.6244} \qquad \text{[III-1]}$$

where Q is the streamflow per unit time [$l \cdot s^{-1}$] and d is the water depth [m], with an R^2 of 0.91. This equation is in close agreement with a theoretical discharge, resulting from the Poleni formula applied to trapezoidal cross-sections (Bollrich, 2000; Ceperley et al., 2018).

III-2.3 Bedload monitoring

A Swiss Plate Geophone (SPG) system developed by the Swiss Federal Research Institute WSL was used in this research (Rickenmann et al., 2012, 2014b; Wyss et al., 2016a; Nicollier et al., 2021). The SPG system is typically made of a line of steel plates embedded across a river channel. Bedload particles in motion induce a vibration of the steel plates, which is recorded by a geophone sensor mounted below each plate (Rickenmann, 2017). The response of the SPG system under various conditions (e.g. impact magnitude, transport intensities, flow velocities, grain-size mixture) has been investigated in both laboratory and field experiments (Wyss et al., 2016a, 2016b, 2016c; Antoniazza et al., 2020; Nicollier et al., 2021), and successful calibrations of the SPG system using independent concurrent sampling of bedload have been achieved for multiple monitoring stations (Rickenmann et al., 2012, 2014b; Habersack et al., 2017; Kreisler et al., 2017; Rickenmann and Fritschi, 2017; Nicollier et al., 2019, 2020, 2021).

At the VdN monitoring station, 10 plates of the SPG system were mounted side-by-side across the channel width (Figure III-2b, III-2c). The plates are made of stainless steel and have a standardized size of 492 mm in width, 358 mm in length (in flow direction), and 15 mm in thickness, with a total mass of 21 kg (Rickenmann et al., 2012; Wyss et al., 2016a; Rickenmann, 2017; Antoniazza et al., 2020). The plates are mounted in a steel frame, which is embodied in a concrete check dam across the channel (Figure III-2b, III-2c). The plates are mounted flush with the riverbed upstream to avoid biasing approach flow conditions. Below each plate, a 20 DX geophone sensor from Geospace technologies (Houston, Texas, USA) is mounted in a PC801 LPC Landcase set in an aluminum box (Rickenmann et al., 2012; Rickenmann, 2017), and the plates are isolated from each other with elastomer elements.

During bedload transport events, particles rolling, sliding and saltating over the SPG system produce impact shocks that generate a change in the electrical voltage sensed by the geophone. The geophone signal was found to be proportional to the total mass of bedload in transport (Rickenmann et al., 2012, 2014b; Rickenmann and Fritschi, 2017). The SPG is connected to an industrial PC that records the geophone signal at a frequency of 10 kHz. Geophone data are then summarized in the number of impulses per minute, which corresponds to the number of times the geophone raw electrical signal exceeds a pre-defined threshold. In previous studies of bedload transport using the SPG system (Rickenmann et al., 2012; Rickenmann and Fritschi, 2017; Antoniazza et al., 2020), this threshold was set to 0.1 V in order to include the smallest detectable grain-size fractions (~10-20 mm), whilst at the same time being greater by at least one order of magnitude than the noise level for flow conditions without bedload transport. Over the period 2016-2020, an equivalent of 30 full days are considered as unreliable SPG monitoring. Of these, ~ 10 are days whose data have to be excluded due to work on the measurement station, although these were almost always days with no bedload transport activity. The remaining missing data correspond to ~20 days of power failure at the monitoring station.

III-2.4 Geophone calibration

The Swiss Plate Geophone (SPG) system requires a robust calibration to transform the recorded signal into an actual mass of bedload in transport. This is typically achieved by collecting bedload samples during natural transport events that can be directly related to the signal measured by the sensors (Rickenmann et al., 2012, 2014b; Rickenmann and Fritschi, 2017; Nicollier et al., 2019, 2020, 2021).

At the VdN, we used a mobile sediment basket to collect the calibration samples (Figure III-2a). The sediment basket was mounted with rollers on a rail fixed on the downstream side of the concrete weir where the SPG are imbedded. Using a system of ropes and pulleys, the sediment basket was moved along the rail and located directly downstream of a given plate. Doing so, every particle that impacts this plate can be collected in the sediment basket. For this purpose, the sediment basket (530 mm) was slightly wider than a SPG (492 mm). The sediment basket had an initial capacity of ~ 100 kg, but we expanded it during the calibration sampling by removing the downstream-facing panel and replacing it by a net that increased the sampling capacity to ~ 500 kg (Figure III-2a). A removable lid was also built for the basket to prevent the collection of particles while positioning the basket at the plate targeted for calibration (Figure III-2c).

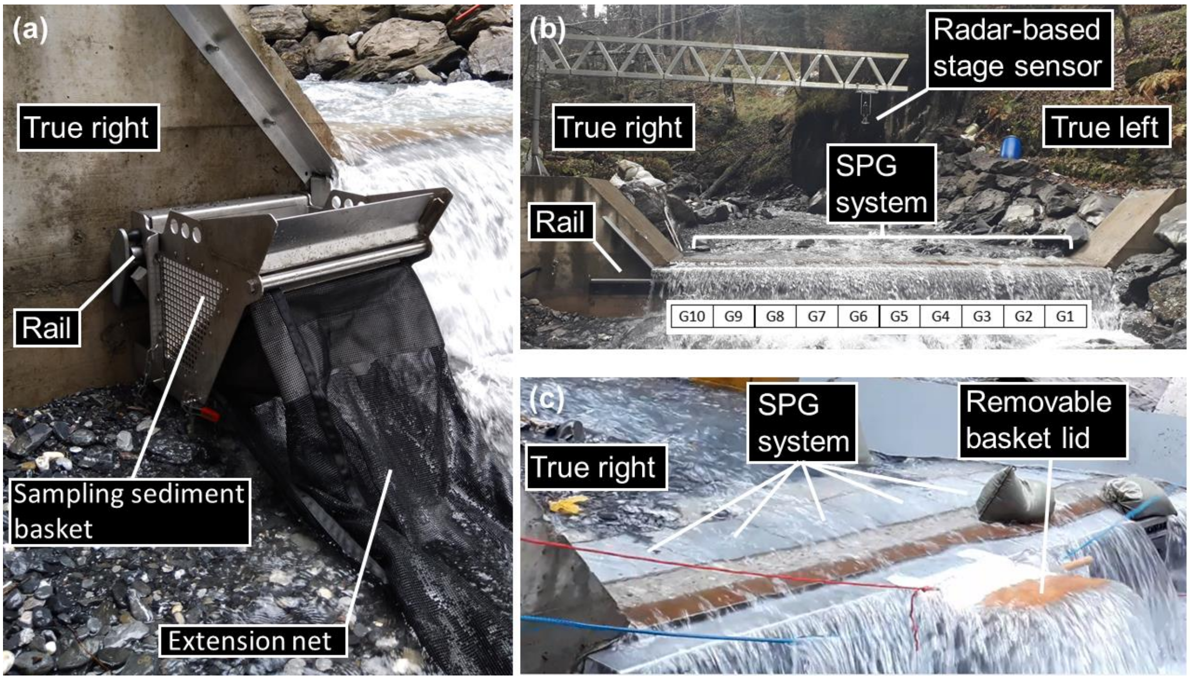

Figure III-2. (a) The sediment sampling basket (with the extension net) placed on the rail; (b) General view of the VdN monitoring station. The radar-based stage sensor monitoring the water surface is set above the stream at the end of a steel arm. Geophone plates are labelled G1 to G10 from the true left to true right bank. The rail that supports the mobile sediment basket is visible to the left of the waterfall; (c) View of the SPG system along the concrete weir, and of the sediment sampling basket in experiment conditions. The blue ropes are used to pull the basket across the section. The red rope is used to remove the lid at the start of a sampling.

Every bedload sample was collected using the following protocol: (a) the sediment basket (with the net extension) was emptied of sediment, covered with the lid and placed at the true right end of the rail (Figure III-2a); (b) one operator standing on the true left bank pulled the basket until it was positioned directly downstream of the targeted SPG. Marks on the ropes on both basket sides allowed precise basket positioning (± 0.01 m). Once positioned, ropes were secured on both banks to keep the basket stable during bedload sampling; (c) on the true right bank, a second operator removed the basket lid whilst a third operator simultaneously started the geophone raw recording (10 kHz) from the station laptop; (d) particles that impacted the targeted plate fell into the basket and progressively filled up the extension net. Bedload sampling lasted between 40 seconds and 10 minutes according to the intensity of bedload transport; (e) once the sampling time had elapsed and/or the sampling net was sufficiently filled, the second and third operators rapidly pulled the basket back using the ropes. Pulling back the basket typically lasted 2 to 3 seconds, which minimized the risk of collecting additional unwanted particles while bringing the basket back to the bank position; (f) all the bedload particles collected in the basket and extension net were emptied to labelled storage boxes (i.e. sample number, name of the associated calibration file, number of the calibrated plate, sampling duration).

Calibration samples were collected during four days of fieldwork distributed within the 2019 and 2020 snowmelt seasons (details for each calibration sample are available in Supporting Information III-S1). The specific fieldwork days were picked in order to have a range of flow (and so bedload transport) conditions with sampled discharges ranging from 0.88 to 2.69 $m^3 \cdot s^{-1}$. In total, 55 bedload samples were collected using the mobile sediment basket. Samples were alternatively collected over plates G5, G6, G7 and G8. This choice was motivated by a range of reasons. First, an impact experiment conducted over every SPG showed that all the plates at the VdN monitoring station responded similarly to impacts of comparable magnitude (Antoniazza et al., 2020); hence, a unique calibration coefficient could be used for all the different plates at this site (i.e. equations [III-2] and [III-3] below). Second, plates G5, G6, G7 and G8 recorded together ~ 69 % of the total bedload transport during the investigated period (2016-2020).

In previous studies to calibrate the SPG system in the field, the sampled bedload mass M_{tot} (Rickenmann and McArdell, 2007, 2008; Rickenmann et al., 2012, 2014b; Wyss et al., 2016c) or the unit bedload transport rate q_{b} (Habersack et al., 2017; Kreisler et al., 2017; Rickenmann and Fritschi, 2017; Rickenmann, 2018; Rickenmann et al., 2020) were related to the number of impulses N_{imp} or to the impulse rate *IMPT*, respectively, and typically for particles with a diameter larger than 19 mm. This limit was retained for its closeness to the threshold of detection of the SPG system (~10-20 mm). In our samples, particles between 9.5 and 19 mm represent on average ~13% of the total mass.

After collection, bedload samples were brought from the field to the laboratory of the Swiss Federal Research Institute WSL, and were sieved to include only particles greater than 19 mm. Each sample was then weighted using an industrial scale (precision of 10^{-3} kg). The mass of each sample is reported in Supporting Information III-S1, together with the number of impulses N_{imp} exceeding 0.1 V (Rickenmann et al., 2012; Antoniazza et al., 2020). The average grain-size distribution of the calibration samples is also provided in Supporting Information III-S1 (Figure III-S.1).

Previous research on the calibration of the SPG system (Rickenmann et al., 2012, 2014b; Rickenmann and Fritschi, 2017; Nicollier et al., 2019, 2020, 2021) found that the mass of the material that impacted a given plate could be linearly related to the number of impulses recorded by the associated geophone sensor, i.e. :

$$M_{\mathrm{tot}} = c_1 * N_{\mathrm{imp}} \qquad \text{[III-2]}$$

where M_{tot} [kg] is the mass of material that impacted a given plate, c_1 [kg] is a field-site dependent constant and N_{imp} $[-]$ is the recorded number of impulses.

Knowing the sampling duration (Supporting Information III-S1) and the width over which bedload occurs (i.e. roughly 0.5 m of plate width), the relationship can also be expressed in terms of rates, such as:

$$q_{\mathrm{b}} = c_2 * IMPT \qquad \text{[III-3]}$$

where q_{b} is a unit transport rate [kg·min^{-1}·m^{-1}], c_2 [kg·m^{-1}] is a field-site dependent constant, and *IMPT* an impulse rate [min^{-1}].

In this study, a linear regression line was fitted through the origin and the 55 calibration samples for both absolute and rate values. Linear relationships have indeed shown to perform well for most of the sites equipped with the SPG system, notably in Switzerland and Austria (Rickenmann et al., 2012, 2014b; Rickenmann and Fritschi, 2017; Rickenmann, 2018). The slope of the relationship gives the c_1 and c_2 coefficients, and a R^2 was calculated. The 95% confidence intervals were also calculated as:

$$CI = \pm t\sqrt{\frac{\sum e^2}{n-2}\left[\frac{1}{n} + \frac{(x_0-\bar{x})^2}{\sum x^2 - n\bar{x}^2}\right]} \qquad \text{[III-4]}$$

where t is the t-value of Student, e are the residual values, n is the number of calibration samples, x_0 are the values of the independent variable *N*$_{\mathrm{imp}}$ in the time-series, x are the values of the independent variable *N*$_{\mathrm{imp}}$ in the calibration set, and $\bar{x}$ is the mean of x. When bedload masses are summed over a given time-period (e.g. months, years), the associated uncertainty is calculated following a summation rule:

$$\sigma_{\mathrm{mass}} = \pm t\left[\sum_{i=1}^{T} {CI_i}^2\right]^{0.5} \qquad \text{[III-5]}$$

where σ_{mass} [kg] is the uncertainty in mass summed over a time-period T. In this paper, bedload masses were estimated with a 95 % confidence interval, with $t = 1.96$.

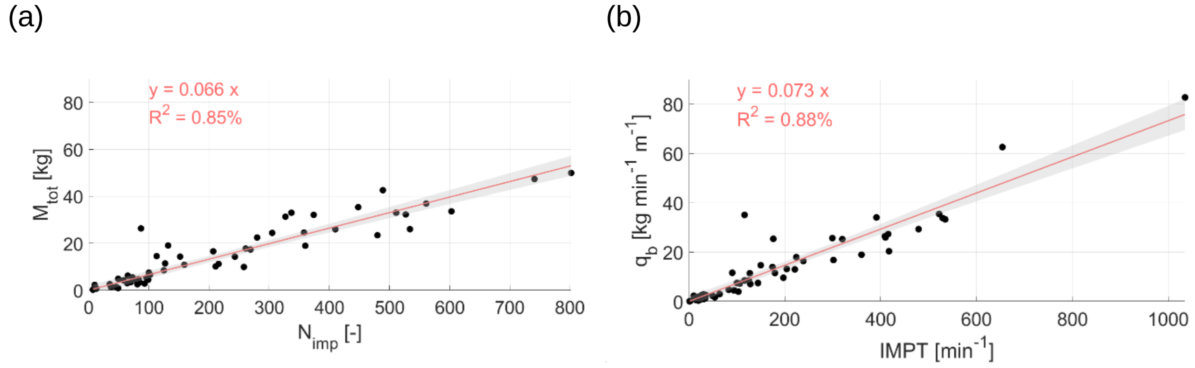

Figure III-3. Calibration relationship derived from 55 bedload samples (> 19 mm) at the VdN in (a) absolute (with coefficient c_1) and (b) rate terms (with coefficient c_2). The shaded area gives the 95% confidence intervals calculated from [4], which are used to propagate the uncertainty into transformed bedload mass and unit bedload transport rates. The fit was forced through 0 using the ‘polyfitzero’ Matlab function (Mikovski, 2021).

In Figure III-3a and III-3b, the relationships between the number of impulses N_{imp} and the bedload mass M_{tot} on the one hand, and between the impulse rate *IMPT* and the unit transport rate q_{b} on the other hand, are best expressed by a linear regression passing through the origin. The slope coefficients were 0.066 for total mass (c_1) and 0.073 for unit transport rate (c_2) and the R^2 were 0.85 and 0.88 respectively. The collection of calibration samples over a wide range of impulses (i.e. 99.4 % of 1-minute data points with bedload over the five-year time-series fall within the calibration domain) further allows narrow confidence intervals over most of the domain of interest, which translates into transport rate uncertainties that are low compared to the transport rates themselves.

Earlier studies interested in the calibration of the SPG system found that slope coefficients c_1 and c_2 may vary according to a range of factors, which include flow velocity (Wyss et al., 2016a, 2016b; Nicollier et al., 2021), bed roughness (Wyss et al., 2016a, 2016b) and particle grain size (Wyss et al., 2016c; Nicollier et al., 2021). Furthermore, an impact experiment conducted by Antoniazza et al. (2020) at several bedload monitoring sites equipped with the SPG system (including the VdN) showed that ~10-20% of the signal recorded on a given impacted plate propagates into the neighbouring non-impacted plates despite the isolating elastomer elements. These elements likely influence the relationship between the SPG impulse count and the actual mass of bedload in transport shown in the scatter in Figure III-3. Nevertheless, these sources of variability are implicitly included in the slope coefficients proposed here, the bedload samples being collected for a range of natural streamflow and bedload transport rates that covers various flow conditions, grain-size distribution and rates of signal propagation. The scatter is moreover relatively low. Therefore, the calibration of the SPG system presented here is considered to be reliable.

III-2.5 Data analysis

The quantification of bedload transport over the five years of observation (2016-2020), and the identification of the hydrological events driving them it, were performed through three main complementary analyses.

III-2.5.1 Bedload and hydraulic forcing

First, absolute time-series of bedload transport over the period of interest, together with the streamflow time-series, were computed. Bedload transport was then integrated across different time-scales (e.g. years, months) to quantify its variability. Annual erosion rates were also derived from the total volume of bedload exported for comparison with other watersheds where such data are available.

In addition, an estimate of the hydraulic forcing of bedload transport at the VdN was performed, by comparing daily measured bedload transport with the daily predicted one, based on transport capacity calculations. The transport capacity calculations used a set of shear stress-based sediment transport equations proposed in the work of Schneider et al. (2015) and Rickenmann (2020), which have been shown to perform relatively well in Alpine streams with comparable characteristics to the Avançon de Nant. A total shear stress approach combined with a slope-dependent reference shear stress was used as it was shown to perform as well as other treatments, such as a constant reference shear stress combined with a reduced shear stress (Schneider et al., 2015; Rickenmann, 2020). A reference shear stress approach was preferred to an excess (unit) discharge or excess shear stress approach because the latter was shown to produce a much too steep increase in the transport capacity with increasing unit discharge or increasing dimensionless shear stress (Rickenmann, 2018). The set of equations represents a modified form of the Wilcock and Crowe (2003) equation, which predicts daily bedload transport rate Q_{b} [kg·s^{-1}] (of particles greater than 4 mm) using the total shear stress (i.e. transport capacity-based), and integrating bedload transport over the entire channel width:

$$W^{*} = 0.002\left(\frac{\tau_{D50}^{*}}{\tau_{rD50}^{*}}\right)^{16.1} \qquad \text{for } \frac{\tau_{D50}^{*}}{\tau_{rD50}^{*}} < 1.143 \text{ and D} > 4 \text{ mm} \qquad \text{[III-6.1]}$$

$$W^{*} = 14\left(1-\frac{0.85}{\left(\frac{\tau_{D50}^{*}}{\tau_{rD50}^{*}}\right)^{0.7}}\right)^{4.5} \qquad \text{for } \frac{\tau_{D50}^{*}}{\tau_{rD50}^{*}} \geq 1.143 \text{ and D} > 4 \text{ mm} \qquad \text{[III-6.2]}$$

where $W^{*}$is the dimensionless transport rate, and where the dimensionless bed shear stress τ_{D50}^{*}, the dimensionless reference bed shear stress τ_{rD50}^{*} and the total transport rate Q_{b} [kg·s^{-1}] are defined as:

$$\tau_{D50}^{*} = \frac{r_h S}{R D_{50}} \qquad \text{[III-7]}$$

$$\tau_{rD50}^{*} = 0.56\, S^{0.5} \qquad \text{[III-8]}$$

$$Q_{\mathrm{b}} = b * \rho_s * W^{*} * \frac{(g * r_h * S)^{1.5}}{R * g} \qquad \text{[III-9]}$$

In the set of equations, r_h [m] is the hydraulic radius, S [-] is the channel gradient, $R = \rho_s/\rho - 1$ [-] is the relative sediment density (with the sediment density $\rho_s = 2650$ kg/m^3 and the water density $\rho = 1000$ kg/m^3), D_{50} [m] is the median of the surface grain-size distribution, $g = 9.81$ [m/s^2] is the gravitational acceleration.

In this study, the ~20 m long natural reach upstream of the monitoring station was selected to perform the calculations, because the hydraulic conditions within that reach were considered more representative than those at the weir to calculate the bedload transport capacity. In this reach, a mean slope S of 0.04 was measured in a total station survey, the median of the bed grain-size distribution $D_{50} =$ 0.06 m was estimated through line-by-number counts on emerged areas of the bed (e.g. bars) using a 7 pixels per cm resolution orthophoto. The hydraulic radius $r_h = (b + mh)h \;/\; (b + 2h * \sqrt{1 + m^2})$ was estimated for every 1-min measured water depth h [m] within the trapezoidal natural channel cross-section. In the calculations, $b = 5.8\, m$ is the average channel width, and $m = h / tan(45) = h$ is the increase in channel width [m] with depth [m], with the slope of the channel banks set to 1:1. Additional details on the reach over which the transport capacity calculations are performed, as well as details on the calculation of the representative classes of the streambed grain-size distribution, are provided in Supporting Information III-S2.

In order to calculate the hydraulic conditions in the natural section upstream of the monitoring station, discharge measurements were combined with the flow resistance equations proposed in Rickenmann and Recking (2011), with dimensionless mean flow velocity U^{**} and discharge q^{**}:

$$U^{**} = 1.443 * \, q^{**0.6}\left[1 + \left(\frac{q^{**}}{43.78}\right)^{0.8214}\right]^{-02435} \qquad \text{[III-10.1]}$$

$$U^{**} = \frac{U}{\sqrt{g * S * D_{84}}} \qquad \text{[III-10.2]}$$

$$q^{**} = \frac{Q/b}{\sqrt{g * S * D_{84}{}^{3}}} \qquad [III-10.3]$$

$$h = D_{84} * m_1 * q^{**m_2} \qquad [III-10.4]$$

where U is the depth-averaged flow velocity [m/s], Q is the discharge measured at the monitoring station [m^3/s] and D_{84} = 0.36 m is the 84th percentile of grain-size distribution, estimated following the same procedure than the D_{50}. Coefficients $m_1 = 1.6^{-1}$ and $m_2 = 0.455$ follow Rickenmann and Recking (2011). Once Q_b was calculated for every 1-minute time-step, it was then integrated over each day to obtain daily predicted bedload masses.

III-2.5.2 Classification of the hydrological drivers of bedload

The contribution of different hydrological drivers to total bedload transport were identified in the streamflow time-series. We were particularly interested to investigate the proportion of bedload transported during rainfall-induced streamflow variations, during melt-induced streamflow variations, and during the co-occurrence of rainfall-induced and melt-induced streamflow variations, because these are the hydrological drivers expected to be able to trigger bedload transport, either separately or in combination.

The first step identified daily flow hydrographs influenced by rainfall. To do so, precipitation and temperature data were obtained from the RhiresD and TabsD datasets of MeteoSwiss. The RhiresD and TabsD datasets represent respectively daily precipitation (rainfall and snowfall equivalent, [mm]) and daily mean temperature [°C] interpolated at a spatial resolution of 1 km^2 from the dense precipitation-gauge and temperature sensor networks of MeteoSwiss (MeteoSwiss, 2019, 2017). Eighteen 1-km^2 cells of the RhiresD and TabsD grids covering partially or entirely the VdN were retained, and their coordinates are reported in Supporting Information III-S3. From the RhireD precipitation dataset, a gross partitioning between rainfall and snowfall was performed, by summing for each grid cell the precipitation that occurred when the temperature of a given grid cell was above or below 1°C, respectively.

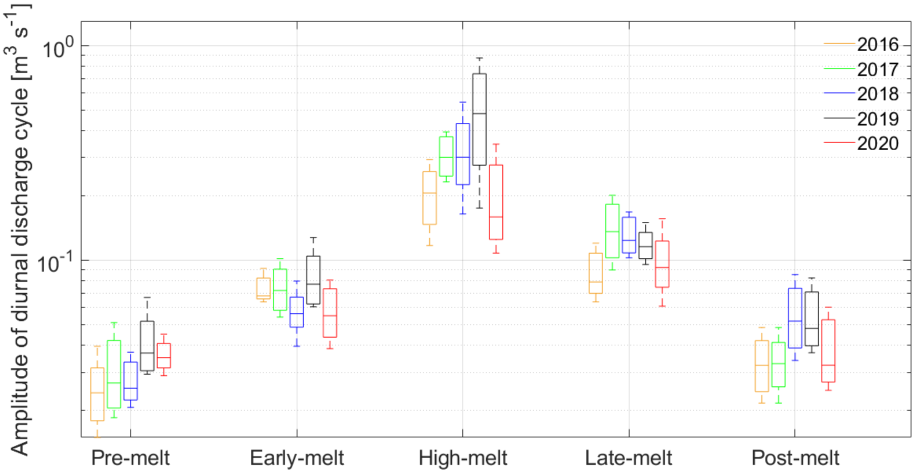

Figure III-4. Distribution of daily Q_{amp} values (10th, 25th, 50th, 75th and 90th percentiles) within each period (i.e. pre-melt, early-melt, high-melt, late-melt, post-melt) for "not rain-forced" daily flow hydrographs of all investigated years (2016-2020).

In an early stage of the work, an automatic classification of "rain-forced" and "not rain-forced" daily flow hydrographs was attempted, following Mutzner et al. (2015). It used a set of criteria combining the removal of snowy days (precipitation occurring during days where mean temperatures are below 1°C), the depth of rainfall (of days where mean temperatures are above 1°C), the amplitude of daily flow hydrographs and the timing throughout the day of high flows and low flows (i.e. to differentiate between rainfall-driven and melt-driven changes in daily flow hydrographs). However, no sensible set of criteria covering the range of flow hydrograph responses was identified using this approach, notably due to (1) the variable depth of rainfall generating a flow hydrograph response; (2) the variable daily mean temperature generating snowfall or rainfall (i.e. visible in the direct response to precipitation in the flow hydrograph); (3) the variable recession time of rainfall-driven events; and (4) a large variability in the amplitude and timing of daily low and high flows.

Therefore, a visual classification of the 1827 daily flow hydrographs into the two classes “rain-forced” and “not rain-forced” was undertaken. It used daily precipitation data, daily mean temperature data and daily flow hydrograph (i.e. amplitude, timing of high flows and low flows) to support the classification, but without setting fixed arbitrary thresholds in temperature, precipitation and/or the daily flow hydrograph, which were found to be unsuitable at the previous stage. Each daily flow hydrograph was first considered in terms of its amplitude and the timing of high flows and low flows. Then, daily precipitation and mean temperature data were used to determine whether any daily flow hydrograph was possibly influenced by rainfall. The daily flow hydrograph of the antecedent day was also systematically used to identify possible recession curves in the daily flow hydrograph of the subsequent day. This approach allowed inclusion within the “rain-forced” category of days where rainfall visually induced a response in the flow hydrograph, including potential recession curves in the subsequent day(s). Within the class “not rain-forced” daily flow hydrographs, it also allowed the inclusion of days with precipitation, but where the latter did not induce a response in the flow hydrograph. This may include snowfall, light rainfall or rainfall stored in a pre-existing snowpack or in the soil. Note that we are interested here in determining whether any daily flow hydrograph variation is (directly or indirectly) caused by rainfall, and not in the exact paths (e.g. surface water, subsurface water) the flow is following. Examples of typical daily flow hydrographs classified in each category (i.e. “rain-forced” or “not rain-forced”) are provided in Supporting Information III-S4. Annual flow hydrographs, variations in daily precipitations and daily mean temperatures for each year of observation (2016-2020) are available in Supporting Information III-S5.

Once daily flow hydrographs influenced by rainfall were identified within the streamflow time-series of each year (2016-2020), we partitioned periods of the year with differing melt intensity. The method used to classify daily flow hydrographs according to melt intensity follows Mutzner et al. (2015), and is based on the amplitude of daily melt discharge cycles. To identify days with clear melt signal, only the previously classified “not rain-forced” days are considered (Figure III-S.4b, S.5b, S.6b, S.7b). For each “not rain-forced” day, a daily flow hydrograph variation was calculated by subtracting a 24-hour moving average from the measured streamflow, to obtain a so-called detrended flow hydrograph Q_{det} [$\mathrm{m}^3 \cdot \mathrm{s}^{-1}$] (Mutzner et al., 2015). The amplitude of the daily flow hydrograph cycle Q_{amp} [$\mathrm{m}^3 \cdot \mathrm{s}^{-1}$] was estimated as half the difference between the maximum and the minimum value in the detrended daily flow hydrograph (Gribovszki et al., 2010; Mutzner et al., 2015). A visual inspection of the variation in both Q_{det} (Figure III-S.8c, S.9c, S.10c, S.11c, S.12c) and Q_{amp} (Figure III-S.8d, S.9d, S.10d, S.11d, S.12d) throughout each year permitted the identification of coherent periods of time when daily flow hydrographs of “not rain-forced” days would recurrently vary within a comparable range (Figure III-4). We labelled them the pre-melt period, the early-melt period, the high-melt period, the late-melt period, and the post-melt period.

Table III-1. Dates of start and end of the five identified periods (pre-melt, early-melt, high-melt, late-melt, post-melt) for each investigated year, determined based on the range of variability in Q_{amp} values (25th, 50th and 75th percentile value reported here), and a visual inspection of the variation of both Q_{det} (Figure III-S.8c, S.9c, S.10c, S.11c, S.12c) and Q_{amp} through time (Figure III-S.8d, S.9d, S.10d, S.11d, S.12d).

		Pre-melt **50th** **[25th, 75th]**	**Early-melt** **50th** **[25th, 75th]**	**High-melt** **50th** **[25th, 75th]**	**Late-melt** **50th** **[25th, 75th]**	**Post-melt** **50th** **[25th, 75th]**
2016	Dates	Jan. 1st – Apr.10th	Apr. 11th – May 5th	May 6th – Aug. 11th	Aug. 12th – Aug. 28th	Aug. 29th – Dec. 31th
	Q_{amp} [m^3 s^{-1}]	0.02 [0.02, 0.03]	0.07 [0.07, 0.08]	0.21 [0.16, 0.25]	0.08 [0.07, 0.1]	0.03 [0.03, 0.04]
2017	Dates	Jan. 1st – Apr. 2nd	Apr. 3rd – May 13h	May 14th – Jun. 21th	Jun. 20th – Sep. 4th	Sep. 5th – Dec. 31th
	Q_{amp} [m^3 s^{-1}]	0.03 [0.02, 0.04]	0.07 [0.06, 0.09]	0.3 [0.25, 0.37]	0.14 [0.1, 0.18]	0.03 [0.03, 0.04]
2018	Dates	Jan. 1st – Apr. 7th	Apr. 8th – Apr. 16th	Apr. 17th – Jun. 24th	Jun. 25th – Sep. 4th	Sep. 5th – Dec. 31th
	Q_{amp} [m^3 s^{-1}]	0.03 [0.02, 0.03]	0.06 [0.05, 0.06]	0.3 [0.24, 0.4]	0.12 [0.1, 0.16]	0.05 [0.04, 0.07]
2019	Dates	Jan. 1st – Apr. 4th	Apr. 5th – May. 15th	May. 16th – Jul. 8th	Jul. 9th – Aug. 29th	Aug. 30th – Dec. 31th
	Q_{amp} [m^3 s^{-1}]	0.04 [0.03, 0.05]	0.08 [0.06, 0.1]	0.48 [0.31, 0.69]	0.12 [0.1, 0.13]	0.05 [0.04, 0.07]
2020	Dates	Jan. 1st – Apr. 4rd	Apr. 5th – Apr. 9th	Apr. 10th – Jul. 20th	Jul. 21th – Sep. 5th	Sep. 6th – Dec. 31th
	Q_{amp} [m^3 s^{-1}]	0.04 [0.03, 0.04]	0.06 [0.05 0.07]	0.16 [0.13, 0.25]	0.09 [0.08, 0.11]	0.03 [0.03, 0.05]

At the VdN, the pre-melt period extends from January 1st to the onset of the melt season in early spring (i.e. April), and typically presents Q_{amp} median values between 0.02 and 0.04 [m^3·s^{-1}] (Figure III-4; Table III-1). The early-melt period represents the onset of the snowmelt season, during which the amplitude of the diurnal hydrograph cycles Q_{amp} remains however relatively low, with median values ranging between 0.06 and 0.08 [m^3·s^{-1}] (Figure III-4; Table III-1). The high-melt period is the period with high rates of snowmelt, during which the amplitude of the diurnal hydrographs is the highest, with median values typically greater than

0.16 [$m^3 \cdot s^{-1}$] (Figure III-4; Table III-1). The late-melt represents the period where a distinctive decrease in the amplitude of the diurnal hydrograph cycles is observed as the watershed snow content decreases, but where the remaining snowmelt still generates intermediate values of Q_{amp}, with median ranging from 0.08 to 0.14 [$m^3 \cdot s^{-1}$] (Figure III-4; Table III-1). The post-melt is the period where remaining melt from the previous winter no longer produces large variations in Q_{amp}, and where the amplitude of 'not rain-forced days' diurnal discharge hydrographs mainly relies on the evapotranspiration cycle, and/or the melt of the potential first winter snowfall. The post-melt period spans from the late summer until the end of the year, with median values typically ranging between 0.03 and 0.05 [$m^3 \cdot s^{-1}$]. The determined date of the start and end of each period for each year, and the distribution of Q_{amp} values within them are reported in Table III-1. Results of the classification (Table III-1; Figure III-4) show on the one hand the relatively low overlap between Q_{amp} values of different periods within the same year. On the other hand, it exhibits a remarkable consistency of Q_{amp} values within a same period across years. It is important to note that given the specific meteorological conditions (e.g. temperatures, snow volumes) of a given year, the different periods may start and end at very different dates (Table III-1). If the pre-melt and post-melt periods do present a distribution of daily discharge amplitude that varies within a comparable range, they are quite different in terms of watershed hydrology and bedload dynamics. Indeed, the pre-melt corresponds to a rather cold period with a great amount of snow in the watershed, while the post-melt includes autumn storms, a more prominent evapotranspiration cycle, and the potential occurrence of the first winter snowfall in a watershed mostly free of snow cover. This is why we keep the two periods separated.

From this hydrological analysis, we were able to partition each year into the five periods of differing melt intensity (i.e. pre-melt, early-melt, high-melt, late-melt and post-melt), and also to establish within them whether rainfall was additionally influencing or not the daily flow hydrograph ("rain-forced" and "not rain-forced" days). Bedload could then be integrated along those different categories, separately or in combination, to investigate the proportion of bedload transport driven by the different hydrological categories (i.e. rainfall-induced, melt-induced or a combination of both). The classification further allowed determination of the magnitude-frequency of daily bedload transport at the VdN for the different hydrological categories. The magnitude of bedload transport is calculated for both the daily total bedload mass transported [kg], and for the daily maximum bedload rate reached [$kg \cdot min^{-1}$]. The frequency is calculated from the number of days within a given category that equals or exceeds a given bedload magnitude.

III-2.5.3 Determination of erosion rates inferred from bedload transport

Third, it is common to divide sediment export volumes by the average sediment density (i.e. 2650 $kg \cdot \mathrm{m}^{3^{-1}}$; Hinderer et al., 2013), and by the associated watershed area (i.e. 13.4 km^2), to give annual erosion rates inferred from bedload transport. Although such calculations assume that sediment was eroded in the year that it was exported, we perform them here for comparative purposes with other watersheds where such data are available. Note that in addition to bedload particles < 19 mm, the erosion rates presented here do not include the suspended load, which is likely to represent a substantial proportion of the annual total mechanical erosion. At the VdN, we estimate it to represent at least 50% of the sediment budget (Turowski et al., 2010; Hinderer et al., 2013).

III-3 Results

III-3.1 Absolute bedload time-series, transported masses and hydraulic forcing

Five years of measurement of streamflow and bedload transport rates are presented in Figure III-5a. Streamflow follows the general trends expected for a snowmelt-dominated Alpine watershed at this altitude (Figure III-4, Table III-1), with low baseflow during the winter season (pre-melt), increasing slowly during April at the onset of the melt season (early-melt), and more steadily during late May-early June. Streamflow then peaks in the period June-July at the maximum of the snowmelt season (high-melt), and decreases progressively as watershed snow content declines through the summer season (late-melt), and autumn (post-melt). This general seasonal trend is disrupted by sudden storms, especially during the summer and the autumn, that can generate periods of short-duration high streamflow. As expected, bedload transport also occurs during periods of high-magnitude streamflow, either during the snowmelt season or during storms throughout the year, with the exception of the winter period, when the lowest bedload transport rates tend to be observed.

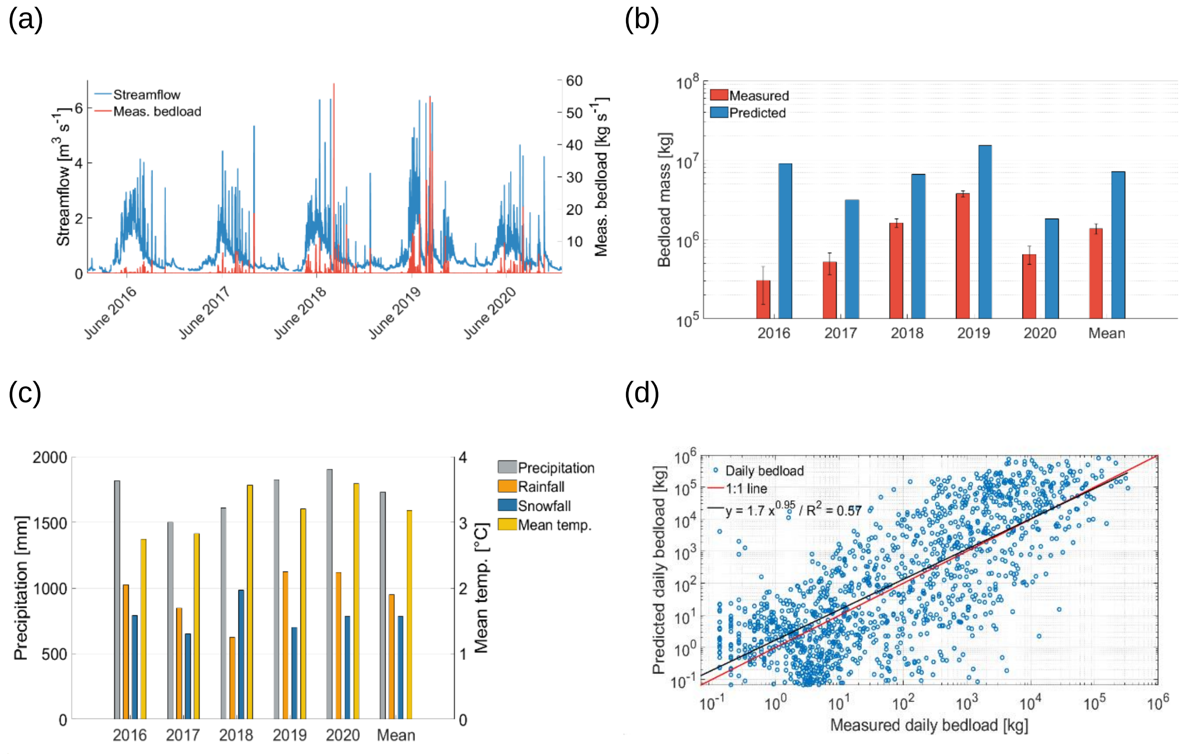

Figure III-5. (a) Measured time-series of streamflow (in blue) and bedload transport rates (in red) over the five years of observation (2016-2020); (b) measured annual bedload masses (in red) predicted annual bedload masses (in blue) for each of the five years of observation. Note the logarithmic y-scale; (c) annual mean temperature (in yellow), precipitation (in gray), rainfall (in orange), snowfall (in dark blue), for each of the five years of observation; (d) relationship between daily predicted and daily measured bedload transport over the five years of observation. The red line is the 1:1 relationship, and the black line is the best-fit power law regression.

Annual bedload mass varies significantly among the five years of observation (Figure III-5b). 2019 had a much higher annual bedload mass, with $3.75\cdot10^6$ kg (± $3.29\cdot10^3$ kg), followed by the year 2018 with $1.62\cdot10^6$ kg (± $1.95\cdot10^3$ kg). The years 2016, 2017 and 2020 recorded a lower total bedload mass with $0.30 \cdot 10^6$ kg (± $1.51 \cdot 10^3$ kg), $0.52 \cdot 10^6$ kg (± $1.57\ 10^3$ kg) and $0.65 \cdot 10^6$ kg (± $1.65 \cdot 10^3$ kg), respectively. Over the five years investigated, the average annual mass of bedload exported from the VdN is $1.37 \cdot 10^6$ kg (± $1.99\ 10^3$ kg). From 2016 to 2020, the average annual erosion rate inferred from bedload transport at the Vallon de Nant is 0.039 $\mathrm{mm \cdot y^{-1}}$ (± $5.6 \cdot 10^{-5}$ mm). Annual and monthly transported bedload masses throughout the five years of measurement, and their estimation uncertainty, are reported in Supporting Information III-S6.

The differences observed in the annual bedload yield at the VdN do not scale directly with either the total amount of precipitation (rainfall and/or snowfall) a given year received, or with mean annual temperatures (Figure III-5b, III-5c). The annual sum of RhiresD daily precipitation (over the 18 1-km^2 cells selected for the VdN; Table III-S.2) shows indeed that the year 2020 received the greatest amount of precipitation (~1905 mm), followed by the years 2019 (~1825 mm), 2016 (~1810 mm), 2018 (~1610 mm) and 2017 (~1500 mm). A gross estimate of rainfall (i.e. sum of daily precipitation of RhiresD where daily mean temperature TabsD is equal or above 1°C) suggests that the year 2019 received the greatest amount of rainfall (~1125 mm), followed by the year 2020 (~1120 mm), 2016 (~1020 mm), 2017 (~850 mm) and 2018 (~625 mm). A gross estimate of snowfall (i.e. sum of daily precipitation of RhiresD where daily mean temperature TabsD is equal or below 1°C) suggests that the year 2018 received the greatest amount of snow (~985 mm), followed by the year 2016 (~790 mm), 2020 (~785 mm), 2019 (~700 mm) and 2017 (~650 mm). Regarding the annual mean temperature, the three warmest years are indeed the three most active in terms of bedload transport (2019, 2018, 2020), but with proportions that do not really scale with temperature. This decorrelation between precipitation, temperature and bedload transport is notably expected to be due to temporary storage in different hydrological compartments of the watershed (e.g. soil, snowpack). Note that precipitation in the RhiresD dataset is expected to be underestimated due to snow undercatch (Freudiger et al., 2016).

Regarding the shear stress-based estimate of bedload, calculated from equations [III-6 to III-10] (Figure III-5b, in blue), the hydraulic forcing based on time-integrated transport capacity tends to overestimate the actual measured bedload (Figure III-5b, in red), with factors between 3 (2020) and 30 (2016) of difference. Part of the overestimation is due to the difference between the threshold of detection of the SPG system (particles of 10-20 mm) and the grain-size domain under which the equations [III-6 to III-10] were validated (particles > 4 mm). Whilst these differences are substantial, our estimations remain somehow lower than many bedload predictions, which typically exceed bedload measurements by one or more order(s) of magnitude (Recking, 2013; Schneider et al., 2015; Yager et al., 2015; Ancey, 2020a, 2020b). Comparing the relative difference between years, the annual predicted bedload mass seems to scale approximatively for the years 2017-2020, but not for the year 2016, with regards to relative yearly differences in the measured bedload mass (Figure III-5b).

The relationship between the daily bedload mass derived from the SPG system measurements, and the daily bedload mass predicted from the time-integrated shear stress (i.e. transport capacity) equations is presented in Figure III-5d. The relationship shows a relatively good agreement with the 1:1 line, with the exponent of the power law regression being close to 1, and an R^2 of 0.57, which illustrates the importance of hydraulic forcing for bedload transport. Yet, transport capacity calculations may be sensitive to the measurement of parameters b, S, D_{50} and D_{84} in equations [III-6 to III-10], which also contain uncertainties. Thus, a Monte Carlo sensitivity analysis was performed by combining random values of these parameters (within a plausible range) to evaluate how they affect the transport capacity calculations. Details on the Monte Carlo sensitivity analysis are available in Supporting

Information III-S7. After 1000 simulations, results (Figure III-S.14) showed a relative non-sensitivity to the estimate of parameters *b*, *S* and D_{84}, but a greater sensivity to the estimate of D_{50} . Yet, the value of 0.06 m for the D_{50} lies in the range that optimizes the transport capacity calculations. As such, the measurement of parameters *b*, *S*, D_{50} and D_{84} performed in this study appears appropriate with regards to transport capacity calculations, and with regards to the sensitivity of the parameters they are based upon.

In Figure III-5d, the scatter around the trend line has up to three orders of magnitude of difference between the daily measured and predicted bedload mass for both over- and underestimation, which also emphasizes the limits of hydraulic-based estimates of bedload. Reasons for this discrepancy may be found in either erroneous estimates of the hydraulic forcing, or the temporally variable availability in sediment both at the bed and from the drainage network (e.g. sediment pulses; Elgueta-Astaburuaga et al., 2018). The density of data points below the 1:1 line in Figure III-5d (particularly for smaller loads) may suggest that the shear stress-based equations tend on average to underestimate the transported bedload mass. Yet, the data points above the 1:1 line (i.e. overestimation of predicted bedload as compared to the measured one; logarithmic y-scale) have on average more weight when summing up daily values to annual loads, and largely compensate the underestimates of bedload at lower magnitude transport on a daily time-scale (Figure III-5b).

III-3.2 Bedload transport, rainfall and the melt season

Bedload was summed for each year for “rain-forced” and “not rain-forced” days based on the classification of daily flow hydrographs (Figure III-6a). Results show that a significantly greater proportion of annual bedload transport takes place during “rain-forced” daily flow hydrographs, as compared with “not rain-forced” daily flow hydrographs. On average over the five years of observation, ~86% of the annual bedload budget (75% to 91%) occurs during “rain-forced” daily flow hydrographs, while “not rain-forced” flow hydrographs (which notably include the melt-only signal) represent on average ~14 % of the annual bedload budget (9% to 25%). Note that “rain-forced” days may occur throughout the year, therefore they may be associated with a melt signal of varying intensity.

Bedload transport was further summed by year for each of the five periods that have been identified based on the amplitudes of the daily flow hydrographs of “not rain-forced” days (Figure III-6b). Results show that while the pre-melt and early-melt periods record no, or a negligible proportion (~ 1 %) of annual bedload, the high-melt season represents on average ~59 % (45% to 89 %) of the annual transported bedload. The late-melt period is the second period carrying the highest proportion of material, with on average ~31 % of the annual load (1-44 %), including year 2016 where a comparatively lower proportion of annual bedload was transported (1 %). The post-melt period was also responsible for a non-negligible part of the annual transported bedload, ~9 % on average (4% to 13 %). Note that each period contains both “rain-forced” and “not rain-forced” days.

Bedload was also investigated by combining the two categories, that is “rain-forced” and “not rain-forced” daily flow hydrographs, and the five periods with differing melt intensity (Figure III-6c). Results show that the greatest masses of bedload are consistently transported during “rain-forced” days of the high-melt season throughout the five years of observation, representing on average ~47 % of the annual bedload. Then, the second highest volumes are transported during “rain-forced” days of the late-melt period, with an average of ~30 % of the annual bedload. In third place come “not rain-forced” days of the high-melt period, with an average of ~12 % of the annual bedload. Fourth place is occupied by “rain-forced” days of the post-melt season, with an average of ~9% of the annual bedload. The “not rain-forced” days of the late-melt season with an average of ~2% of the annual bedload is in fifth place. These are followed by the other categories, which carry a negligible proportion of the annual bedload transport (< 1 %).

(a)

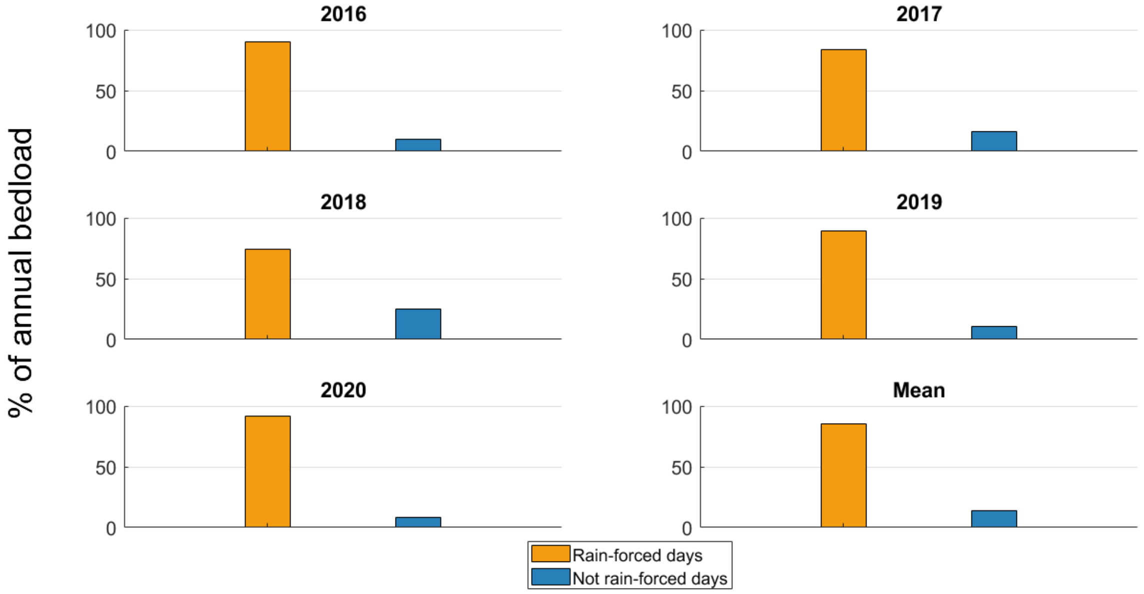

(b)

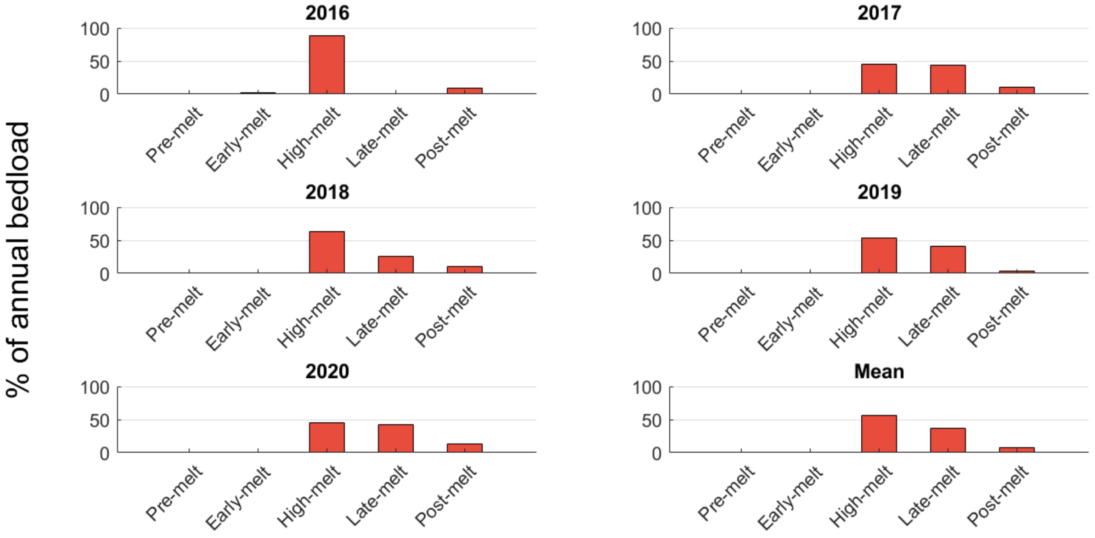

(c)

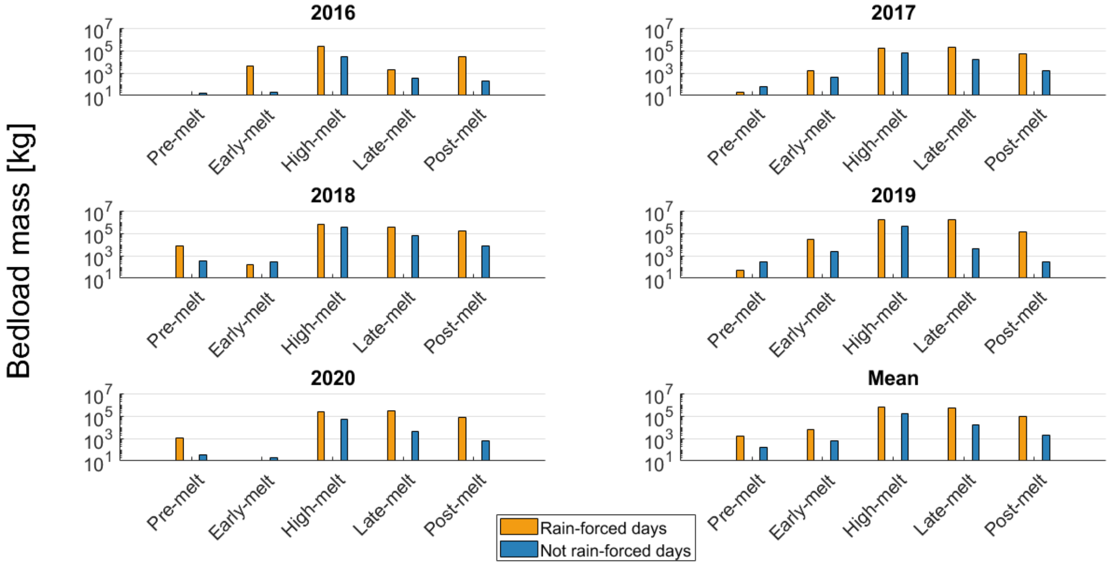

Figure III-6. In (a), the proportion of annual bedload transport between “rain-forced” and “not rain-forced” days is presented for each of the five years of observation (2016-2020) and on average over the five years. In (b), the proportion of annual bedload transported for each of the five periods identified in flow hydrographs is presented (i.e. pre-melt, early-melt, high-melt, late-melt and post-melt) for each of the five years of observation and on average over the five years. In (c), total transported bedload mass per year and on average for each of the five periods, and between categories “rain-forced” and “not rain-forced” is presented. Note the logarithmic y-axes in Figure III-6c.

III-3.3 Bedload transport magnitude-frequency

A progressive decline in the magnitude of daily bedload transport is observable with increasing frequency (expressed as a percentage of days), for both the total mass of bedload transported per day (Figure III-7a), and for the daily maximum transport rate reached (Figure III-7b).

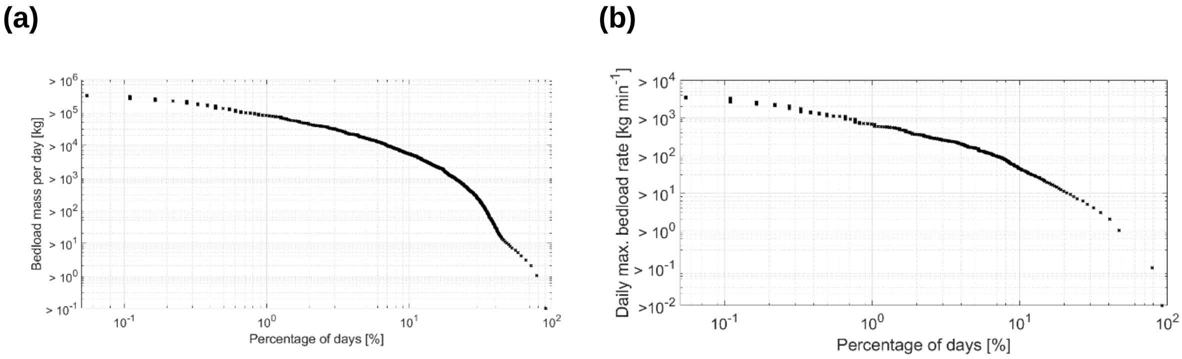

Figure III-7. Magnitude-frequency relationship of daily bedload transport at the VdN throughout the five years of observation (2016-2020) for both (a) the daily bedload total mass transported and (b) the daily maximum transport rate reached.

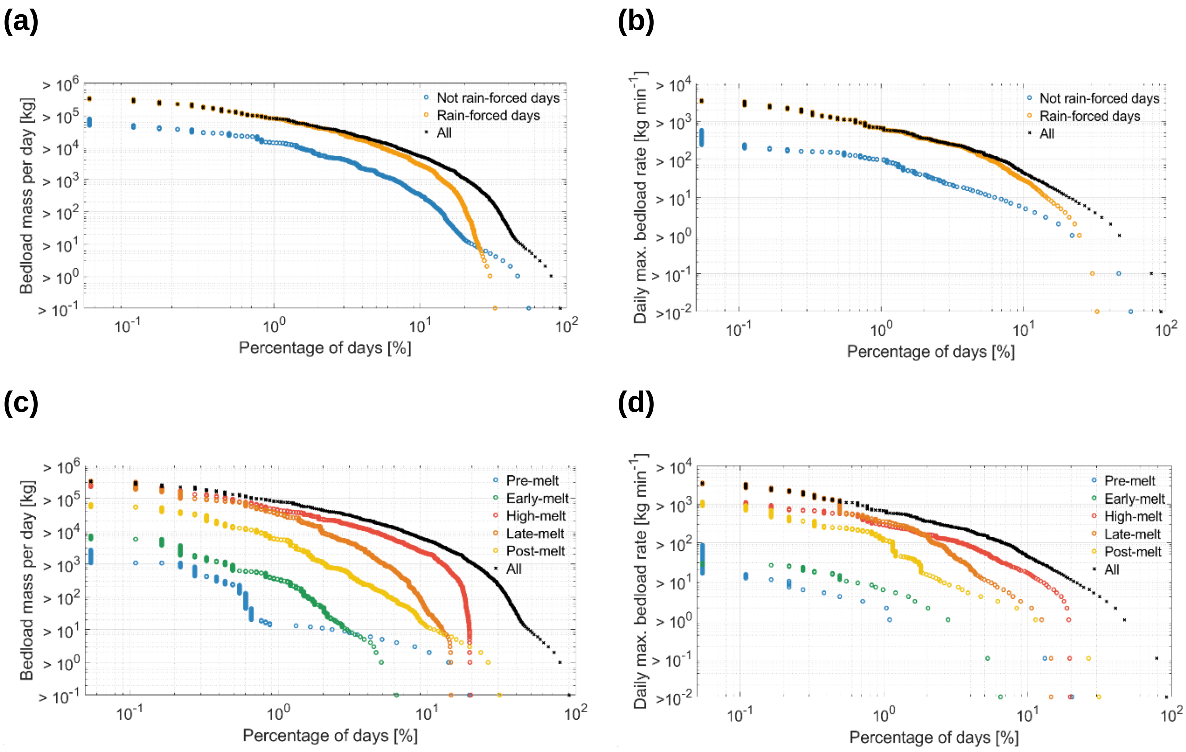

Figure III-8. Magnitude-frequency relationship of daily bedload transport at the VdN between “rain-forced” and “not rain-forced” days for both (a) the daily bedload total mass transported and (b) the daily maximum transport rate reached, and between the five identified periods with differing melt intensity for both (c) the daily bedload total mass transported and (d) the daily maximum bedload rate reached.

The largest daily bedload total mass is $3.34 \cdot 10^{5}$ kg, while the highest daily maximum transport rate is $3.5 \cdot 10^{3}$ kg·min^{-1}. For ~0.6% of days (= 11 days) throughout the five years of observation daily bedload mass exceeds 10^{5} kg; for ~0.6% of days, daily maximum rate is > 10^{3} kg·min^{-1}. At intermediate magnitude-frequency, ~7% of days (= 128 days) have a daily bedload mass exceeds 10^{4} kg, and ~7% of days when daily maximum rates are greater than 10^{2} kg·min^{-1}. As magnitude further decreases (i.e. daily mass < 10^{4} kg; daily peak rate < 10^{2} kg·min^{-1}) and frequency increases (> 128 days), there is a steep decline in the magnitude-frequency relationship for both variables (Figure III-7).

In Figure III-9, the magnitude-frequency relationships for daily bedload transport between “rain-forced” and “not rain-forced” days, and between the five periods with differing melt intensity, for both the daily bedload mass transported (Figure III-9a) and the daily maximum transport rate reached (Figure III-9b), are presented. For daily total mass (Figure III-9a), at low frequencies (< 0.6 % of days, 11 days), high magnitudes (> 10^{5} kg) are found during “rain-forced” days of the high-melt and late-melt periods. Then come “rain-forced” days of the post-melt period and “not rain-forced” days of the high-melt period (10^{4}-10^{5} kg), followed by “rain-forced” days of the early-melt and “not rain-forced” days of the late-melt period (10^{3}-10^{4} kg). “Rain-forced” days of the pre-melt period, and “not rain-forced” days of the post-melt, early-melt and pre-melt periods all record relatively low bedload magnitudes (< 10^{3} kg), even at these low frequencies of occurrence. At intermediate frequencies (0.6-2% of days, 11-37 days), the highest magnitudes are recorded for, in decreasing order: “Rain-forced – high-melt”; “Rain-forced – late-melt”; “Not rain-forced – high-melt”; “Rain-forced – post-melt”; “Not rain-forced – late-melt”; followed by the other categories, which carry less substantial masses of bedload. At high frequencies (> 2%), the magnitude of the pair “Rain-forced – Late-melt” days decrease more rapidly than the pairs “Rain-forced – High-melt” and “Not Rain-forced – High-melt”.

(a)

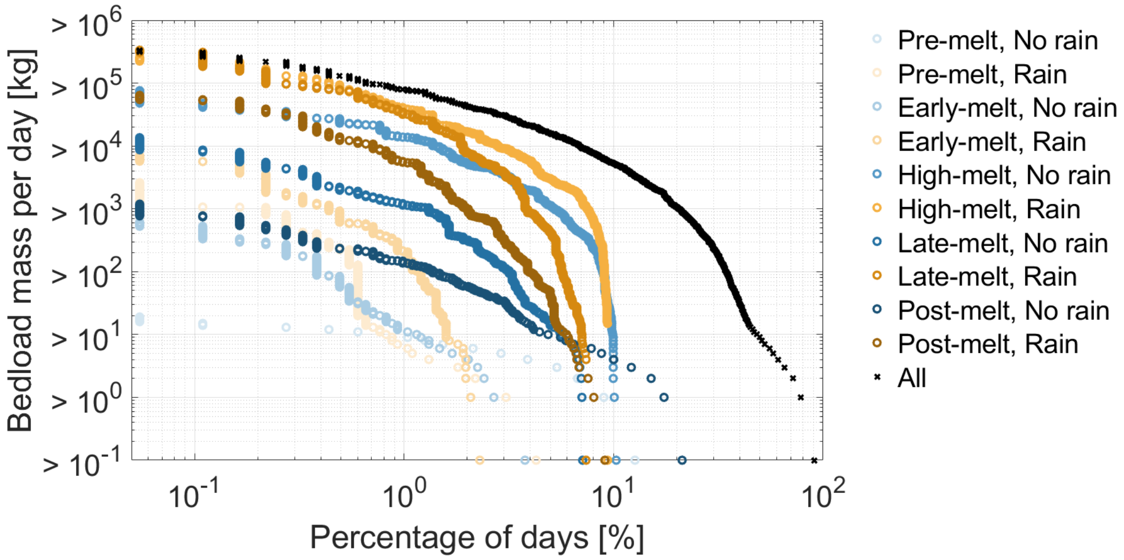

(b)

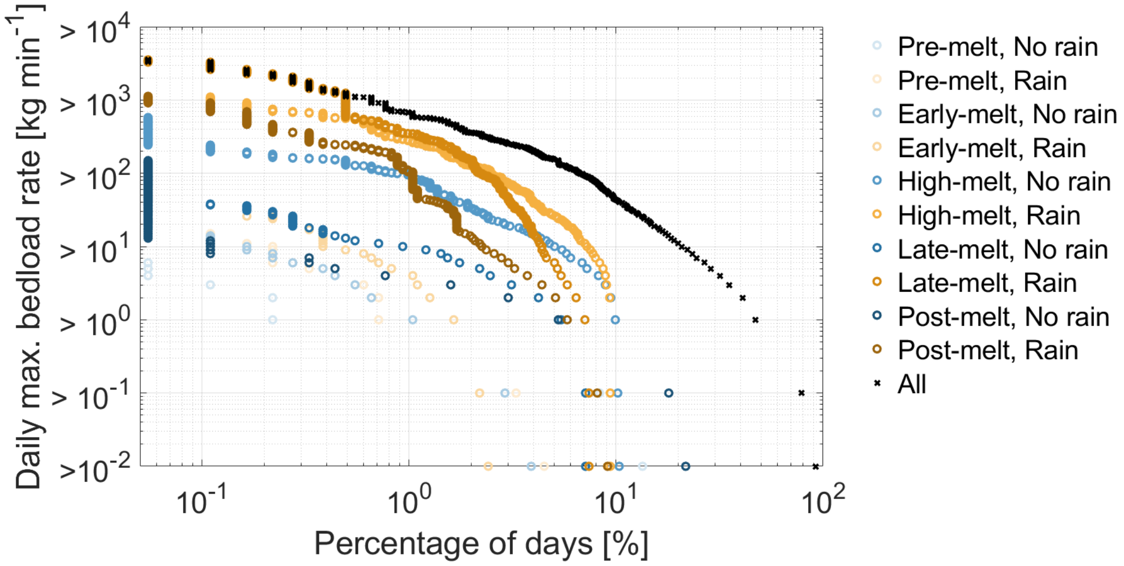

Figure III-9. Magnitude-frequency relationship of daily bedload transport at the VdN between the five identified periods with differing melt intensity and between "rain-forced" days and "not rain-forced" days for both (a) the daily bedload total mass transported and (b) the daily bedload maximum transport rate reached.

Regarding daily maximum transport rates (Figure III-9b), for low frequencies (< 0.6 % of days, 11 days), the highest bedload intensity (> $3 \cdot 10^3$ kg·min^{-1}) is associated with "rain-forced" days of the late-melt period, followed by "rain-forced" days of the high-melt period, "rain-forced" days of the post-melt period, "not rain-forced" days of the high-melt period and "not rain-forced" days of the late-melt period, followed by the other categories. At intermediate frequencies (0.6-2 % of days, 11-37 days), the highest bedload intensities are found in "rain-forced" days of the high-melt and late-melt periods, followed by "rain-forced" days of the post-melt period, and "not rain-forced" days of the high-melt period, followed by the other categories. At high frequencies (> 2%), the magnitude of the pair "Rain-forced – Late-melt" days decrease more rapidly than the pairs "Rain-forced – High-melt" and "Not Rain-forced – High-melt". The magnitude-frequency of daily bedload transport for each year separately integrated over the different hydrological categories developed in this paper is available in Supporting Information III-S8.

III-4 Discussion

III-4.1 Annual bedload masses and their variability

Average annual erosion rates estimated from bedload transport export at the VdN can be compared with other Alpine watersheds where bedload data have been reported. To make the inter-basin comparison appropriate, we only selected headwater watersheds that are between 5 and 85 km^2 in size, and with a glaciated area < 40%. These two variables, together with associated annual transport capacity, channel gradient and the geological setting, were shown to considerably affect annual bedload export (Lauffer and Sommer, 1982; Spreafico and Lehmann, 1994; Rickenmann, 1997; Turowski et al., 2010; Rickenmann, 2012; Hinderer et al., 2013; Rickenmann et al., 2020). Details of the watersheds presented in Figure III-10 are available in Supporting Information III-S9 (Table III-S.4), with the associated references.

With an average of 0.039 mm·y^{-1}, the VdN is a relatively active watershed in terms of bedload export as compared with other reported Alpine watersheds (Figure III-10), both glaciated and unglaciated. The VdN (3 % glaciated) has comparable erosion rates to some watersheds that are more glaciated, such as the Fischbach (16%), the Ruetz (20%), the Minstigerbach (20%) and the Lonza (37 %), but lower erosion rates than more active watersheds such as the Haut Glacier d'Arolla (27%) or the Val Roseg (30%) (Spreafico and Lehmann, 1994; Tockner et al., 2002; FOEN, 2010; Lane et al., 2017; Rickenmann, 2018). These comparisons are however complicated by the basin Sediment Delivery Ratio (SDR) which commonly decreases with increasing watershed area, reflecting that larger basins store more material than smaller ones (Hinderer et al., 2013), and that specific bedload transport capacities (per unit watershed area) decrease due to decreasing channel steepness (Rickenmann and Koschni, 2010).

When looking at the inter-annual variability in exported bedload over the five years investigated, the VdN has a factor of 10 difference between the least (2016) and the most (2019) active year (Figure III-5b). This is more than reported for the Fischbach and the Ruetz basins, where ~10 years of monitoring suggest a factor 4.5 and 5 between the least and the most active year, respectively (Rickenmann, 2018; Rickenmann et al., 2020). The factor is less than reported for the Rio Cordon, where annual loads between 0 and $1.5 \cdot 10^6$ kg have been observed over three-decades of survey (Rainato et al., 2017). Inter-annual differences may reflect mean annual temperatures, the annual quantity of precipitation (both snowfall and rainfall), and/or the time-integrated shear stress, although our results suggest no simple systematic relationships between bedload export and such variables, Of greater importance may be the intensity and timing of the hydrological events taking place (e.g. watershed snow content, timing and magnitude of the melt, timing and magnitude of rainfall, baseflow intensity; Figure III-5, III-6, III-8, III-9), and also changes in sediment availability.

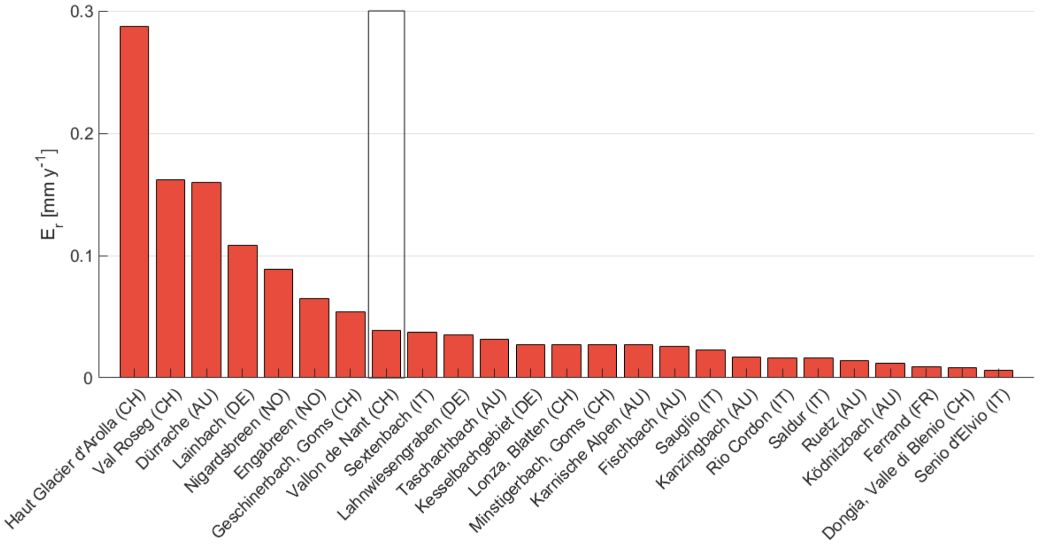

Figure III-10. Erosion rates calculated from exported bedload at multiple headwater Alpine watersheds with comparable area and glacier cover as the VdN. The VdN is highlighted with a black box.

III-4.2 Hydraulic forcing and bedload transport

The prediction of bedload transport using shear stress-based (i.e. transport capacity) equations has emphasized the importance of hydraulic forcing of bedload transport (Figure III-5a, 5b, 5d). The relationship between the measured and predicted daily bedload mass (Figure III-5d), is notably in general agreement with the 1:1 line, and with previous research, which used the same modified form of the Wilcock and Crowe (2003) equations to compare measured and predicted bedload mass (Schneider et al., 2015; Rickenmann et al., 2020; Rickenmann, 2020).

Although it is clear that the hydraulic forcing is of importance, the considerable overestimation of the predicted annual bedload as compared to the annual measured bedload (Figure III-5b), and the considerable scatter in the relationship between daily measured bedload mass and predicted daily bedload mass (Figure III-5d), illustrates the importance of other drivers of bedload transport rate. A poor representation of hydraulics near the bed in the driving equations of bedload, in particular around the threshold of motion, represents one set of uncertainties around shear stress-based estimates of bedload transport (Gomez, 1991; Buffington and Montgomery, 1997). In addition, temporal changes in sediment availability, both as a function of bed material mobility (i.e. bedload pulses; Elgueta-Astaburuaga et al., 2018), and as a function of sediment supply from the drainage network (i.e. “travelling bedload”; Piton and Recking, 2017), is another dimension of bedload transport that is poorly covered by capacity-based transport equations (Rickenmann, 2020). Because the VdN system is likely to oscillate between capacity-limited and supply-limited conditions, the same hydraulic forcing is not expected to systematically induce the same amount of bedload, and this discrepancy is notably visible in the general overestimation of bedload masses at the VdN when applying the transport capacity-based equations (equations [III-6 to III-10]; Figure III-5b).

Many studies have attempted to assess changes in streambed state and associated sediment mobility. Flood regime history in terms of magnitude-frequency was notably found to be an important factor regarding bed armoring cycles and associated sediment mobility (Mao, 2018; Masteller et al., 2019; Rickenmann, 2020). Also, the infiltration of fine material into the bed matrix was also hypothesized as an important control on bed sediment mobility (Venditti et al., 2010; An et al., 2019). Some research has also attempted to identify potential seasonal trends in sediment availability within Alpine watersheds. Mao et al. (2014) have for instance related the direction of hysteresis loops between streamflow and bedload transport rates to seasonal change in sediment supply from the drainage network. Yet, the balance between bed state and supply from the drainage network in terms of sediment production could not be partitioned. Therefore, the extent to which sediment availability changes through time, and how it affects the relationship between streamflow and bedload transport, remains poorly constrained (Elgueta-Astaburuaga and Hassan, 2019; Reid et al., 2019; Rickenmann, 2020). Sediment availability being a complex variable to quantify, a possible approach for future research could be based upon probabilistic estimate of bedload according to the hydrological conditions met in a given Alpine watershed. For instance, the results of this study have shown the higher probability of having large bedload transport events during rainy days occurring when the melt signal is strong and baseflow is high, which could reflect both hydraulic forcing and sediment availability conditions, as well as higher particle velocity and sediment connectivity throughout the watershed (Dell'Agnese et al., 2015). Future research should focus on obtaining distributed estimates of bedload flux to properly quantify change in sediment availability, and its effect on the streamflow-bedload relationship. This could be performed either through the deployment of a network of passive bedload sensors (Cook et al., 2018; Misset et al., 2021), or through repeated topographical surveys at high spatial and temporal resolutions (Antoniazza et al., 2019; Bakker et al., 2019; James et al., 2020; Dai et al., 2021).

III-4.3 Magnitude-frequency of daily bedload transport during rainfall and the melt season

The approach adopted in this paper allows, for the first time, the comparison of a relatively long-term continuous time-series of bedload export with the hydrological patterns of an Alpine watershed. The visual inspection of 1827 daily flow hydrographs, supported with temperature and precipitation datasets, permitted distinction of daily flow hydrographs influenced by rainfall from the ones that were not. The amplitude of daily flow hydrographs of “not rain-forced” days (Mutzner et al., 2015) was further used to identify five periods with differing melt intensity – the pre-melt, early-melt, high-melt, late-melt and post-melt periods – that were recurrently met throughout the five years of observation on the one hand, and which varied within a same range of discharge amplitude on the other hand (Figure III-4; Table III-1).

The results of this study show that the largest quantities of bedload export were associated with a combined occurrence of rainfall at times when baseflow is high and when the snowmelt signal is strong (Figure III-6, Figure III-8, Figure III-9). This concerns both the total amount of bedload transported, and the maximum bedload transport rate reached. At this period of the year, the lower and/or exposed parts of the watershed have already lost snow cover, reducing the storage capacity of the snowpack and exposing more sediment. At higher elevations and/or in sheltered areas of the watershed, large volumes of snow may still be available. Melt has commonly started and subsurface water storage is typically high in the lower parts of the watershed, which is visible in the high baseflow in these periods (Figure III-5a). When rain occurs in such conditions, the remaining snow cover may provide additional rapid melt but only little additional water storage capacity for incoming water inputs, and significant surface runoff is produced. As the subsurface may already be saturated due to melt and percolation through the snowpack and infiltration into the soil, little incoming water can be absorbed (Corripio and López-Moreno, 2017; Musselman et al., 2018; Li et al., 2019), and a rapid increase in the streamflow hydrograph is expected, favorable to sediment mobilization and bedload transport. In addition, the extension of the stream network (Michelon et al., 2021) may access new sedimentary sources. In comparison, incoming rain occurring earlier in the year (e.g. pre-melt and early-melt period; Figure III-6, Figure III-8, Figure III-9), when the snowpack is colder, more extensive and deeper, can be at least partly stored within the snowpack or in the underlying soil, thus producing a comparatively smaller streamflow response. Retraction of the stream network during this period (Michelon et al., 2021) also reduces the access to sedimentary sources. Under such conditions, little bedload is transported.

Rainfall occurring later in the year, once the watershed snow water equivalent has decreased and the melt signal is not as strong anymore (e.g. post-melt period), can also produce significant amounts of bedload, but to a lesser extent than rainfall occurring during the high-melt and late-melt periods (for both total bedload per day and daily maximum transport rate), notably because the baseflow is lower (Figure III-5a). Intense summer and autumn storms are expected to produce rapid streamflow response and increase bedload transport capacity (Rainato et al., 2017; Rickenmann, 2020). Those events can produce high transport capacity discharge and bedload transport events (both in terms of total bedload and daily maximum transport rate). However, their magnitude decreases much more rapidly with increasing frequency than for bedload transported during the high-melt and late-melt season (for both “rain-forced” and “not rain-forced” days; Figure III-6, Figure III-8, Figure III-9), again due to lower baseflow at this period of the year. This means that whilst rainfall events of the post-melt season matter for low-frequency high-magnitude events, their role in terms of annual total bedload transported seems less important. Whilst “rain-forced” days dominate the bedload signal at all magnitude-frequency combinations, snowmelt events alone is still capable of transporting a substantial amount of bedload during the high-melt and late-melt periods (Figure III-6, Figure III-8, Figure III-9), when the baseflow is higher.

The dataset to which the observation made in this paper can be best compared is the study of Rainato et al. (2017). The authors investigated the magnitude-frequency of bedload transport events over three decades at the Rio Cordon Alpine watershed (Italian Alps), which was shown to deliver comparable annual bedload yields to the VdN (Figure III-10). Over the 31 bedload transport events recorded during the period 1986-2014, a slight majority of them (17) occurred during the period when snow was still (or already) likely present within the watershed (e.g. May-June; November). Yet, a substantial proportion of bedload transport events (14) also took place when the likelihood of having considerable remaining snow had decreased (e.g. July-October). Therefore, the imbalance between bedload transport occurring during the melt season (including rainy days of the melt season), and bedload transport occurring during rainfall once the watershed snow content has significantly decreased, seems to be greater at the VdN as compared with the Rio Cordon. This may be due to particularly intense rainfall during the late summer and autumn at the Rio Cordon, combined with changes in the connectivity of sedimentary sources through the season (Rainato et al., 2017). However, with no complete hydrological study (e.g. melt signal, rainfall versus melt-driven bedload transport) of the events producing bedload at the Rio Cordon, a direct comparison with the categories developed in this paper remains difficult.

III-4.4 Bedload transport perspectives under climate change

The dataset presented in this paper shows the importance of the seasonal timing of hydrological drivers for triggering bedload transport, where the seasonal timing is a proxy for the extension of the stream network (Michelon et al., 2021), for the baseflow level and for the strength of the melt signal. These results are of importance in the perspective of understanding how bedload transport in Alpine watersheds may evolve with climate change, because the latter is likely to affect both the timing of occurrence and the magnitude of the bedload-driving hydrological events.

A summary of the meteorological, hydrological and bedload transport patterns highlighted over the five years of observation at the VdN, and projections on how these variables could evolve with climate change, is provided in Figure III-11. Current mean temperature, rainfall and snowfall have been estimated with the RhiresD and TabsD datasets over the period 2016-2020. Discharge and bedload data come from the VdN monitoring station. Rough projections of mean temperature, rainfall, snowfall and baseflow for the end of the 21th century (2085) for the Western Alps were performed using the datasets presented in CH2018 (2018) and FOEN (2021) for the RCP4.5 scenario (i.e. moderate warming). Under this scenario, mean temperatures are projected to rise for all seasons, especially in summer, while mean snowfall should decrease for all seasons, notably in spring and autumn. Mean rainfall is project to decrease in the summer, and rise in the other seasons, notably in winter (CH2018, 2018; FOEN, 2021; Figure III-11). The intensity of extreme precipitation events in all seasons is expected to follow the increase that is already observed. Increase in intensity is estimated to be about +20% in magnitude by the end of the century, for both hourly events and multi-day events (CH2018, 2018).

The impacts of these general climatic trends on high Alpine water resources have long been known (Horton et al., 2006). These impacts are largely related to the evolution of the seasonal snow line (i.e. the average elevation at which snow falls), which is expected to rise by between 300 m and 600 m by the end of the 21th century (CH2018, 2018). Indeed, the wintertime increase in precipitation is projected to not be able to compensate the large loss in snow volume caused by the increase in temperature, except at very high elevations (FOEN, 2021). Less precipitation will thus be stored as snow and the formation of a seasonal snow cover will occur later in the year, with a shift in maximum snow heights from March to February (CH2018, 2018). Snowmelt is projected to occur earlier in the year, leading to significant shifts of the seasonal streamflow regimes of high elevation watersheds (CH2018, 2018; FOEN, 2021). Groundwater recharge is also expected to evolve with climate change, with an increase of groundwater recharge in winter and spring, and a decrease in summer and autumn, which is of importance to determine change in baseflow (FOEN, 2021).

As a consequence of these changes, the hydrological regime of currently snow-dominated Alpine watersheds such as the VdN is expected to shift to a more rain-influenced streamflow regime by the end of the 21st century, with less snow accumulation, with gentler and earlier snowmelt, and with a monthly streamflow maximum occurring earlier in the year (FOEN, 2021). This will namely result in a marked increase of winter streamflow (+ 80-100%), a moderate increase in spring streamflow (+ 20-40%), a marked decrease in summer streamflow (-40 to -60%), and a moderate decrease in autumn streamflow (FOEN, 2021). Yet, mean annual streamflow is expected to remain generally stable, or to decrease slightly (FOEN, 2021). Regarding high streamflow events, no detailed climate-model based projections are currently available for Alpine water resources at catchment-scale because the CH2018 climate scenarios have not been yet downscaled for hydrological purposes to local Alpine conditions.

How could bedload transport evolve together with changes in the hydrological drivers within snowmelt-dominated Alpine watersheds? The increase in the magnitude and frequency of extreme precipitation events, and in the associated magnitude and frequency of high streamflows, has led some researchers to argue for a probable increase in the amount of bedload that will be transported under climate change conditions (CH2018, 2018; Speerli et al., 2020; FOEN, 2021). However, these predictions do not take into account possible change in the hydrological drivers responsible for bedload transport, and this statement can be challenged, to some extent, by the results presented in this study.

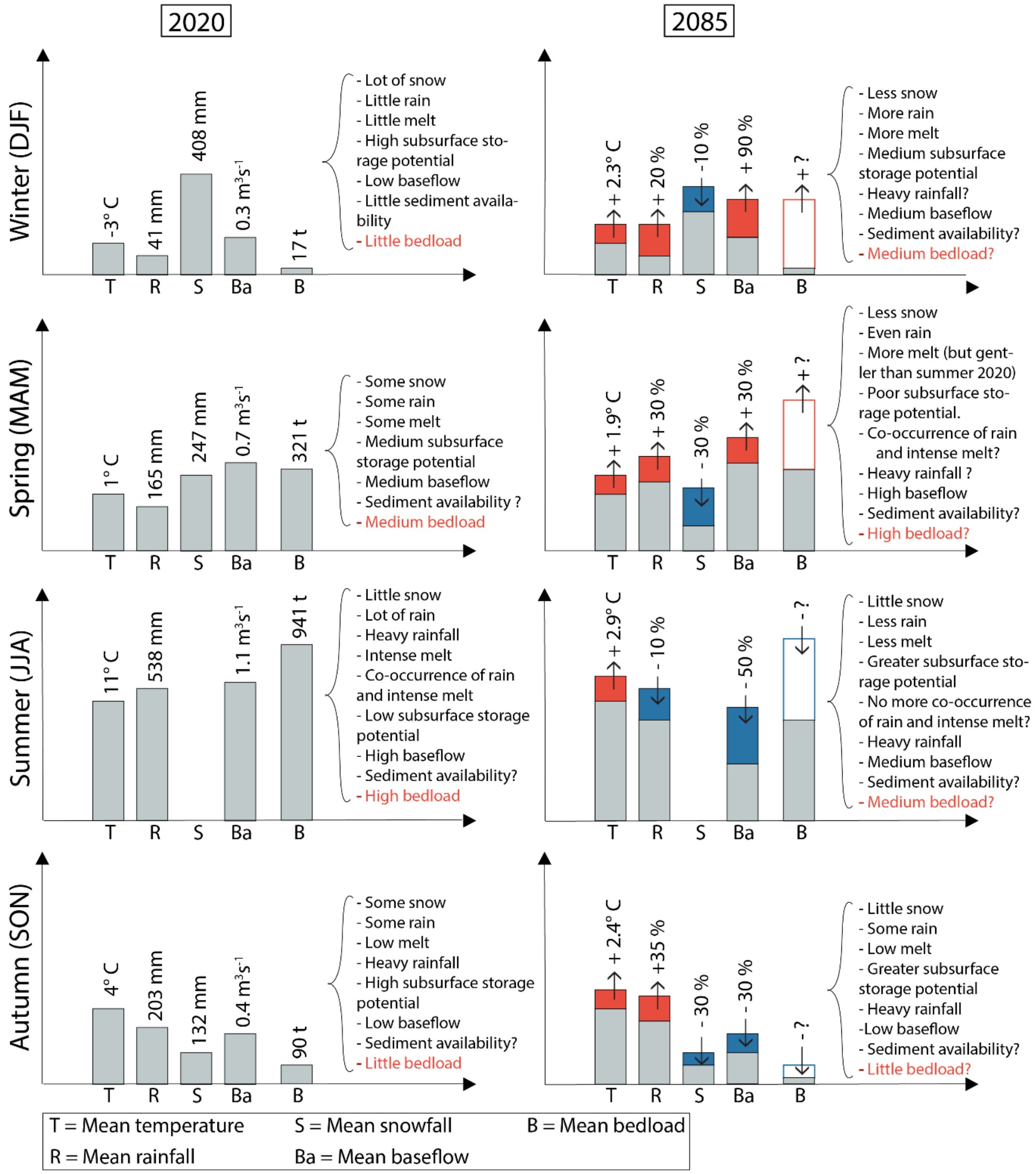

Figure III-11. Summary of the meteorological, hydrological and bedload transport patterns observed at the VdN (left panels) over the period 2016-2020. Projections on possible evolutions, and main uncertainties to solve regarding seasonal change in bedload transport with climate change (right panels).

From a hydrological regime shift perspective, the periods of high-melt and late-melt will occur earlier in the year, at lower baseflow (i.e. resulting from a reduced winter snowpack). This shift to earlier periods in the year might reduce the daily melt amplitude because the melt period is shifted to colder periods of the year (Musselman et al., 2017). Accordingly, the contribution of the melt-only events to bedload transport, especially important during the high-melt and late-melt periods, is likely to decrease together with annual snow volumes, due to the combined effect of lowered baseflow and lowered daily flow amplitudes. The results here show that while it may not affect significantly transport maxima, it may be of importance regarding annual bedload totals (Figure III-6, Figure III-8, Figure III-9).

Translating these changes into meteorological spring and summer periods, we can expect the amount of bedload transport throughout the spring to rise, while the amount of bedload transported throughout the summer can be expected to decrease. A central question that needs to be addressed is whether the importance of the combined occurrence of heavy rainfall over a watershed where the melt signal is strong and baseflow is high – as occurs currently especially during summer – will be maintained with climate change, or whether a disconnection between the high-melt and late-melt periods and the projected occurrence of heavy rainfall may take place under climate change conditions. If the latter situation occurs, a decrease in the bedload contribution of rain events during the high-melt and late-melt periods is possible in the future.

Another central question regards how the predicted increase in winter rainfall and winter streamflow will impact bedload transport. This general increase of liquid water availability in winter will most likely increase winter bedload transport, but the question of the magnitude of the increase is key. During winter rainfall events within watersheds that continue to show a significant seasonal snow cover, the incoming water may be stored to some extent, filtering out the streamflow and bedload response, as it is visible for current rainfall taking place during the pre-melt and early-melt periods. Thus, the response of any one watershed to winter warming and the occurrence of winter rainfall is likely to depend on its hypsometry (CH2018, 2018).

The last central question regards the increase in heavy rainfall throughout the year. Given that high-magnitude bedload transport events were shown to occur following heavy rainfall events, their timing of occurrence, notably with regards to the co-occurrence with high melt intensity or with high baseflow, may matter to determine the magnitude of the answer of streamflow and bedload transport. It is therefore of great importance to quantify the extent to which the increase in magnitude and frequency of rainfall will affect both maximum values of bedload transport rates and annual bedload export, and whether these events will have the capacity of compensating and/or overcoming reductions of bedload transport that may take place during other periods of the year.

Estimates of the evolution of bedload transport under climate change conditions need also to include expected changes in sediment availability within Alpine watersheds, because the latter matters to determine actual sediment export, whatever transport capacity the streams reach (Lane et al., 2017; Lane and Nienow, 2019; Figure III-10). Sediment availability is also expected to change together with climate change, but the sign of the trend remains uncertain. On the one hand, permafrost degradation is thought to increase sediment supply from rockwalls and rockslopes (Ravanel and Deline, 2011; Messenzehl et al., 2018), and glacier retreat increases the volume of unstabilized easily-remobilizable material (Ballantyne, 2002a; Carrivick and Heckmann, 2017; Lane et al., 2017; Mancini and Lane, 2020; Antoniazza and Lane, 2021). Also, the increase in magnitude and frequency of rainfall may increase the frequency of debris flows (Stoffel et al., 2014) and landslides (Huggel et al., 2012). On the other hand, the effects of climate change may also reduce sediment production, and associated processes (e.g. debris flow) by negative feedbacks such as due to the reduction in the frequency of frost-thaw cycles (Hirschberg et al., 2021). Similarly, the sustained paraglacial adjustment of Alpine watersheds following the Little Ice Age is thought to lead to the progressive stabilization of glacially-conditioned material (Ballantyne, 2002a; Porter et al., 2019; Antoniazza and Lane, 2021) and to a disruption of sediment connectivity within Alpine watersheds (Micheletti et al., 2015; Micheletti and Lane, 2016; Lane et al., 2017; Mancini and Lane, 2020), which may cause a progressive decrease in sediment transfer. In this context, a critical uncertainty remains to know whether sediment connectivity could also be sustainably enhanced by the increase in the magnitude and frequency of heavy rainfall and high flows (Cossart and Fort, 2008; Porter et al., 2019); or decreased due to feedbacks associated with landscape adjustment to climate change.

III-5 Conclusion

This paper presents a five-year time-series (2016-2020) of bedload transport monitored with the Swiss Plate Geophone (SPG) system at the VdN Alpine watershed, in the Western Swiss Alps. The analysis of five years of observation shows the importance of the co-occurrence of rainfall with a strong snowmelt signal and/or a high baseflow for producing frequently high-magnitude and intermediate-magnitude bedload transport. High-magnitude low-frequency bedload transport is also shown to occur when the melt signal is much weaker in the presence of rainfall, but the magnitude-frequency of daily bedload masses declines much quicker than when the melt signal is still strong due to lower baseflow. Although rainfall seems to represent the dominant driver of bedload transport (both during and after the snowmelt period), bedload transport can also be caused by the melt-only events. The latter contributes more by proportion to bedload totals, than to maximum transport rates. The analysis also shows the importance of sediment availability in influencing the relationship between streamflow and bedload transport, which requires more attention within future research.

There are concerns that bedload transport in Alpine watershed may increase associated with the magnitude and frequency of rainfall-induced high stream flows. However, the results of this study show that the timing and co-occurrence of hydrological drivers (i.e. rainfall, melt, baseflow) matters in determining the magnitude and frequency of bedload transport. As such, it is not clear yet how those elements and their temporal interplay will evolve under climate change conditions.

III-S Supporting Information

III-S1 Samples used for the SPG calibration

Table III-S.1. Sample number, sampling date, geophone number *G*, sampling duration [min], number of impulses (> 0.1 V) N_{imp} [-], M_{tot} sample mass (> 19 mm) [kg], impulse rate *IMPT* [m^{-1}] and unit bedload transport rate q_b [kg·min^{-1}·m^{-1}].

Sample	Date	G	Duration [min]	N_{imp} (> 0.1 V) [-]	Mtot (> 19 mm) [kg]	*IMPT* [m^{-1}]	q_b [kg·min^{-1}·m^{-1}]
1	21.05.2019	G7	5.00	49	4.865	19.60	1.95
2	21.05.2019	G8	5.00	534	25.972	197.17	9.59
3	21.05.2019	G8	1.50	87	26.293	116.00	35.06
4	21.05.2019	G7	1.00	102	6.573	204.00	13.15
5	21.05.2019	G7	2.00	83	4.693	83.00	4.69
6	21.05.2019	G7	3.00	159	10.835	106.00	7.22
7	21.05.2019	G8	2.00	125	8.463	125.00	8.46
8	21.05.2019	G8	2.00	127	11.397	127.00	11.40
9	21.05.2019	G8	1.00	58	4.236	116.00	8.47
10	21.05.2019	G8	2.00	100	7.476	100.00	7.48
11	21.05.2019	G6	4.00	99	4.462	49.50	2.23
12	21.05.2019	G5	6.00	93	2.821	31.00	0.94
13	21.05.2019	G7	4.00	46	1.321	23.00	0.66
14	21.05.2019	G8	10.00	152	14.288	30.40	2.86
15	21.05.2019	G8	10.00	73	5.461	14.60	1.09
16	21.05.2019	G8	3.00	802	49.898	534.67	33.27
17	21.05.2019	G7	2.00	410	25.932	410.00	25.93
18	21.05.2019	G6	3.00	81	2.516	54.00	1.68
19	21.05.2019	G8	3.00	216	11.186	144.00	7.46
20	22.05.2019	G7	5.00	37	1.372	14.80	0.55
21	22.05.2019	G8	5.00	65	6.194	26.00	2.48
22	22.05.2019	G8	5.00	70	3.462	28.00	1.38
23	22.05.2019	G5	10.00	7	0.207	1.40	0.04
24	22.05.2019	G8	1.50	132	19.03	176.00	25.37
25	22.05.2019	G8	1.50	96	5.300	128.00	7.07
26	22.05.2019	G6	5.00	38	1.505	15.20	0.60
27	22.05.2019	G7	5.00	80	3.729	32.00	1.49
28	22.05.2019	G8	2.00	64	2.978	64.00	2.98
29	22.05.2019	G5	10.00	13	0.671	2.60	0.13
30	22.05.2019	G8	2.00	10	2.289	10.00	2.29
31	22.05.2019	G7	5.00	49	0.879	19.60	0.35
32	22.05.2019	G8	5.00	85	3.403	34.00	1.36
33	10.06.2020	G6	4.50	337	32.984	149.78	14.66
34	10.06.2020	G6	5.00	258	9.886	103.20	3.95
35	10.06.2020	G8	4.50	211	10.125	93.78	4.50
36	10.06.2020	G6	3.50	305	24.396	174.29	13.94
37	10.06.2020	G6	4.00	603	33.549	301.50	16.77
38	10.06.2020	G6	2.50	511	32.984	408.80	26.39
39	10.06.2020	G6	2.50	489	42.553	391.20	34.04

40	10.06.2020	G6	2.50	374	32.075	299.20	25.66
41	10.06.2020	G6	2.70	561	36.874	415.56	27.31
42	10.06.2020	G6	3.00	358	24.519	238.67	16.35
43	10.06.2020	G8	2.80	741	47.304	529.29	33.79
44	10.06.2020	G8	2.50	113	14.500	90.40	11.60
45	10.06.2020	G6	2.00	360	18.922	360.00	18.92
46	10.06.2020	G6	2.20	527	32.232	479.09	29.30
47	10.06.2020	G6	1.00	327	31.281	654.00	62.56
48	10.06.2020	G6	1.00	261	17.726	522.00	35.45
49	11.06.2020	G6	2.80	448	35.344	320.00	25.25
50	11.06.2020	G6	3.00	269	17.301	179.33	11.53
51	11.06.2020	G6	2.50	280	22.412	224.00	17.93
52	11.06.2020	G6	2.00	35	2.564	35.00	2.56
53	11.06.2020	G6	2.20	243	14.276	220.91	12.98
54	11.06.2020	G6	0.40	207	16.544	1035.00	82.72
55	11.06.2020	G6	2.30	480	23.392	417.39	20.34

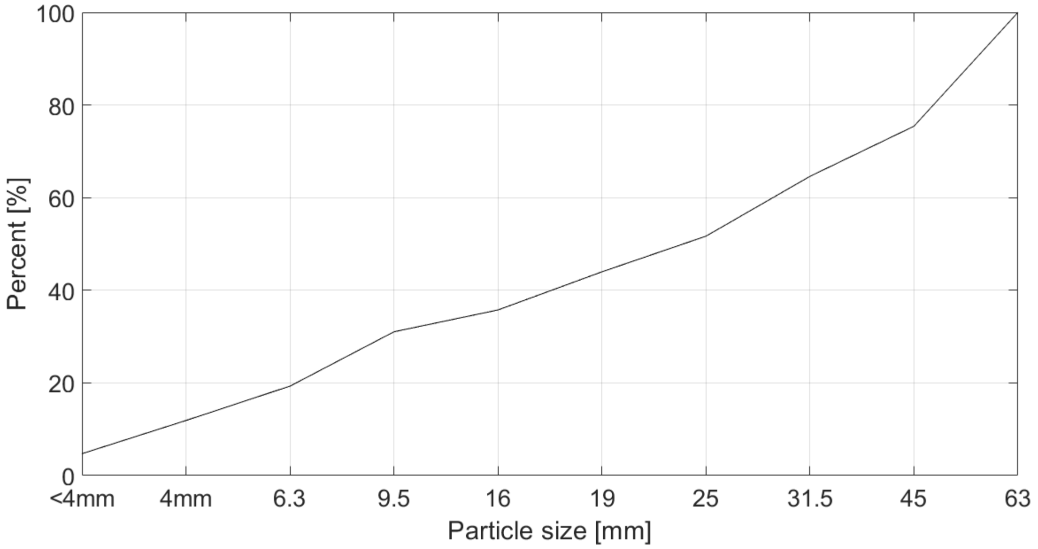

Figure III-S.1. Average grain-size distribution of the 55 bedload samples collected at the Vallon de Nant to calibrate the SPG system. Note that the x-axis is not linear.

III-S2 Procedure to estimate the representative grain-size classes D_{50} and D_{84}.

The ~20 m-long reach of the AdN and over which the transport-capacity calculations were performed is shown in an orthophoto in Figure III-S.1, with the SPG monitoring system to the right. Water flows from left to right.

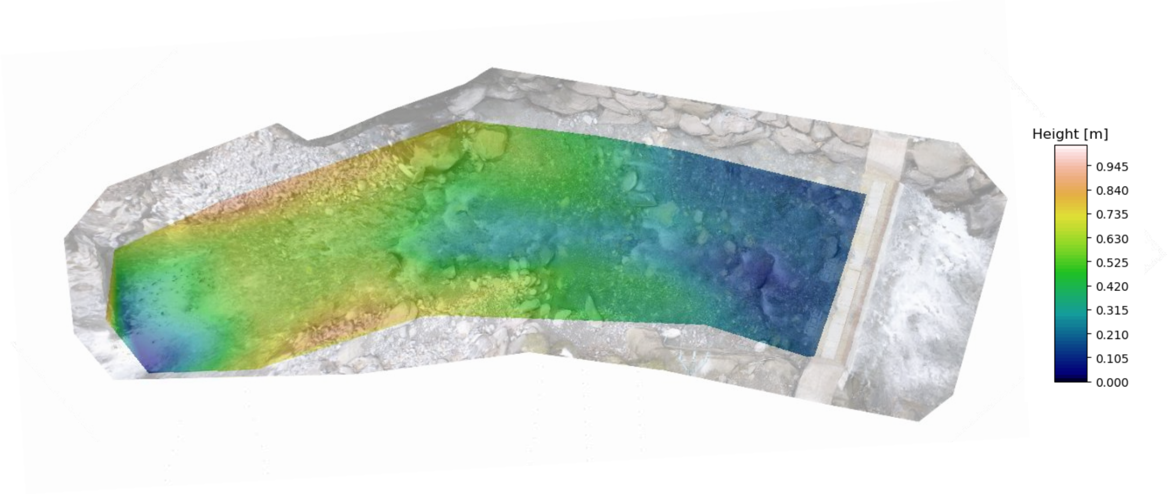

Figure III-S.2. Seven pixels per cm orthophoto of the ~20 m reach upstream of the SPG monitoring station, over which the transport capacity calculations were performed. The colors show the topographic height above the concrete sill of the monitoring station.

Lines were drawn through emerged areas of the streambed (e.g. bars; Figure III-S.3) in the ~20 m reach upstream of the SPG monitoring station (Figure III-S.2), and the representative surface grain-size classes D_{50} and D_{84} were measured manually from a line-by-number count.

Figure III-S.3. Lines through the emerged areas of the streambed, based on which the representative grain-size class D_{50} and D_{84} were determined.

III-S3 Meteorological datasets

Table III-S.2. Index of the eighteen cells of the RhiresD (daily precipitations) and TabsD (mean daily temperature) grids of MeteoSwiss that are covering partially or entirely the Vallon de Nant watershed. The coordinates are provided in the Swiss coordinate system CH1903.

N°	x-coordinate	y-coordinate
1	571500	117500
2	571500	116500
3	572500	116500
4	572500	117500
5	573500	117500
6	572500	118500
7	573500	118500
8	574500	118500
9	572500	119500
10	573500	119500
11	574500	119500
12	575500	119500
13	573500	120500
14	574500	120500
15	575500	120500
16	573500	121500
17	574500	121500
18	574500	122500

III-S4 Daily flow hydrograph classification

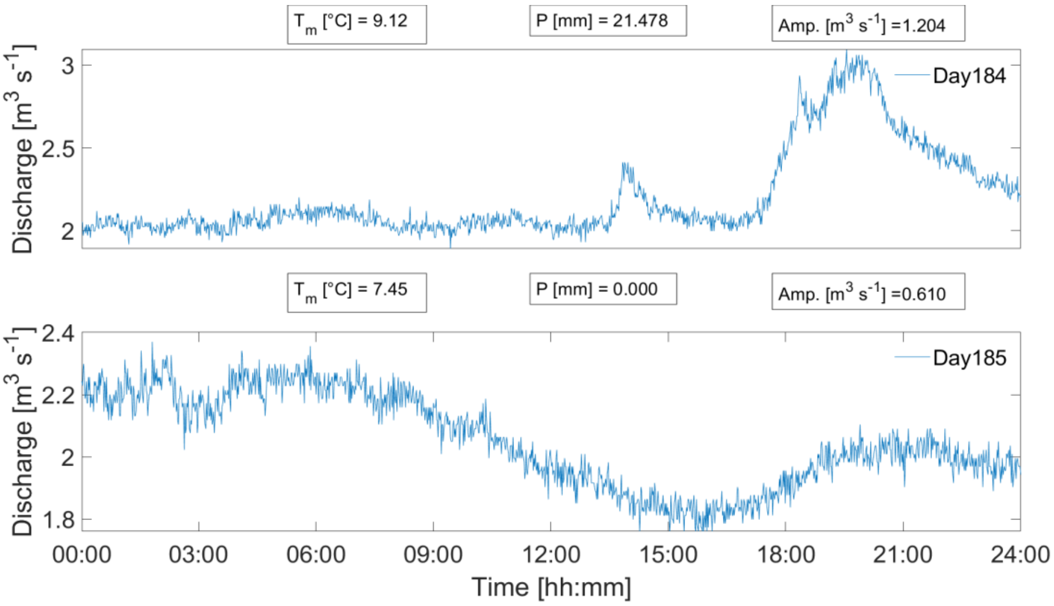

Figure III-S.4. Substantial precipitation occurs during day 184, with daily mean temperature above 0°C. A response is visible in the daily flow hydrograph (blue line), with a double-peak high flow with relatively steep increase, and gentler recession. During day 185, no precipitation occurs but the recession of the flood is still visible. Thus, both days were classified as “rain-forced” in this case.

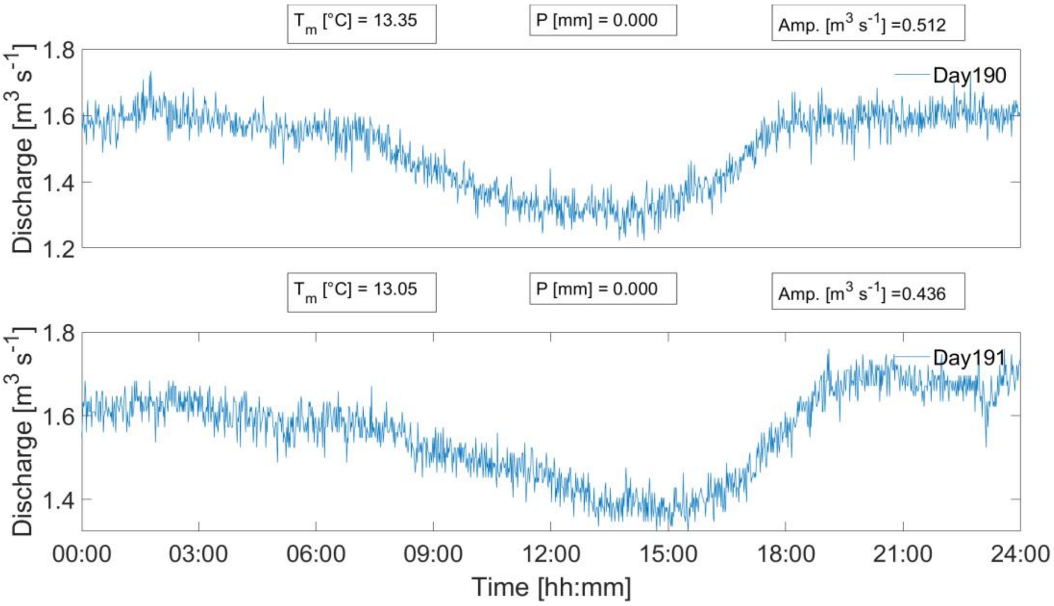

Figure III-S.5. Daily mean temperatures of days 190 and 191 are relatively high, and no precipitation occurs in either day. Both daily discharge amplitudes are nevertheless distinct, with a flow recession observable during the night, which spans until midday (e.g. vegetation evapotranspiration forcing; Mutzner et al., 2015), before the streamflow increases again during the late afternoon. Both daily signals are typical of a melt daily flow hydrograph, and were therefore classified as “not rain-forced”.

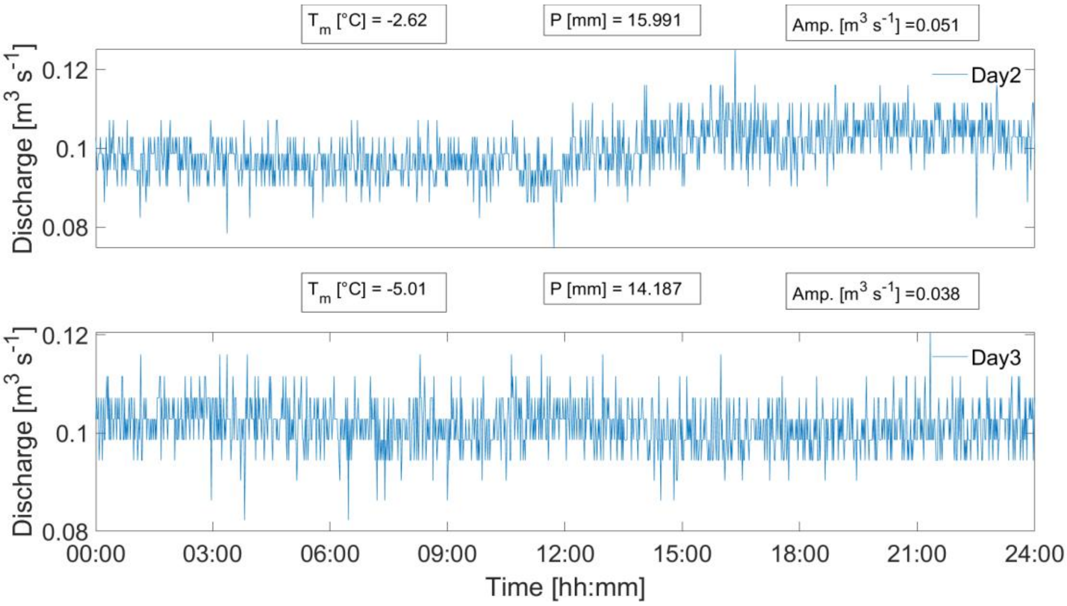

Figure III-S.6. Substantial precipitation occurs during both Day 2 and Day 3, while the daily mean temperature are well below 1°C. No clear response in flow hydrographs is visible and the daily discharge amplitude is very low. Therefore, the precipitation are thought not to force the daily flow hydrographs (i.e. likely snowfalls in this case) and both daily flow hydrographs were classified as “not rain-forced”.

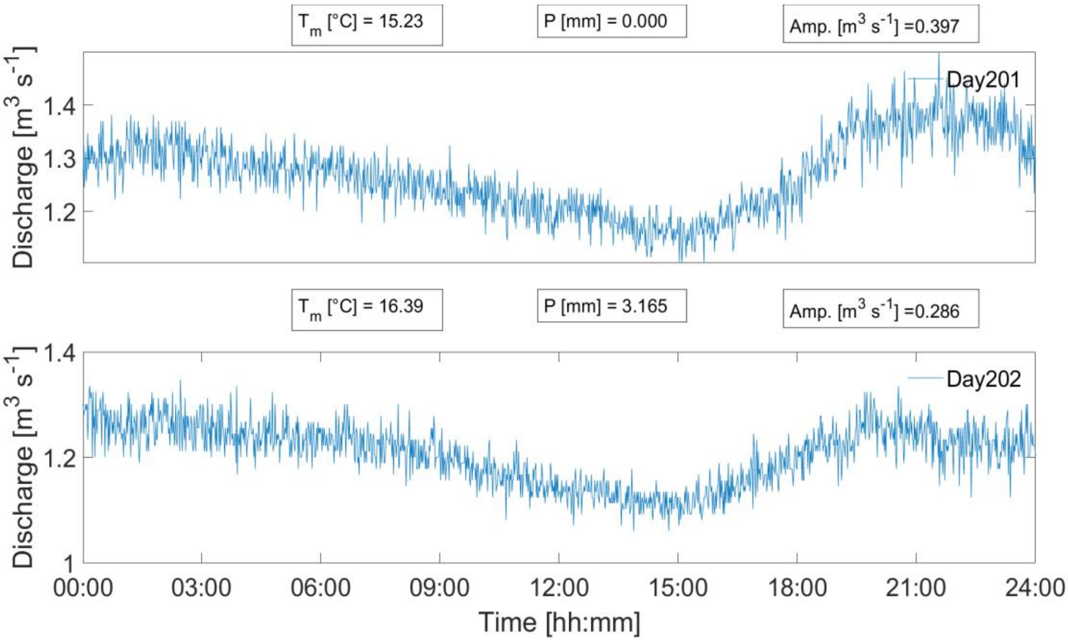

Figure III-S.7. Daily mean temperature is high on Day201 and no precipitation occurs. The flow hydrograph presents a typical melt signal. On Day202, daily mean temperatures is still high and precipitation does occur, but the flow hydrograph retains a typical shape of melt signal and seems not to be affected by the precipitation (as compared with Day201). Therefore, the precipitation on Day202 is considered to be too light to induce a flow hydrograph response and both days were classified as “not rain-forced”.

III-S5 Bedload transport and the melt season

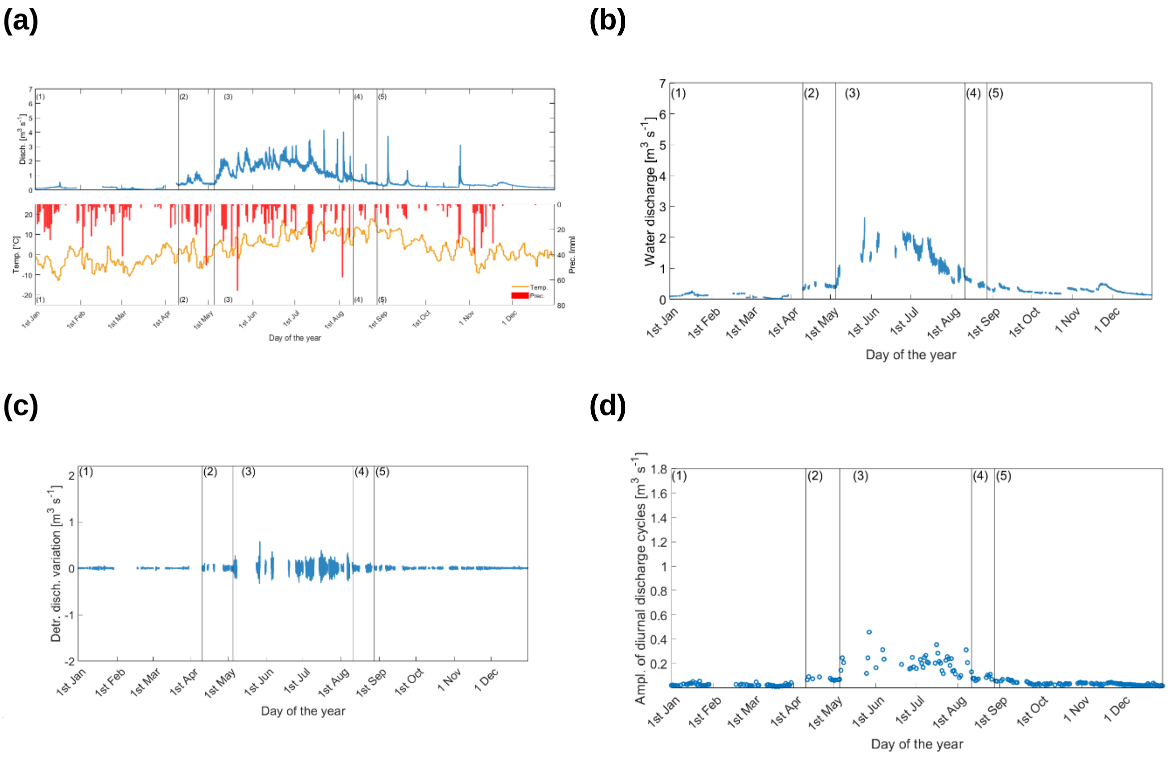

Figure III-S.8. (a) Discharge time-serie of the AdN for the year 2016 (top) with daily precipitation and daily mean temperature (bottom); (b) discharge time-serie with removal of data for days with rainfall; (c) detrended discharge variation and (d) amplitude of the diurnal discharge cycle.

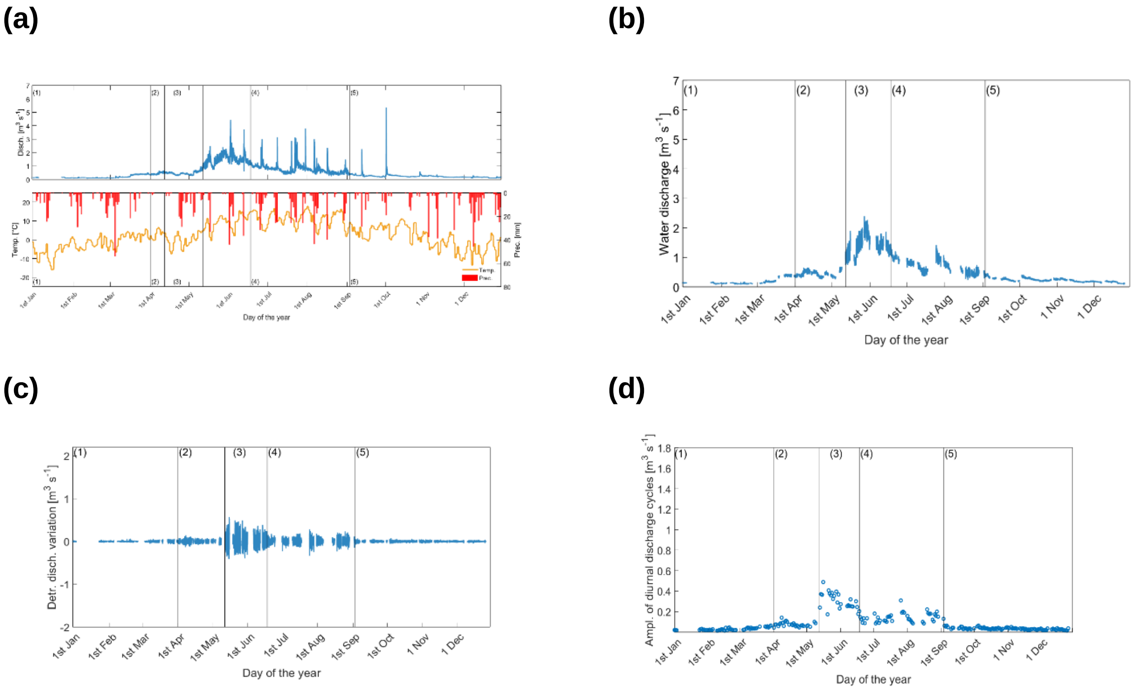

Figure III-S.9. (a) Discharge time-serie of the AdN for the year 2017 (top) with daily precipitation and daily mean temperature (bottom); (b) discharge time-serie with removal of data for days with rainfall; (c) detrended discharge variation and (d) amplitude of the diurnal discharge cycle.

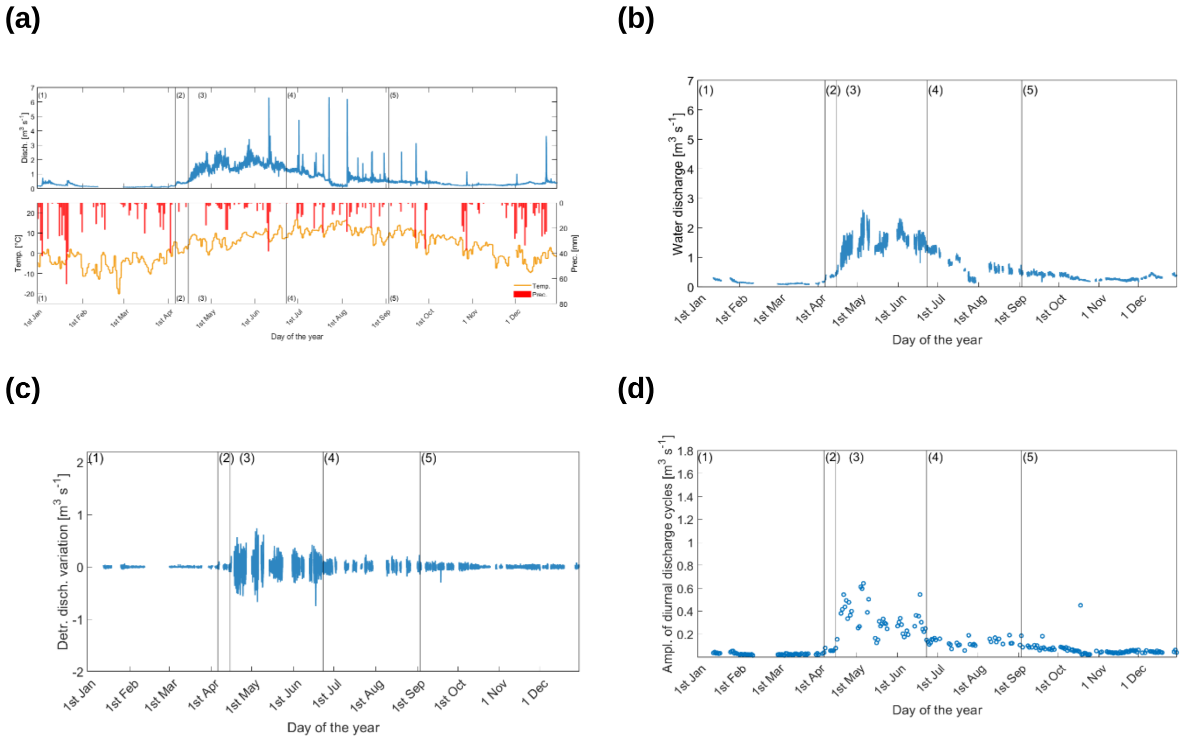

Figure III-S.10. (a) Discharge time-serie of the AdN for the year 2018 (top) with daily precipitation and daily mean temperature (bottom); (b) discharge time-serie with removal of data for days with rainfall; (c) detrended discharge variation and (d) amplitude of the diurnal discharge cycle.

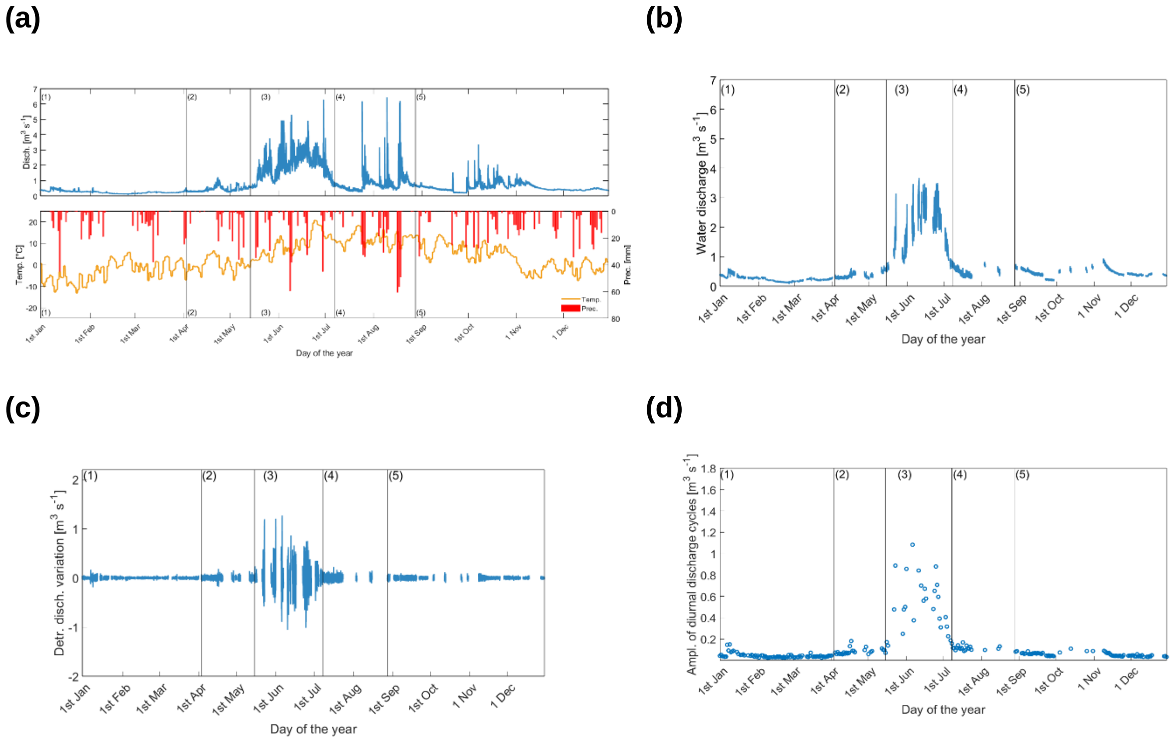

Figure III-S.11. (a) Discharge time-serie of the AdN for the year 2019 (top) with daily precipitation and daily mean temperature (bottom); (b) discharge time-serie with removal of data for days with rainfall; (c) detrended discharge variation and (d) amplitude of the diurnal discharge cycle.

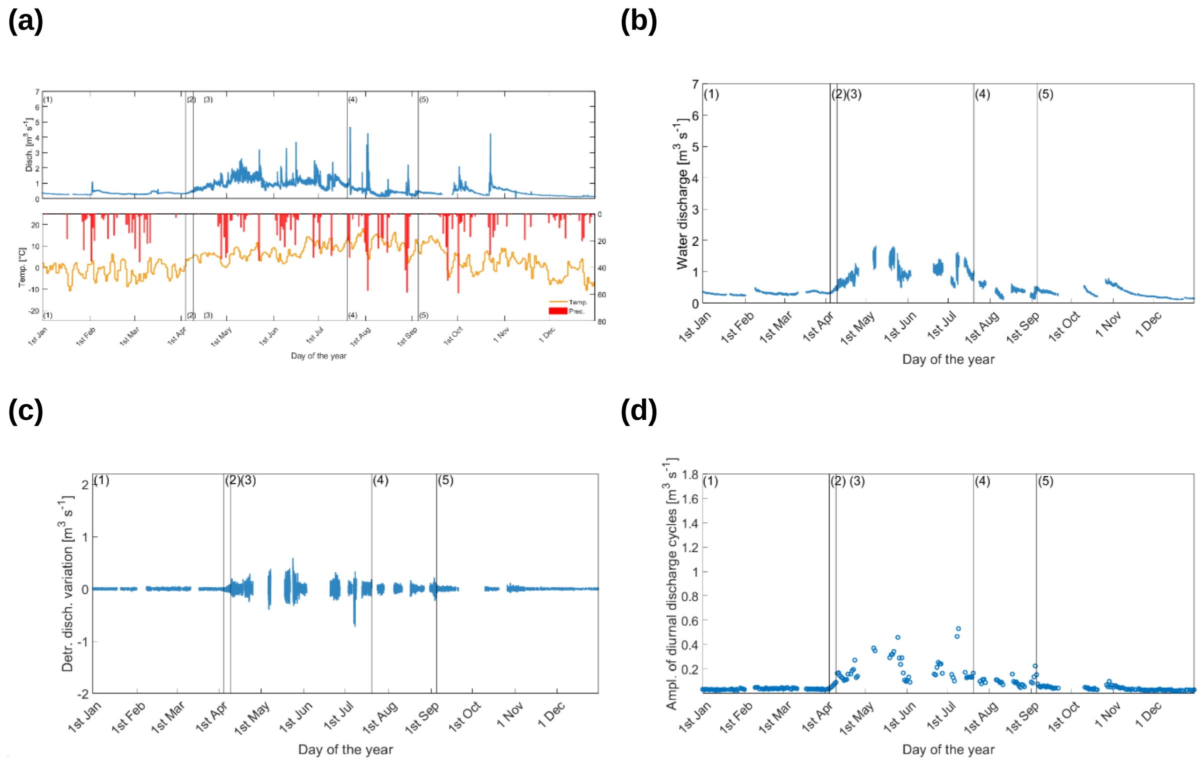

Figure III-S.12. (a) Discharge time-serie at the Vallon de Nant for the year 2020 (top) with daily precipitation and daily mean temperature (bottom); (b) discharge time-serie with removal of data for days with rainfall; (c) detrended discharge variation and (d) amplitude of the diurnal discharge cycle.

III-S6 Bedload transport masses

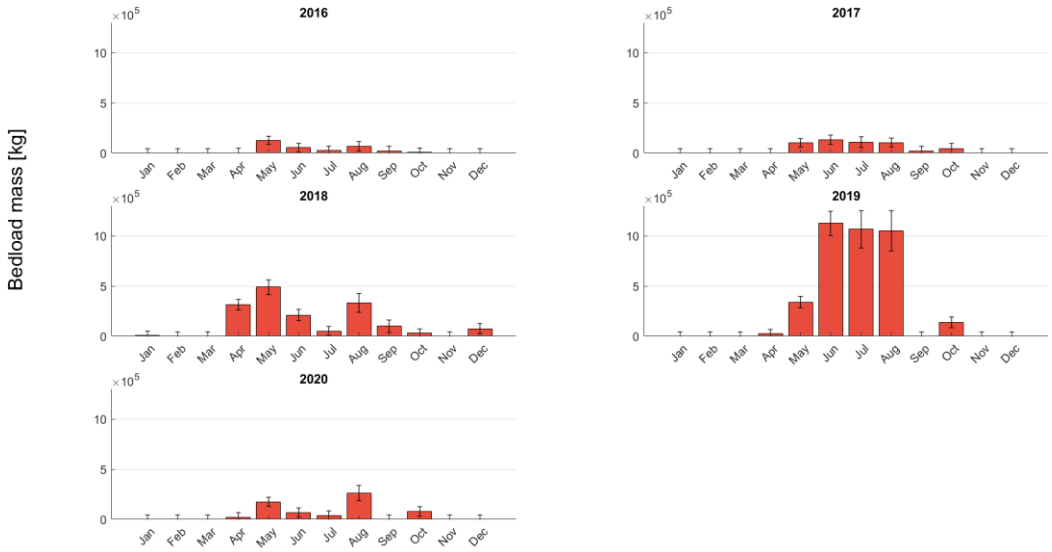

Figure III-S.13. Monthly bedload transport mass [kg] at the Vallon de Nant watershed over the five years of observation (2016-2020).

Table III-S.3. Annual and monthly bedload masses over the five years of observation (2016-2020).

Mass [·10^4 kg] **± uncertainty [10^4 kg]**	**2016**	**2017**	**2018**	**2019**	**2020**
January	0.0000 ± 0.044	0.0046 ± 0.044	0.074 ± 0.044	0.048 ± 0.044	0.0015 ± 0.044
February	0.0020 ± 0.043	0.0026 ± 0.042	0.0210 ± 0.042	0.0076 ± 0.042	0.0022 ± 0.043
March	0.0000 ± 0.044	0.0027 ± 0.044	0.0240 ± 0.044	0.0110 ± 0.044	0.1100 ± 0.044
April	0.4600 ± 0.043	0.1000 ± 0.043	31.4000 ± 0.051	2.6300 ± 0.043	2.3100 ± 0.043
May	12.5700 ± 0.042	10.4200 ± 0.043	48.8400 ± 0.074	34.0000 ± 0.056	17.5900 ± 0.045
June	5.3000 ± 0.042	13.4400 ± 0.047	21.0000 ± 0.056	112.5800 ± 0.12	7.0500 ± 0.044
July	2.4300 ± 0.044	10.9300 ± 0.051	5.1000 ± 0.045	106.7000 ± 0.19	3.7600 ± 0.046
August	6.8100 ± 0.045	10.5800 ± 0.045	33.4900 ± 0.095	105.1500 ± 0.2	26.2000 ± 0.075
September	2.1000 ± 0.044	2.1200 ± 0.044	10.1400 ± 0.061	0.0770 ± 0.043	0.1200 ± 0.043
October	0.6300 ± 0.044	4.2300 ± 0.053	2.9400 ± 0.045	13.8400 ± 0.054	8.1200 ± 0.047
November	0.0055 ± 0.043	0.0290 ± 0.043	0.3300 ± 0.043	0.2200 ± 0.043	0.0280 ± 0.043
December	0.0000 ± 0.044	0.0150 ± 0.044	7.5800 ± 0.051	0.0045 ± 0.044	0.0081 ± 0.044
Total	30.3000 ± 0.150	51.9000 ± 0.160	161.0000 ± 0.200	375.3000 ± 0.300	65.3000 ± 0.170

III-S7 Monte Carlo sensitivity analysis of the transport capacity calculations

The measurement in the field of parameters *b*, *S*, D_{50} and D_{84} used in the transport capacity calculation in equations [III-6 to III-10] contains uncertainties. As such, a Monte Carlo sensitivity analysis was run to evaluate how the variations in these parameters would affect the performance of the transport capacity calculations.

First, a range of plausible values for each parameter was defined, based on field measurements and their variability. Average width *b* (= 5.8 m) was set to vary between 4 and 10 m. Average slope *S* (= 0.04 m/m) was set to vary between 0.01 and 0.1 m/m. The median of the grain size distribution D_{50} (= 0.06 m) was set to vary between 0.02 and 0.15 m. The 84th percentile of the grain-size distribution D_{84} (= 0.36 m) was set to vary between 0.2 and 0.5 m. Second, 1000 simulations were run, combining random values of *b*, *S*, D_{50} and D_{84} within their own plausible range, to calculate the associated transport capacity using equations [III-6 to III-10]. Third, the performance of each simulation was assessed by calculating the regression between the daily predicted bedload mass (i.e. transport capacity-based) and the daily measured bedload (i.e. such as in Figure III-5d). The coefficient, the exponent and the R^2 of the regression were used to assess the performance of each simulation, knowing that best simulation should have a coefficient that tends towards 1, an exponent that tends towards 1 and a R^2 that tends towards 1.

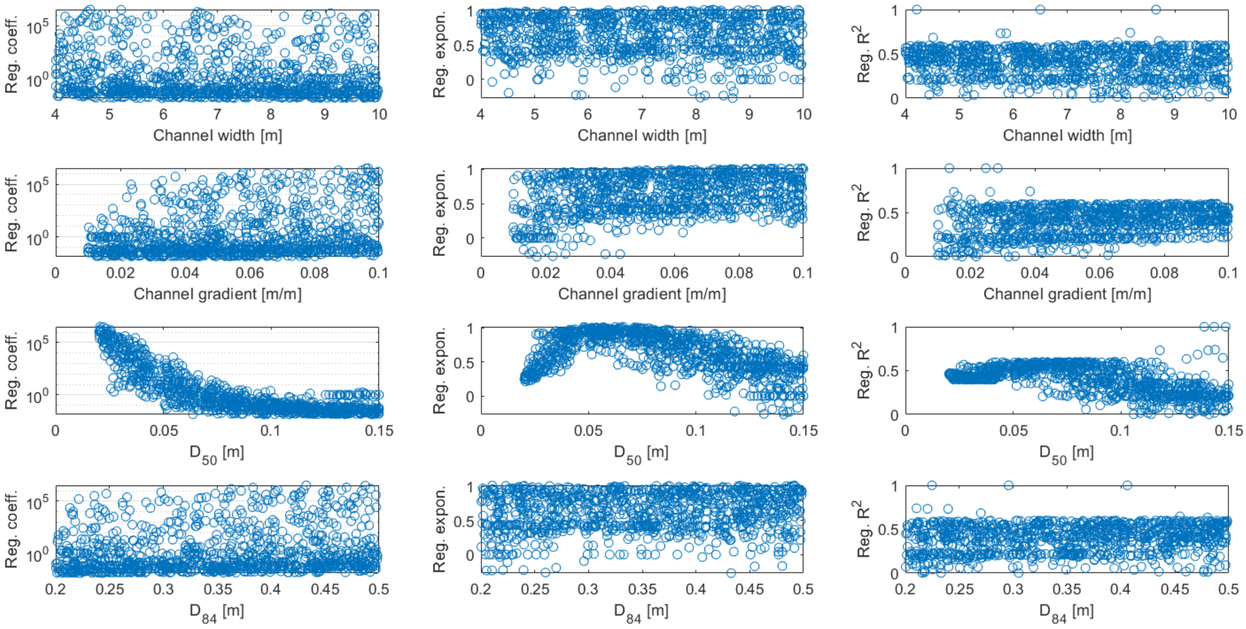

Figure III-S.14. Results of the Monte Carlo sensitivity analysis. The first, second and third column show respectively the scatter in the coefficient, the exponent and the R^2 of the regressions for each of the four parameters *b*, *S*, D_{50} and D_{84} (one for each line of plot).

Results in Figure III-S.14 show that the transport capacity calculations are relatively non-sensitive to the choice of parameters *b*, *S* and D_{84}, with a high density of simulations with a coefficient that tends towards 1, an exponent that tends towards 1 and the best R^2 around 0.6. This is close to the regression obtained in Figure III-5d in the main manuscript, with a coefficient of 1.7, an exponent of 0.95 and a R^2 of 0.57. The simulations are however more sensitive to the choice of parameter D_{50}, with too small values resulting in higher coefficients and smaller exponents, and too high values of D_{50} resulting in too small exponents and lower

R^2. Yet, the D_{50} value measured in the field (= 0.06 m) appears to optimize the coefficient, the exponent and the R^2. As such, the parameters b, S, D_{50} and D_{84} measured in the field and used in the transport capacity calculations appear sensible with regards to the sensitivity analysis.

III-S8 Magnitude-frequency relationship of daily bedload at the Vallon de Nant

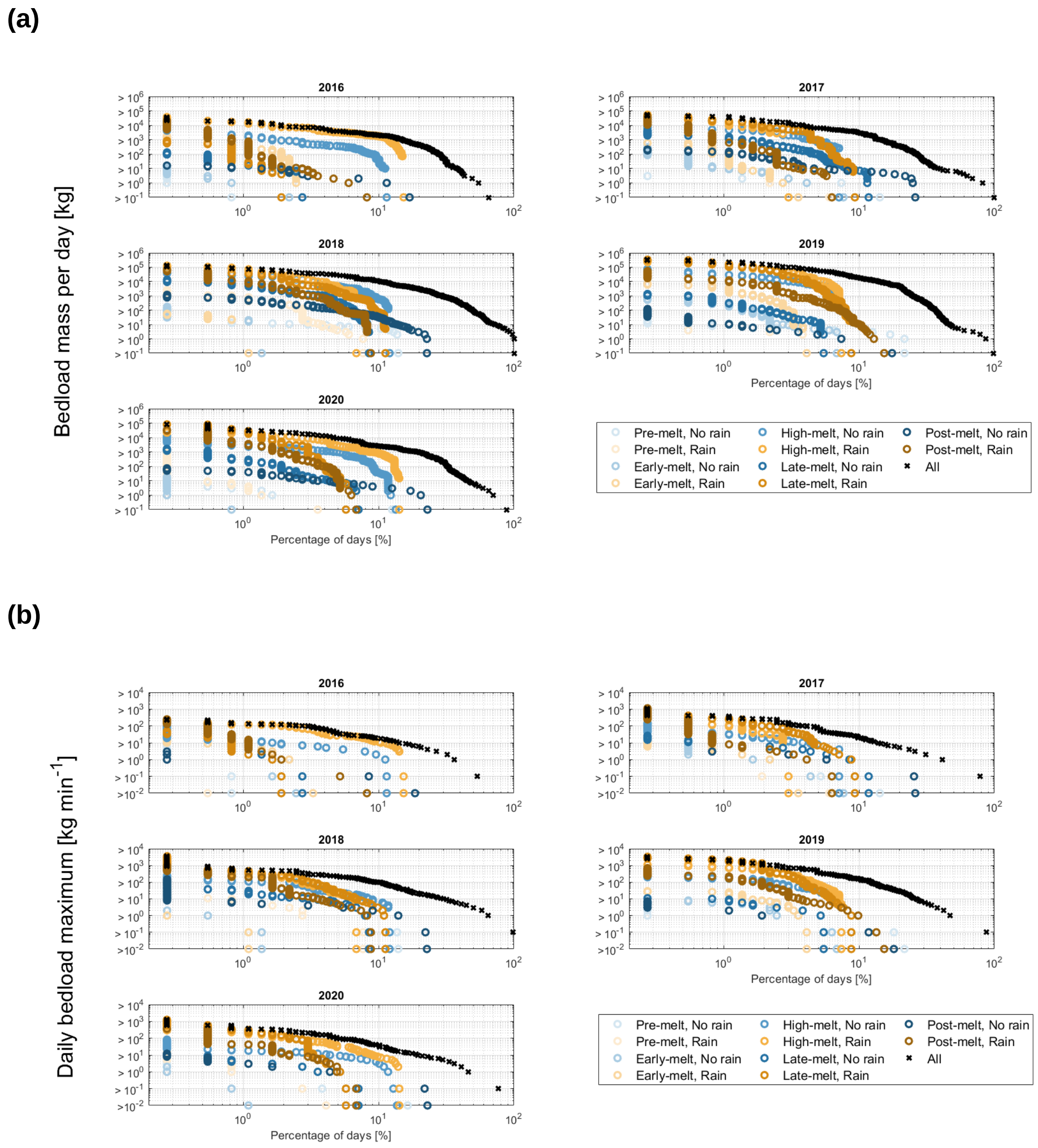

Figure III-S.15. Magnitude-frequency relationship of daily bedload transport at the Vallon de Nant watershed for each of the five years of observation (2016-2020) between the five periods of the melt season and between “rain-forced” and “not rain-forced” days for both (a) the daily bedload mass and (b) the daily bedload maximum transport rate.

The magnitude-frequency relationship of daily bedload at the Vallon de Nant is investigated for the five different years separately in Figure III-S.15, due to the various climatic conditions they each encounter (e.g. timing of the melt, snow heights in the watershed, timing and heights of rainfall). Regarding daily bedload mass (Figure III-S.15a), “rain-forced” days of the high-melt period seems to invariably lead to the greatest magnitudes. In most years (i.e. 2017, 2018, 2019, 2020), “rain-forced” days of the late-melt period is the second category producing the highest magnitude daily bedload mass. They tend to be followed by “rain-forced” days of the post-melt period and “not rain-forced” days of the high-melt period, at similar magnitude. Then comes “not rain-forced” days of the late-melt period, followed by the other categories left. This mostly confirms the observations made for all years combined in the main manuscript (Figure III-9).

At intermediate frequencies (0.6-10% of days) and magnitudes (10^1 – 10^3 kg), there is greater inter-year variability, and while days of the high-melt period (both “rain-forced” and “not rain-forced” tend to consistently play a substantial role (e.g. 2016, 2020), “rain-forced” days of the late-melt period may also be significant (e.g. 2017, 2019), so can be “rain-forced” days of the post-melt period, and “not-rain-forced” days of the late-melt period. Regarding daily bedload maximum transport rates (Figure III-S.15b), “rain-forced” days of the high-melt, late-melt and post-melt periods are systematically (i.e. throughout the five years) greater than “not rain-forced” days of the same periods for high-magnitude peaks (> 500 kg·min^{-1}), but “not rain-forced” days of the high-melt period also tend to produce high-magnitude peaks during a high number of days (e.g. 2016, 2019, 2020).

III-S9 Catchment erosion rates calculated from bedload transport export

Table III-S.4. Characteristics of a selection of Alpine headwater catchments where annual exported bedload masses are available. Catchments were selected for their similarity with the Vallon de Nant in terms of catchment area and glacier cover. The catchment area, the glacier cover, the main geological unit, the average annual bedload exported mass, the proportion of bedload with regards to suspended load, the annual erosion rate due to bedload, the total mechanical erosion rate (bedload + suspended load) and the associated references are notably reported.

River	Area [km2]	Glacier cover [%]	Geological unit	Annual bedload mass [tkm^{-2}a^{-1}]	Annual bedload mass [kg]	Prop. bedload [%]	Annual bedload ero. [mm a^{-1}]	Total mechanical ero. [mm a^{-1}]	Ref.
Vallon de Nant (CH)	13.4	3	Northern Helvetian Alps	-	1’368’500	-	0.039	-	This study
Haut Glacier d’Arolla (CH)	12.7	27	Westerne Crystalline Alps	-	9’672’500	-	0.287	-	Sharp et al. (1993), Lane et al. (2017)
Kesselbachgebiet (DE)	8	0	Northern Calcarous Alps	71	568’000	39	0.027	0.073	Becht et al. (1989)
Lahnwiesengraben (DE)	17	0	Northern Calcarous Alps	92	1’564’000	10	0.035	0.354	Schmidt and Morche (2006)
Lainbach (DE)	19	0	Northern Calcarous Alps	285	5’415’000	35	0.108	0.327	Schmidt and Morche (2006)
Dürrache (AU)	55	0	Northern Calcarous Alps	425	23’375’000	63	0.16	0.254	Lauffer and Sommer (1982)
Geschinerbach, Goms (CH)	6	0	Westerne Crystalline Alps	142	8’52’000	41	0.054	0.14	Spreafico and Lehmann (1994)
Lonza, Blatten (CH)	78	37	Westerne Crystalline Alps	72	5’616’000	22	0.027	0.13	FOEN (2010)
Minstigerbach, Goms (CH)	15	20	Westerne Crystalline Alps	72	1’080’000	36	0.027	0.08	Spreafico and Lehmann (1994)

Dongia, Valle di Blenio (CH)	7	0	Southern Crystalline Alps	20	140’000	39	0.008	0.02	Spreafico and Lehmann (1994)
Karnische Alpen (AU)	24	0	Eastern Crystalline Alps	72	1’728’000	34	0.027	0.085	Vorndran (1985)
Val Roseg (CH)	67	30	Eastern Crystalline Alps	428	28’676’000	7	0.162	0.184	Tockner et al. (2002)
Ruetz (AU)	28	20	Eastern Crystalline Alps	-	1’010’000	10	0.014	0.12	Rickenmann (2018, 2020)
Fischbach (AU)	71	16	Eastern Crystalline Alps	-	4’863’000	10	0.026	0.23	Rickenmann (2018, 2020)
Kanzingbach (AU)	22	0	Eastern Crystalline Alps	46	1’012’000	53	0.017	0.033	Lauffer and Sommer (1982)
Taschachbach (AU)	60.6	0.3	Eastern Crystalline Alps	83	5’029’800	23	0.0313	0.1377	Lauffer and Sommer (1982)
Ködnitzbach (AU)	28.4	0	Eastern Crystalline Alps	32	908’800	18	0.012	0.068	Lauffer and Sommer (1982)
Rio Cordon (IT)	5	0	Southern Calcarous Alps	35	209’000	21	0.016	0.039	Rainato et al. (2017)
Sauglio (IT)	7	0	Southern Calcarous Alps	62	434’000	40	0.023	0.063	Tropeano (1991)
Sextenbach (IT)	46	0	Southern Calcarous Alps	99	4’554’000	31	0.037	0.129	Vorndran (1985)
Senio d'Elvio (IT)	10	0	Southwest Sedimentary Alps	16	160’000	38	0.006	0.366	Tropeano (1991)
Saldur (IT)	61.7	4	Southwest Sedimentary Alps	.	2'650’000	-	0.016	-	Comiti et al. (2019)
Ferrand (FR)	82	1	Southwest Sedimentary Alps	25	2’050’000	9	0.009	0.137	Mano et al. (2009)
Engabreen Glacier (NO)	50	1	Norvegian Crystalline Alps	173	8’650’000	39	0.065	0.166	Gurnell (1987)
Nigardsbreen Glacier (NO)	65	1	Norvegian Crystalline Alps	236	1’5340’000	57	0.089	0.157	Gurnell (1987)

IV – Anatomy of an Alpine bedload transport event: a watershed-scale seismic-network perspective

Personal contribution to the research article

I conceptualized the study with the help of Stuart Lane (SL) and Michael Dietze (MD), following an initial promising test data collection conducted in 2018 in the Vallon de Nant. I wrote the funding application to the associated SNSF Doc.Mobility project, with the support of SL, MD and Dieter Rickenmann (DR), which was successful. I wrote two other successful applications in the frame of this project with the support of SL and MD, to the Investment Fund of the Faculty of Geosciences and Environment (FINV-FGSE) on the one hand, and to the Geophysical Instrument Pool Potsdam (GIPP) of the GFZ on the other hand, to obtain the needed equipment. Under the supervision of SL and MD, I deployed a network of 31 seismic sensors across the Vallon de Nant Alpine watershed during the entire melt season of 2020 (April to October). In the summer of 2020, I collected the field data (river morphology, grain-size distribution, active seismic experiments) needed to invert time-series for every seismic sensor. From October 2020, and for a period of 6 months, I went to the GFZ-Potsdam and undertook the processing of the seismic data under the supervision of MD and Jens Turowski (JT), which I later pursued at UNIL with the help of Davide Mancini (DM) and SL. We later focused on one high-magnitude bedload transport event that took place on August 3rd 2020. I analyzed coarse material mobilization, transfer and storage throughout the Vallon de Nant Alpine watershed using the seismic network data and a morphological change analysis, under the supervision of SL. I wrote the initial draft of the manuscript, which was later revised multiple times by all co-authors, until we submitted it to the *Journal of Geophysical Research: Earth Surface*, where it is currently under review.

Anatomy of an Alpine bedload transport event: a watershed-scale seismic-network perspective

Gilles Antoniazza[1,2], Michael Dietze[3,4], Davide Mancini[1], Jens M. Turowski[3], Dieter Rickenmann[2], Tobias Nicollier[2], Stefan Boss[2] and Stuart N. Lane[1]

[1]University of Lausanne, Institute of Earth Surface Dynamics (IDYST), Lausanne, Switzerland.
[2]Swiss Federal Research Institute WSL, Mountain Hydrology and Mass Movements, Birmensdorf, Switzerland.
[3]German Research Center for Geosciences (GFZ), Section 4.6 Geomorphology, Potsdam, Germany.
[4]Georg-August University Göttingen, Faculty of Geosciences and Geography, Göttingen, Germany.

Reference: Antoniazza, G., Dietze, M., Mancini, D. Turowski, J. M., Rickenmann, D., Nicollier, T., Boss, S. & Lane, S. N. (under review). Anatomy of an Alpine bedload transport event: a watershed-scale seismic network perspective. *Submitted to Journal of Geophysical Research: Earth Surface.*

Abstract: The way Alpine rivers mobilize, convey and store coarse material during high-magnitude events is poorly understood, notably because it is difficult to obtain measurements of bedload transport at the watershed scale. Seismic sensor data, evaluated with appropriate seismic physical models, can provide that missing link by yielding absolute time-series of bedload transport. Low cost and ease of installation allows for networks of sensors to be deployed, providing continuous, watershed-scale insights into bedload transport dynamics. Here, we deploy a network of 24 seismic sensors to capture the motion of coarse material in a 13.4 km^2 Alpine watershed during a high-magnitude bedload transport event. First, we benchmark the seismic inversion routine with an independent time-series obtained with a calibrated acoustic system. Then, we apply the procedure to the other seismic sensors across the watershed. Spatially-distributed time-series of bedload transport reveal a relative inefficiency of Alpine watersheds in evacuating coarse material, even during a relatively infrequent high-magnitude bedload transport event. Significant inputs measured for some tributaries were rapidly attenuated as the main river crossed less hydraulically-efficient reaches, and only a comparatively negligible proportion of the total amount of material mobilized in the watershed was exported at the outlet. Cross-correlation analysis of the time-series suggests that a faster moving water wave (re-)mobilizes local material and bedload is expected to move slower, and over shorter distances. Multiple periods of competent flows are likely to be necessary to evacuate the coarse material produced throughout the watershed during individual source-mobilizing bedload transport events.

Key points:

- For the first time, a high-magnitude bedload transport event is captured at the watershed scale by a network of 24 seismic sensors.
- A comparatively low proportion of the material mobilized in the watershed during the event is exported at the outlet (2.5 %).
- Multiple periods of competent flows are necessary to evacuate coarse material produced during individual source-mobilizing events.

Key-words: Bedload transport, environmental seismology, Swiss Plate Geophone system (SPG), coarse material flux, Alpine watershed.

IV-1 Introduction

Bedload transport is an important component of watershed management within Alpine areas, through its conditioning of river morphology, the benefit it delivers to riverine ecosystems, and its important contribution to sediment budgets of lowland fluvial systems (Wohl, 2006, 2013; Badoux et al., 2014a, 2016). Yet, the way Alpine watersheds produce, convey and store coarse material is still poorly understood (Cavalli et al., 2013; Dell'Agnese et al., 2015; Lane et al., 2017; Comiti et al., 2019). This represents a major limit to the usefulness of current bedload transport equations, since knowledge of change in sediment availability through time and space is needed for improving bedload transport predictions of Alpine rivers (Piton and Recking, 2017; Gomez and Soar, 2022).

The morphology of Alpine rivers largely derives from their glacier legacy, with a typical long-profile comprising a succession of steep rockwalls and hillslopes, flatter and wider glacier troughs, and steeper glacier riegls (Hooke, 1991; Cook and Swift, 2012; Egholm et al., 2012; Antoniazza and Lane, 2021). Alpine rivers tend to develop different morphologies along sections that present contrasting topographic and hydraulic properties. In the flatter sections, usually covered by Quaternary material, the river is typically alluvial with plane-bed or braided morphologies (Piton and Recking, 2017; Mao et al., 2017; Lane et al., 2017; Comiti et al., 2019). In the steeper and sometimes more confined sections, semi-alluvial reaches tend to develop cascades or step-pool morphologies (Recking et al., 2012; Turowski, 2012; Yager et al., 2012a). The streambed is made of a mixture of alluvial deposits and immobile or poorly-mobile larger particles issuing from hillslope processes (e.g. landslides, debris flow), from deglaciation deposits, or from bedrock outcrops. Along these reaches, the streambed is typically armored, resulting in limited sediment availability (Turowski et al., 2009; Recking et al., 2012; Yager et al., 2012a; Piton and Recking, 2017). Alpine rivers are also often colluvial in their headwater reaches, which means that there may be intermittent material supply from tributaries (Piton and Recking, 2017; Rainato et al., 2017).

The efficiency with which bedload is mobilized, transported and deposited may vary between these different morphological sections (Dell'Agnese et al., 2015; Lane et al., 2017; Comiti et al., 2019). Alluvial reaches may alternatively act as sediment sources or sinks, but may not always be hydraulically efficient in conveying coarse material (Dell'Agnese et al., 2015; Lane et al., 2017; Mao et al., 2017). Semi-alluvial reaches are steeper, but also rougher, and evidence suggests that bedload may 'travel' without major reworking of the underlying streambed along those sections (Mueller and Pitlick, 2005; Recking et al., 2012; Piton and Recking, 2017). In colluvial systems, tributaries may supply material into the main channel, as long as their (diffusive) alluvial fans are not disconnecting the main river from the steep gullies draining the hillslopes (Lane et al., 2017; Rainato et al., 2017; Mancini and Lane, 2020). In this context, multiple studies have advocated a relative inefficiency of Alpine watersheds in conveying coarse material (Cavalli et al., 2013; Dell'Agnese et al., 2015; Lane et al., 2017). Despite questioning of the ability of high-magnitude flow events to increase hillslope coupling and to permit the efficient transfer of large amount of bedload through various morphological reaches of Alpine watersheds (Cavalli et al., 2013; Dell'Agnese et al., 2015; Lane et al., 2017; Rainato et al., 2017, 2018), this premise has been rarely tested with field data.

A primary reason for the lacking empirical support of limited export efficiency is the difficulty of monitoring bulk bedload transport throughout Alpine watersheds. Particle tracking experiments have provided insights into the motion of individual particles across different morphological sections of Alpine watersheds (Schneider et al., 2014; Dell'Agnese et al., 2015; Mao et al., 2017; Rainato et al., 2018), but the extrapolation of individual particle motion to total bedload transfer is subject to uncertainty. Repeated topographic surveys have also yielded information on coarse material dynamics (Lane et al., 2017; Antoniazza et al., 2019; Bakker et al., 2019; Comiti et al., 2019), but such techniques provide only coarse temporal resolution, and cannot resolve processes during transport events. Recent advances in indirect acoustic sensing have allowed substantial advances in the continuous monitoring of bedload transport in natural settings (Downing, 2010; Mizuyama et al., 2010a; Rickenmann et al., 2012, 2014b; Kreisler et al., 2017; Rickenmann, 2018, 2020; Antoniazza et al., 2022). Yet, the deployment of acoustic sensors typically requires stable cross-sections (e.g. weirs) to be mounted efficiently, which represents substantial installation costs and ecological impacts (Rickenmann, 2017), and limits the monitoring of bedload transport at multiple locations across Alpine watersheds.

Environmental seismology (Cook and Dietze, 2022) provides an alternative. Out-of-bank seismometers have been shown to record the energy emitted by bedload transport in a specific frequency band (Burtin et al., 2011; Tsai et al., 2012; Roth et al., 2016; Bakker et al., 2020). As this frequency is normally different to that associated with other fluvial processes, such as turbulence, absolute time-series of bedload transport may be inferred (Gimbert et al., 2019; Bakker et al., 2020; Lagarde et al., 2021) through the inversion of appropriate physical models (Tsai et al., 2012; Gimbert et al., 2014). Passive seismic sensors are comparatively cheap, easy to deploy in a non-invasive way and require little maintenance such that they can be distributed as networks to investigate bedload transport at multiple locations at the watershed scale (Cook et al., 2018; Coviello et al., 2019; Chmiel et al., 2022). Networks of seismic sensors have been deployed to investigate the dynamics of floods (Schmandt et al., 2017; Chmiel et al., 2022; Piantini et al., 2022), debris flows (Walter et al., 2017; Coviello et al., 2019; Chmiel et al., 2021) and glacier lake outburst floods (Cook et al., 2018; Maurer et al., 2020). To date, no study has sought to determine spatially-distributed absolute time-series of bedload transport in order to evaluate the efficiency of Alpine watersheds in conveying coarse material during a high-magnitude bedload transport event.

In this contribution, we investigate coarse material flux during a high-magnitude bedload transport event throughout an Alpine watershed. To do so, we deployed a network of 24 seismic sensors across the 13.4 km^2 Vallon de Nant watershed in the Swiss Alps, which alternates between alluvial, semi-alluvial and colluvial reaches. In a first step, we compare the absolute time-series of bedload transport obtained from a calibrated acoustic bedload monitoring device with an independent time-series of bedload transport inverted from a seismic sensor located nearby. After evaluation and confirmation of the validity, the seismic approach is used to invert time-series of bedload transport from the other 23 seismic sensors distributed across the watershed. The resulting dataset is used to investigate coarse material fluxes at the watershed scale during the studied high-magnitude bedload transport event. Combined with a morphological change analysis, we discuss the efficiency of coarse material transfers in the watershed at the scale of the studied bedload transport event, and place it into a longer time-scale perspective.

IV-2 Material and methods

IV-2.1 Study site

The Vallon de Nant (VdN) is a 13.4 km^2 Alpine watershed located in South-Western Switzerland (Figure IV-1), at ~1’200 to ~3’050 m a.s.l. Through its position at the north-western margin of the European Alps, and due to the local high relief (notably on its eastern side), it forms a natural barrier to westerly and north-westerly air streams (Vittoz and Gmür, 2009; Lane et al., 2016). It receives a substantial amount of annual precipitation (~ 1850 mm·y^{-1}), predominantly in summer (Dutoit, 1983; Vittoz and Gmür, 2009; Lane et al., 2016; Antoniazza et al., 2022). Given its high elevation, a significant proportion (~45 % in the year 2020) of annual precipitation occurs as snowfall (Thornton et al., 2021, 2022; Antoniazza et al., 2022), and snow cover may persist until late spring-early summer in the less sun-exposed areas (e.g. valley bottom, gullies, hillslope base) of the watershed (Dutoit, 1983; Vittoz and Gmür, 2009; Lane et al., 2016; Thornton et al., 2021, 2022; Antoniazza et al., 2022). A small debris-covered glacier (Glacier des Martinets) occupies ~3% of the watershed (in 2020), supplying only negligible amounts of ice melt. Thus, the hydrological regime of the watershed is dominated by snowmelt and rainfall (Ceperley et al., 2020; Mächler et al., 2021; Michelon et al., 2021, 2022; Thornton et al., 2021, 2022; Antoniazza et al., 2022).

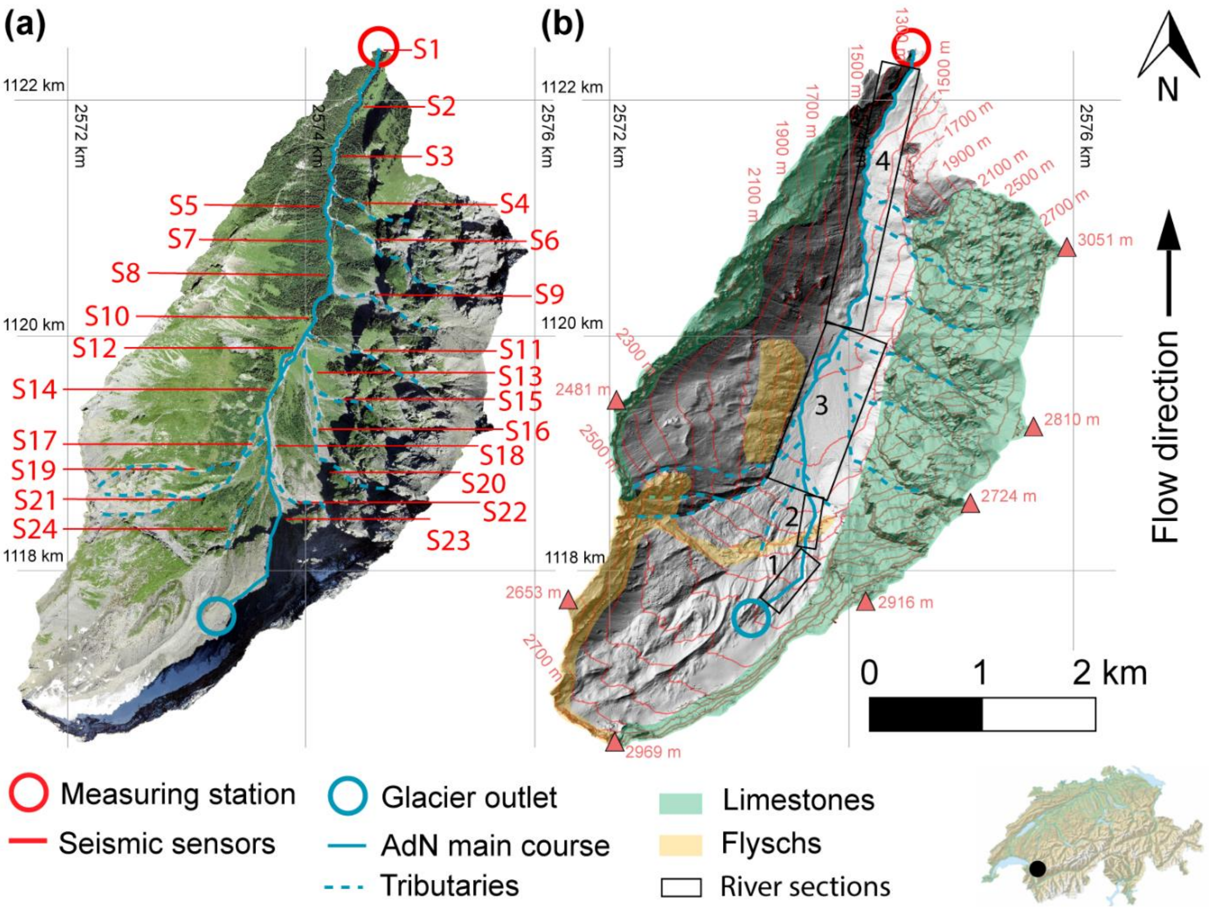

Figure IV-1. The Vallon de Nant Alpine watershed in (a) a 0.1-m orthophoto (2020) and in (b) a hillshade (2020) based on the the 0.5-m resolution LIDAR-based SwissAlti3d digital elevation model (Acknowledgments ©Swisstopo). Coordinates are provided in the CH1903+ Swiss system. The streamflow and SPG monitoring station at the outlet is labelled with a red circle. Seismic sensors deployed during the year 2020 are labelled S1 to S24 from downstream to upstream in (a). The Glacier des Martinets outlet and the Avançon de Nant (AdN) main course are labelled with a blue circle and blue line, respectively. The main temporarily-flowing tributaries are labelled with a dashed blue line. In (b), the main bedrock outcrops are delineated in green (limestones of the 'Nappe de Morcles-Doldenhorn') and in yellow (flyschs of the Northern Helvetic), the rest of the surface in gray being covered by Quaternary sediment. Numbered black boxes in (b) are used to differentiate between different river sections in the text description.

Geologically, the watershed comprises rocks from the calcareous sedimentary series (limestones of Secondary age) belonging to the Helvetic domain (inverse flank of the ‘Nappes de Morcles – Doldenhorn’). There are also softer North-Helvetic Tertiary flyschs outcropping locally in the southern part of the watershed (Figure IV-1b; Badoux, 1971; Thornton et al., 2018). Whilst limestones are subject to karstification at different rates (i.e. depending on their composition), flyschs are expected to be much less permeable, which gives the Vallon de Nant complex hydro-geological properties (Thornton et al., 2018, 2022). The geomorphology of the Vallon de Nant largely derives from its glacial legacy (Hooke, 1991; Cook and Swift, 2012; Egholm et al., 2012; Antoniazza and Lane, 2021), with a typical ‘staircase’ profile made of a succession of steep rockwalls and hillslopes, flatter glacier troughs, and steeper glacier riegls (Figure IV-1b). Bedrock only outcrops in the steeper sections (i.e. rockwalls, riegls), while the flatter sections (i.e. rockwall feet, glacier troughs) are covered by substantial depths (up to 80 m) of Quaternary till, which forms important aquifers (Thornton et al., 2022).

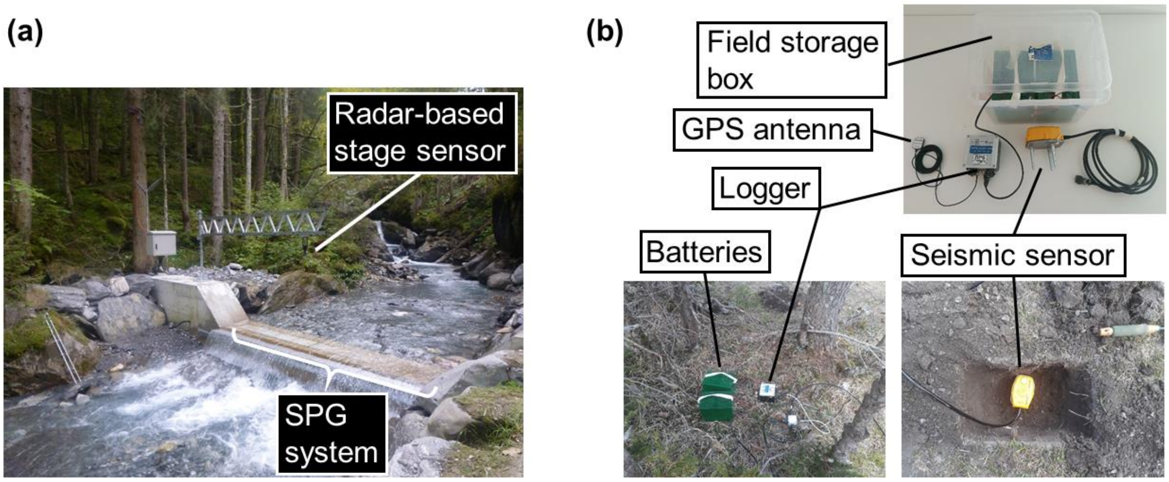

Figure IV-2. In (a), monitoring station at the Vallon de Nant outlet. Streamflow is continuously measured through a radar-based stage sensor, and 10 calibrated units of the SPG system provide a continuous monitoring of bedload transport. In (b), the seismic equipment (logger, sensor, GPS antenna, batteries, storage box) used in this study, with an example of field setting.

From the glacier snout (2’313 m a.s.l.), the Avançon de Nant (AdN) flows through a glacier trough (~0.5 km, 44%; Section 1 in Figure IV-1b) covered by Quaternary sediment (essentially moraines with depths between 10 and 50 m; Thornton et al., 2022), then through a steeper (~0.3 km, 65%) riegl crossing a flysch outcrop (Section 2), before reaching a flatter (~1.7 km, 13%) section (Section 3) in another glacier trough, with depths of Quaternary material between 10 and 80 m (Thornton et al., 2022). Along this reach, the AdN wanders between large Quaternary coalescent alluvial fans and develops a braided morphology, as an alluvial system. At the margin of the trough, the AdN enters a more topographically-constrained section (Section 4), and alternates between semi-alluvial step-pool and alluvial wandering reaches (~ 2.9 km, 9 %). The AdN is also fed by ~10 steep (40% - 65%) tributaries (dashed blue lines in Figure IV-1) that are mainly active during the snowmelt season, or briefly during storm events (i.e. colluvial system), and which form large diffusive coalescent fans at the hillslope base (Lane et al., 2016; Antoniazza et al., 2022; Figure IV-1). They essentially feed the AdN main course in Sections 3 and 4, and alternatively cross limestone outcrops, flysch outcrops and/or Quaternary deposits (Figure IV-1b). Their setting may make them prone to both bedload transport events as well as debris-flow events (Rickenmann and Koschni, 2010; Lane et al., 2016).

Between 2014 and 2015, a hydrological and bedload monitoring station (Figure IV-2a) was built at the outlet of the watershed (1’200 m. a.s.l.; red circle in Figure IV-1) through a collaboration between the University of Lausanne, the Swiss Federal Institute for Forest, Snow and Landscape Research WSL, and the ETH Zürich (Physics of Environmental Systems). Since 2016, it allows for the continuous monitoring of both streamflow and bedload transport (1-min resolution), through a calibrated radar-based stage sensor, and 10 calibrated units of a Swiss Plate Geophone (SPG) system (Rickenmann et al., 2012, 2014b), respectively. Antoniazza et al. (2020, 2022) and (Nicollier et al., 2021, 2022a, 2022b) describe the system and its calibration in detail. In this contribution, we used data from the monitoring station (i) to set the investigated bedload transport event into comparative context with other events that took place over the period 2016-2020; and (ii) as a benchmark method to evaluate the seismic inversion approach for bedload transport sensing.

IV-2.2 Seismic inversion approach

IV-2.2.1 Seismic monitoring

This study focuses on a high-magnitude bedload transport event that took place on August 3rd, 2020, the largest captured in the seismic time-series. In addition to the outlet SPG monitoring station, the event was simultaneously captured by a network of 24 seismic stations comprising 4.5 Hz PE6/B geophones and Cube3ext loggers (DiGOS, Germany), installed across the VdN watershed (Figure IV-1, Figure IV-2b). Sensors were installed to capture signal from the AdN main channel, and the major tributary inputs (Figure IV-1). Thus, the sensors covered ~9’800 m of channel length, with an average of one sensor per ~400 m of channel. One of the seismic sensors was installed next to the SPG monitoring station to be able to evaluate the performance of the seismic inversion approach in this environment. Following Bakker et al. (2020), each sensor was placed at 5-30 meters from the channel, buried at ~0.3 m underground to be isolated from surface seismic noise (e.g. rainfall, wind), oriented to the north and leveled horizontally (Figure IV-2b). The loggers were set to record the seismic signal with a frequency of 200 Hz, and a gain of 32. They were powered by two 9V-200Ah air alkaline batteries mounted in parallel. An internal active GPS antenna (BY-GPS-07) also recorded time continuously (Figure IV-2b), allowing synchronization of the measurements of the different seismic loggers, as well as data of the monitoring station (Figure IV-2a).

IV-2.2.2 Seismic model application

In order to inverse bedload transport time-series from the seismic signal recorded by each sensor, a mixed turbulence (Gimbert et al., 2014) and bedload transport (Tsai et al., 2012) physical model assembled by Dietze et al. (2019) as a ‘Fluvial Model Inversion’ (FMI) was applied, using the R package “eseis” (v. 0.4.0) developed by Dietze (2018). The approach assumes that the seismic spectrum recorded near a river during a bedload transport event is dominated by a combination of force fluctuations in the fluid due to turbulence and coarse particles impacting the bed (Schmandt et al., 2017; Gimbert et al., 2019; Dietze et al., 2019; Bakker et al., 2020), which result in seismic power in different, yet overlapping frequency bands. The turbulence model of Gimbert et al. (2014) predicts the power spectral density (PSD) of vertical Raleigh waves induced by the flow interacting with roughness elements present along both the bed and the banks. The bedload model of Tsai et al. (2012) predicts the power spectral density (PSD) of vertical Raleigh waves generated by the impacts of saltating particles on the riverbed, assuming that the coarsest particles in transport (> D_{90}) are responsible for the largest seismic signal recorded (Tsai et al., 2012; Dietze et al., 2019; Gimbert et al., 2019;

Bakker et al., 2020; Lagarde et al., 2021). The FMI consists in relating in a least-squared procedure the measured empirical seismic spectrum with synthetic ones produced by the paired models for random combinations of water depth h and unit bedload transport rate q_b estimated within their own plausible range, to invert the most likely values of h and q_b at each targeted time-step (Dietze et al., 2019).

Bedload transport and water depths were inverted from the paired FMI, requiring constraints on nine parameters, which can be separated into three classes following Lagarde et al. (2021); (1) the river morphology parameters, which include the channel gradient θ [radians], the channel width W [m], and the distance between the channel centerline and the seismic sensor r_0 [m]; (2) the grain-size distribution (GSD) parameters, which include the median grain-size D_{50} [m] and the standard deviation σ_g [-] of a parametric log-raised cosine function fitted to discrete measured particle classes (Tsai et al., 2012); and (3) the seismic ground properties, which are described by Green's function as (Tsai et al., 2012; Bakker et al., 2020):

$$v_\mathrm{p} = v_\mathrm{p0}(f/f_0)^{-\xi} \qquad \text{[IV-1a]}$$

$$v_\mathrm{g} = v_\mathrm{p}/(1+\xi) \qquad \text{[IV-1b]}$$

$$K = K_0(f/f_0)^{\eta} \qquad \text{[IV-1c]}$$

where, v_p is the phase velocity of the Raleigh wave [m·s^{-1}], v_p0 is the phase velocity of the Raleigh wave at a frequency f_0 = 1 Hz, f is the frequency [Hz], ξ [-] a dimensionless exponent used to scale a frequency-dependent decay in seismic signal, v_g the wave group velocity [m·s^{-1}], K [-] a dimensionless quality factor, K_0 [-] a dimensionless quality factor at a frequency f_0 = 1 Hz, and η [-] a dimensionless exponent that expresses the change in the quality factor K with frequency. To these nine site-specific parameters, two constants complete the paired FMI: the water density ρ_w = 1000 [kg·m^{-3}] and the sediment density ρ_s = 2650 [kg·m^{-3}].

IV-2.2.3 Model parameterization

The river morphology parameters were derived from RTK-dGPS survey using a Trimble R10 device, combined with measurements performed on a 0.1-m orthophoto (2020) and a 0.5-m resolution Alti3d Digital Elevation Model (2020) from the aerial campaigns of the Swiss Federal Office of Topography (Swisstopo). For each of the 24 seismic stations, the position of the seismic sensor was measured to derive the sensor-to-river distance r_0; the positions of both channel edges were identified to derive the channel width W; and the average channel gradient θ was computed over a reach of ~100 m encompassing the seismic sensor location. The coordinates of the 24 seismic sensor locations, together with the river morphology parameters measured at each site, are available in Supporting information IV-S1 (Table IV-S.1).

The grain-size distribution parameters were derived from a line-by-number count (Wolman, 1954; n = 100) of mobile particles on the riverbed (Bakker et al., 2020; Lagarde et al., 2021) performed at each of the 24 seismic sensor locations. The particles were then separated into 10 size classes (Bakker et al., 2020; Supporting Information IV-S.2), and the parameters D_{50} and σ_g were derived following Tsai et al (2012) from a best-fit log-raised cosine function out of n = 10^4 runs. The grain-size distribution parameters measured at each of the 24 seismic sensor locations are available in Supporting Information S2 (Table IV-S.2; Figure IV-S.1).

The seismic ground property parameters were derived from an active seismic survey undertaken individually for each seismometer following Bakker et al. (2020). First, a second seismic sensor was installed on the opposite bank from a given seismic station targeted for the ground seismic parameterization. Both loggers were set to record at 800 Hz in order to capture the active seismic signal at the highest possible rate. A metallic plate with dimensions 0.3 m x 0.3 m x 0.01 m (thickness) and a mass of ~15 kg was set in line with the two seismic stations, and its position was recorded using a RTK-dGPS Trimble R10 device. The line made by the two seismic stations and the impact plate was orthogonal to the streamflow, and the impact plate was set at one end of the line. During periods of low streamflow to minimize signal contamination by turbulence, the plate was repeatedly struck 20 times using a sledgehammer, in order to derive for each impact the decay in surface wave velocity v_{g} with frequency, according to the arrival time of the active seismic signal at the two sensors. To do so, we first deconvolved the raw seismic signal according to the sensor characteristics. We also removed the mean and the seismic signal was detrended to avoid artifacts in the calculation of the power spectral density function (Lagarde et al., 2021). Following Bakker et al. (2020), the seismic signal was band-pass filtered for 50% overlapping intervals of 6 Hz, and a Hilbert envelope was calculated to identify the signal peak amplitude of each hammer blow. Knowing both distance and arrival time delay (i.e. in peak amplitude) between the active seismic source and the sensors, the surface wave velocity v_{g} was derived, and its decay with frequency allowed to constrain parameters v_{p0} and ξ in equations [IV-1a] and [IV-1b].

Second, the position of the impact plate was changed multiple times (~4-10) to vary the distance (~5-100 m) between the seismic sensor and the active seismic source. At each impact location, the position of the plate was measured using an RTK-dGPS Trimble R10, and 20 consecutive impacts were performed using a sledgehammer. This experiment was used to quantify the attenuation in seismic power with distance to the seismic source K (or quality factor, equation [IV-1c]), and assess its frequency dependency (η in equation [IV-1c]). To do so, signal spectrograms were computed from the detrended seismic signal using the Welch's method (Welch, 1967), averaging seismic power at 1 s intervals using 80% overlapping sub-windows of 0.5 s.

The active seismic experiments were repeated at each seismic sensor location to derive site-specific ground seismic properties, with the exceptions of sensor groups S10-S12, S16-S20 and S22-S23-S24, where a single active seismic experiment encompassing each group of sensors was performed, thanks to their geographical proximity. Parameters v_{p0} and ξ from equations [IV-1a] and [IV-1b], and parameters K_0 and η from equation [IV-1c], estimated at each of the 24 seismic sensor locations based on active seismic experiments, are reported in Supporting Information IV-S3 (Table IV-S.3, Figure IV-S.2 and IV-S.3).

IV-2.2.4 Model application

Using the parameters determined in 2.2.3, combined with range of plausible water level h (0.1 to 1 m) and unit bedload transport rates q_{b} (10^1 to 10^5 kg·min^{-1}) estimated from the monitoring station data, $2 \cdot 10^4$ synthetic spectra are produced in the FMI, and compared to the empirical spectrum in a least-squared procedure (Dietze, 2018; Dietze et al., 2019). Doing so, the values of h and q_{b} minimizing the error between the synthetic and the empirical spectra are determined at 1-min resolution. Since we are interested in bedload transport, the inversion is performed focusing on a range of frequencies (25-60 Hz) in which bedload noise is normally found (Tsai et al., 2012; Schmandt et al., 2017; Bakker et al., 2020), optimizing the inversion of q_{b} at the expense of h. We do not further consider the inversions of h in the frame of this study. This procedure is applied to every sensor, providing with 24 absolute time-series of bedload transport, at 1-min resolution, over the duration of the 3rd of August 2020 event and distributed across the Vallon de Nant watershed.

IV-2.3 Data analysis

IV-2.3.1 Evaluation of the seismic inversion approach

The seismic inversion approach was first applied to the data recorded by the seismic sensor that was located near to the SPG monitoring station (~20 m). Doing so, the seismically-inverted flux could be compared to a second and independent measurement of bedload transport over the event of interest, allowing assessment of the performance of the inversion approach. Note that both measuring systems may have different capabilities and limits, notably in terms of the minimal detectable grain-size, which means that the comparison must be undertaken with care. After evaluation, the same seismic inversion approach was then applied to the other 23 sensors distributed in the VdN watershed but using the site-specific parameters following the procedure described in 2.3.3 and 2.3.4. The site-specific parameters are reported in Supporting Information IV-S1, IV-S2 and IV-S3.

IV-2.3.2 Spatially-distributed seismic monitoring of bedload transport

Once the inversion procedure was applied to the 24 seismic sensors, spatially-distributed time-series of bedload transport for the event of interest were obtained. Three statistics were used to characterize the bedload transport event measured at each sensor location: (1) the mass of bedload transported over the event duration; (2) the timing of the start and end of the bedload transport event, and the timing of the major (multiple hours in duration) bedload transport waves; and (3) the lag and propagation velocity between spatially-consecutive bedload transport time-series.

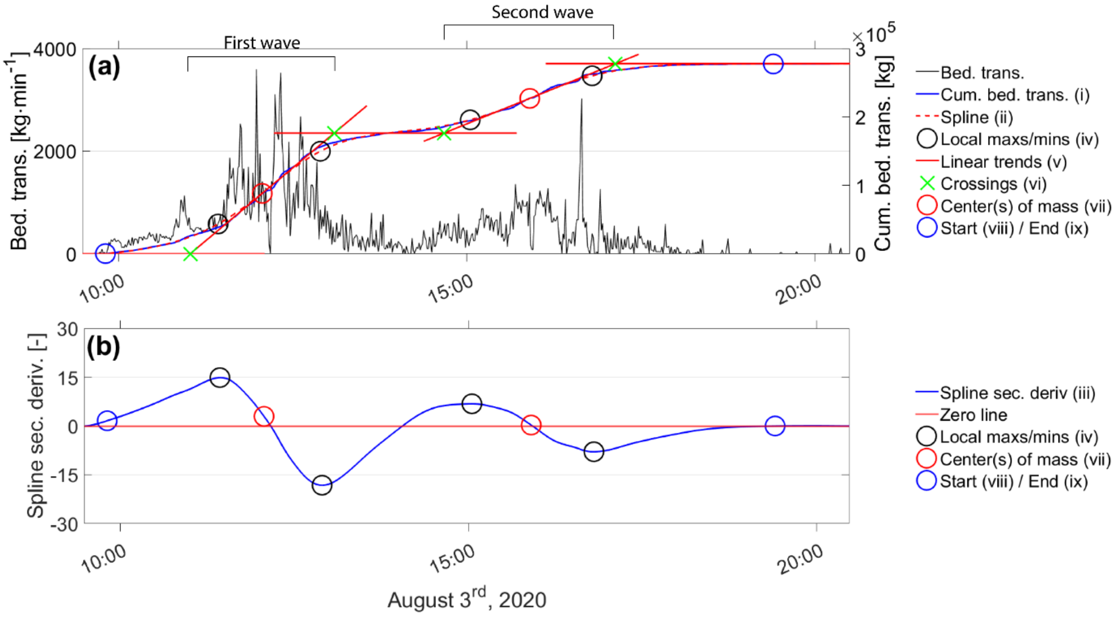

Figure IV-3. Example of the procedure applied to each of the 24 seismic-inverted bedload transport time-series to determine: (1) the mass of bedload transported over the event duration; (2) the timing of the bedload transport event starting and ending points, and the timing of the major (multiple hours in duration) bedload transport waves; and (3) the lag and propagation velocity between spatially-consecutive bedload transport time-series. The example is provided for seismic sensor S1 located near to the monitoring station.

Objective criteria applicable to every time-series were used to automatically determine these statistics. An example of how this was done is provided in Figure IV-3 for sensor S1 located near to the monitoring station and where two major bedload transport waves were identified. Note that two major bedload waves were identified on the majority of the seismic sensors (20 out of 24), one sensor (S19) recorded only one major bedload transport wave and one sensor (S6) recorded three of them. The remaining two sensors (S9 and S15) recorded no bedload transport.

At step (i), we calculated a cumulative sum of bedload transport rates over the duration of the bedload transport event for each sensor (blue line in Figure IV-3a). At step (ii), we fitted a smoothing spline to each cumulative distribution (dashed red line in Figure IV-3a). At step (iii), we calculated the second derivative of the spline (blue line in Figure IV-3b) to obtain (iv) inflexion points (i.e. local maxima and minima in the second derivative; black circles in Figure 3a and 3b). At step (v), we calculated the equation of the lines meeting each pair of consecutive inflexion points (red lines in Figure IV-3a). The slope coefficient of the lines before, in-between and after any bedload wave was set to zero, and the crossing points between trend lines (green crosses in Figure IV-3a) was retained as the start and end points of each major bedload wave (vi). At step (vii), we computed the center of mass of each major bedload wave (red circles in Figures IV-3a and IV-3b), by taking the mid-point between trend line crossings marking a linear increase in the spline fit. At step (viii), the starting point of the bedload transport event was set at the crossing between the spline fit and bedload transport rate zero line. At step (ix), the end of the bedload transport event was determined as the point from which the spline fit reaches an upper plateau (i.e. a second derivative greater than -0.01; blue circles in Figures IV-3a and IV-3b).

Integration of the bedload transported mass between the start (vii) and end points (viii) gave us (1) the bedload mass transported over the duration of the event at each seismic sensor location. It allows quantification of the change in the transported bedload mass across the watershed during the studied bedload transport event, and the relationship between the transported mass and contributing area (measured on a 0.5-m digital elevation model of 2020). The timing of the bedload transport start (vii) and end (viii) points, as well as the timing of the major bedload transport waves (vi), allowed us to calculate (2) to compare the timing of the bedload transport event at the different seismic sensor locations. To characterize the temporal lag between time-series of bedload transport measured at two spatially consecutive seismic sensors, and the associated propagation velocity, a cross-correlation analysis was performed. Using the distance between two spatially consecutive sensors measured on a 0.1-m orthophoto of 2020, propagation velocities between pairs of spatially-consecutive sensors were computed to obtain (3).

IV-2.3.3 Morphological change analysis

In order to place the 3rd of August 2020 bedload transport event into a longer-term perspective of sediment fluxes throughout Alpine watersheds, we perform a morphological change analysis. It is derived from two 0.5-m resolution LIDAR-based (Swisstopo aerial campaigns) SwissAlti3d digital elevation models (DEM) of 2016 (August 25th) and 2020 (August 6th), which were derived from two point clouds with an initial mean density of 15-20 pts·m^{-2}. In a first step, we verified the co-registration of the two Swisstopo DEMs by computing the distribution of errors between stable areas of the two DEMs (Minute et al., 2019; Cucchiaro et al., 2020; Pitscheider et al., 2022). Selected stable areas (i.e. grassy lands, bedrock) covered all together about 0.12 km^{-2}, were evenly distributed across the watershed, and presented various degrees of slope (i.e. valley bottom, hillslopes). A systematic error of μ = 0.16 m ($\sigma = 0.11\ m$) was identified between the two Swisstopo DEMs, and we applied a best-fit function between the stable areas of the two DEMs to model the co-registration error. Error in Z for each XY coordinates was minimized by applying the following correction:

$$Error_Z = p_{00} + p_{10} * X + p_{01} * Y \qquad \text{[IV-2]}$$

where $Error_Z$ [m] is the vertical co-registration error, p_{00} = 290.2, p_{10} = -1.364 x 10^{-4} and p_{01} = 0.5455 x 10^{-4} are coefficients, X [m] are easting coordinates and Y [m] northing coordinates. We applied the correction to every XY cells of the DEM of 2021, and removed the modelled error $Error_Z$ from the elevation Z of the DEM of 2021. Distribution of error in the same stable areas between the DEM of 2019, and the corrected DEM of 2021, showed a reduced error with μ = -0.07 m and $\sigma = 0.09$ m.

Once DEM co-registration was successfully verified, the altitude of the DEM of 2019 were substracted cell-by-cell from the altitude of the DEM of 2021 in order to obtain erosion and deposition depths across the watershed area over the survey interval. Volumetric changes were then obtained by multiplying cumulated vertical changes by the DEM cell resolution (0.5 x 0.5 m). A threshold of detection was set as LoD = ± 0.2 m, corresponding twice the standard deviation of the residual error after co-registration.

To increase the efficiency of the morphological change analysis, and to avoid potential large errors in the steep rockwalls (Minute et al., 2019; Pitscheider et al., 2022) present throughout the watershed, we followed former research that has limited morphological change analysis to the Sediment Contributing Area (SCA) (Altmann et al., 2021; Pitscheider et al., 2022), that is all sedimentary sources connected by active unvegetated channels to the main drainage network. The delineation of the SCA was done using a 0.1 m resolution orthophoto of 2020 (Cavalli et al., 2017; Minute et al., 2019; Pitscheider et al., 2022). Patterns of erosion and deposition encompass the effects of the 3rd of August 2020 bedload transport event, but also multiple other bedload transporting events that have taken place in this time interval (Antoniazza et al., 2022). Note that while seismic sensing measures bedload transport only, morphological change analysis may also include finer material transported in suspension.

IV-3 Results

IV-3.1 The August 3rd 2020 bedload transport event

The August 3rd 2020 bedload transport event was the largest one recorded during the year 2020 at the outlet monitoring station, with a peak water depth of 0.39 m (4.3 $m^3 \cdot s^{-1}$), and a peak of bedload transport of 1240 $kg \cdot min^{-1}$ measured simultaneously (~12:15). Over its duration (Figure IV-4), ~73’700 kg of bedload were exported at the outlet according to the SPG recording, which represents 11% of the bedload that was transported over the year 2020 (Antoniazza et al., 2022). In comparison to the period 2016-2020 analyzed by Antoniazza et al. (2022), the 3rd of August 2020 flood is the 5th largest in terms of bedload transport rate peak, the largest being monitored on August 6th 2018, with a bedload transport rate peak measured at 3540 $kg \cdot min^{-1}$. Meteoswiss datasets RhiresD and TabsD (MeteoSwiss, 2017, 2019) of daily precipitation and daily mean temperature show that 57.4 mm of precipitation (with a mean daily temperature of 5.75°C) fell over the Vallon de Nant on August 3rd 2020, likely as rainfall given the > 1°C daily mean temperature. The hydrological analysis performed by Antoniazza et al. (2022) further indicates that daily melt cycles on August 3rd, 2020 (outside of rainfall events) were visible in the flow hydrograph, meaning that a signal related to snowmelt was present in the watershed, and that baseflow was still relatively high (~0.5 $m^3 \cdot s^{-1}$). Heavy rainfall and high baseflow thus combined to produce a rapid increase in streamflow (Figure IV-4), with two successive waves between 11:00 and 13:00, and between 15:00 and 18:00 on August 3rd. Generally, bedload transport followed the same trend as streamflow, with two larger waves taking place with a comparable timing to streamflow peaks on August 3rd.

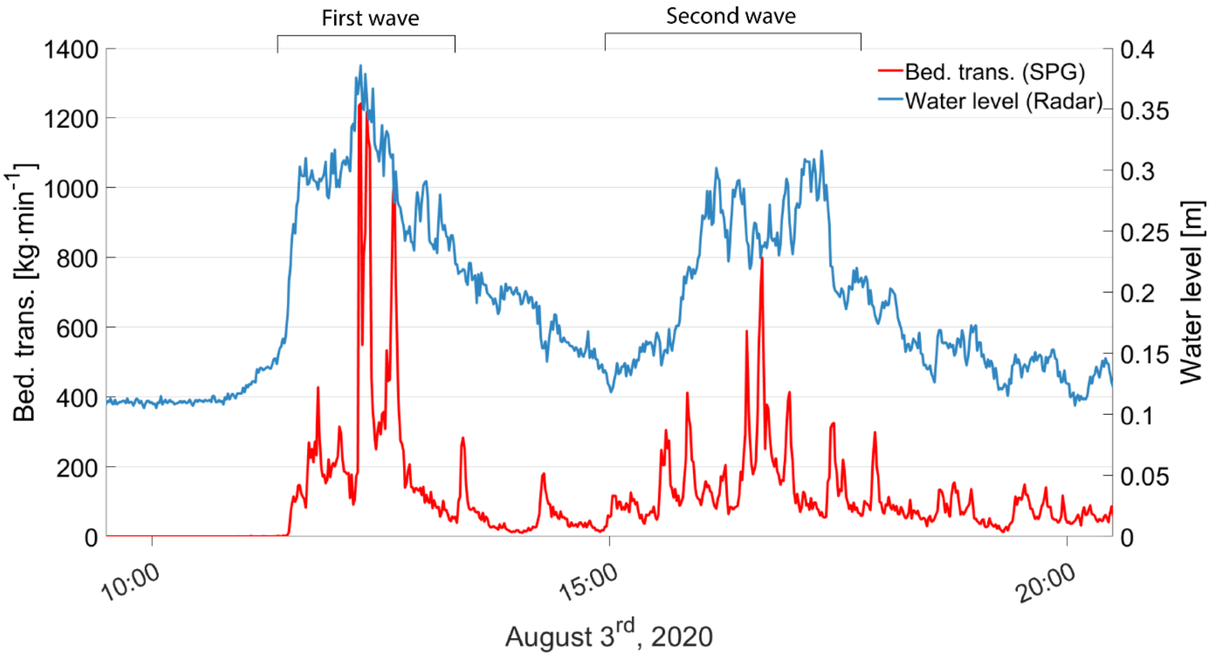

Figure IV-4. The 3rd of August 2020 bedload transport event measured at the Vallon de Nant outlet monitoring station. Bedload transport time-series measured with the 10 calibrated SPG units is plotted (in red) together with the radar-based water level time-series (in blue).

IV-3.2 Evaluation of the seismic inversion approach

At the seismic sensor located close to the SPG monitoring station, the dGPS-RTK survey combined with GIS measurements gave a channel width of W = 6 m, a channel gradient θ = 0.06 radians, and a distance between the seismic sensor and the river centerline r_0 = 5 m. The application of a best-fit log-raised cosine function to a line-by-number count of riverbed mobile material gave D_{50} = 0.06 m, and σ_g = 0.9 (Figure IV-5a).

Data from the active experiment were then used to derive the seismic ground property parameters v_{p0}, ξ, K and η in equations [IV-1a], [IV-1b] and [IV-1c]. The decay in wave group velocity with frequency between the two seismic loggers spaced 12 m away on opposite banks was found to be best expressed with v_{p0} = 482 m·s-1 and ξ = 0.25 (Figure IV-5b), by combining equations [IV-1b] and [IV-1c]. These values are close to, though a bit lower, than the ones found by Bakker et al. (2020) for a similar active seismic experiment conducted in an alluvial channel; but substantially lower than the ones proposed by Tsai et al. (2012) for a generic bedrock site (Figure IV-5b). Seismic power rapidly decreased with distance at the different frequencies towards background signal level (Figure IV-5c). Change in the quality factor K with frequency was estimated using equation [IV-1c], and gave K_0 = 17.3 and η = 0.14 (Figure IV-5d). The frequency dependency of K is not very strong, which is consistent with the constant value of K = 20 proposed by Tsai et al. (2012). The value of the exponent η = 0.14 is also close to the one found in Bakker et al. (2020) for an alluvial channel (η = 0.15; Figure IV-5d).

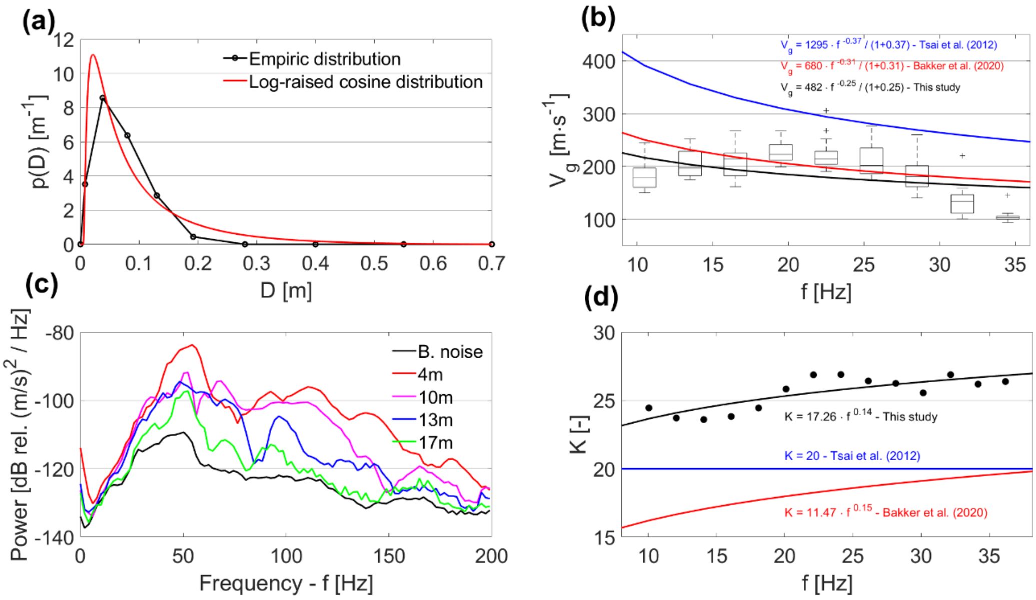

Figure IV-5. Parameter estimate for the seismic sensor S1 located close to the SPG monitoring station (see also Figure IV-1). In (a), best-fit log-raised cosine function applied to a line-by-number count of mobile bed material (n = 100), to derive parameters D_{50} and σ_g. In (b), decay in wave group velocity with frequency between two seismic sensors located on opposite banks. The boxplots show the variability for 20 repeated impacts with a sledgehammer. The regression curve (black) describes the wave group velocity decay with frequency, based on equations [IV-1a] and [IV-1b], and the parameters found by Bakker et al. (2020) for an alluvial channel (in red), and proposed by Tsai et al. (2012) for a generic bedrock site (in blue), are presented for comparative purpose. In (c), attenuation of seismic power with distance. Lines represent the average of 20 repeated impacts using a sledgehammer (i.e. without including pauses between sledgehammer blows), and the line in black shows the background noise of periods without active seismic experiment. In (d), change in the quality factor K with frequency according to equation [IV-1c]. The parameters found by Bakker et al. (2020) for an alluvial channel (in red), and proposed by Tsai et al. (2012) for a generic bedrock site (in blue) are presented for comparative purpose.

Following the field-based estimation of the nine parameters in the FMI, the time-series of bedload transport were inverted (Figure IV-6). The August 3rd 2020 bedload transport event is well visible on the seismic power spectrogram (Figure IV-6a), with two consecutive periods (11:00-13:00 and 15:00-18:00) recording substantially more seismic energy (i.e. > -110 dB) than the preceding (09:30-11:00), interceding (13:00-15:00) or following (18:00-20:30) ones. In Figure IV-6b, the results of the bedload transport seismic inversion are presented (in black), together with the time-series of bedload transport (SPG measurement, in red) and of water depth (radar measurement, in blue). Results of the inversion show that the seismic-based time-series of bedload transport varies together with changes in the seismic power, with bedload transport rate being low during periods of weak seismic energy and peaking up to 2740 kg·min^{-1} at its maximum (12:18).

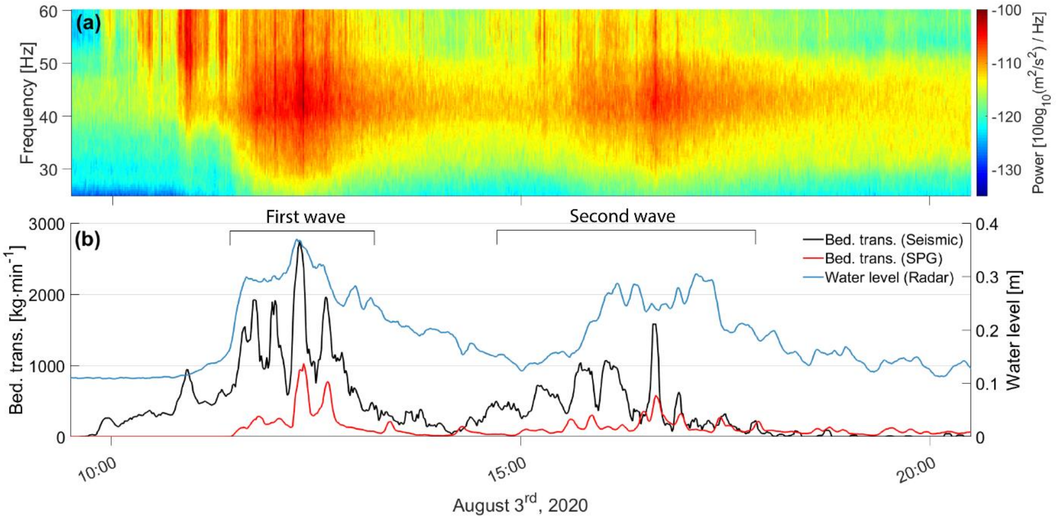

Figure IV-6. In (a), seismic power spectrogram of the 3rd August 2020 bedload transport event for the seismic sensor S1 located close (~20 m) to the SPG monitoring station. In (b), bedload transport time-series (in black) inverted using the FMI constrained with the nine field-based parameter estimates. The bedload transport time-series measured at the SPG monitoring station is also provided (in red) for evaluation purposes, as well as the water level time-series measured with the radar-based stage sensor (in blue). Note that a 5-min moving average has been applied to all three time-series.

The general trend of the bedload transport event sensed with the SPG monitoring system is identified by the bedload seismic inversion (Figure IV-6b). On August 3rd 2020 both monitoring systems recorded a first wave with greater peak at 11:00 – 13:00, and a second with smaller peak at 15:00 – 18:00. Outside of these periods of high bedload activity, both monitoring systems measured no or little bedload transport (e.g. 18:00-20:30). The timing of the greater bedload transport peaks (seismic-inverted bedload transport > 1000 kg·min^{-1}) is relatively synchronous for both monitoring systems: there are 3 minutes of lag in the peak of the first major bedload transport wave (~ 12:15), and 1 minute of lag in the peak of the second major bedload transport wave (~ 16:40), while both waves last multiple hours. For the second major bedload wave (16:00 – 18:00), the radar-based water level sensor measures multiple high peaks in streamflow, while both bedload transport monitoring systems recorded a higher transport peak occurring in-between in a period of relatively lower streamflow (at ~ 16:40). This confirms in this instance that the FMI is indeed able, based on different frequency bands, to differentiate between seismic sources related to either water or bedload transport, and that inverted bedload transport is not only a function of increasing water depth and increasing turbulence rate.

The seismic inversion of bedload transport generally tends to overestimate the SPG-derived bedload fluxes, to a factor of 4 on average for bedload transport rates greater than 60 kg·min^{-1} (1 kg·s^{-1}). Over the duration of the bedload transport event, ~50 % of the 1-minute data points are below a factor 3 of difference, and the two previously identified bedload peaks (~12:15 and ~16:40) both present a factor 2.7 of difference. The measurement of bedload is expected to become more uncertain towards low transport rates, especially around the threshold of motion, for both measuring systems. This is notably visible at the beginning of the flood (10:00-11:00), where the seismic-inverted bedload flux rises substantially, while the SPG monitoring measures no bedload transport. Over the duration of the bedload transport event (Figure IV-6), the seismic inversion of bedload transport gives a total transported mass of 2.8

$\times 10^5$ kg, which represents in average a factor 3.8 of difference (74 % greater) compared to the 0.74 $\times 10^5$ kg measured by the SPG system.

IV-3.3 Spatially-distributed bedload transported mass

The seismic power spectrograms of every sensor (columns 1 and 3 in Figure IV-7) show more seismic energy recorded on August 3rd between 11:00 and 18:00, as compared to preceding and following periods. In most instances, two distinct periods of higher seismic energy (11:00 – 13:00 and 15:00 – 18:00) corresponding to the two bedload waves identified in Figure IV-6, are observable (e.g. S1, S3, S5, S6, S7, S8, etc.). Sensors close to the continuously flowing main channel (e.g. S1, S2, S3, S5, S7, S8, S10) tend to record more seismic energy throughout the period due to permanent turbulence, as compared to temporally-flowing tributaries (e.g. S4, S6, S9, S15, S19), which only show higher seismic energy during discrete hydrological events. Seismic power spectrograms may not be directly comparable to each other due to site-specific differences (e.g. ground seismic properties, distance to seismic source), which are not yet taken into account at this stage of the processing. For instance, sensor S12 – located along the main channel – seems to record relatively little seismic energy, but this is likely because it was positioned relatively far (~30 m) from the flow. Figure IV-7 (columns 2 and 4) shows the results of seismic inversion. The two bedload waves identified in Figure IV-6 at sensor S1 are visible – with differences in timing and magnitude at S2, S3, S7, S8 and S10 (upper limit of the semi-alluvial Section 4 in Figure IV-1). From S10 on, it becomes harder to track the bedload waves since the main channel is now fed by multiple tributaries draining relatively large sub-catchments (Figure IV-1). The two waves are nevertheless visible at S12, S13, S14, S16, S17, S21 and S22. While large bedload waves were sensed in some tributaries (e.g. S4, S6, S11, S16, S17), no or little bedload transport was measured within others (e.g. S9, S15, S19). Although no bedload transport was inverted for S9 and S15, higher seismic energy is visible at the timing of the bedload transport event. As its frequency was outside of the bedload-specific bands, this is likely related to passage of a bedload-free water wave.

The time-series of bedload transport are combined into sub-catchment groups (a-f) in Figure IV-8, to visualize bedload transport patterns throughout the watershed, and the mass of bedload transported over the duration of the event is presented in the associated Figure IV-9. Starting from upstream, two sub-catchments (d, f) recorded large amounts of bedload (> 10^6 kg), in particular measured at sensors S16, S17 and S21. In contrast, substantially less bedload (10^5 – 5 $\times 10^5$ kg) was transported through sub-catchment (e), which drains the upper watershed area (i.e. where the glacier lies; Section 1 in Figure IV-1).

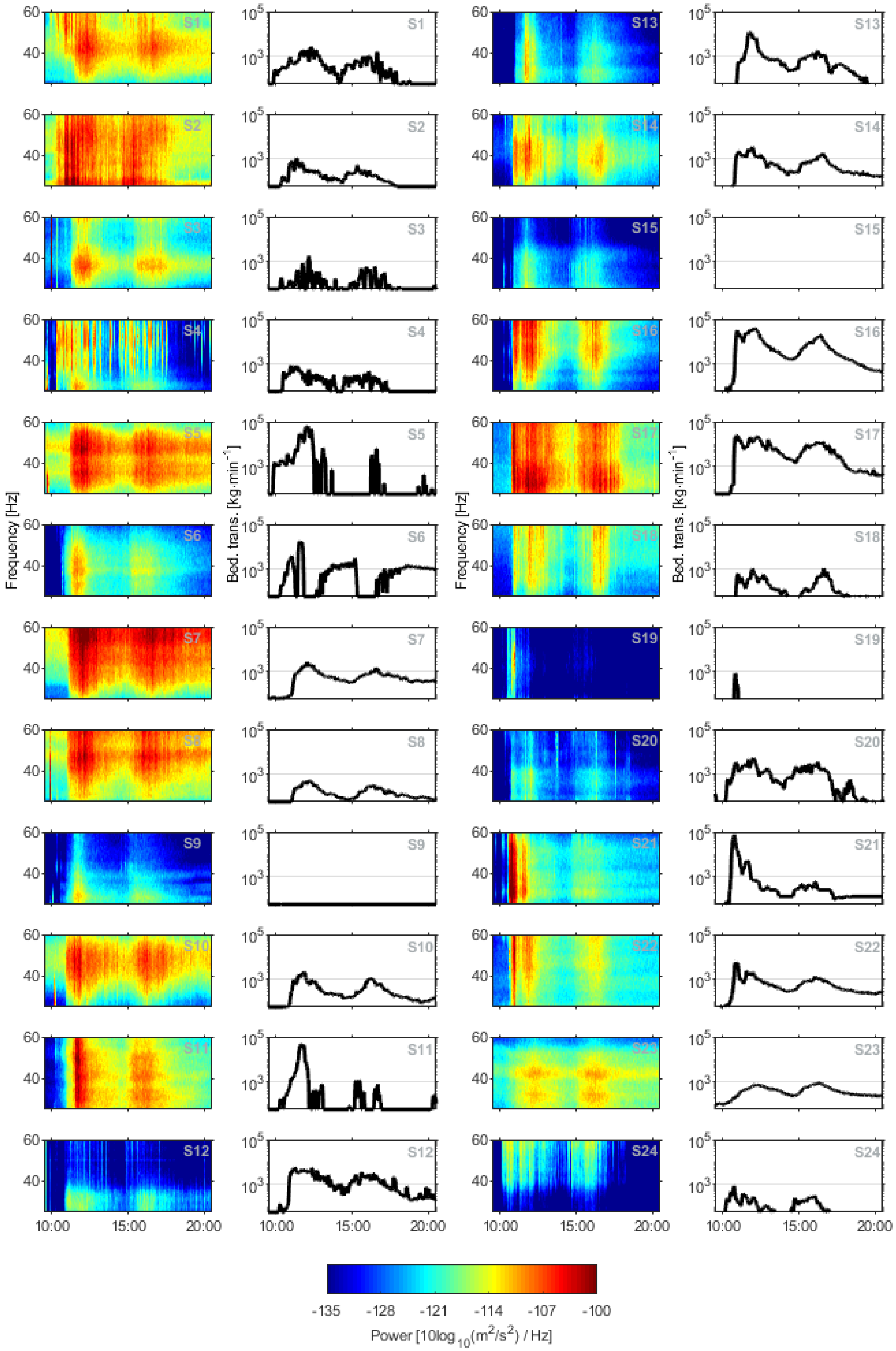
Frequency [Hz]
Sed. trans. [kg·min^{-1}]
60
40
10^5
10^3
S1
S2
S3
S4
S5
S6
S7
S8
S9
S10
S11
S12
S13
S14
S15
S16
S17
S18
S19
S20
S21
S22
S23
S24
10:00
15:00
20:00
-135
-128
-121
-114
-107
-100
Power [10log$_{10}$(m^2/s^2) / Hz]

Figure IV-7 (above). Seismic power spectrograms and seismic-inverted bedload transport time-series for the 24 seismic sensors distributed in the Vallon de Nant Alpine watershed. The inversion focuses on the bedload transport event that took place on August 3rd 2020.The seismic sensors are labelled S1 to S24 from downstream (the SPG monitoring station) to upstream (Figure IV-1). Note the y-axis log-scale in the seismic-inverted bedload transport time-series, and that a 5-min moving average has been applied to time-series of bedload transport.

In sub-catchment (d), the large amount of bedload (> 10^6 kg) measured at S21 and S17 seem to be already substantially attenuated at S14 (10^5 – 5 ×10^5 kg). In sub-catchment (e), bedload is supplied from three different tributaries, and less bedload is transported downstream of their confluence at S18. In sub-catchment (f), bedload transport increases from S20 (5 × 10^5 – 10^6 kg) to S17 (> 10^6 kg), before decreasing at S13 (5 ×10^5 – 10^6 kg), with no tributary input from S15. In sub-catchment (c), larger amounts of bedload are transported at S13 (5 ×10^5 – 10^6 kg) supplied from sub-catchment (f), than there are at S14 (10^5 – 5 ×10^5 kg) supplied from sub-catchments (d) and (e) combined. There is still a substantial amount of bedload transported at S12 (5 × 10^5 – 10^6 kg), which drains all sub-catchments (d), (e) and (f). Although bedload transport at S12 combines with a significant tributary input coming from S11 (> 10^6 kg), substantially less bedload is transported at S10 (10^5 – 5 ×10^5 kg) at the downstream end of sub-catchment (c), which also corresponds to the end of the braided river reach (Section 3 in Figure IV-1).

There is comparatively less bedload transported throughout sub-catchment (b), where different sensors (S10, S8, S7) measured between 10^4 and 5 ×10^5 kg of material. Heading downstream over consecutive sensors, there is more bedload material measured at S10, less at S8 and more again at S7, with no tributary input from S9, which confirms that erosion also takes place. There is another substantial tributary input from S6 (5 ×10^5 - 10^6 kg), which combines with supply from S7 in the main channel (10^5 – 5 ×10^5 kg) to produce an important bedload flux at S5 in the main channel (> 10^6 kg). This large sediment flux rapidly attenuates throughout sub-catchment (a), where 10^4 – 5 ×10^5 kg of material are measured over the different sensors (S1, S2, S3). Again, a greater mass of bedload transport is measured at S1 and S2 as compared to S3 located upstream, which emphasizes the occurrence of erosion.

If we take within each headwater tributary the sensor that has recorded the greatest mass of material over the duration of the event (i.e. sensors S4, S6, S11, S16, S17, S22, S23 and S24), and sum their respective mass, we can state that a minimum of 1.1 ×10^7 kg of bedload material was mobilized in the headwater channels during the 3rd of August 2020 bedload transport event. In comparison, only 2.8 ×10^5 kg is exported at the outlet (sensor S1), which represents 2.5 % of what has been mobilized. This is a minimal estimate, since it assumes that only deposition took place downstream of the headwater sensors, while evidence of erosion (greater bedload mass at downstream sensors compared to upstream ones) has also been observed (e.g. between S8 and S7, between S3 and S2). In addition, we do not know if the bedload material measured at two consecutive sensors is the same, and in what proportion, or whether deposition and erosion also occurs in-between sensors. Thus, it is likely that an even lower proportion of the total amount of bedload mobilized through the watershed is actually exported at the outlet. Note that we do not find any obvious difference in the mobilized amount of material between the tributaries draining the flysch outcrops (e.g. S19, S21, S23 and S24), or the ones draining limestone outcrops (e.g. S20, S11, S6), suggesting the likely prominent importance of local material availability, either from bedrock weathering or Quaternary-deposited stocks.

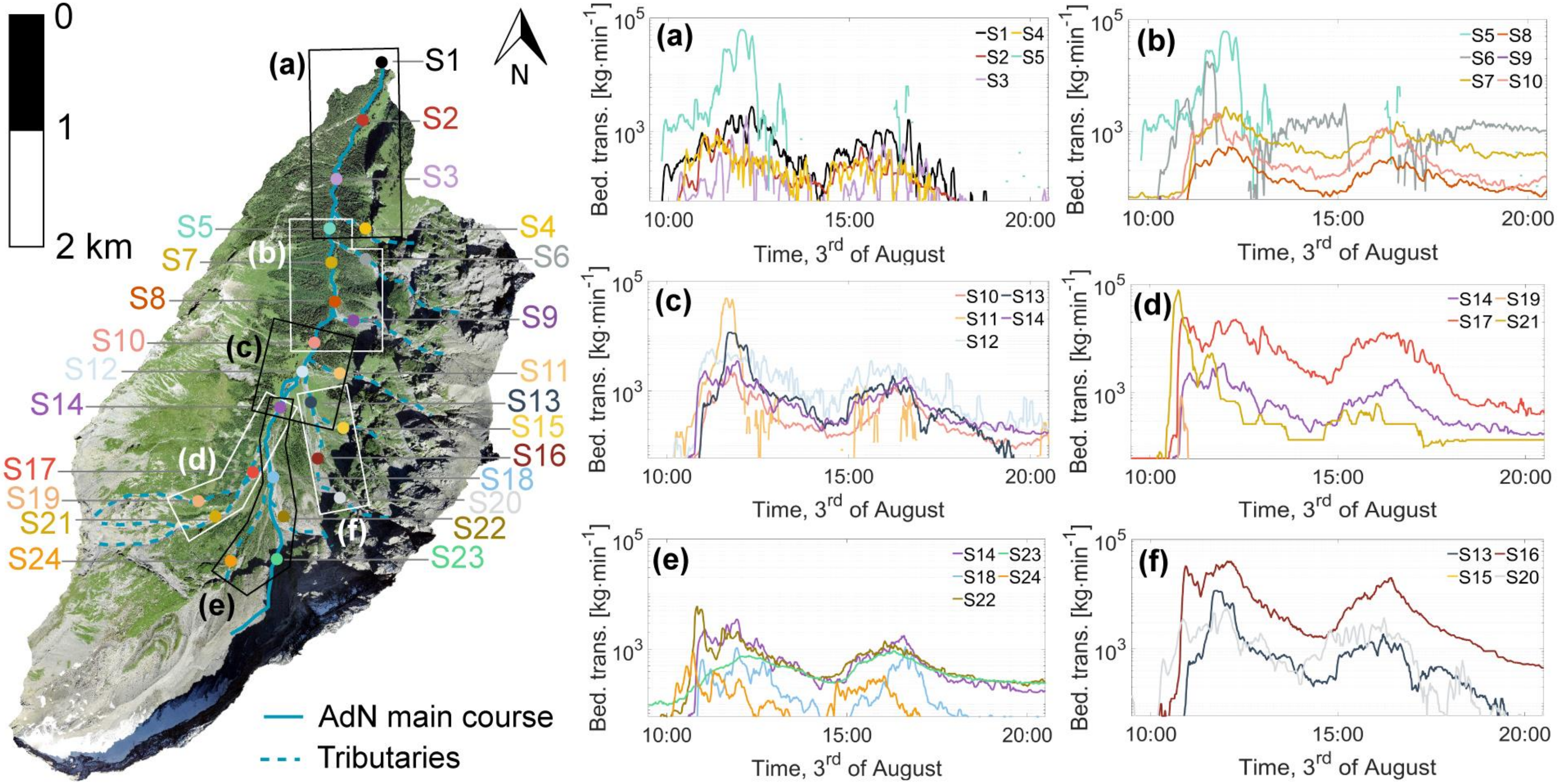

Figure IV-8. Time-series of bedload transport on August 3rd 2020 (09:30 – 20:30) for the 24 seismic sensors deployed in the Vallon de Nant Alpine watershed. The dots represent the location of the seismic sensors and their color corresponds to the color of the time-series of bedload transport in the graphs to the right. Time-series of bedload transport are combined into sub-catchment groups (a-f) to better visualize how bedload moves through the watershed. Note that a 5-minutes moving average has been applied to time-series of bedload transport. Acknowledgments ©Swisstopo.

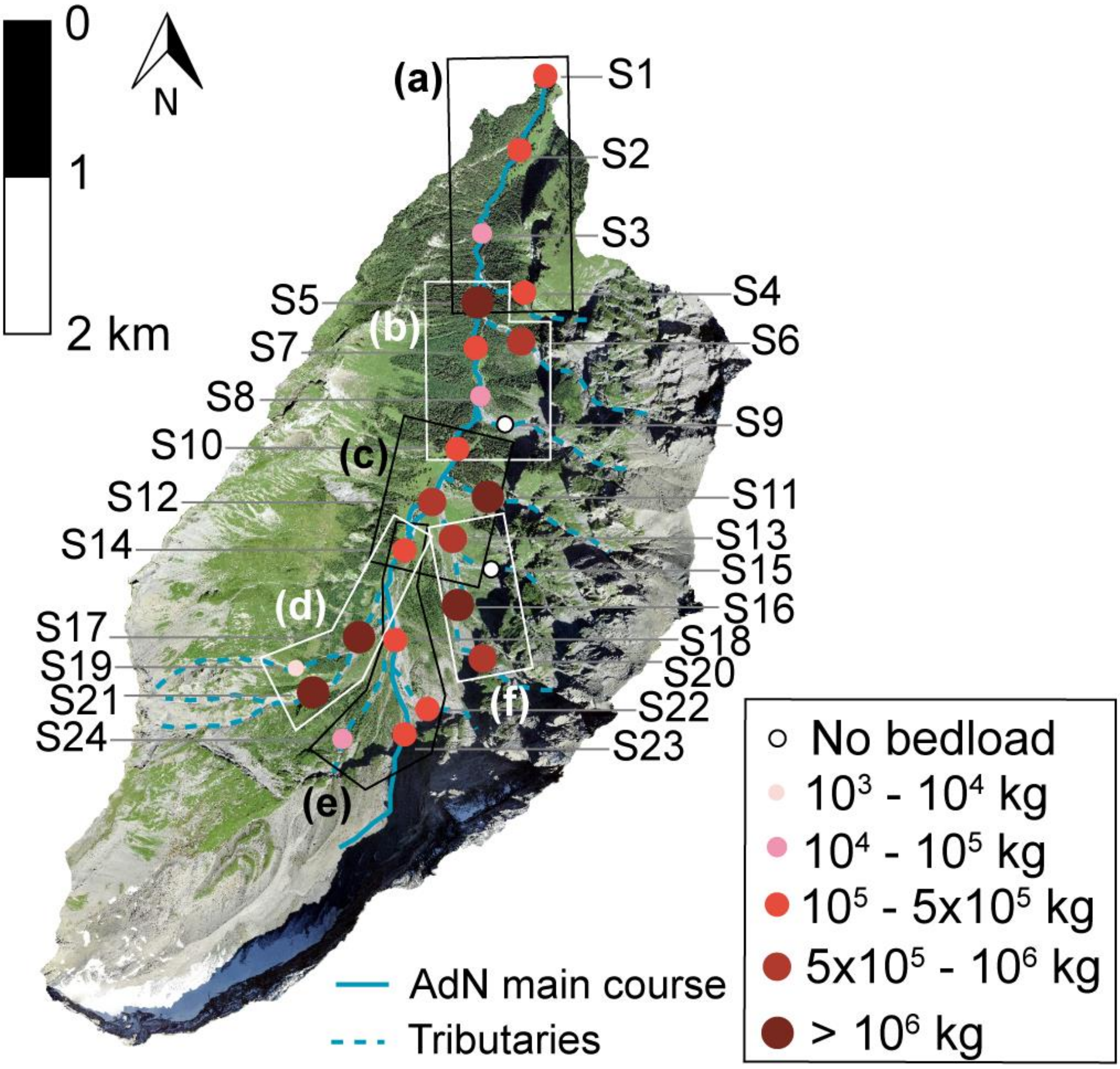

Figure IV-9. Mass of bedload transported over the duration of the 3rd of August 2020 bedload transport event in the Vallon de Nant Alpine watershed, at the 24 locations where a seismic sensor was deployed. Time-series of bedload transport are combined into sub-catchment groups (a-f) to better visualize how bedload moves through the watershed. Acknowledgments ©Swisstopo.

Channel gradient, contributing area, the bedload mass transported over the duration of the event and the transported bedload mass per unit area at each of the 24 seismic sensor locations are presented in Figure IV-10, along with the relationships between contributing area and the transported bedload mass. The data presented in Figure IV-10 are available in Supporting Information IV-S4. Channel gradient is lower within the main channel (e.g. S1, S3, S5, S7, S10), and greater in the tributaries feeding it (e.g. S4, S6, S9, S11). Gradient also tends to increase towards the watershed head, where multiple steeper tributaries combine to form the AdN main channel (Figure IV-1; Figure IV-10a). Contrastingly, contributing area decreases upstream (Figure IV-10b), and seismic sensors located within the AdN main channel drain a much larger area than the tributaries feeding them. There is a negative power law relationship between gradient (G) and contributing area (CA), such as $G = 23 * CA^{-0.33}$ ($R^2 = 0.71$).

As observed in Figure IV-8 and IV-9, both the transported bedload mass (Figure IV-10c) and the transported bedload mass per unit area (Figure IV-10d) tends to be greater in the steep tributaries (e.g. S4, S6, S11, S16, S17) as compared to the AdN main channel (e.g. S1, S2, S3, S7, S8, S10), which suggests a strong filtering of the bedload signal between the headwater tributaries and the watershed outlet. This observation is confirmed by a negative power law relationship (R^2 = 0.13) between contributing area and the bedload mass transported over the duration of the event (Figure IV-10e). The relationship is nevertheless made more complex by high rates of material supply from tributaries into the main channel (e.g. S6 → S5), and by varying mass of material transported throughout different portions of the watershed, also reflecting differences in local sediment availability.

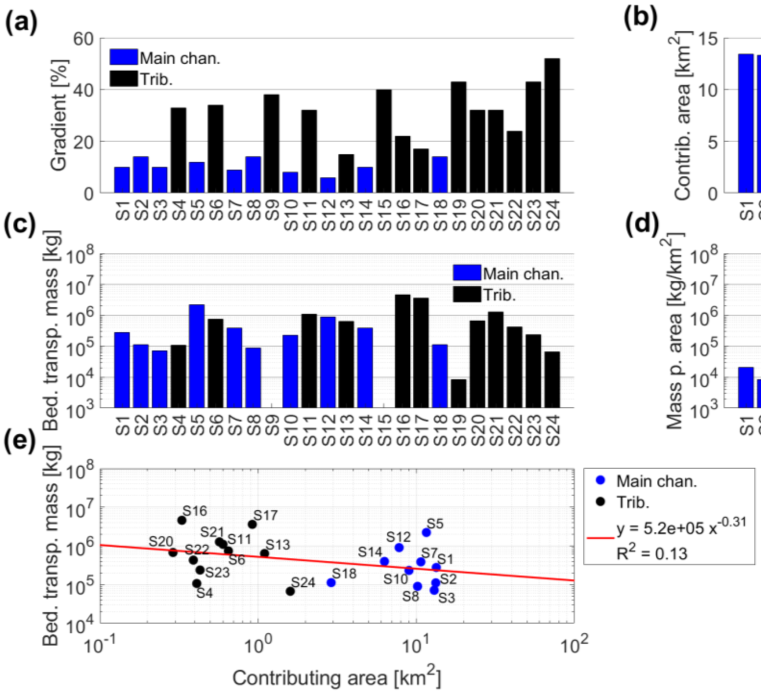

Figure IV-10. Gradient (a), contributing area (b), bedload transported mass over the duration of the event (c), and transported bedload mass per unit area (d) at each of the 24 seismic sensor locations. In (e), relationship between contributing area and the bedload mass transported over the duration of the event.

IV-3.4 Spatially-distributed bedload transport timing

The start and end of bedload transport (blue circles) and the timing of the major bedload transport waves (red circles) at each seismic sensor location are presented in Figure IV-11a. Starting from upstream, the bedload transport event begins relatively synchronously on the headwater tributaries (S19 to S24), at ~10:00 on August 3rd. The timing of the bedload waves indicates an earlier activity in sub-catchment (d) at S19 (i.e. one wave at 10:54) and S21 (i.e. two waves at 10:49 and 14:55), as compared to sub-catchment (f) (i.e. two waves at 11:44 and 15:44). The different headwater tributaries in sub-catchment (e) show a substantial variability in the timing of the bedload transporting event, with the two waves occurring earlier at S24 (i.e. 11:15 and 15:34), then at S22 (i.e. 11:32, 16:21), and finally at S23 (i.e. 12:24 and 16:39). The tracking of the bedload transport event downstream from headwater tributaries is made more complex by the multiple tributaries transporting different amounts of sediment at different times, over river reaches of different lengths and with different transport efficiency. A general lag in downstream direction (decreasing from S24) in the timing of the bedload starting point, and in the timing of the two major bedload waves, is observable in Figure IV-11a, notably in the upper part of the watershed (sensors S24 to S7).

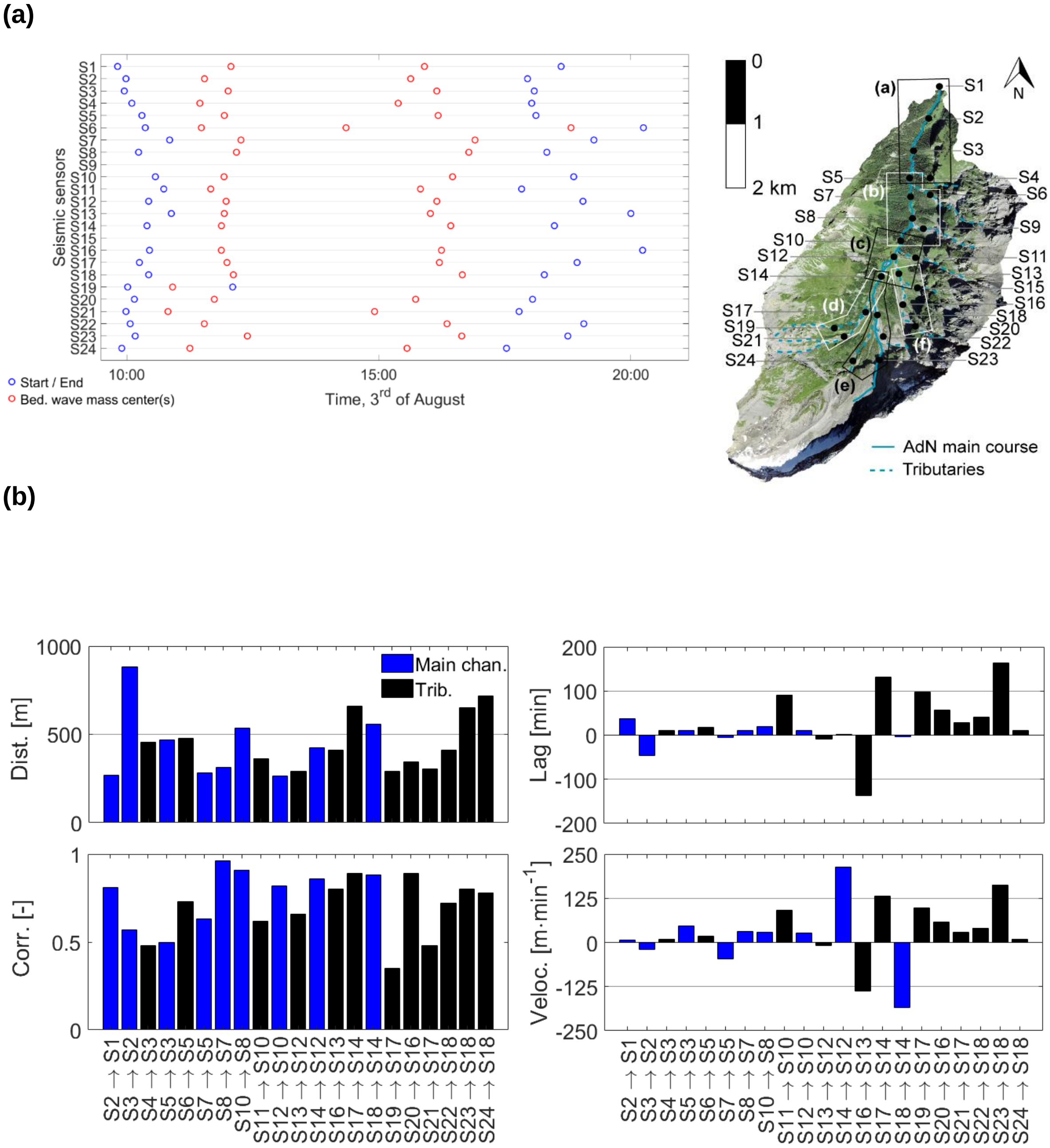

Figure IV-11. In (a), start and end of the bedload transporting event (blue circles) and timing the major bedload transport waves (red circles) measured at the 24 seismic sensor locations, from upstream (S24) to downstream (S1). In (b), inter-sensor distance [m] (top left), estimated lag [min] between time-series of bedload transport measured at two spatially-consecutive seismic sensors (top right), and associated correlation r-values [r] (bottom left), as well as estimated bedload transport velocity [m·min^{-1}] between sensor pairs (bottom right). Acknowledgments ©Swisstopo.

Figure IV-11b presents the inter-sensor distance [m] (up left), the lag between two consecutive bedload transport time-series [min] (up right), the maximum r-values [-] corresponding to that lag (bottom left), and the associated propagation velocity [m·min^{-1}] (bottom right). The data in Figure IV-11b are available in Supporting Information IV-S5. Cross-correlation analysis shows a rapid propagation of the bedload transport event through sub-catchment (d), with velocities of 97 m·min^{-1} between S19 and S17 (r = 0.35) and of 28 m·min^{-1} between S21 and S17 (r = 0.48). The bedload transporting event also propagates rapidly through sub-catchment (f), with a velocity of 57 m·min^{-1} between S20 and S16 (r = 0.89). In sub-catchment (e), smaller propagation velocities (10 m·min^{-1}) were estimated from S24 to S18 (r = 0.78), and higher ones (41 m·min^{-1}) between S22 to S18 (r = 0.72). The bedload transport event occurs almost synchronously at S18 (two waves at 12:07 and 16:39) and at S23 (i.e. two waves at 12:24 and 16:39; Figure IV-11a), whilst they are located 651 m away. Either S18 is first supplied by S24 and S22 which showed an earlier activity, or local hydrological and sediment availability conditions generate a mobilization that may be, at least partly, independent from the upstream event propagation.

The bedload transporting event propagates very rapidly between S17 and S14 (132 m·min^{-1}, r = 0.89), which also raises the question whether a spatially-continuous propagation of the event from upstream is reasonable. A later activity at S18 as compared to S17 and S14 (i.e. two waves at 11:43 and 16:26) suggests that S14 at the downstream end of sub-catchment (d) is first supplied by S17, and later by S18, which explains the negative velocity measured between S14 and S18. In the downstream part of sub-catchment (e), the bedload transport event occurs almost simultaneously at both S16 and S13, while they are located 411 m away. The same observation is to be made for sensor pairs S12 and S14, where a short 2-min lag has been measured between sensors spaced 426 meters away, which may also explain the negative velocity measured between S12 and S13. A 10-minute lag is measured between S10 and S12 spaced 263 m away, which gives a velocity of 26 m·min^{-1} (r = 0.82). S10 is also fed by a tributary input from S11, which shows a high velocity 91 m·min^{-1} (r = 0.62). Earlier activity at S11 suggests that S10 may be first supplied by the tributary, and shortly after by S12 in the main channel (Figure IV-11a).

The propagation of the bedload transport event downstream from S10, to S8 and S7, shows a clear consistency, with velocities of 28 m·min^{-1} (r = 0.91) and 31 m·min^{-1} (r = 0.96), respectively. A negative velocity is then measured between S5 and S7, and is likely related to an earlier activity in tributary S6 (i.e. waves at 11:29 and 14:21), which supplies material to S5 (18 m·min^{-1}, r = 0.73) before the bedload transport from the main channel at S7 (i.e. waves at 12:16 and 16:54) makes it to S5 (i.e. waves at 11:56 and 16:11). A similar early supply from tributary S4 (i.e. waves 11:27 and 15:23) to S3 (10 m·min^{-1}, r = 0.5) in the main channel (i.e. waves at 12:01 and 16:09) suggests that S3 is first supplied by the tributary input from S4, and later on by material from the main channel at S5. Sensor S2 shows an earlier activity (i.e. waves at 11:32 and 15:38) than sensors located upstream from it, which result in a negative propagation velocity, and also questions the likelihood of a spatially-continuous downstream propagation. Downstream propagation from S2 to S1 (i.e. waves 12:04 and 15:54) results in a velocity of 7 m·min^{-1} (r = 0.81).

IV-3.5 Longer-term morphological change analysis

Morphological change during the period 2016-2020 (Figure IV-12) shows a clear melt and subsidence of the glacier area in the upper watershed (i.e. not accounted in volume change estimates to only focus on sediment erosion and deposition). Substantial erosion is visible in a number of steep gullies feeding the tributaries, notably upstream of S4, S6, S9, S11, S15, S21 and S22. Patches of erosion with substantial depths (i.e. meters) are visible high up in the rockwalls, notably on the eastern face of the Vallon de Nant Alpine watershed. In this tributary-dominated area (zone ‘i' in Figure IV-12 and Table IV-1), 5.435×10^5 [m^3] of material were eroded during the period 2016-2020, which represents 96 % of the total volumetric erosion measured across the whole watershed over the same period. Substantial deposition also took place in this area (0.484×10^5 [m^3]), which represents 55 % of the total volumetric deposition measured across the watershed over the period 2016-2020. Thus, erosion remains largely dominant (92%) with respect to deposition, and 4.951×10^5 [m^3] of material are exported, confirming the likely primary sources of coarse material during bedload transport events such as the one monitored on August 3rd, 2020.

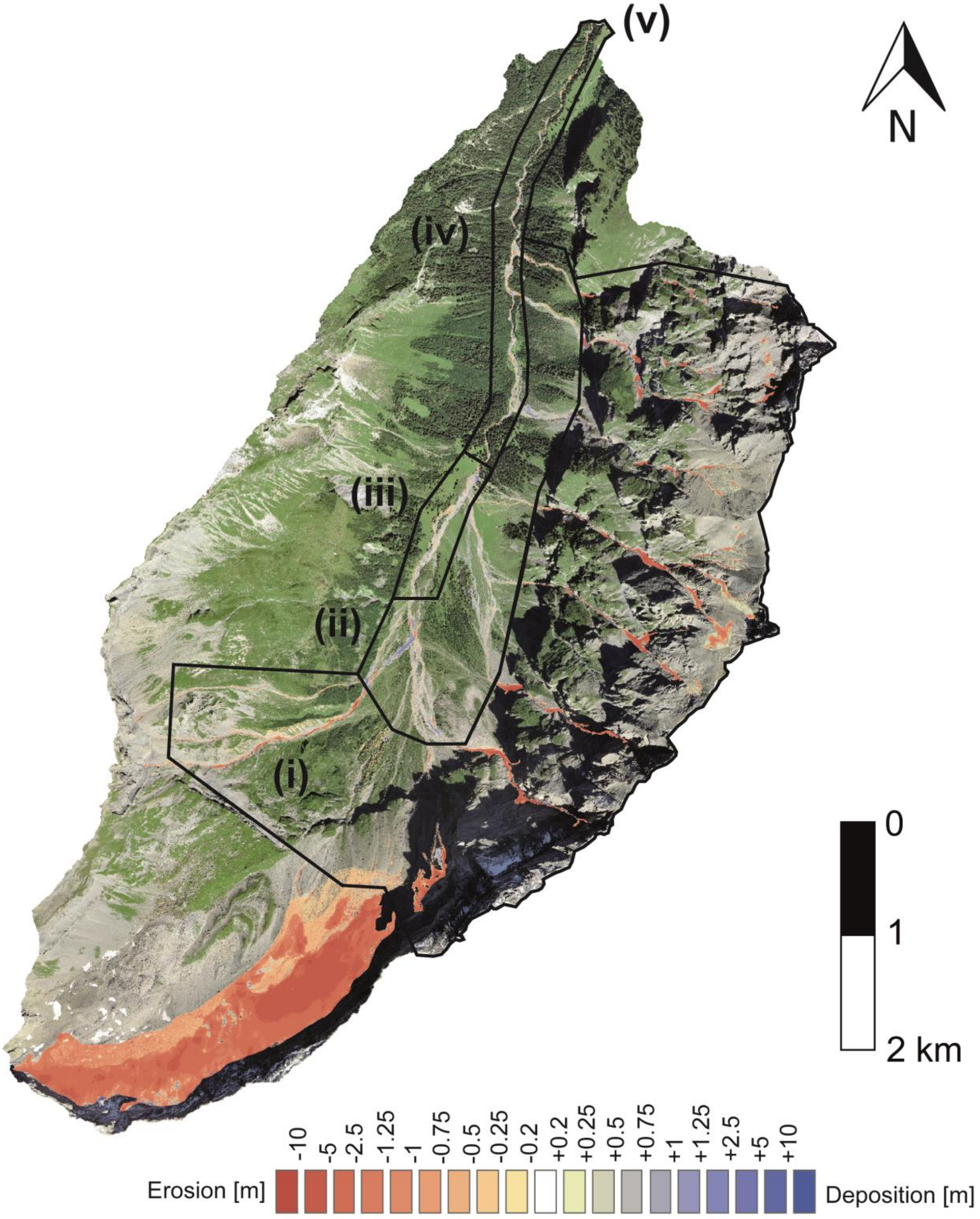

Figure IV-12. Morphological change (erosion and deposition) measured through DEM differencing between two 0.5-m LIDAR-based SwissAlti3d models of 2016 and 2020, over an orthophoto 2020. Acknowledgments ©Swisstopo.

Over the diffusive alluvial fan surfaces at the gully ends (zone ‘ii’ in Figure IV-12 and Table IV-1), morphological change tends to be dominated by deposition (69 % of total volume change). Patches of deposition with substantial depths (i.e. meters) notably occurred downstream of S17, downstream of S22, and to a lower extent downstream of S16. Another zone of deposition is visible on the alluvial fan downsteam of S11, at the confluence with the AdN main channel close to S10. Other depositional zones in similar settings (i.e. over the surface of alluvial fans, or at their feet close to the confluence with the AdN main channel) are visible downstream of S9, S6 and S4. About 35 % of the deposition measured over the whole watershed occurs in this alluvial fan dominated zone. In contrast, erosion is negligible (2.5 % of the erosion measured over the whole watershed), and a net deposition of 0.172 × 10^5 m^3 is measured in this zone over the period 2016-2020.

Along the braided channel section (zone ‘iii’ in Figure IV-12 and Table IV-1), deposition is also dominant with respect to erosion (62 %), notably around S14, S12 and S10; and 5.5 % of the deposition measured across the whole watershed takes place in this zone. Erosion is again negligible (0.5 % of the erosion measured over the whole watershed), and a net deposition of 0.02 × 10^5 [m^3] is measured in it over the period 2016-2020. Many areas of the braided channel zone ‘iii’ also present changeless surfaces. Along the semi-alluvial section (zone ‘iv’ in Figure IV-12 and Table IV-1), morphological changes tend to alternate between shallow patches of both erosion and deposition, with many areas also presenting changeless surfaces. Erosion slightly dominates the sediment budget (56%), and a net balance of -0.01 × 10^5 [m^3] is measured, but both erosion and deposition volumes measured in zone ‘iv’ represent relatively small proportions with regards to the ones measured over the whole watershed (1 % and 4.5 %, respectively). Over the whole watershed (v), erosion dominates the sediment budget (86 %), with a net export of 4.769 × 10^5 m^3.

Table IV-1. Erosion and deposition volumes measured through DEM differencing over the period 2016-2020 (numbers associated to Figure IV-12).

Zone	**Erosion** (volume, percen.)	**Deposition** (volume, percen.)	**Percen. Ero. vs Cumul. change**	**Net balance** [× 10^5 m^3]
(i) Tributaries	-5.435 [× 10^5 m^3] 96 %	+0.484 [× 10^5 m^3] 55 %	92 %	-4.951
(ii) Alluvial fans	-0.141 [× 10^5 m^3] 2.5 %	+0.313 [× 10^5 m^3] 35 %	31 %	+0.172
(iii) Braided section	-0.03 [× 10^5 m^3] 0.5 %	+0.05 [× 10^5 m^3] 5.5 %	38 %	+0.02
(iv) Semi-alluvial section	-0.05 [× 10^5 m^3] 1 %	+0.04 [× 10^5 m^3] 4.5 %	56 %	-0.01
(v) Whole watershed	-5.656 [× 10^5 m^3] 100 %	+0.887 [× 10^5 m^3] 100 %	86 %	-4.769

IV-4 Discussions

IV-4.1 Evaluation of the seismic inversion approach

The two major bedload waves sensed by the SPG monitoring system (Figure IV-4) were both detected in the seismic-inverted time-series (Figure IV-6). Over the duration of the investigated bedload transport event, the instantaneous transport rates [kg·min^{-1}] from the seismic monitoring tended to be higher, on average by a factor of 4, than the bedload transport rates measured with the SPG system for transport rates greater than 60 kg·min^{-1} (1 kg·s^{-1}). The difference was lower for the peaks of the two major bedload waves identified in Figure IV-6 (factor 2.7 of difference). This result is positive and gives confidence to the validity of the FMI since all required parameters were determine beforehand in the field, the inversion was constrained without using measured data, and time-series were not scaled.

A range of reasons can be invoked to explain the residual difference between the SPG and the seismic-inverted time-series. It may be related to poor seismic inversion performance on the one hand. First, uncertainty in seismic inversion of bedload fluxes has been shown to arise in FMI from frequency overlaps between the bedload transport signal and the turbulence signal (Gimbert et al., 2014, 2019; Dietze et al., 2019; Bakker et al., 2020; Dietze et al., 2022). The presence of a waterfall (~1 m high) at the SPG weir (Figure IV-2a) may generate turbulence that contaminates the bedload-specific frequency bands used in the FMI (Schmandt et al., 2017), and may lead to overestimation of the inverted bedload transport rates. This observation aside, we were able to identify peaks in bedload transport rates synchronous with peaks measured with the SPG system, independently from peaks in water depths (as a proxy of turbulence rate; Figure IV-6), giving confidence in the capacity of the FMI to correctly partition between turbulence and bedload transport seismic signal. Water depth is easily measurable using stage sensors (Antoniazza et al., 2022; Nicollier et al., 2022b) or pressure sensors (Dell'Agnese et al., 2015; Comiti et al., 2019). Further research should investigate how much improvement in the seismic inversion of bedload transport is achievable if exact measurements of water depths are used to drive the inversion. Seismic noise induced by rainfall drops may also overlap with bedload-specific frequency bands (Bakker et al., 2022) and contaminate the inversion of transport rates. This may be an explanation for the earlier onset of bedload transport inverted from the FMI as compared to the SPG recording, with strong seismic power recorded into high frequencies (> 45 Hz) in Figure IV-6 between 10:00 and 11:00.

Second, field estimates of the nine parameters needed to constrain FMI are also subject to uncertainty. Dietze et al. (2022) ran Monte Carlo simulations using random combinations of the nine parameters of the FMI picked within their own plausible range, and showed that inverted transport rates varied considerably (within an order of magnitude) between the different simulations. The model was shown to be particularly sensitive to grain-size parameterization (Gimbert et al., 2019; Bakker et al., 2020; Lagarde et al., 2021). In addition, the nine parameters were estimated during low flow conditions, while some of them (e.g. width, grain-size) may be changing through time, notably during flood flow conditions (Gimbert et al., 2019; Bakker et al., 2020; Dietze et al., 2022). In this case, the section was relatively channelized making grain-size the likely cause of most uncertainty, but it emphasizes the need for accurate and representative field measurement of the FMI parameters, and further research may help to constraint the best approach to constraint each of them.

Part of the difference between the SPG and the seismic recording of bedload transport may be due to errors in the SPG recording on the other hand. The fact that over the event duration the total bedload transport mass measured with the SPG system was 74 % smaller than that inverted seismically could also reflect the higher particle detection threshold (> 10-20 mm) of the SPG system (Wyss et al., 2016c; Nicollier et al., 2021; Antoniazza et al., 2022). Smaller particles (1-10 mm) also emit seismic noise and are likely detected by seismometers, although the Tsai et al. (2012) model assumes the coarsest fractions (> D_{90}) to dominate the seismic signal (Lagarde et al., 2021). The difference in particle size detection threshold may nevertheless partly explain the greater mass of bedload transport seismic-inverted. Directly-sampled data for this station (Antoniazza et al., 2022) showed that 20 – 36 % of the sample mass was on average composed of particles that were smaller than the threshold of detection of the SPG system. This interpretation may be further supported by the earlier onset of bedload transport detected by seismic inversion (Figure IV-6; 10:00-11:00), if the onset of transport is size selective and small particles start moving first (Powell et al., 2001; Vericat et al., 2008). It is also possible that at very high transport rates the plates in the SPG are over-passed by some particle sizes (Rickenmann et al., 2012, 2014b), or the signal is saturated by simultaneous particle impacts (Coviello et al., 2022), which may also under-estimate the transport rate.

That said, the difference is comparatively lower than that reported by Lagarde et al. (2021), and similar to that reported by Bakker et al. (2020), where seismic inversions of bedload transport were also compared with an independent measurement of bedload transport. Lagarde et al. (2021) compared their record with a Reid-type slot-sampler, using a similar seismic inversion approach to that applied here. They found differences in transport rate patterns as well as magnitudes with an average difference factor of 100 between instantaneous measures using the two methods. Their results likely reflected the grain-size limit of the slot-sampler (0.11 m), which may have inhibited the collection of the coarsest particles in transport (Lagarde et al. (2021), while the latter (> D_{90}) are again assumed to be responsible for the largest proportion of the seismic signal recorded (Tsai et al., 2012). Bakker et al. (2020) used an Elwha pressure-difference sampler as their benchmark data, and followed a similar seismic inversion approach to the one applied in this study. They reported a difference between the two monitoring systems within a factor of five, although the benchmark data were discrete in time, and not continuous as they are in this study. The good fit between the seismic-inverted bedload flux and the independent SPG monitoring (Figure IV-6), in both relative and absolute terms, provides confidence in the seismic inversion approach followed in this contribution. In addition, the relative coherence in the inverted bedload transport time-series between spatially-consecutive seismic sensors and within individual tributaries (Figure IV-7, IV-8 and IV-9) gives further support with respect to the seismic inversion approach and in the derived bedload transport time-series. We emphasize that while uncertainties remain, the fact that we can readily generate bedload transport estimates across a watershed within an event illustrates the potential for seismic monitoring to unpack the anatomy of a bedload transport event.

IV-4.2 Bedload transport event anatomy

The spatially-distributed absolute time-series of bedload transport (Figure IV-7, Figure IV-8, Figure IV-9) allow a number of observations with respect to the anatomy of a high-magnitude bedload transport event in a steep Alpine watershed.

IV-4.2.1 Coarse material production in headwater tributaries

The observed bedload transport time-series showed that during such an event, it is not necessary to have hillslope-wide mobilization of material sources. Some torrents dominated supply material during the studied event (i.e. S4, S6, S11, S20, S21 and S22, notably), and others had very low transport rates (i.e. S9, S15 and S19). The most active torrents were not spatially contiguous even over what is a relatively small spatial area (maximum distance between any two tributary sensors is 2.5 km). Local tributary characteristics in terms of sediment availability may explain these differences, as well as local rainfall patterns (Michelon et al., 2021). Transported bedload in the headwater tributaries being a factor 2-3 greater than in the AdN main channel suggests that some of it was transported as debris floods or debris flows (Rickenmann and Koschni, 2010). This assertion can be tested by a simple calculation of the ratio between the mean bedload volume V_s [m^3] and the mean runoff volume V_w [m^3] in the main channel (MC) and torrential tributaries (TT), respectively. From Figure IV-4, we can estimate a mean water level of 0.19 m at the outlet monitoring station, which translates into a mean streamflow of 1.34 [m^3·s^{-1}] (Ceperley et al., 2018). Integrated over the duration of the event (11 hours), it means $V_w = 5.3 \times 10^4$ m^3. Scaling the outlet (13.4 km^2) runoff volume by the mean contributing area of main channel (9.82 km^2) and tributaries where bedload transport occurred (0.66 km^2), $V_{w\_MC} = 3.9 \times 10^4$ m^3 and $V_{w\_TT} = 0.26 \times 10^4$ m^3. The mean bedload volume is $V_{s\_MC} = 181$ m^3 in the main channel, and $V_{s\_TT} = 462$ m^3 in the tributaries. This translates into a ratio of bedload volume V_s over runoff volume V_w of 0.005 in the main channel, and of 0.18 in the tributaries. The difference is greater than an order of magnitude, and is in line with the partitioning between fluvial bedload transport and debris flow transport observed by Rickenmann and Koschni (2010). It confirms that coarse material in the tributaries was – at least partly – transported as debris floods or debris flows during the studied event, while fluvial bedload transport was dominant in the main channel.

IV-4.2.2 Attenuation in the transported bedload through the watershed

The dataset shows how the basin itself rapidly attenuates (i.e. deposition occurs) the signal of hillslope erosion (Jerolmack and Paola, 2010; Ganti et al., 2014), in this case primarily due to the presence of diffusive and therefore hydraulically less-efficient alluvial fans (e.g. downstream from S11) and braided sections (e.g. downstream of S16 and S17). Even large tributary inputs that would reach the main AdN channel are rapidly deposited to some extent (e.g. S6 tributary inputs to the main channel at S5 were largely attenuated by S3). These observations emphasize that attenuation of bedload transport is substantial for the studied high-magnitude bedload transport event, and that only a comparatively smaller proportion of the material mobilized in the watershed during the event is exported to the outlet (2.5 %). This is notably a consequence of the profile of formerly-glaciated landscapes, where the 'staircase' succession of steeper (e.g. rockwalls, rockslopes, riegls) and flatter (glacier troughs) sections significantly impact hydraulic efficiency (Hooke, 1991; Cook and Swift, 2012; Dell'Agnese et al., 2015; Lane et al., 2017; Antoniazza and Lane, 2021). There are few field data against which the present results can be compared, but the latter are in line with numerical simulations of coarse material transport in Alpine rivers, where large inputs from steep headwater tributaries were also rapidly deposited when reaching the flatter hydraulically less-efficient main channel network (Ferguson et al., 2006; Rickenmann et al., 2014a).

The attenuation of the bedload transport signal from headwater tributaries towards the outlet is also visible in the negative power law relationship between contributing area and the mass of bedload transported over the duration of the event (Figure IV-10e). It confirms a declining bedload transport Sediment Delivery Ratio (SDR) with distance downstream which was as yet only quantified in natural settings for the suspended load (Brown, 1949; Wu et al., 2018). As implied above, a primary driver of this decline is the transition from tributaries to the main river (compare the points on Figure IV-10e) and a transition from debris flow to fluvial bedload transport (Rickenmann and Koschni, 2010). The rate of attenuation is the greatest throughout the braided Section 3 (down to S10), while the bedload transport magnitude presents less variability through the mixed semi-alluvial and alluvial Section 4 (Figure IV-7,

Figure IV-8, Figure IV-9). This relative constancy of the bedload transport magnitude through what is a quite long river reach (~2.8 km) is encouraging with regards to the development of 'Early Warning systems' for bedload transport events (Badoux et al., 2012; Chmiel et al., 2021).

IV-4.2.3 Propagation of the bedload transporting event

From Figure IV-11, we identified that the bedload transport event first started in sub-catchment (d) and was later fed by sub-catchment (e) and (f), with relatively more material mobilized in (f). The analysis further emphasized the importance of tributary inputs for the timing and downstream propagation of the bedload transporting event, with bedload transport supply from some tributaries (e.g. S11, S6, S4) occurring sometimes earlier than the bedload wave moving through the main AdN channel (Figure IV-11a). Analysis of inter-sensor propagation velocities (Figure IV-11b) showed a substantial variability, but tended to be greater in steep tributaries (e.g. S11 → 10, S19 → S17, S20 → S16, S22 → S18) than within flatter sections of the main channel (e.g. S2 → S1, S8 → S7, S10 → S8, S12 → S10). Nevertheless, evidence of almost simultaneous bedload transport onset over sensors located multiple hundreds of meters away (e.g. S12 → S14, S13 → S16, S14 → S17, S14 → S18) questions the extent to which the same bedload material travels through the watershed and is sensed by multiple sensors, or whether we are rather facing a water wave that travels faster and (re-)mobilizes local material.

Typical values of bedload particle step-lengths and velocities measured within Alpine watersheds during individual flooding events may give insights in this question. Vázquez-Tarrío et al. (2019) reviewed particle tracking experiments and compiled results from 217 episodes of bedload particle transport measured in 30 gravel-bed rivers, during floods of varying magnitude (dimensionless stream power from 1.5^{-2} to 1.5^{0} [-]), and along reaches with contrasting gradient (i.e. 0.1 to 15 %) and morphologies (i.e. riffle-pool, step-pool, plane-bed, multithread). Mean particle travel distance during individual floods ranged from a few meters to a few hundred meters, mostly less than 200 meters (83% of events). Our seismic sensors were spaced from 268 to 882 meters, which makes it generally unlikely that the same bulk bedload transport was sensed over consecutive sensors, although the review by Vázquez-Tarrío et al. (2019) does not contain mean particle transport distances associated to debris-flow events, which may be greater (Coviello et al., 2019; Chmiel et al., 2021; Schimmel et al., 2022).

Mao et al. (2017) derived virtual bedload particle velocities (i.e. because of the possibility of resting periods in-between detections) between 10^{-5} and 35 $m \cdot min^{-1}$ along a 13%-slope reach (plane-bed and step-pool morphology) of a glacier-fed river. Along a 4%-slope pool-riffle and step-pool river reach, Olinde and Johnson (2015) measured average particle step-lengths of 12.4 m and average transport duration of 0.5 min, which translated into an average velocity of ~24 $m \cdot min^{-1}$, but particle steps were interspersed by resting periods that could last up to 190 hours. Much higher velocities were reported for debris-flow events: between 180 and 600 $m \cdot min^{-1}$ in Schimmel et al. (2022), between 60 to 420 $m \cdot min^{-1}$ in Chmiel et al. (2021), and between 84 and 300 $m \cdot min^{-1}$ in Coviello et al. (2019). In this study, propagation velocities derived from consecutive seismic sensors ranged from 7 $m \cdot min^{-1}$ up to ~100 $m \cdot min^{-1}$, outside of the previously identified sensor pairs where bedload transport was almost simultaneous.

It is well-known that bedload transport is an intermittent process, characterized by periods particle of motion interspersed by periods of rest, both following an exponential distribution with thin-tails (i.e. the bulk bedload moving roughly homogeneously; Einstein, 1937; Ganti et al., 2010; Hassan et al., 2013; Ganti et al., 2014), although heavy-tailed super-diffusive distribution (i.e. few frontrunners being transported over larger distances than the bulk) have also been reported, typically over short durations (i.e. the flood scale; Liébault et al., 2012; Hassan et al., 2013; Phillips et al., 2013). The relatively long distance between the seismic sensors deployed in the frame of this study (268 to 882 meters), as well as the relatively high propagation velocities derived from the cross-correlation analysis (7 m·min^{-1} up to ~100 m·min^{-1}), makes it quite unlikely that the same bulk bedload transport is actually able to travel at such pace throughout the watershed.

The slower velocities derived from the cross-correlation analysis (Figure IV-11b) fall within the same range as the higher velocities found in particle tracking experiments (Olinde and Johnson, 2015; Mao et al., 2017), which means that some frontrunner particles may have been transported over longer distances (Hassan et al., 2013) and were consecutively measured by multiple seismic sensors. Yet, it is more likely that the bulk bedload transport travels more slowly, and therefore that derived velocities correspond to the propagation of a water wave, which (re-)mobilizes locally coarse material that is then transported over shorter distances. Using seismic networks, Cook et al. (2018) estimated the water wave of a GLOF to travel at velocities between 300 and 540 m·min^{-1}, and Chmiel et al. (2022) reported velocities of a flash-flood in France between 300 and 360 m·min^{-1}. The faster propagation velocities we derived from cross-correlation analysis (e.g. S12 → S14, S13 → S16, S14 → S17, S14 → S18) are not out-of-bounds with regards to the propagation velocity of other water waves reported in the literature. The fact that the tributaries have involved debris-flows may counter the argument that bedload is locally mobilized by a faster water wave. Indeed, greater velocities have been reported in the literature for this specific process (Coviello et al., 2019; Chmiel et al., 2021; Schimmel et al., 2022); and these are within the same range as those derived for the tributaries from the cross-correlation analysis (e.g. S11 → 10, S19 → S17, S20 → S16).

Previous hydrological research in the Vallon de Nant Alpine watershed has shown, through combined piezometer network, thermal imaging using an uncrewed airborne vehicle, isotope analysis and hydrological modelling (Michelon et al., 2022; Thornton et al., 2022), that substantial groundwater release takes place throughout Section 3 (Figure IV-1), where almost simultaneous bedload transport waves were measured in some instances between sensors spaced hundreds of meters away (e.g. S12 → S14, S14 → S17). Local hydrological conditions (e.g. notably associated with vertical hyporheic fluxes) may locally reduce the critical shear stress required for entrainment, and may increase sediment mobilization and transport capacity independently from the downstream propagation of the water wave, translating into simultaneous bedload transport mobilized at different locations of the watershed. The effect of groundwater release on coarse material mobilization deserves more attention in future research. Valuable knowledge of the respective propagation of water waves and bedload waves through Alpine watersheds may be gained from the deployment of distributed acoustic sensors (DAS), km-long fiber optic cables able to deliver seismic data almost continuously in space and time (Zhan, 2019; Lior et al., 2021).

IV-4.3 Longer-term perspectives on watershed-scale sedimentary fluxes

The seismic sensor network deployed in the frame of this study revealed the anatomy of a high-magnitude bedload transport event in terms of coarse material production in headwater tributaries, bedload transport attenuation throughout the watershed and event timing and propagation velocity. We now place these observations in a longer perspective of coarse material flux throughout Alpine watersheds with the help of the morphological change analysis.

During the studied event – with the 5th greatest bedload transport peak of the period 2016-2020 – the proportion of coarse material exported at the outlet was negligible (2.5%) compared to that mobilized throughout the watershed, and notably in headwater tributaries, which means that substantial deposition took place within the main channel network. Supply exceeded capacity and the event was deposition-dominated (Turowski et al., 2013a). If such events were the rule, it would mean the main channel network would be aggrading on the longer term. This assertion can be confronted to a set of summary statements made from the morphological change analysis. First, 88 % of the material volume mobilized in the headwater tributaries are exported at the outlet over the period 2016-2020, which is substantially more than the proportion measured during the 3rd of August flood (2.5 %). This means that we do not observe on longer term the general aggradation of the channel network we would see if the substantial deposition measured during the 3rd of August event was the rule in terms of bedload transport event dynamics. Instead, material mobilized in headwater tributaries and deposited within the main channel network during high-magnitude events such as the one that occurs on August 3rd 2020 is likely then progressively evacuated by subsequent competent flows. Those empirical data are in line with the 'graded channel theory' of Mackin (1948) and (Lane, 1955), where streams adjust on the longer term their gradient by producing erosion and deposition to evacuate material supplied from upstream. As reported as a characteristic of hillslope to river sediment transport coupling (Newson, 1980), lower competent flows than that reported here for the 3rd August 2020 may be more geomorphically effective because of the sediment delivered, but not evacuated during the August 2020 event.

Second, results of the morphological change analysis show that a greater proportion of material exported from headwater tributaries is stored within alluvial fans (6 %) over the period 2016-2020, than within the braided section (1 %) and the semi-alluvial section (1 %). During the 3rd of August 2020 event, a considerable attenuation in transported bedload was also observed within the braided river reach (Figure IV-8, Figure IV-9). This means that in the longer term, material deposited within alluvial braided channel or semi-alluvial reaches during high-magnitude events may be more easily reworked and exported during subsequent competent flows (Mackin, 1948; Lane, 1955) than the one deposited over the diffusive surface of alluvial fans.

Third, the fact that 96 % of the erosion takes place in the headwater tributary zone, and that little erosion proportionally occurs in the other morphological units (e.g. alluvial fans, braided channels, semi-alluvial channels) tends to confirm the view of Piton and Recking (2017) on the importance of 'travelling bedload'. Bedload produced in distal headwater tributary sources seems to be transported in the main channel network without inducing in proportion major (re)mobilization, in particular along alluvial fans and semi-alluvial reaches. The latter play a role of storage or conveyor, rather than a sedimentary source. This trend was clear in the semi-alluvial section during the 3rd of August event, where the bedload transport magnitude was held relatively constant through a substantial length of channel (~2.8 km; Figure IV-8, Figure IV-9). This behaviour can be related to the concept of 'washload' developed for the suspended load, consisting of particles found in the water column with sizes finer than the ones composing the bed (Vanoni, 2006; Turowski et al., 2010; Piton and Recking, 2017), mobilized in distal sources and conveyed through a main channel network that experiences little erosion or deposition.

High-magnitude events in the tributaries such as the one that occurred on August, 3rd 2020 may thus likely play an important role with regards to longer term coarse material fluxes by providing material into the main channel network from areas of the watershed where large sedimentary sources are available (e.g. steep slopes at the top of rockwalls, tributary gullies, the glacier area), but which may not always be well connected during low to intermediate flows (Cavalli et al., 2013; Lane et al., 2017; Comiti et al., 2019; Buter et al., 2022). By supplying material into the main channel network, high-magnitude events in the tributaries may therefore supply new material which will on the longer term be remobilized during subsequent low, intermediate and high magnitude events in the main channel network (Cavalli et al., 2013; Turowski et al., 2013a; Lane et al., 2017), balancing the sediment budget towards the ‘grade’ on the longer term (Mackin, 1948; Lane, 1955).

The morphological change analysis shows a net sediment export of 4.679×10^5 m^3 over the period 2016-2020. By computing bedload export from the SPG measurement over the exact same period (August 25th 2016 to August 6th 2020), 0.025×10^5 m^3 are derived, that is about 0.5%. This would mean that 99.5% of the total volumetric sediment exported from the Vallon de Nant Alpine watershed is composed of material not detected by the SPG system. A large proportion of it is likely transported through suspension, which can represent > 90% of Alpine watershed sedimentary budget (Turowski et al., 2010; Hinderer et al., 2013). Some fraction of it may also be due to bedload particles missed by the SPG system, typically if they are smaller than the size detection threshold of 10-20 mm (Nicollier et al., 2022a, 2022b), if saturation occurs at high bedload transport rates (Coviello et al., 2022), or if particle hops are greater than the SPG streamwise length when turbulence rate is higher (Schneider et al., 2014). But errors in the volumetric erosion and deposition may also arise from residual error in the DEMs used in the morphological change analysis (Lindsay and Ashmore, 2002; Bater and Coops, 2009; Wheaton et al., 2010).

IV-5 Conclusion

The way Alpine watersheds mobilize, convey and store coarse material is poorly constrained, which limits the accuracy of current bedload transport predictions. Environmental seismology applied to Alpine rivers, and combined with appropriate seismic physical models, provides absolute time-series of bedload transport, with an average factor 4 of difference in this study when compared to an independent calibrated time-series of bedload transport. The application of the FMI to streams where saltation is not the only transport mode (Tsai et al., 2012; Gimbert et al., 2019), and where model parameters (e.g. grain-size, channel width, ground seismic properties) are not stationary through time, may be subject to substantial uncertainties, especially if direct concurrent bedload measures (of the transported mass and/or of the mobilized grain-size) are not undertaken. Outside of these cases, distributed seismic networks have the potential for tracking the motion of coarse material through Alpine watersheds and may help to constraint better and to improve prediction of bedload transport fluxes in the future.

The 24 seismic sensors deployed during this study, and the spatially-distributed time-series of bedload transport derived from them, have shown the relative inefficiency of the Vallon de Nant Alpine watershed in evacuating coarse material, even during what is a relatively infrequent high-magnitude bedload transport event. Large inputs measured in some of the tributaries, likely transported at least partly as debris-floods or debris flows, were indeed rapidly attenuated as the flow was crossing less hydraulically-efficient reaches, and only a comparatively negligible proportion of the total amount of material mobilized in the headwater tributaries is actually exported at the outlet. Not every tributary transported bedload during the studied event, even at this small spatial scale, which underlines the importance of local sediment availability. Cross-correlation analysis of the time-series suggested that a faster water wave was (re-)mobilizing local material, and coarse sediment was expected to move slower, and over shorter distances. Multiple periods of competent flows are necessary to evacuate the coarse material mobilized throughout the watershed during the studied event. High-magnitude bedload transport events in the tributaries nevertheless appeared to be important to supply new material in the main channel network from poorly-connected sourcing areas of the watershed, which are on the longer term progressively evacuated from it by subsequent competent flows

IV-S Supporting Information

IV-S1 Seismic sensor location and river morphology parameters

Table IV-S.1. Seismic station coordinates (in CH1903+ Swiss coordinate system) and river morphology parameters. W [m] is the channel width, r_0 [m] is the sensor-to-river distance and θ [radians] is the channel average gradient.

Sensor ID	X [m]	Y [m]	Z [m a.s.l.]	W [m]	r_0 [m]	θ [radians]
S1	2’574’634.45	1’122’486.97	1’195.52	6	5	0.10
S2	2’574’562.88	1’122’204.91	1’239.95	5	6	0.14
S3	2’574’221.68	1’121’474.76	1’308.92	5	7	0.10
S4	2’574’358.68	1’121’130.53	1’396.03	8	10	0.32
S5	2’574’183.40	1’121’041.48	1’357.25	8	13	0.12
S6	2’574’534.44	1’120’779.26	1’499.50	7	16	0.33
S7	2’574’208.85	1’120’786.14	1’386.63	5	8	0.09
S8	2’574’224.16	1’120’488.44	1’415.50	4	7	0.14
S9	2’574’392.68	1’120’296.45	1’516.13	6	12	0.36
S10	2’574’032.51	1’120’063.88	1’466.63	5	5	0.08
S11	2’574’274.62	1’119’871.97	1’550.79	8	12	0.31
S12	2’573’933.32	1’119’828.17	1’482.72	7	30	0.06
S13	2’574’058.52	1’119’553.27	1’519.41	4	20	0.15
S14	2’573’723.20	1’119’501.53	1’514.27	6	19	0.10
S15	2’574’260.44	1’119’406.99	1’593.43	7	18	0.38
S16	2’574’056.94	1’119’173.46	1’589.80	7	9	0.22
S17	2’573’469.90	1’118’959.20	1’565.62	4	25	0.17
S18	2’573’707.51	1’118’994.74	1’580.77	5	15	0.14
S19	2’573’168.35	1’118’843.45	1770.45	4	10	0.41
S20	2’574’118.72	1’118’844.82	1’689.67	8	26	0.31
S21	2’573’263.68	1’118’679.25	1’707.30	6	11	0.31
S22	2’573’771.07	1’118’623.49	1’665.49	7	25	0.24
S23	2’573’679.65	1’118’370.85	1’757.85	5	25	0.41
S24	2’573’411.55	1’118’360.45	1’808.75	8	28	0.48

IV-S2 Grain-size distribution parameters

Table IV-S.2. Parameters D_{50} and σ_g of the best-fit log-raised cosine function at each of the 24 seismic sensor location.

Sensor ID	$\boldsymbol{D_{50}}$ **[m]**	$\boldsymbol{\sigma_g}$ **[-]**
S1	0.06	0.9
S2	0.06	1
S3	0.06	0.8
S4	0.06	0.4
S5	0.06	0.5
S6	0.06	0.4
S7	0.06	1
S8	0.06	1
S9	0.06	0.9
S10	0.05	0.9
S11	0.06	0.7
S12	0.06	0.5
S13	0.05	0.7
S14	0.06	0.8
S15	0.05	0.7
S16	0.06	0.5
S17	0.05	0.8
S18	0.06	0.9
S19	0.06	0.4
S20	0.06	0.5
S21	0.05	0.5
S22	0.06	0.5
S23	0.06	0.9
S24	0.06	0.5

Line-by-number counts (Wolman, 1954) of b-axis mobile particles of the bed (n = 100) were performed at each of the 24 seismic sensor locations. Particles were partitioned into 10 classes (0.0001 – 0.008 m, 0.008 - 0.038 m, 0.038 – 0.08 m, 0.08 – 0.13 m, 0.13 – 0.192 m, 0.192 – 0.28 m, 0.28 – 0.4 m, 0.4 – 0.55 m, 0.55 – 0.7 m), and a best-fit raised-log cosine function was fitted to each empirical sample (best of 10^4 trials), following Tsai et al. (2012). Results of the best-fit at each seismic sensor location is presented in Figure IV-S.1, and the associated parameters D_{50} [m] and σ_g used for the seismic inversion are provided in Table IV-S.2.

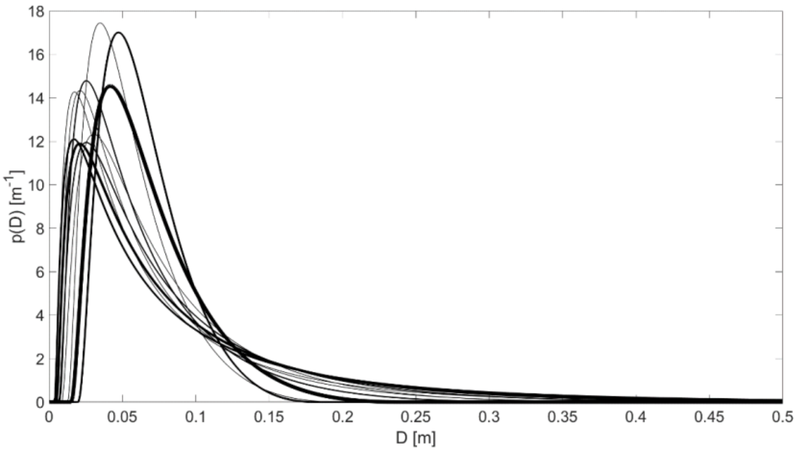

Figure IV-S.1. Best-fit log-raised cosine distribution of 24 samples (n=100) of mobile particle of the bed at each seismic sensor location. The thicker the line, the greater the number of seismic sensor locations that share the same D_{50} and σ_g values (i.e. Table IV-S.2), from a single seismic sensor location sharing the same parameter values (i.e. thin line), up to six seismic sensor locations sharing the same parameter values (i.e. thick line). Note that seismic sensor locations presenting the same D_{50} and σ_g values were estimated based on site-specific and different line-by-number counts.

IV-S3 Ground seismic parameters

Table IV-S.3. Ground seismic parameters estimated at the different seismic station locations based on active seismic surveys. v_{p0} is the phase velocity of the Raleigh wave at a frequency f_0 = 1 Hz and ξ [-] a dimensionless exponent used to scale a frequency-dependent decay in seismic signal (equations [IV-1a] and [IV-1b] in the main manuscript). K_0 is a dimensionless quality factor at a frequency f_0 = 1 Hz and η [-] a dimensionless exponent that expresses the change in the quality factor K with frequency (equation [IV-1c] in the main manuscript). Note that a single active seismic experiment encompassing multiple sensors has been performed for the group S10/S12, S16/S20 and S22/23/24 thanks to their geographical proximity.

Sensor ID	v_{p0} [m·s^{-1}]	ξ [-]	K_0 [-]	η [-]
S1	482	0.25	17	0.14
S2	131	0.27	10	0.01
S3	447	0.21	11	0.15
S4	368	0.34	8	0.31
S5	430	0.18	30	0.07
S6	452	0.08	6	0.53
S7	397	0.27	15	0.17
S8	370	0.30	15	0.17
S9	400	0.15	14	0.18
S10	400	0.30	11	0.15
S11	660	0.30	14	0.14
S12	400	0.30	11	0.15
S13	447	0.21	11	0.15
S14	300	0.35	10	0.18
S15	576	0.19	9	0.38
S16	389	0.12	10	0.21
S17	420	0.26	10	0.15
S18	405	0.28	16	0.24
S19	359	0.27	5	0.49
S20	389	0.12	10	0.21
S21	359	0.27	5	0.49
S22	350	0.42	11	0.30
S23	350	0.42	11	0.30
S24	350	0.42	11	0.30

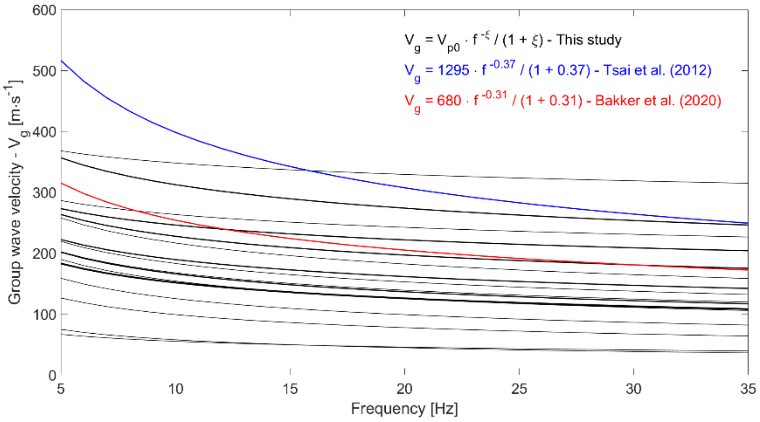

Figure IV-S.2. Best-fit regression of decay in wave group velocity with frequency (equations [IV-1a] and [IV-1b] in the main manuscript) based on active seismic experiments for each of the 24 seismic sensor locations. Each line is fitted through the average value of 20 repeated sledgehammer impacts (see also Figure IV-5b in the main manuscript). The thicker the line, the greater the number of seismic sensor locations that share the same v_{p0} and ξ values (i.e. Table IV-S.3), from a single seismic sensor location sharing the same parameter values (i.e. thinner line), up to three seismic sensor locations sharing the same parameter values (i.e. thicker line). Note that seismic sensor locations presenting the same v_{p0} and ξ values were estimated based on a single active seismic experiment encompassing multiple sensors thanks to their geographical proximity. The parameters found by Bakker et al. (2020) for an alluvial channel (in red), and proposed by Tsai et al. (2012) for a generic bedrock site (in blue) are presented for comparative purpose.

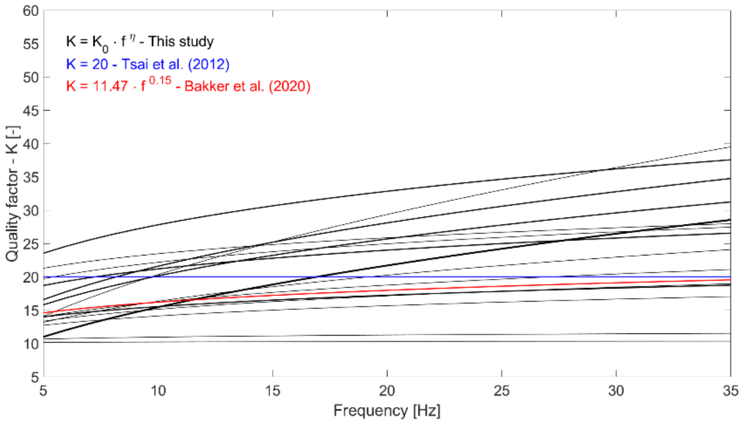

Figure IV-S.3. Best-fit regression of decay in seismic power with distance, and its frequency-depedency (equations [IV-1a] and [IV-1b] in the main manuscript) based on active seismic surveys for each of the 24 seismic sensor locations. Each line is fitted through the average of 20 repeated sledgehammer impacts, (see also Figure 5d in the main manuscript). The thicker the line, the greater the number of seismic sensor locations that share the same K_0 and η values (i.e. Table IV-S.3), from a single seismic sensor location sharing the same parameter values (i.e. thinner line), up to three seismic sensor locations sharing the same parameter values (i.e. thicker line). Note that seismic sensor locations presenting the same K_0 and η values were estimated based on a single active seismic experiment encompassing the location of the different sensors. The parameters found by Bakker et al. (2020) for an alluvial channel (in red), and proposed by Tsai et al. (2012) for a generic bedrock site (in blue) are presented for comparative purpose.

IV-S4 Stream characteristics at each of the 24 seismic sensor locations

Table IV-S.4. Channel type (MC = main channel, TT = torrential tributary), channel gradient, contributing area, the bedload transported mass and the bedload transported mass per unit area at each of the 24 seismic sensor locations.

Sensor ID	Type	Channel gradient [%]	Contributing area [km^2]	Percentage contr. area [%]	Bedload transp. mass [kg]	Bedload transp. mass per unit area [kg/km^2]
S1	MC	10	13.4	100	$0.28 \cdot 10^6$	$0.02 \cdot 10^6$
S2	MC	14	13.3	99	$0.11 \cdot 10^6$	$0.008 \cdot 10^6$
S3	MC	10	13.0	97	$0.07 \cdot 10^6$	$0.005 \cdot 10^6$
S4	TT	33	0.41	3	$0.28 \cdot 10^6$	$0.26 \cdot 10^6$
S5	MC	12	11.6	87	$2.22 \cdot 10^6$	$0.19 \cdot 10^6$
S6	TT	34	0.65	5	$0.74 \cdot 10^6$	$1.14 \cdot 10^6$
S7	MC	9	10.7	80	$0.39 \cdot 10^6$	$0.04 \cdot 10^6$
S8	MC	14	10.2	76	$0.09 \cdot 10^6$	$0.009 \cdot 10^6$
S9	TT	38	0.42	3	0	0
S10	MC	8	9.0	67	$0.23 \cdot 10^6$	$0.03 \cdot 10^6$
S11	TT	32	0.6	4	$1.10 \cdot 10^6$	$1.83 \cdot 10^6$
S12	MC	6	7.8	58	$0.90 \cdot 10^6$	$0.12 \cdot 10^6$
S13	TT	15	1.1	8	$0.64 \cdot 10^6$	$0.58 \cdot 10^6$
S14	MC	10	6.3	47	$0.40 \cdot 10^6$	$0.06 \cdot 10^6$
S15	TT	40	0.42	3	0	0
S16	TT	22	0.33	2	$4.59 \cdot 10^6$	$13.92 \cdot 10^6$
S17	TT	17	0.92	7	$3.61 \cdot 10^6$	$3.92 \cdot 10^6$
S18	MC	14	2.9	22	$0.11 \cdot 10^6$	$0.04 \cdot 10^6$
S19	TT	43	0.07	0.5	$0.008 \cdot 10^6$	$0.12 \cdot 10^6$
S20	TT	32	0.29	2	$0.67 \cdot 10^6$	$2.33 \cdot 10^6$
S21	TT	32	0.57	4	$1.27 \cdot 10^6$	$2.23 \cdot 10^6$
S22	TT	24	0.39	3	$0.43 \cdot 10^6$	$1.10 \cdot 10^6$
S23	TT	43	0.43	3	$0.24 \cdot 10^6$	$0.55 \cdot 10^6$
S24	TT	52	1.6	12	$0.07 \cdot 10^6$	$0.04 \cdot 10^6$

IV-S5 Propagation velocities

Table IV-S.5. Lag [min] maximizing the cross-correlation r [-], inter-sensor distance [m] and associated propagation velocity [m·min^{-1}].

S_x → S_y	Lag [min]	r [-]	Dist [m]	Velocity [m·min^{-1}]
S2 → S1	38	0.81	268	7
S3→ S2	-46	0.57	882	-19
S4 → S3	47	0.48	457	10
S5 → S3	10	0.5	469	47
S6 → S5	26	0.73	476	18
S7 → S5	-6	0.63	283	-47
S8 → S7	10	0.96	314	31
S10 → S8	19	0.91	534	28
S11 → S10	4	0.62	364	91
S12 → S10	10	0.82	263	26
S13 → S12	-32	0.66	291	-9
S14 → S12	2	0.86	426	213
S16 → S13	-3	0.8	411	-137
S17 → S14	5	0.89	658	132
S18 → S14	-3	0.88	556	-185
S19 → S17	3	0.35	290	97
S20 → S16	6	0.89	343	57
S21 → S17	11	0.48	303	28
S22 → S18	10	0.72	409	41
S23 → S18	4	0.8	651	163
S24 → S18	73	0.78	716	10

V – Synthesis and perspectives

This Chapter synthesizes from the results of the three main contributions of this thesis, brings in additional information from the complementary contributions introduced in Chapter I and in which I was a co-author (indicated with a *), and from other recent relevant literature, to evaluate the status of bedload transport science and to draw perspectives on future research needs. It focuses on the two main axes treated in this thesis: the development of acoustic and seismic monitoring of bedload transport in steep Alpine streams (V.1), and their application to gain new understanding of coarse material fluxes throughout steep Alpine watersheds (V.2). The Chapter finishes with specific conclusions on the thesis perspectives (V.3).

V-1 Developments in the monitoring of bedload transport in steep Alpine streams

This section begins by considering developments and limits in the acoustic Swiss Plate Geophone (SPG) system to continuously monitor bedload transport in steep Alpine streams, and in particular at the recent efforts to obtain transferable calibration coefficients across SPG sites (V-1.1). It then discusses developments in seismic sensing of bedload transport in steep Alpine streams, notably based through the comparison with a calibrated SPG time-series (V-1.2). It finally looks at wider implications for the monitoring of bedload transport in steep Alpine streams, in particular its spatial dimension (V-1.3).

V-1.1 The Swiss Plate Geophone system (SPG)

Multiple studies have reported successful site-specific calibration of the SPG system using concurrent bedload transport samples (Rickenmann et al., 2012; Kreisler et al., 2017; Habersack et al., 2017; Halfi et al., 2020). The reported calibrations had levels of explanation (R^2) ranging between 0.85 and 0.99 (Rickenmann, 2017). The calibration campaign conducted at the Vallon de Nant SPG site and reported in Chapter III of this thesis showed a comparable performance, with $R^2 = 0.85$. Yet, the collection of bedload transport samples to calibrate the SPG system requires considerable field effort, which would be reduced if calibration coefficients were transferable across SPG sites.

Comparison of SPG calibration performance revealed about a factor 20 of difference in impulse-to-mass relationship of individual bedload samples from different sites, and about a factor 6 of difference between mean calibration values of different SPG sites (Rickenmann et al., 2012, 2014b; Habersack et al., 2017; Rickenmann and Fritschi, 2017; Kreisler et al., 2017). Previous research identified flow velocity (Wyss et al., 2016a, 2016b), grain-size distribution (Wyss et al., 2016c; Nicollier et al., 2021) and particle transport mode (i.e. rolling, sliding, saltation; Chen et al., 2021) as important factors of explaining variability in SPG calibration coefficients between sites. Although the results of the impact experiment presented in Chapter II of this thesis confirmed that the response of individual SPG units was in most cases consistent within and across sites, the propagation of energy between SPG units was identified as an additional important factor of variability in SPG calibration. Building on these findings, Nicollier et al*. (2022b) designed a filtering method that used SPG signal time-frequency information to identify and to eliminate 'apparent' impacts automatically, either induced by signal propagation between SPG units, or by off-plate impacts (e.g. on the concrete sill in which the plates are embedded). The application of this filtering method to calibration datasets from multiple SPG sites substantially improved (~30%) the general level of explanation of the transported bedload mass by the recorded impulses (with R^2 increasing from 0.8 to 0.91). It enabled the derivation of a single calibration coefficient for total bedload transport transferable across multiple SPG sites. Following this work, Nicollier et al*. (2022) developed a method to infer fractional bedload transport from SPG data, using both signal frequency and amplitude, resulting in calibration coefficients for 10 different grain-sizes that were transferable across multiple SPG sites. Thus, Nicollier et al*. (2022a, 2022b) accounted for two (propagating noise and grain-size) of the four previously mentioned factors of inter-site variability in calibration coefficients for the total bedload transport. The remaining scatter is likely attributable to inter-site differences in mean flow velocity and associated transport mode, which still represent two important factors of inter-site variability that are not yet accounted in any SPG calibration routine.

Future research needed to improve the inter-site transferability of SPG calibration coefficient should primarily focus on these specific aspects. They could be investigated in more detail by repeating the single grain-size experiments of Nicollier et al*. (2022a) but adding a high-speed camera (Chen et al., 2021) to identify the transport mode of individual particles impacting a SPG, and by monitoring continuously hydraulic conditions (i.e. flow velocity and water depth) to find further generalizable relations between transport conditions and the SPG signal response. A deeper understanding of plate vibration modes according to impact location and energy, and how they transfer to the SPG signal (Chen et al., 2022; Portogallo et al., 2022), may also be valuable. Due to the multiple factors influencing the SPG response, a machine learning approach (Chmiel et al., 2021; Rickenmann et al*., 2022) may also help to constrain the most prominent elements influencing the inter-site variability in SPG calibration coefficients.

In a recent publication, Coviello et al. (2022) noted a potential issue related to the set-up of fixed impulse thresholds as a proxy for bedload transport magnitude in the SPG signal processing, such as performed in many calibration works (Rickenmann et al., 2012; Rickenmann and Fritschi, 2017; Habersack et al., 2017; Kreisler et al., 2017). They identified a risk of the signal being saturated (Arattano et al., 2014) during periods of intense bedload transport despite high-resolution raw signal recording (5-10 kHz), and showed that fixed impulse thresholds could result in an underestimation of annual bedload transport rates as high as ~20%, and underestimation in peak bedload transport rate up to about an order of magnitude. Instead of threshold-based impulse counts, they recommend the use of time-integrated signal power as a proxy of bedload transport magnitude. Investigation of the most representative proxy for bedload transport in the raw SPG signal deserves more attention in future research. Using a finer temporal resolution for packet definition, corresponding more-closely to single particle impacts, could improve individual particle detection (Nicollier et al*., 2022a, 2022b).

The SPG system is also limited by a detection threshold for particles with diameters of 10-20 mm (Wyss et al., 2016c; Nicollier et al., 2021), with the risk of missing the finer fraction of the bedload transport. Previous research (Rickenmann et al*., 2017, 2022) has found that accelerometer-mounted acoustic sensors may be more effective than geophones to capture the finest fraction of the bedload grain-size distribution (< 10 mm). In that sense, the newly-developed square-pipe system (SPS) (Rickenmann et al*., 2022), which is mounted with two geophone sensors, one accelerometer and one microphone, allows for the accurate sensing of a potential broader spectrum of the grain-size distribution than the SPG. Its manufacture and installation being easier and cheaper, it also presents a substantial potential to equip many streams in various settings. Yet, the diversity of impact-based acoustic devices in use in terms of sensors (e.g. piezoelectric, geophone, microphone, accelerometer), structures (e.g. plate, pipe, column) and dimensions, limits to some extent the comparability of research outcomes (Rickenmann and McArdell, 2007; Mizuyama et al., 2010a; Rickenmann, 2017; Rickenmann et al*., 2022). Different acoustic devices are sensitive to both common (e.g. grain-size) and contrasting (e.g. insulation) factors, which may limit the inter-comparison of time-series acquired with different systems. The community would probably benefit from a relative homogenization of such acoustic monitoring devices leading to a smaller number of better-constrained sensing systems. Such choice should be driven by the long-term reliability of the mounted sensor, its ability to sense a broad spectrum of the bedload grain-size distribution at various transport rates, cost and ease-of-deployment of the device, and system design that minimizes the risk of missing particles (Rickenmann, 2017; Rickenmann et al.*, 2022).

The deployment of impact-based acoustic monitoring systems is also often limited to streams of small to intermediate size, due to the heavy engineering works they typically require (Mizuyama et al., 2010a; Rickenmann et al., 2012, 2017; Habersack et al., 2017; Kreisler et al., 2017; Antoniazza et al., 2022). In that sense, recent progress in the continuous monitoring of bedload transport using hydrophones (Geay et al., 2020) and ADCPs (Rennie et al., 2017) have the potential to deliver relevant complementary datasets, in particular for larger Alpine rivers. Yet, such approaches may be less effective than impact-based acoustic monitoring systems in steep Alpine streams due to low relative flow depths and high turbulence rates (Rickenmann, 2017; Rennie et al., 2017; Geay et al., 2020).

V-1.2 Environmental seismology

Previous research has demonstrated the potential of environmental seismology to derive continuous time-series of bedload transport in steep Alpine streams (Bakker et al., 2020; Lagarde et al., 2021; Dietze et al., 2022). Yet, the applied Fluvial Inversion Model (FMI) (Dietze et al., 2019) is based on a set of assumptions (e.g. particle vertical impacts on the bed, no sliding nor rolling of particles at the bed surface, different frequency bands for turbulence and bedload transport), which may not always be valid in steep streams with shallow water and complex turbulence patterns (Gimbert et al., 2019; Bakker et al., 2020). In addition, the inversion procedure that transforms the seismic signal into bedload transport time-series using the FMI requires nine field parameters, whose estimates in the field also contains uncertainty and may not be stationary.

Despite these multiple sources of uncertainty in the FMI, the comparison between seismic-inverted time-series of bedload transport with the one obtained with the calibrated SPG, performed in Chapter IV, showed promising results. First, the general variability in bedload transport rates (i.e. periods of lower and higher magnitude) measured with the SPG was also captured by the seismic-inverted time-series. Second, the timing of the greatest peaks in bedload transport rates was simultaneous for both measuring systems. Third, both time-series presented comparable magnitude in absolute terms, with in an average factor of four of difference, reducing to under three for bedload transport peaks. Residual differences may be attributed to erroneous assumptions in the FMI, or non-representative estimates of the nine control parameters, but errors may also arise from the SPG recording (e.g. particle threshold of detection, saturation or missed particles at higher bedload transport rates). The performance of the FMI is encouraging given that all required parameters were determined beforehand in the field, the inversion was constrained by no measured data, and no scaling of time-series was performed. In that sense, it is likely that reliable time-series of bedload transport can be acquired at substantially lower cost with environmental seismology (about a factor 100 in the Vallon de Nant case). Field effort to constrain the FMI is also lower than collecting calibration samples for the SPG system.

Further research may help to improve the performance of the FMI further. This could be achieved in controlled flume experiments, where seismic recordings are combined with a continuous monitoring of flow hydraulic conditions (e.g. water depth, flow velocity) and of particle trajectories, for instance using ‘smart pebbles’ (Gimbert et al., 2019), to systematically test the physical assumptions of the FMI at various streamflow and bedload transport rates. Following such an approach, Gimbert et al. (2019) could for instance confirm the near-vertical impact trajectories of bedload particles impacting the bed in a steep turbulent flume. FMI improvement could also be achieved through a systematic testing and detailed description of the best procedure to determine the nine parameters needed to constrain the inversion, and in particular grain-size distribution parameters, upon which the FMI has shown to be very sensitive (Lagarde et al., 2021; Dietze et al., 2022). Streamflow being an easily measurable variable, further research should investigate how much improvement in the seismic inversion of bedload transport is achievable if exact measurements of water depths are used in the FMI to drive the inversion.

Because seismic sensors are cheap, non-invasive and easily deployable, another critical strength of the environmental seismology approach lies in the possibility of distributing sensors spatially. Networks of seismic sensors have the potential to track the mobilization, transfer and storage of coarse material throughout Alpine watersheds, and to provide critical insight on the key balance between stream transport capacity (C) and upstream material supply (S) needed for improving bedload transport predictions (Lane, 1955; Piton and Recking, 2017; Gomez and Soar, 2022). In that sense, the network of seismic sensors deployed across the Vallon de Nant and presented in Chapter IV provides with one of the first attempts to understand the spatial structure of bedload transport throughout a steep Alpine watershed. This aspect is further treated in section V.2. Note that the application of the Fluvial Inversion Model to seismic records where independent measures of bedload transport are not available to assess the performance of the inversion must be undertaken with care, notably due to the possibility of the FMI model assumptions to be locally erroneous or model parameters to be locally poorly estimated.

V-1.3 Wider implications for bedload transport monitoring

Acoustic and seismic techniques allow important developments in the continuous monitoring of bedload transport in steep Alpine streams, with the potential to also capture the process spatial variability when sensors can be deployed as networks (Cook et al., 2018; Chmiel et al., 2022; Piantini et al., 2022). Even then, sensor spatial coverage is limited in practice by a trade-off between spatial density and the spatial scale over which time-series of bedload can be obtained, so that it is difficult to equip an entire watershed with a density of sensors that permits for spatial continuity in monitoring. This means that there are often spatial gaps between the sensor network points (Cook et al., 2018; Chmiel et al., 2022), where bedload transport dynamics are unknown. In addition, acoustic and seismic methods do not fingerprint the transported bedload, so that we do not know whether the same coarse material is measured over consecutive sensors of the network, or whether deposition and remobilization of different material occurs in between points of the sensor network. In this context, three main complementary approaches may help to fill the spatial gaps in bedload transport monitoring collected with networks of sensors in future research.

First, distributed acoustic sensors (DAS), km-long fiber optic cables, can deliver seismic data almost continuously in space and time (Zhan, 2019; Lior et al., 2021). Through application of the FMI, they present an important potential for simultaneous capture of the time-space variability in both streamflow and bedload transport. Their spatial-scale of deployment (i.e. kilometric) may yet be limited to survey restricted lengths of channel, and may not provide with spatially-continuous datasets at the watershed scale. But they may be extremely relevant to survey stream reaches (Piantini et al., 2022), or for measuring processes expressed only across a narrow spatial scale, such as debris-flows (Coviello et al., 2019; Chmiel et al., 2021).

Second, repeated topographic surveys of Alpine watersheds, notably using laser scanning (Anderson and Pitlick, 2014; Williams et al., 2014; Mancini and Lane, 2020) and UAV-based Sfm-MVS photogrammetry (Eltner et al., 2015; Smith and Vericat, 2015; Tamminga et al., 2015; James et al.*, 2020) techniques, can provide spatially-continuous datasets of erosion and deposition patterns at multi-kilometric scale through DEM differencing. Assuming mass conservation through the surveyed area, spatially-variable bedload transport rates can be acquired through the application of the ‘morphological method’ (Lane et al., 1995; Ashmore and Church, 1998). Whilst the most recent applications of the morphological method to date have profited from progress in laser scanning and photogrammetry over relatively small spatial scales (Antoniazza et al*., 2019; Bakker et al*., 2019; Dai et al*., 2021), Chapter IV showed how routine national-scale mapping can now provide data with the precision and resolution needed for precise estimates of erosion and deposition with a multi-year frequency. Lower temporal frequencies are potentially a problem for the morphological method as they may lead to compensating erosion and deposition between survey dates that leads to under-estimates of transport rates (Lindsay and Ashmore, 2002; Antoniazza et al.*, 2019). However, the acoustic sensing in Chapter IV showed that bedload transport advection lengths in steep Alpine streams are short (for a theoretical explanation of why this is the case, see Ganti et al., 2014). The frequency of survey needed to avoid compensation will therefore be a function of typical advection lengths, which can be estimated from a seismic sensor network (Chapter IV), or from particle tracking experiments (see below). Integration of the known number of events with advection lengths should then be a means of constraining the extent of compensation in morphological methods involving low frequency survey data but over very large spatial extents.

Third, particle tracking experiments allow to fingerprint part of the bulk bedload transport at a multi-kilometric scale, which provides important information on particle thresholds of motion, step-lengths, resting periods and velocity (Liébault et al., 2012; Hassan et al., 2013; Dell'Agnese et al., 2015; Mao et al., 2017; Cassel et al., 2017; Vázquez-Tarrío et al., 2019). In that sense, these experiments may bring valuable complementary information to datasets acquired with distributed networks of sensors, because of the possibility to track individual particle motion and to relate it to the bulk bedload transport measured at different points of the sensor network. A particle tracking experiment using passive RFID PIT-tags has been conducted at the Vallon de Nant Alpine watershed in the frame of this PhD project, but the dataset has not yet been fully analyzed. These may also be combined with the morphological method.

V-2 Applications to understanding bedload transport in steep Alpine streams

This section draws from the time-series of bedload transport acquired with the SPG system and with the environmental seismology to identify the new understanding of bedload transport in steep Alpine streams that this thesis has developed. It starts by discussing the hydrological drivers of bedload transport in Alpine watersheds, and how climate change may affect bedload transport in the future through its effect on Alpine hydrology (V-2.1). It then investigates the question of the spatial structure of bedload transport throughout steep Alpine watersheds during individual flow events (V-2.2). It finishes by looking at wider implications and needs for the understanding of coarse material mobilization, transfer and storage throughout steep Alpine watersheds at longer time-scales (V-2.3).

V-2.1 Hydrological drivers of bedload transport

The five-year time-series of streamflow and SPG-acquired bedload transport analyzed in Chapter III of this thesis permitted investigation of the relationship between transport capacity (C) and measured bedload transport rates. Capacity-based bedload transport predictions were shown to scale in average with the measured bedload transport rate ($R^2 = 0.57$), which confirms streamflow as a primary driver of bedload transport (Kreisler et al., 2017; Habersack et al., 2017; Rickenmann, 2018, 2020). Instant values nevertheless spanned three orders of magnitude, reflecting fluctuations in bedload transport that are independent of changes in streamflow. Those may be due to temporally-variable upstream material supply (S) and both autogenic (Gomez, 1983; Gomez et al., 1989; Parker and Toro- Escobar, 2002) and exogenic (e.g. Chapter III) controls. Autogenic fluctuations were shown to especially express at shorter time-scales, typically up to about one hour, while stronger correlation between streamflow and bedload transport emerge at longer time-scales (Heimann, 2015; Aigner et al., 2017; Rickenmann, 2018, 2020). However, such correlations assume that the relationship between bedload transport and streamflow is statistically stationary. It is quite possible that there are times when they are more covarying than others. It is not clear that current statistical approaches capture these covariate effects at all well and other approaches, such as using wavelet decomposition may be appropriate to identify the frequency and the strength of association.

At time-scales longer than those associated with autogenic fluctuations, a range of hydrological processes can lead to streamflow variations within Alpine watersheds, and through it trigger bedload transport. These hydrological processes notably include ice and snowmelt, rainfall, and the co-occurrence of rainfall and melt events (Mutzner et al., 2015; Corripio and López-Moreno, 2017; Musselman et al., 2018). In a 12%-glacierized watershed of the Italian Alps (Saldur river), Comiti et al. (2019) found that glacier-melt contribution to annual bedload transport budget was substantially greater than the one induced by snowmelt or rainfall events, and that the bedload signal was much more tightly related to temperature than precipitation forcing. In a 14%-glacierized watershed of the Italian Alps (Sulden river), Coviello et al. (2022) found that glacier-melt and snowmelt were important drivers of bedload transport (~50% of annual budgets), but that rainfall events could disproportionally contribute to annual bedload budgets in some years (30-70%). In a nival-dominated Alpine watershed of the Italian Alps (Rio Cordon), Rainato et al. (2017) found over a 30-year period that a slight majority of the bedload transport events (17 out of 31) were taking place in periods (e.g. May-June and November) where snowmelt was likely contributing substantially to streamflow variations, but an important proportion (14 events) also occurred when the likelihood of substantial contribution of snowmelt to streamflow was smaller (July-October). Results of Chapter III acquired in the nival-dominated the Vallon de Nant Alpine watershed emphasized that mixed rainfall and snowmelt events contributed on average to 77% of annual bedload budgets. Melt-only events contributed in average to 14% of annual bedload budget, and rainfall-only events occurring in the late-summer and autumn to the remaining 9%.

These different results probably illustrate a shift that many Alpine watersheds are experiencing, depending on their hypsometry and climate, as the proportion of glacier contribution to streamflow decreases, from glacier-melt being a dominant driver of bedload transport (Rickenmann, 2018; Comiti et al., 2019; Coviello et al., 2022), to mixed snowmelt and rainfall events being dominant drivers (Micheletti and Lane, 2016; Rainato et al., 2017; Antoniazza et al., 2022), towards heavy rainfall being dominant drivers (Turowski et al., 2009; Rainato et al., 2017). Yet, the respective contribution of ice-melt, snowmelt and heavy rainfall, and how they combine to drive bedload transport capacity (C), is still too poorly constrained and deserves more attention in future research. This requires longer time-series of both streamflow and bedload transport (to include inter-annual variability). Data are needed in settings with variable climatic conditions (in terms of glacier-melt, snowmelt and heavy rainfall contributions). A particular challenge is that the monitoring stations needed to provide multi-decadal time-series of bedload transport from a range of different Alpine settings do not exist. A new project funded by the Swiss National Science Foundation between the University of Lausanne and the University of Bolzano-Bozen seeks to do this by exploiting the rich datasets held by hydropower companies.

Through its effect on Alpine hydrology, there is no doubt that climate change will further impact the hydrological drivers of bedload transport (CH2018, 2018; Brunner et al., 2019). In glacierized watersheds, glacier-melt may start earlier and last longer with decreasing volume of snowfall (Brunner et al., 2019; Zekollari et al., 2019), until a ‘peak water’ is reached and glacier subsidies are no longer able to maintain such high melt rates (Sorg et al., 2014; Huss and Hock, 2018). In theory, this also leads to a ‘peak sediment’ (Ballantyne, 2002a, 2002b; Carrivick and Heckmann, 2017; Lane et al., 2021; Zhang et al., 2022). In nival-dominated

Alpine watersheds, discussion in Chapter III emphasizes that melt seasons are expected to occur earlier in the spring and the contribution of snowfall to precipitation is expected to decrease, leading possibly to more bedload being transported during higher streamflow winter and spring, and less bedload being transported during drier summer and fall (CH2018, 2018; Antoniazza et al., 2022). In rainfall-dominated Alpine watersheds, precipitation forcing is thought to become dominant (Rainato et al., 2017). The timing of heavy rainfall (with regards to melt periods and baseflow height) and their intensity, is already key in determining transport capacity (C) under current climatic conditions in all glacier-dominated, nival-dominated and rainfall-dominated watersheds (Rainato et al., 2017; Antoniazza et al., 2022; Coviello et al., 2022). It will become even more important with the projected increase in the magnitude-frequency of heavy rainfall events and streamflow under climate change conditions (CH2018, 2018; Zekollari et al., 2019; Brunner et al., 2019). In this context, progress in hydrological models of Alpine streams (Antonetti and Zappa, 2018; Brunner et al., 2019; Zekollari et al., 2019; Maruffi et al., 2022) may help to improve prediction changes in transport capacity (C) under climate change conditions in Alpine watersheds with different hypsometry and climate. However, and as explained below, it is likely that the much bigger challenge is how to predict when and where bedload-sized sediment is supplied to steep Alpine streams under a changing climate (Lane et al., 2021).

V-2.2 Spatial structure of bedload transport throughout steep Alpine watersheds during individual flow events

The network of seismic sensors deployed across the Vallon de Nant and presented in Chapter IV of this thesis provides one of the firsts attempt to quantify the spatial structure of bedload transport throughout a steep Alpine watershed during a high-magnitude bedload transport event. The study revealed the relative inefficiency of steep Alpine watersheds in evacuating coarse material, even during what was a relatively infrequent high-magnitude event (1-2 years return period). Significant inputs measured in some headwater channels were rapidly attenuated as the main river crossed less hydraulically-efficient reaches, and only a comparatively negligible proportion of the total amount of material mobilized in the watershed was exported at the outlet during the event that mobilized it. Cross-correlation analysis of the time-series suggested that a faster moving water wave initially (re-)mobilized local material; and then entrained bedload moved more slowly, and over shorter distances. Multiple periods of competent flows were shown to be necessary to evacuate the coarse material produced throughout the watershed during individual source-mobilizing bedload transport events, which was confirmed by a longer-term morphological change analysis. By supplying material into the main channel network, high-magnitude events in the tributaries therefore make new material available from poorly-connected areas (Cavalli et al., 2013; Lane et al., 2017; Mancini and Lane, 2020) of the watershed (e.g. steep slopes at the top of rockwalls, tributary gullies, proglacial areas), which can be remobilized during subsequent competent flow events throughout the main channel network (Mao et al., 2014; Comiti et al., 2019; Buter et al., 2022; Coviello et al., 2022). The acquired dataset thus provides important insights into the respective role of smaller and higher magnitude flow events in the mobilization, transfer and storage of coarse material in steep Alpine watersheds.

This result has important implications with regards to the shift in hydrological drivers of bedload transport under climate change conditions identified in section V-2.1. For Alpine watersheds such as the Vallon de Nant, we saw that climate change likely means a transition from a dominant control of streamflow by mixed snowmelt and rainfall events, towards a domination of rainfall events only (CH2018, 2018; Zekollari et al., 2019; Brunner et al., 2019). In this context, there may be longer periods of non-competent flows interspersed by short rainfall-driven periods of high streamflow transport capacity (C). Given the relative inefficiency of steep Alpine watersheds to convey coarse material found in Chapter IV during individual flow events, even if its magnitude was high, this could translate into an overall slower rate of coarse material transfer throughout Alpine watersheds under climate change conditions in such environments. The result would be longer term aggradation in valley bottoms. In turn, it suggests the need to consider carefully inferred relationships between terrace development and climate change in Alpine environments. There has been recent debate regarding the concept of complex response in river basins (Macklin et al., 2022). Complex response refers to the autogenic feedbacks that lead to sequences of terrace formation and incision in river basins. Its occurrence challenge whether or not historical terrace formation and incision can be used to infer exogenic (e.g. climate) changes. Macklin et al. (2022) argue that complex response has rarely been validated in field experiments, with most evidence coming from laboratory studies. In their study of a Mediterranean basin at the Holocene time-scale, they argued for strong evidence of exogenic drivers of sedimentation history. The work presented in Chapter IV, however, emphasizes the complexity of aggradation (and erosion) in steep Alpine drainage watersheds. Likely future terrace development (and terrace incision) will be complex both because of the evidence in Chapter IV of autogenic forcing, and because of the evidence in Chapters III and IV that shows that simple climate change to sediment supply relationships do not exist, at least in steep Alpine watersheds.

Analysis of the spatial structure of bedload transport in Chapter IV also permitted to identify rockwalls and headwater tributaries as important sources of coarse material, while alluvial fans and braided sections formed important storage areas. Semi-alluvial reaches rather played a role of conveyor. This brought evidence of substantial ‘travelling bedload’ (Piton and Recking, 2017) in the multi-kilometric lower semi-alluvial section of the Vallon de Nant watershed. This has important implications for the prediction of bedload transport with transport capacity-based equations (C), because bedload transport may be locally composed of finer material than the one of the bed, which may explain part of the scatter found in Chapter III in the relationship between measured and predicted bedload transport rates (Kreisler et al., 2017; Habersack et al., 2017; Rickenmann, 2018, 2020). Yet, the fact that bedload transport magnitude was held relatively constant over a multi-kilometric semi-alluvial reach was positive with regards to the development of ‘early warning systems’ for bedload transport events (Badoux et al., 2012; Chmiel et al., 2021).

V.2.3 Spatial structure of bedload transport throughout steep Alpine watersheds at longer time-scales

Temporal variability in bedload transport rates was shown not only to reflect variability in the hydrological drivers and associated transport capacity (C) (V-2.1), but also the activation of different sedimentary sources (S) across steep Alpine watersheds (e.g. proglacial areas, tributary gullies, the main river bed, hillslopes; Mao et al., 2014; Comiti et al., 2019; Coviello et al., 2022, Buter et al., 2022). Mao et al. (2014) used the direction of hysteresis loops to infer the activation of different sediment sources in a steep Alpine watershed of the Italian Alps (Saldur river) during a multi-year period. Clockwise hysteresis loops (i.e. peak bedload transport occurring before peak streamflow) were dominant during the earlier snowmelt season (June-July). These were attributed to readily-available proximal sedimentary sources associated with river banks and the river bed. In turn these were related to bank collapse during winter-time, poor bed packing and/or easily-mobilizable material deposited during previous floods. In contrast, counter-clockwise hysteresis (i.e. peak bedload transport occurring after peak streamflow) were dominant in the later snowmelt and early glacier-melt periods. These were attributed to the activation of more distal sedimentary sources (e.g. subglacial, proglacial and periglacial areas). By that time, readily-available coarse material sources of the proximal channel network were exhausted, and the time needed by the bedload waves to travel from more distal sediment sources to the outlet induced a lag in the peak bedload transport as compared to the peak streamflow. In the same Saldur watershed, Comiti et al. (2019) showed that bedload transport rates were much higher (by five to six orders of magnitude) for comparable streamflow during the late-summer glacier-melt (August) than during the early-summer snowmelt (June-July), emphasizing a seasonal increase in sediment availability. This increase was associated with the activation of both higher elevation sedimentary sources as the snowline rises, and activation from the bed in the main channel network as its mobility increased with enhanced supply (Venditti et al., 2010; Ancey et al., 2015; Kammerlander et al., 2017).

Although the progressive snowline rise is likely to activate more sedimentary sources within any one year in steep Alpine watersheds, the respective contribution of (a) proximal sedimentary sources (e.g. the river banks and bed in the main channel network); and (b) more distal sedimentary sources (e.g. torrential tributaries, hillslopes, proglacial areas); remains unclear in terms of exported bedload yield over longer time-scales. First, this is due to complex thresholds in bed mobility state across steep Alpine watersheds, where antecedent flows of low to intermediate intensity, depending on their magnitude and frequency, may alternatively increase (Reid et al., 1985; Mao, 2012; Roth et al., 2017; Masteller et al., 2019) or decrease (Marquis and Roy, 2012; Mao et al., 2017) the overall bed stability. Second, it is due to the complex role of high-magnitude events in coarse material mobilization. On the one hand, they may mobilize distal sedimentary sources that may not be well-connected during low to intermediate flows (e.g. tributary gullies, subglacial area, proglacial area, periglacial area), such as observed in Chapter IV. On the other hand, they may destabilize the bed structure and enhance sediment availability within the main channel network (e.g. from banks, bars, and the bed matrix), for periods up to a decade (Turowski et al., 2009; Rainato et al., 2017). Third, the contribution of different sedimentary sources (proximal versus distal sources) is obscured by the time needed by bedload particles to travel through steep Alpine watersheds (Dell'Agnese et al., 2015; Mao et al., 2017). This emphasizes the need to acquire spatially-distributed datasets of bedload transport throughout steep Alpine watersheds across longer time periods, to better constrain temporal changes in upstream sediment supply and sources of coarse material (S).

At time-scales longer than individual years (e.g. decades), changes in sediment supply (S) throughout steep Alpine watersheds also depend on the legacy of glaciation (Church and Ryder, 1972; Ballantyne, 2002b, 2002a; Antoniazza and Lane*, 2021). Paraglacial adjustment of Alpine landscapes was assumed to produce an exponential decrease in material export with time (Church and Ryder, 1972; Ballantyne, 2002b). This was assumed to be due to their progressive adjustment to non-glacial conditions associated with the progressive exhaustion or disconnection from active transport corridors, and/or negative feedbacks in coarse material mobility (e.g. sediment sorting, soil development, vegetation encroachment) (Church and Slaymaker, 1989; Carrivick et al., 2013; Baewert and Morche, 2014; Lane et al., 2017; Miller and Lane, 2019). Since Quaternary climatic variability has produced glaciations of varying magnitude at various temporal scales (Bingham et al., 2010; Patterson et al., 2014), and assuming that the duration of the paraglacial adjustment scales with the magnitude of a given glaciation, it is likely that an observed sediment yield actually represents a mixed signal from different glaciations at different stages of adjustment. For instance, contemporaneous coarse material fluxes measured within steep Alpine watersheds probably originate from a mixed signal of Little Ice Age paraglacial adjustment, which is still in an early phase (Lane et al., 2017; Carrivick and Heckmann, 2017; Lane and Nienow, 2019), together with the one of Last Glacial Maximum. The latter is in a later phase of adjustment, but still influences Alpine streams and leads to some extent to coarse material supply through the legacy of glacially-conditioned deposits and landforms, in which current processes may operate (Ballantyne, 2002a, 2002b; Baewert and Morche, 2014; Cordier et al., 2017; Roussel et al., 2018). Glacial legacy therefore provides an additional important context to understand the spatial structure of bedload transport at longer time-scales, and delivers a theoretical framework transferable across most Alpine watersheds. In this context, landscape evolution models (Heckmann et al., 2018; Mahoney et al., 2018) may be of help to better constrain how coarse material mobilization, transfer and storage is likely to evolve throughout steep Alpine watersheds at different time-scales, and through it determine changes in upstream material supply (S). There could be synergy between the measurements reported in V.1 and the development of such models as the latter remain largely unvalidated for bedload transport because of a lack of high quality control data.

V-3 Conclusions

This synthesis chapter has sought to set the findings of the three core chapters of this thesis in a wider context and drawing in additional work with which I have been involved. These conclusions finish the Chapter by making one key point. It is the synergy between developments in measurement and the scientific questions associated with bedload transport that is the essence of what this thesis has sought to achieve. Despite being a relatively mature science area, innovations in bedload transport measurement (Chapters II and IV) are substantially increasing our understanding of the elusive process by which coarse sediment is mobilized, transported and deposited in steep Alpine watersheds (Chapters III and IV). In turn, and as this Chapter has shown, this understanding emphasizes the need for further methodological innovation notably in combining monitoring methods that are temporally-rich but spatially-poor (e.g. SPG-based monitoring systems), those that are spatially-rich but temporally-poor (e.g. the ‘morphological method’, particle tracking experiments) and those that are “in between” such as the seismic methods reported in this Chapter IV.

VI – Conclusions

This thesis was concerned with improving our ability to measure bedload transport in steep Alpine streams, by developing and applying acoustic and seismic techniques, so as to gain a new understanding of coarse material mobilization, transfer and storage in steep Alpine watersheds. This Chapter summarizes the main research outcomes along the two main research axes introduced in Chapter I. First, the improvement in the monitoring of bedload transport using acoustic and seismic techniques is summarized (VI-1). Second, the new understanding of coarse material mobilization, transfer and storage throughout steep Alpine watersheds is described (VI-2).

VI-1 Developments in acoustic and seismic monitoring of bedload transport in steep Alpine streams

A SPG system at the Vallon de Nant was successfully calibrated using concurrent bedload samples, which brought additional knowledge on the site-specific calibration of the SPG system. An impact experiment was conducted at four SPG sites to identify factors of variability in inter-site calibration coefficients. Although the response of individual SPG units within and across sites was in most case consistent, the inter-plate signal propagation due to poor insulation was identified as a new and important factor in SPG calibration. Time-frequency information of the SPG signal can be used to identify and to eliminate ‘apparent’ impacts automatically. This permits substantial reduction in the inter-site variability in calibration coefficients, and enables the derivation of a single calibration coefficient for total bedload transport transferable across SPG sites.

Environmental seismology can also provide reliable time-series of bedload transport, with an average factor four of difference in this study when compared to the independent calibrated SPG-based measurements. Seismometers being cheap, easily deployable, non-invasive and requiring little maintenance, they present an enormous potential to equip many Alpine rivers, and so to allow time-series of bedload transport in different settings to be obtained. When deployed as networks at multiple locations in steep Alpine watersheds, they can also provide spatially-distributed time-series of bedload transport, and may capture the time-space variability in bedload transport rates needed to improve bedload transport predictions. The application of the Fluvial Inversion Model to seismic records where no independent measurement of bedload transport are available must be undertaken with care, notably due to the possibility of model assumptions to be locally erroneous or model parameters to be locally poorly estimated.

VI-2 New understanding of coarse material mobilization, transfer and storage throughout steep Alpine watersheds

Despite three orders of magnitude of scatter in instantaneous values, capacity-based bedload transport predictions were shown to scale on average with the measured bedload transport rate in the Vallon de Nant Alpine watershed, confirming streamflow variations as a dominant driver of bedload transport. Analysis of the hydrological drivers of bedload transport in the watershed showed that mixed rainfall and snowmelt events contributed on average to 77% of annual bedload budgets. Melt-only events contributed on average to 14% of annual bedload budget, and rainfall-only events to the remaining 9%. By impacting Alpine hydrology, climate change may induce shifts in bedload transport dynamics. In nival-dominated Alpine watersheds such as the Vallon de Nant, melt seasons are expected to occur earlier in the spring and the contribution of snowfall to precipitation is expected to decrease, possibly leading to more bedload being transported during higher-discharge winter and spring events, and less bedload being transported during drier summer and fall. The timing and intensity of heavy rainfall (with regards to melt periods and baseflow height) will be key in determining exactly the nature of changes in bedload transport capacity under changing climate.

The distributed seismic sensing of a high-magnitude bedload transport event in the Vallon de Nant highlighted the relative inefficiency of steep Alpine watersheds in evacuating coarse material, even during what was a relatively high-magnitude event. Bedload transport resulting from significant inputs measured for some tributaries was rapidly attenuated as the main river crossed less hydraulically-efficient reaches, and only a comparatively negligible proportion of the total amount of material produced in the watershed was exported at the outlet. Cross-correlation analysis of the time-series suggests that a faster moving water wave (re-)mobilized local material and bedload was expected to move slower, and over shorter distances. Multiple periods of competent flows were thought to be necessary to evacuate the coarse material produced throughout the watershed during individual source-mobilizing bedload transport events. This pointed to the need to consider whether under climate change conditions longer periods of non-competent flows interspersed by short duration rainfall-driven high streamflow, may lead to a slowdown of coarse material transfer in such settings and longer-term aggradation. High-magnitude bedload transport events in the tributaries played an important role in providing material into the main channel network from areas of the watershed where large sedimentary sources were available (e.g. steep slopes at the top of rockwalls, tributary gullies, proglacial areas), but which were not always be well connected during low to intermediate flows. By supplying material into the main channel network, high-magnitude events in the tributaries therefore made new material available, which were remobilized during subsequent competent flows throughout the main channel network. This highlighted the respective contribution of smaller versus higher magnitude bedload transport in coarse material fluxes throughout steep Alpine watersheds, and helped to constrain changes in sediment supply through time.

VII – References

Abbott, J.E., Francis, J.R.D., 1977. Saltation and suspension trajectories of solid grains in a water stream. Philosophical Transactions of the Royal Society of London. Series A, Mathematical and Physical Sciences 284, 225–254.

Aigner, J., Kreisler, A., Rindler, R., Hauer, C., Habersack, H., 2017. Bedload pulses in a hydropower affected alpine gravel bed river. Geomorphology, SEDIMENT DYNAMICS IN ALPINE BASINS 291, 116–127. https://doi.org/10.1016/j.geomorph.2016.05.015

Altmann, M., Haas, F., Heckmann, T., Liébault, F., Becht, M., 2021. Modelling of sediment supply from torrent catchments in the Western Alps using the sediment contributing area (SCA) approach. Earth Surface Processes and Landforms 46, 889–906. https://doi.org/10.1002/esp.5046

An, C., Parker, G., Hassan, M.A., Fu, X., 2019. Can magic sand cause massive degradation of a gravel-bed river at the decadal scale? Shi-ting River, China. Geomorphology 327, 147–158. https://doi.org/10.1016/j.geomorph.2018.10.026

Ancey, C., 2020a. Bedload transport: a walk between randomness and determinism. Part 1. The state of the art. Journal of Hydraulic Research 58, 1–17.

Ancey, C., 2020b. Bedload transport: a walk between randomness and determinism. Part 2. Challenges and prospects. Journal of Hydraulic Research 58, 18–33.

Ancey, C., Bohorquez, P., Heyman, J., 2015. Stochastic interpretation of the advection-diffusion equation and its relevance to bed load transport. Journal of Geophysical Research: Earth Surface 120, 2529–2551. https://doi.org/10.1002/2014JF003421

Anderson, S., Pitlick, J., 2014. Using repeat lidar to estimate sediment transport in a steep stream. Journal of Geophysical Research: Earth Surface 119, 621–643.

Andrews, E.D., 1983. Entrainment of gravel from naturally sorted riverbed material. Geological Society of America Bulletin 94, 1225–1231.

Annandale, G.W., 2016. Overview of Sedimentation Issues, in: Extending the Life of Reservoirs: Sustainable Sediment Management for Dams and Run-of-River Hydropower, Directions in Development - Energy and Mining. The World Bank, pp. 23–44. https://doi.org/10.1596/978-1-4648-0838-8_ch3

Antonetti, M., Zappa, M., 2018. How can expert knowledge increase the realism of conceptual hydrological models? A case study based on the concept of dominant runoff process in the Swiss Pre-Alps. Hydrology and Earth System Sciences 22, 4425–4447. https://doi.org/10.5194/hess-22-4425-2018

Antoniazza, G., Bakker, M., Lane, S.N., 2019. Revisiting the morphological method in two-dimensions to quantify bed-material transport in braided rivers. Earth Surface Processes and Landforms 44, 2251–2267. https://doi.org/10.1002/esp.4633

Antoniazza, G., Lane, S.N., 2021. Sediment yield over glacial cycles: A conceptual model. Progress in Physical Geography: Earth and Environment 0309133321997292. https://doi.org/10.1177/0309133321997292

Antoniazza, G., Nicollier, T., Boss, S., Mettra, F., Badoux, A., Schaefli, B., Rickenmann, D., Lane, S.N., 2022. Hydrological Drivers of Bedload Transport in an Alpine Watershed. Water Resources Research 58, e2021WR030663. https://doi.org/10.1029/2021WR030663

Antoniazza, G., Nicollier, T., Wyss, C.R., Boss, S., Rickenmann, D., 2020. Bedload Transport Monitoring in Alpine Rivers: Variability in Swiss Plate Geophone Response. Sensors 20, 4089. https://doi.org/10.3390/s20154089

Arattano, M., Abancó, C., Coviello, V., Hürlimann, M., 2014. Processing the ground vibration signal produced by debris flows: the methods of amplitude and impulses compared. Computers & Geosciences 73, 17–27. https://doi.org/10.1016/j.cageo.2014.08.005

Ashmore, P.E., Church, M., 1998. Sediment transport and river morphology: a paradigm for study. Gravel-bed Rivers in the Environment 115–148.

Ashworth, P.J., Ferguson, R.I., 1989. Size-selective entrainment of bed load in gravel bed streams. Water Resources Research 25, 627–634.

Ashworth, P.J., Ferguson, R.I., 1986. Interrelationships of channel processes, changes and sediments in a proglacial braided river. Geografiska Annaler: Series A, Physical Geography 68, 361–371.

Badoux, A., Andres, N., Techel, F., Hegg, C., 2016. Natural hazard fatalities in Switzerland from 1946 to 2015. Natural Hazards and Earth System Sciences 16, 2747–2768.

Badoux, A., Andres, N., Turowski, J., 2014a. Damage costs due to bedload transport processes in Switzerland. Natural Hazards and Earth System Sciences 14, 279–294. https://doi.org/10.5194/nhess-14-279-2014

Badoux, A., Graf, C., Rhyner, J., Kuntner, R., McArdell, B.W., 2009. A debris-flow alarm system for the Alpine Illgraben catchment: design and performance. Nat Hazards 49, 517–539. https://doi.org/10.1007/s11069-008-9303-x

Badoux, A., Peter, A., Rickenmann, D., Junker, J., Heimann, F., Zappa, M., Turowski, J.M., 2014b. Geschiebetransport und Forellenhabitate in Gebirgsflüssen der Schweiz: mögliche Auswirkungen der Klimaänderung. Wasser Energie Luft 106, 200–209.

Badoux, A., Turowski, J.M., Mao, L., Mathys, N., Rickenmann, D., 2012. Rainfall intensity–duration thresholds for bedload transport initiation in small Alpine watersheds. Natural Hazards and Earth System Sciences 12, 3091–3108. https://doi.org/10.5194/nhess-12-3091-2012

Badoux, H., 1971. Feuille 1305 Dent de Morcles.

Baewert, H., Morche, D., 2014. Coarse sediment dynamics in a proglacial fluvial system (Fagge River, Tyrol). Geomorphology, Sediment flux and sediment budget studies in cold environments: new approaches and techniques 218, 88–97. https://doi.org/10.1016/j.geomorph.2013.10.021

Bakker, M., Antoniazza, G., Odermatt, E., Lane, S.N., 2019. Morphological Response of an Alpine Braided Reach to Sediment-Laden Flow Events. Journal of Geophysical Research: Earth Surface 124, 1310–1328. https://doi.org/10.1029/2018JF004811

Bakker, M., Gimbert, F., Geay, T., Misset, C., Zanker, S., Recking, A., 2020. Field Application and Validation of a Seismic Bedload Transport Model. Journal of Geophysical Research: Earth Surface 125, e2019JF005416. https://doi.org/10.1029/2019JF005416

Bakker, M., Legout, C., Gimbert, F., Nord, G., Boudevillain, B., Freche, G., 2022. Seismic modelling and observations of rainfall. Journal of Hydrology 610, 127812. https://doi.org/10.1016/j.jhydrol.2022.127812

Ballantyne, C.K., 2002a. Paraglacial geomorphology. Quaternary Science Reviews 21, 1935–2017. https://doi.org/10.1016/S0277-3791(02)00005-7

Ballantyne, C.K., 2002b. A general model of paraglacial landscape response. The Holocene 12, 371–376. https://doi.org/10.1191/0959683602hl553fa

Barrière, J., Krein, A., Oth, A., Schenkluhn, R., 2015. An advanced signal processing technique for deriving grain size information of bedload transport from impact plate vibration measurements. Earth Surface Processes and Landforms 40, 913–924. https://doi.org/10.1002/esp.3693

Barton, J.S., Slingerland, R.L., Pittman, S., Gabrielson, T.B., 2010. Monitoring coarse bedload transport with passive acoustic instrumentation: A field study. US Geol. Surv. Sci. Invest. Rep 5091, 38–51.

Bater, C.W., Coops, N.C., 2009. Evaluating error associated with lidar-derived DEM interpolation. Computers & Geosciences 35, 289–300. https://doi.org/10.1016/j.cageo.2008.09.001

Bathurst, J.C., 1987. Bed load discharge equations for steep mountain rivers. Sediment transport in gravel-bed rivers 453–491.

Becht, M., Füssl, M., Wetzel, K.-F., Wilhelm, F., 1989. Das Verhältnis von Feststoff-und Lösungsaustrag aus Einzugsgebieten mit carbonatreichen pleistozänen Lockergesteinen der Bayerischen Kalkvoralpen.

Bingham, R.G., King, E.C., Smith, A.M., Pritchard, H.D., 2010. Glacial geomorphology: Towards a convergence of glaciology and geomorphology. Progress in Physical

Geography: Earth and Environment 34, 327–355. https://doi.org/10.1177/0309133309360631

Bollrich, G., 2000. Technische Hydromechanik 1, 5. Auflage. Verlag Bauwesen, Berlin.

Bridge, J.S., 2009. Rivers and floodplains: forms, processes, and sedimentary record. John Wiley & Sons.

Brown, C.B., 1949. Sediment transportation, in: House, R. Engineering Hydraulics. New-York, pp. 769–857.

Brunner, M.I., Farinotti, D., Zekollari, H., Huss, M., Zappa, M., 2019. Future shifts in extreme flow regimes in Alpine regions. Hydrology and Earth System Sciences 23, 4471–4489. https://doi.org/10.5194/hess-23-4471-2019

Buffington, J.M., Montgomery, D.R., 1997. A systematic analysis of eight decades of incipient motion studies, with special reference to gravel-bedded rivers. Water Resources Research 33, 1993–2029.

Bunte, K., Abt, S.R., 2005. Effect of sampling time on measured gravel bed load transport rates in a coarse-bedded stream. Water Resources Research 41.

Bunte, K., Abt Steven R., Potyondy John P., Ryan Sandra E., 2004. Measurement of Coarse Gravel and Cobble Transport Using Portable Bedload Traps. Journal of Hydraulic Engineering 130, 879–893. https://doi.org/10.1061/(ASCE)0733-9429(2004)130:9(879)

Burtin, A., Bollinger, L., Vergne, J., Cattin, R., Nábělek, J.L., 2008. Spectral analysis of seismic noise induced by rivers: A new tool to monitor spatiotemporal changes in stream hydrodynamics. Journal of Geophysical Research: Solid Earth 113. https://doi.org/10.1029/2007JB005034

Burtin, A., Cattin, R., Bollinger, L., Vergne, J., Steer, P., Robert, A., Findling, N., Tiberi, C., 2011. Towards the hydrologic and bed load monitoring from high-frequency seismic noise in a braided river: The “torrent de St Pierre”, French Alps. Journal of hydrology 408, 43–53.

Buter, A., Heckmann, T., Filisetti, L., Savi, S., Mao, L., Gems, B., Comiti, F., 2022. Effects of catchment characteristics and hydro-meteorological scenarios on sediment connectivity in glacierised catchments. Geomorphology 402, 108128. https://doi.org/10.1016/j.geomorph.2022.108128

Carrivick, J.L., Geilhausen, M., Warburton, J., Dickson, N.E., Carver, S.J., Evans, A.J., Brown, L.E., 2013. Contemporary geomorphological activity throughout the proglacial area of an alpine catchment. Geomorphology, Sediment sources, source-to-sink fluxes and sedimentary budgets 188, 83–95. https://doi.org/10.1016/j.geomorph.2012.03.029

Carrivick, J.L., Heckmann, T., 2017. Short-term geomorphological evolution of proglacial systems. Geomorphology, Sediment cascades in cold climate geosystems 287, 3–28. https://doi.org/10.1016/j.geomorph.2017.01.037

Cassel, M., Dépret, T., Piégay, H., 2017. Assessment of a new solution for tracking pebbles in rivers based on active RFID. Earth Surface Processes and Landforms 42, 1938–1951. https://doi.org/10.1002/esp.4152

Cavalli, M., Goldin, B., Comiti, F., Brardinoni, F., Marchi, L., 2017. Assessment of erosion and deposition in steep mountain basins by differencing sequential digital terrain models. Geomorphology, SEDIMENT DYNAMICS IN ALPINE BASINS 291, 4–16. https://doi.org/10.1016/j.geomorph.2016.04.009

Cavalli, M., Trevisani, S., Comiti, F., Marchi, L., 2013. Geomorphometric assessment of spatial sediment connectivity in small Alpine catchments. Geomorphology, Sediment sources, source-to-sink fluxes and sedimentary budgets 188, 31–41. https://doi.org/10.1016/j.geomorph.2012.05.007

Ceperley, N., Michelon, A., Escoffier, N., Mayoraz, G., Boix Canadell, M., Horgby, A., Hammer, F., Antoniazza, G., Schaefli, B., Lane, S., Rickenmann, D., Boss, S., 2018. Salt Gauging And Stage-Discharge Curve, Avançon De Nant, Outlet Vallon De Nant Catchment. https://doi.org/10.5281/zenodo.1154798. Version V1.0.0 [Data set]. Zenodo.

Ceperley, N., Zuecco, G., Beria, H., Carturan, L., Michelon, A., Penna, D., Larsen, J., Schaefli, B., 2020. Seasonal snow cover decreases young water fractions in high Alpine catchments. Hydrological Processes 34, 4794–4813. https://doi.org/10.1002/hyp.13937

CH2018, 2018. CH2018 - Climate Scenarios for Switzerland, Technical Report. National CEntre for Cliamte Services, Zürich.

Chapuis, M., Dufour, S., Provansal, M., Couvert, B., de Linares, M., 2015. Coupling channel evolution monitoring and RFID tracking in a large, wandering, gravel-bed river: Insights into sediment routing on geomorphic continuity through a riffle–pool sequence. Geomorphology 231, 258–269. https://doi.org/10.1016/j.geomorph.2014.12.013

Chen, Z., He, S., Nicollier, T., Ammann, L., Badoux, A., Rickenmann, D., 2022. Finite element modelling of the Swiss plate geophone bedload monitoring system. Journal of Hydraulic Research 60, 792–810. https://doi.org/10.1080/00221686.2022.2059585

Chen, Z., He, S., Nicollier, T., Ammann, L., Badoux, A., Rickenmann, D., 2021. Signal response of the Swiss plate geophone monitoring system impacted by bedload particles with different transport modes. Earth Surface Dynamics Discussions 1–35. https://doi.org/10.5194/esurf-2021-72

Chmiel, M., Godano, M., Piantini, M., Brigode, P., Gimbert, F., Bakker, M., Courboulex, F., Ampuero, J.-P., Rivet, D., Sladen, A., Ambrois, D., Chapuis, M., 2022. Brief communication: Seismological analysis of flood dynamics and hydrologically triggered earthquake swarms associated with Storm Alex. Natural Hazards and Earth System Sciences 22, 1541–1558. https://doi.org/10.5194/nhess-22-1541-2022

Chmiel, M., Walter, F., Wenner, M., Zhang, Z., McArdell, B.W., Hibert, C., 2021. Machine Learning Improves Debris Flow Warning. Geophysical Research Letters 48, e2020GL090874. https://doi.org/10.1029/2020GL090874

Church, M., Ferguson, R.I., 2015. Morphodynamics: Rivers beyond steady state. Water Resources Research 51, 1883–1897. https://doi.org/10.1002/2014WR016862

Church, M., Ryder, J.M., 1972. Paraglacial sedimentation: a consideration of fluvial processes conditioned by glaciation. Geological Society of America Bulletin 83, 3059–3072.

Church, M., Slaymaker, O., 1989. Disequilibrium of Holocene sediment yield in glaciated British Columbia. Nature 337, 452.

Comiti, F., Mao, L., Penna, D., Dell'Agnese, A., Engel, M., Rathburn, S., Cavalli, M., 2019. Glacier melt runoff controls bedload transport in Alpine catchments. Earth and Planetary Science Letters 520, 77–86. https://doi.org/10.1016/j.epsl.2019.05.031

Cook, K.L., Andermann, C., Gimbert, F., Adhikari, B.R., Hovius, N., 2018. Glacial lake outburst floods as drivers of fluvial erosion in the Himalaya. Science 362, 53–57. https://doi.org/10.1126/science.aat4981

Cook, K.L., Dietze, M., 2022. Seismic Advances in Process Geomorphology. Annual Review of Earth and Planetary Sciences 50, 183–204. https://doi.org/10.1146/annurev-earth-032320-085133

Cook, S.J., Swift, D.A., 2012. Subglacial basins: Their origin and importance in glacial systems and landscapes. Earth-Science Reviews 115, 332–372. https://doi.org/10.1016/j.earscirev.2012.09.009

Cordier, S., Adamson, K., Delmas, M., Calvet, M., Harmand, D., 2017. Of ice and water: Quaternary fluvial response to glacial forcing. Quaternary Science Reviews, Quaternary fluvial archives: advances from the first 20 years of FLAG (the Fluvial Archives Group) 166, 57–73. https://doi.org/10.1016/j.quascirev.2017.02.006

Corripio, J.G., López-Moreno, J.I., 2017. Analysis and Predictability of the Hydrological Response of Mountain Catchments to Heavy Rain on Snow Events: A Case Study in the Spanish Pyrenees. Hydrology 4, 20. https://doi.org/10.3390/hydrology4020020

Cossart, E., Fort, M., 2008. Sediment release and storage in early deglaciated areas: Towards an application of the exhaustion model from the case of Massif des Écrins

(French Alps) since the Little Ice Age. Norsk Geografisk Tidsskrift - Norwegian Journal of Geography 62, 115–131. https://doi.org/10.1080/00291950802095145

Coviello, V., Arattano, M., Comiti, F., Macconi, P., Marchi, L., 2019. Seismic Characterization of Debris Flows: Insights into Energy Radiation and Implications for Warning. Journal of Geophysical Research: Earth Surface 124, 1440–1463. https://doi.org/10.1029/2018JF004683

Coviello, V., Vignoli, G., Simoni, S., Bertoldi, W., Engel, M., Buter, A., Marchetti, G., Andreoli, A., Savi, S., Comiti, F., 2022. Bedload fluxes in a glacier-fed river at multiple temporal scales. Water Resources Research n/a, e2021WR031873. https://doi.org/10.1029/2021WR031873

Cucchiaro, S., Maset, E., Cavalli, M., Crema, S., Marchi, L., Beinat, A., Cazorzi, F., 2020. How does co-registration affect geomorphic change estimates in multi-temporal surveys? GIScience & Remote Sensing 57, 611–632. https://doi.org/10.1080/15481603.2020.1763048

Dai, W., Xiong, L., Antoniazza, G., Tang, G., Lane, S.N., 2021. Quantifying the spatial distribution of sediment transport in an experimental gully system using the morphological method. Earth Surface Processes and Landforms 46, 1188–1208. https://doi.org/10.1002/esp.5094

Dell'Agnese, A., Brardinoni, F., Toro, M., Mao, L., Engel, M., Comiti, F., 2015. Bedload transport in a formerly glaciated mountain catchment constrained by particle tracking. Earth Surface Dynamics 3, 527–542. https://doi.org/10.5194/esurf-3-527-2015

Dell'Agnese, A., Mao, L., Comiti, F., 2014. Calibration of an acoustic pipe sensor through bedload traps in a glacierized basin. CATENA 121, 222–231. https://doi.org/10.1016/j.catena.2014.05.021

Dietze, M., 2018. The R package "eseis"–a software toolbox for environmental seismology. Earth Surface Dynamics 6, 669–686.

Dietze, M., Bell, R., Ozturk, U., Cook, K.L., Andermann, C., Beer, A.R., Damm, B., Lucia, A., Fauer, F.S., Nissen, K.M., Sieg, T., Thieken, A.H., 2022. More than heavy rain turning into fast-flowing water – a landscape perspective on the 2021 Eifel floods. Natural Hazards and Earth System Sciences 22, 1845–1856. https://doi.org/10.5194/nhess-22-1845-2022

Dietze, M., Lagarde, S., Halfi, E., Laronne, J.B., Turowski, J.M., 2019. Joint Sensing of Bedload Flux and Water Depth by Seismic Data Inversion. Water Resources Research 55, 9892–9904. https://doi.org/10.1029/2019WR026072

Downing, J., 2010. Acoustic gravel-momentum sensor. US Geological Survey Scientific Investigations Report 5091, 143–158.

Downing, J., Farley, P.J., Bunte, K., Swingle, K., Ryan, S.E., Dixon, M., 2003. Acoustic gravel-transport sensor: description and field tests in Little Granite Creek, Wyoming, USA. IAHS PUBLICATION 193–200.

Dust, D., Wohl, E., 2012. Conceptual model for complex river responses using an expanded Lane's relation. Geomorphology 139–140, 109–121. https://doi.org/10.1016/j.geomorph.2011.10.008

Dutoit, A., 1983. La végétation de l'étage subalpin du Vallon de Nant. Université de Lausanne. Lausanne.

Egholm, D.L., Pedersen, V.K., Knudsen, M.F., Larsen, N.K., 2012. Coupling the flow of ice, water, and sediment in a glacial landscape evolution model. Geomorphology 141–142, 47–66. https://doi.org/10.1016/j.geomorph.2011.12.019

Einstein, H.A., 1950. The Bed-load Function for Sediment Transportation in Open Channel Flows. U.S. Department of Agriculture.

Einstein, H.A., 1937. Bedload transport as a probability problem. Sedimentation 1027, C1–C105.

Elgueta-Astaburuaga, M.A., Hassan, M.A., 2019. Sediment storage, partial transport, and the evolution of an experimental gravel bed under changing sediment supply regimes. Geomorphology 330, 1–12. https://doi.org/10.1016/j.geomorph.2018.12.018

Elgueta-Astaburuaga, M.A., Hassan, M.A., Saletti, M., Clarke, G.K.C., 2018. The Effect of Episodic Sediment Supply on Bedload Variability and Sediment Mobility. Water Resources Research 54, 6319–6335. https://doi.org/10.1029/2017WR022280

Eltner, A., Baumgart, P., Maas, H.-G., Faust, D., 2015. Multi-temporal UAV data for automatic measurement of rill and interrill erosion on loess soil. Earth Surface Processes and Landforms 40, 741–755. https://doi.org/10.1002/esp.3673

Ferguson, R.I., Cudden, J.R., Hoey, T.B., Rice, S.P., 2006. River system discontinuities due to lateral inputs: generic styles and controls. Earth Surface Processes and Landforms 31, 1149–1166. https://doi.org/10.1002/esp.1309

FOEN, 2021. Effects of climate change on Swiss water bodies. Hydrology, water ecology and water management. (Environmental studies No. 2101:125p.). Federal Office for the Environment FOEN, Bern.

FOEN, 2010. Hydrologisches Jahrbuch Schweiz. Federal Office for the Environment (FOEN).

FOEN, 2005. Les zones alluviales de Suisse.

Freudiger, D., Frielingsdorf, B., Stahl, K., Steinbrich, A., Weiler, M., Griessinger, N., Seibert, J., 2016. Das Potential meteorologischer Rasterdatensätze für die Modellierung der Schneedecke alpiner Einzugsgebiete. Hydrologie und Wasserbewirtschaftung 60, 353–367. https://doi.org/10.5675/HyWa_2016,6_1

Gabbud, C., Bakker, M., Clémençon, M., Lane, S.N., 2019. Hydropower Flushing Events Cause Severe Loss of Macrozoobenthos in Alpine Streams. Water Resources Research 55, 10056–10081. https://doi.org/10.1029/2019WR024758

Gabbud, C., Lane, S.N., 2016. Ecosystem impacts of Alpine water intakes for hydropower: the challenge of sediment management. WIREs Water 3, 41–61. https://doi.org/10.1002/wat2.1124

Ganti, V., Lamb, M.P., McElroy, B., 2014. Quantitative bounds on morphodynamics and implications for reading the sedimentary record. Nat Commun 5, 3298. https://doi.org/10.1038/ncomms4298

Ganti, V., Meerschaert, M.M., Foufoula-Georgiou, E., Viparelli, E., Parker, G., 2010. Normal and anomalous diffusion of gravel tracer particles in rivers. Journal of Geophysical Research: Earth Surface 115. https://doi.org/10.1029/2008JF001222

Geay, T., Belleudy, P., Gervaise, C., Habersack, H., Aigner, J., Kreisler, A., Seitz, H., Laronne, J.B., 2017. Passive acoustic monitoring of bed load discharge in a large gravel bed river. Journal of Geophysical Research: Earth Surface 122, 528–545. https://doi.org/10.1002/2016JF004112

Geay, T., Zanker, S., Misset, C., Recking, A., 2020. Passive Acoustic Measurement of Bedload Transport: Toward a Global Calibration Curve? Journal of Geophysical Research: Earth Surface 125, e2019JF005242. https://doi.org/10.1029/2019JF005242

Gimbert, F., Fuller, B.M., Lamb, M.P., Tsai, V.C., Johnson, J.P.L., 2019. Particle transport mechanics and induced seismic noise in steep flume experiments with accelerometer-embedded tracers. Earth Surface Processes and Landforms 44, 219–241. https://doi.org/10.1002/esp.4495

Gimbert, F., Tsai, V.C., Lamb, M.P., 2014. A physical model for seismic noise generation by turbulent flow in rivers. Journal of Geophysical Research: Earth Surface 119, 2209–2238. https://doi.org/10.1002/2014JF003201

Gomez, B., 1991. Bedload transport. Earth-Science Reviews 31, 89–132.

Gomez, B., 1983. Temporal variations in bedload transport rates: the effect of progressive bed armouring. Earth Surface Processes and Landforms 8, 41–54.

Gomez, B., Church, M., 1989. An assessment of bed load sediment transport formulae for gravel bed rivers. Water Resources Research 25, 1161–1186.

Gomez, B., Naff, R.L., Hubbell, D.W., 1989. Temporal variations in bedload transport rates associated with the migration of bedforms. Earth Surface Processes and Landforms 14, 135–156.

Gomez, B., Soar, P.J., 2022. Bedload transport: beyond intractability. Royal Society Open Science 9, 211932. https://doi.org/10.1098/rsos.211932

Goodwiller, B., Wren, D.G., Surbeck, C.Q., 2019. Development and calibration of an underwater acoustic data collection system for monitoring coarse bedload transport. Applied Acoustics 155, 383–390. https://doi.org/10.1016/j.apacoust.2019.06.019

Gray, J.R., Laronne, J.B., Marr, J.D., 2010. Bedload-surrogate monitoring technologies. US Department of the Interior, US Geological Survey.

Gribovszki, Z., Szilágyi, J., Kalicz, P., 2010. Diurnal fluctuations in shallow groundwater levels and streamflow rates and their interpretation – A review. Journal of Hydrology 385, 371–383. https://doi.org/10.1016/j.jhydrol.2010.02.001

Gurnell, A.M., 1987. Fluvial sediment yield from alpine, glacierized catchments. Glacio-Fluvial Sediment Transfer: An Alpine Perspective. John Wiley and Sons, New York New York. 1987. p 415-420, 1 tab, 4 ref.

Habersack, H., Kreisler, A., Rindler, R., Aigner, J., Seitz, H., Liedermann, M., Laronne, J.B., 2017. Integrated automatic and continuous bedload monitoring in gravel bed rivers. Geomorphology, SEDIMENT DYNAMICS IN ALPINE BASINS 291, 80–93. https://doi.org/10.1016/j.geomorph.2016.10.020

Habersack, H.M., Nachtneb El, H.P., Laronne, J.B., 2001. The continuous measurement of bedload discharge in a large alpine gravel bed river. Journal of Hydraulic Research 39, 125–133. https://doi.org/10.1080/00221680109499813

Halfi, E., Paz, D., Stark, K., Yogev, U., Reid, I., Dorman, M., Laronne, J.B., 2020. Novel mass-aggregation-based calibration of an acoustic method of monitoring bedload flux by infrequent desert flash floods. Earth Surface Processes and Landforms 45, 3510–3524. https://doi.org/10.1002/esp.4988

Harrison, L.R., Legleiter, C.J., Wydzga, M.A., Dunne, T., 2011. Channel dynamics and habitat development in a meandering, gravel bed river. Water Resources Research 47. https://doi.org/10.1029/2009WR008926

Hassan, M.A., Ergenzinger, P., 2003. Use of tracers in fluvial geomorphology. Tools in fluvial geomorphology 397–423.

Hassan, M.A., Voepel, H., Schumer, R., Parker, G., Fraccarollo, L., 2013. Displacement characteristics of coarse fluvial bed sediment. Journal of Geophysical Research: Earth Surface 118, 155–165.

Hauer, C., Wagner, B., Aigner, J., Holzapfel, P., Flödl, P., Liedermann, M., Tritthart, M., Sindelar, C., Pulg, U., Klösch, M., Haimann, M., Donnum, B.O., Stickler, M., Habersack, H., 2018. State of the art, shortcomings and future challenges for a sustainable sediment management in hydropower: A review. Renewable and Sustainable Energy Reviews 98, 40–55. https://doi.org/10.1016/j.rser.2018.08.031

Hayward, J.A., Sutherland, A.J., 1974. THE TORLESSE STREAM VORTEX-TUBE SEDIMENT TRAP. Journal of Hydrology (New Zealand) 13, 41–53.

Heckmann, T., Cavalli, M., Cerdan, O., Foerster, S., Javaux, M., Lode, E., Smetanová, A., Vericat, D., Brardinoni, F., 2018. Indices of sediment connectivity: opportunities, challenges and limitations. Earth-Science Reviews 187, 77–108. https://doi.org/10.1016/j.earscirev.2018.08.004

Heimann, F.U.M., 2015. Bedload transport in mountain streams: Model development, numeric simulation and time series analysis (Doctoral Thesis). ETH Zurich. https://doi.org/10.3929/ethz-a-010406973

Helley, E.J., Smith, W., 1971. Development and calibration of a pressure-difference bedload sampler.

Heritage, G., Entwistle, N.S., Milan, D., 2019. Evidence of non-contiguous flood driven coarse sediment transfer and implications for sediment management, in: E-Proceedings of the 38th IAHR World Congress. International Association for Hydro-Environment Engineering and Research.

Hicks, D.M., Gomez, B., 2003. Sediment transport. Tools in fluvial geomorphology 324–356.

Hinderer, M., Kastowski, M., Kamelger, A., Bartolini, C., Schlunegger, F., 2013. River loads and modern denudation of the Alps — A review. Earth-Science Reviews 118, 11–44. https://doi.org/10.1016/j.earscirev.2013.01.001

Hirschberg, J., Fatichi, S., Bennett, G.L., McArdell, B.W., Peleg, N., Lane, S.N., Schlunegger, F., Molnar, P., 2021. Climate Change Impacts on Sediment Yield and Debris-Flow Activity in an Alpine Catchment. Journal of Geophysical Research: Earth Surface 126, e2020JF005739. https://doi.org/10.1029/2020JF005739

Hoey, T.B., Sutherland, A.J., 1991. Channel morphology and bedload pulses in braided rivers: a laboratory study. Earth Surface Processes and Landforms 16, 447–462.

Hooke, R.L., 1991. Positive feedbacks associated with erosion of glacial cirques and overdeepenings. GSA Bulletin 103, 1104–1108. https://doi.org/10.1130/0016-7606(1991)103<1104:PFAWEO>2.3.CO;2

Horton, P., Schaefli, B., Mezghani, A., Hingray, B., Musy, A., 2006. Assessment of climate-change impacts on alpine discharge regimes with climate model uncertainty. Hydrological Processes 20, 2091–2109. https://doi.org/10.1002/hyp.6197

Houbrechts, G., Van Campenhout, J., Levecq, Y., Hallot, E., Peeters, A., Petit, F., 2012. Comparison of methods for quantifying active layer dynamics and bedload discharge in armoured gravel-bed rivers. Earth Surface Processes and Landforms 37, 1501–1517. https://doi.org/10.1002/esp.3258

Huggel, C., Clague, J.J., Korup, O., 2012. Is climate change responsible for changing landslide activity in high mountains? Earth Surface Processes and Landforms 37, 77–91. https://doi.org/10.1002/esp.2223

Huss, M., Hock, R., 2018. Global-scale hydrological response to future glacier mass loss. Nature Climate Change 8, 135.

James, M.R., Antoniazza, G., Robson, S., Lane, S.N., 2020. Mitigating systematic error in topographic models for geomorphic change detection: Accuracy, precision and considerations beyond off-nadir imagery. Earth Surface Processes and Landforms n/a. https://doi.org/10.1002/esp.4878

Jerolmack, D.J., Paola, C., 2010. Shredding of environmental signals by sediment transport. Geophysical Research Letters 37. https://doi.org/10.1029/2010GL044638

Kammerlander, J., Gems, B., Kößler, D., Aufleger, M., 2017. Effect of bed load supply on sediment transport in mountain streams. International Journal of Sediment Research 32, 240–252. https://doi.org/10.1016/j.ijsrc.2017.03.004

Kirchner, J.W., Dietrich, W.E., Iseya, F., Ikeda, H., 1990. The variability of critical shear stress, friction angle, and grain protrusion in water-worked sediments. Sedimentology 37, 647–672.

Knighton, D., 2014. Fluvial forms and processes: a new perspective. Routledge.

Koshiba, T., Auel, C., Tsutsumi, D., Kantoush, S.A., Sumi, T., 2018. Application of an impact plate – Bedload transport measuring system for high-speed flows. International Journal of Sediment Research 33, 35–46. https://doi.org/10.1016/j.ijsrc.2017.12.003

Kreisler, A., Moser, M., Aigner, J., Rindler, R., Tritthart, M., Habersack, H., 2017. Analysis and classification of bedload transport events with variable process characteristics. Geomorphology, SEDIMENT DYNAMICS IN ALPINE BASINS 291, 57–68. https://doi.org/10.1016/j.geomorph.2016.06.033

Kuhnle, R.A., Wren, D.G., Hilldale, R.C., Goodwiller, B.T., Carpenter, W.O., 2017. Laboratory Calibration of Impact Plates for Measuring Gravel Bed Load Size and Mass. Journal of Hydraulic Engineering 143, 06017023.

Lagarde, S., Dietze, M., Gimbert, F., Laronne, J.B., Turowski, J.M., Halfi, E., 2021. Grain-Size Distribution and Propagation Effects on Seismic Signals Generated by Bedload Transport. Water Resources Research 57, e2020WR028700. https://doi.org/10.1029/2020WR028700

Lamb, M.P., Brun, F., Fuller, B.M., 2017. Direct measurements of lift and drag on shallowly submerged cobbles in steep streams: Implications for flow resistance and sediment transport. Water Resources Research 53, 7607–7629. https://doi.org/10.1002/2017WR020883

Lane, E.W., 1955. Importance of fluvial morphology in hydraulic engineering. Proceedings (American Society of Civil Engineers); v. 81, paper no. 745.

Lane, S., Antoniazza, G., Dietze, M., Mancini, D., 2021. Bedload transport: Are we doing restoration right in the face of alpine climate change. Presented at the Proceedings of the International Symposium on Bedload Management, pp. 8–10.

Lane, S.N., Bakker, M., Gabbud, C., Micheletti, N., Saugy, J.-N., 2017. Sediment export, transient landscape response and catchment-scale connectivity following rapid climate warming and Alpine glacier recession. Geomorphology 277, 210–227.

Lane, S.N., Borgeaud, L., Vittoz, P., 2016. Emergent geomorphic–vegetation interactions on a subalpine alluvial fan. Earth Surface Processes and Landforms 41, 72–86. https://doi.org/10.1002/esp.3833

Lane, S.N., Gentile, A., Goldenschue, L., 2020. Combining UAV-Based SfM-MVS Photogrammetry with Conventional Monitoring to Set Environmental Flows: Modifying Dam Flushing Flows to Improve Alpine Stream Habitat. Remote Sensing 12, 3868. https://doi.org/10.3390/rs12233868

Lane, S.N., Nienow, P.W., 2019. Decadal-Scale Climate Forcing of Alpine Glacial Hydrological Systems. Water Resources Research 55, 2478–2492. https://doi.org/10.1029/2018WR024206

Lane, S.N., Richards, K.S., Chandler, J.H., 1995. Morphological estimation of the time-integrated bed load transport rate. Water Resources Research 31, 761–772.

Lane, S.N., Tayefi, V., Reid, S.C., Yu, D., Hardy, R.J., 2007. Interactions between sediment delivery, channel change, climate change and flood risk in a temperate upland environment. Earth Surface Processes and Landforms 32, 429–446. https://doi.org/10.1002/esp.1404

Laronne, J.B., Alexandrov, Y., Bergman, N., Cohen, H., Garcia, C., Habersack, H., Powell, D.M., Reid, I., 2003. The continuous monitoring of bed load flux in various fluvial environments. IAHS publication 134.

Lauffer, H., Sommer, N., 1982. Studies on sediment transport in mountain streams of the Eastern Alps, in: Proc., International Commission on Large Dams, 14th Congress, Rio de Janiero. International Association for Hydraulic Research, Rio de Janeiro, Brazil. pp. 431–453.

Lenzi, M.A., D'Agostino, V., Billi, P., 1999. Bedload transport in the instrumented catchment of the Rio Cordon: Part I: Analysis of bedload records, conditions and threshold of bedload entrainment. Catena 36, 171–190.

Leopold, L.B., Emmett, W.W., 1976. Bedload measurements, East Fork River, Wyoming. Proceedings of the National Academy of Sciences 73, 1000–1004. https://doi.org/10.1073/pnas.73.4.1000

Leopold, L.B., Wolman, M.G., Miller, J.P., 2012. Fluvial processes in geomorphology. Courier Corporation.

Li, D., Lettenmaier, D.P., Margulis, S.A., Andreadis, K., 2019. The Role of Rain-on-Snow in Flooding Over the Conterminous United States. Water Resources Research 55, 8492–8513. https://doi.org/10.1029/2019WR024950

Li, D., Lu, X., Walling, D.E., Zhang, T., Steiner, J.F., Wasson, R.J., Harrison, S., Nepal, S., Nie, Y., Immerzeel, W.W., Shugar, D.H., Koppes, M., Lane, S., Zeng, Z., Sun, X., Yegorov, A., Bolch, T., 2022. High Mountain Asia hydropower systems threatened by climate-driven landscape instability. Nat. Geosci. 15, 520–530. https://doi.org/10.1038/s41561-022-00953-y

Liébault, F., Bellot, H., Chapuis, M., Klotz, S., Deschâtres, M., 2012. Bedload tracing in a high-sediment-load mountain stream. Earth Surface Processes and Landforms 37, 385–399. https://doi.org/10.1002/esp.2245

Lindsay, J., Ashmore, P., 2002. The effects of survey frequency on estimates of scour and fill in braided river model. Earth Surface Processes and Landforms 27, 27–43. https://doi.org/10.1002/esp.282

Lior, I., Sladen, A., Rivet, D., Ampuero, J.-P., Hello, Y., Becerril, C., Martins, H.F., Lamare, P., Jestin, C., Tsagkli, S., Markou, C., 2021. On the Detection Capabilities of Underwater Distributed Acoustic Sensing. Journal of Geophysical Research: Solid Earth 126, e2020JB020925. https://doi.org/10.1029/2020JB020925

Mächler, E., Salyani, A., Walser, J.-C., Larsen, A., Schaefli, B., Altermatt, F., Ceperley, N., 2021. Environmental DNA simultaneously informs hydrological and biodiversity characterization of an Alpine catchment. Hydrology and Earth System Sciences 25, 735–753. https://doi.org/10.5194/hess-25-735-2021

Mackin, H., 1948. Concept of the graded river. GSA Bulletin 59, 463–512. https://doi.org/10.1130/0016-7606(1948)59[463:COTGR]2.0.CO;2

Macklin, M.G., Booth, J., Brewer, P.A., Tooth, S., Duller, G.A.T., 2022. How have Cretan rivers responded to late Holocene uplift? A multi-millennial, multi-catchment field experiment to evaluate the applicability of Schumm and Parker's (1973) complex response model. Earth Surface Processes and Landforms 47, 2178–2197. https://doi.org/10.1002/esp.5370

MacVicar, B.J., Roy, A.G., 2011. Sediment mobility in a forced riffle-pool. Geomorphology 125, 445–456. https://doi.org/10.1016/j.geomorph.2010.10.031

Mahoney, D.T., Fox, J.F., Al Aamery, N., 2018. Watershed erosion modeling using the probability of sediment connectivity in a gently rolling system. Journal of Hydrology 561, 862–883. https://doi.org/10.1016/j.jhydrol.2018.04.034

Mancini, D., Lane, S.N., 2020. Changes in sediment connectivity following glacial debuttressing in an Alpine valley system. Geomorphology 352, 106987. https://doi.org/10.1016/j.geomorph.2019.106987

Mano, V., Nemery, J., Belleudy, P., Poirel, A., 2009. Assessment of suspended sediment transport in four alpine watersheds (France): influence of the climatic regime. Hydrological Processes 23, 777–792. https://doi.org/10.1002/hyp.7178

Mao, L., 2018. The effects of flood history on sediment transport in gravel-bed rivers. Geomorphology 322, 196–205. https://doi.org/10.1016/j.geomorph.2018.08.046

Mao, L., 2012. The effect of hydrographs on bed load transport and bed sediment spatial arrangement. Journal of Geophysical Research: Earth Surface 117. https://doi.org/10.1029/2012JF002428

Mao, L., Carrillo, R., Escauriaza, C., Iroume, A., 2016. Flume and field-based calibration of surrogate sensors for monitoring bedload transport. Geomorphology 253, 10–21. https://doi.org/10.1016/j.geomorph.2015.10.002

Mao, L., Dell'Agnese, A., Comiti, F., 2017. Sediment motion and velocity in a glacier-fed stream. Geomorphology 291, 69–79.

Mao, L., Dell'Agnese, A., Huincache, C., Penna, D., Engel, M., Niedrist, G., Comiti, F., 2014. Bedload hysteresis in a glacier-fed mountain river. Earth Surface Processes and Landforms 39, 964–976. https://doi.org/10.1002/esp.3563

Marquis, G.A., Roy, A.G., 2012. Using multiple bed load measurements: Toward the identification of bed dilation and contraction in gravel-bed rivers. Journal of Geophysical Research: Earth Surface 117.

Maruffi, L., Stucchi, L., Casale, F., Bocchiola, D., 2022. Soil erosion and sediment transport under climate change for Mera River, in Italian Alps of Valchiavenna. Science of The Total Environment 806, 150651. https://doi.org/10.1016/j.scitotenv.2021.150651

Masteller, C.C., Finnegan, N.J., Turowski, J.M., Yager, E.M., Rickenmann, D., 2019. History-Dependent Threshold for Motion Revealed by Continuous Bedload Transport Measurements in a Steep Mountain Stream. Geophysical Research Letters 46, 2583–2591. https://doi.org/10.1029/2018GL081325

Maurer, J.M., Schaefer, J.M., Russell, J.B., Rupper, S., Wangdi, N., Putnam, A.E., Young, N., 2020. Seismic observations, numerical modeling, and geomorphic analysis of a glacier lake outburst flood in the Himalayas. Science Advances 6, eaba3645. https://doi.org/10.1126/sciadv.aba3645

May, C.L., Pryor, B.S., 2014. Initial Motion and Bedload Transport Distance Determined by Particle Tracking in a Large Regulated River. River Research and Applications 30, 508–520. https://doi.org/10.1002/rra.2665

Messenzehl, K., Viles, H., Otto, J.-C., Ewald, A., Dikau, R., 2018. Linking rock weathering, rockwall instability and rockfall supply on talus slopes in glaciated hanging valleys

(Swiss Alps). Permafrost and Periglacial Processes 29, 135–151. https://doi.org/10.1002/ppp.1976

MeteoSwiss, 2019. Daily Precipitation (final analysis): Rhires D. Documentation of MeteoSwiss, Grid-Data Products.

MeteoSwiss, 2017. Daily Mean, Minimum and Maximum Temperature: TabsD, TminD, TmaxD. Documentation of MeteoSwiss Grid-Data Products.

Micheletti, N., Lambiel, C., Lane, S.N., 2015. Investigating decadal-scale geomorphic dynamics in an alpine mountain setting. Journal of Geophysical Research: Earth Surface 120, 2155–2175.

Micheletti, N., Lane, S.N., 2016. Water yield and sediment export in small, partially glaciated Alpine watersheds in a warming climate. Water Resources Research 52, 4924–4943.

Michelon, A., Benoit, L., Beria, H., Ceperley, N., Schaefli, B., 2021. Benefits from high-density rain gauge observations for hydrological response analysis in a small alpine catchment. Hydrology and Earth System Sciences 25, 2301–2325. https://doi.org/10.5194/hess-25-2301-2021

Michelon, A., Ceperley, N., Beria, H., Larsen, J., Vennemann, T., Schaefli, B., 2022. Studying the dynamic of a high alpine catchment based on multiple natural tracers. Hydrology and Earth System Sciences Discussions 1–43. https://doi.org/10.5194/hess-2022-48

Mikovski, M., 2021. polfitzero [Matlab function]. https://fr.mathworks.com/matlabcentral/fileexchange/35401-polyfitzero.

Mikuś, P., Wyżga, B., Radecki-Pawlik, A., Zawiejska, J., Amirowicz, A., Oglęcki, P., 2016. Environment-friendly reduction of flood risk and infrastructure damage in a mountain river: Case study of the Czarny Dunajec. Geomorphology, Floods in Mountain Environments 272, 43–54. https://doi.org/10.1016/j.geomorph.2015.11.003

Milhous, R.T., 1973. Sediment transport in a gravel-bottomed stream [WWW Document].

Miller, H.R., Lane, S.N., 2019. Biogeomorphic feedbacks and the ecosystem engineering of recently deglaciated terrain. Progress in Physical Geography: Earth and Environment 43, 24–45. https://doi.org/10.1177/0309133318816536

Minute, F., Comiti, F., Cavalli, M., 2019. Assessing geomorphic changes induced by a debris-flow: a case study in the Dolomites. Rendiconti Online Societa Geologica Italiana 48, 23–28.

Misset, C., Recking, A., Legout, C., Bakker, M., Gimbert, F., Geay, T., Zanker, S., 2021. Using Continuous Turbidity and Seismic Measurements to Unravel Sediment Provenance and Interaction Between Suspended and Bedload Transport in an Alpine Catchment. Geophysical Research Letters 48, e2020GL090696. https://doi.org/10.1029/2020GL090696

Mizuyama, T., Laronne, J.B., Nonaka, M., Sawada, T., Satofuka, Y., Matsuoka, M., Yamashita, S., Sako, Y., Tamaki, S., Watari, M., 2010a. Calibration of a passive acoustic bedload monitoring system in Japanese mountain rivers. US Geological Survey Scientific Investigations Report 5091, 296–318.

Mizuyama, T., Oda, A., Laronne, J.B., Nonaka, M., Matsuoka, M., 2010b. Laboratory tests of a Japanese pipe geophone for continuous acoustic monitoring of coarse bedload. US Geological Survey Scientific Investigations Report 5091, 319–335.

Morach, S., 2011. Geschiebemessungen mittels Geophonen bei hohen Fliessgeschwindigkeiten (Master thesis). ETH Zürich - VAW, Zürich.

Mueller, E.R., Pitlick, J., 2005. Morphologically based model of bed load transport capacity in a headwater stream. Journal of Geophysical Research: Earth Surface 110. https://doi.org/10.1029/2003JF000117

Musselman, K.N., Clark, M.P., Liu, C., Ikeda, K., Rasmussen, R., 2017. Slower snowmelt in a warmer world. Nature Clim Change 7, 214–219. https://doi.org/10.1038/nclimate3225

Musselman, K.N., Lehner, F., Ikeda, K., Clark, M.P., Prein, A.F., Liu, C., Barlage, M., Rasmussen, R., 2018. Projected increases and shifts in rain-on-snow flood risk over western North America. Nature Climate Change 8, 808–812. https://doi.org/10.1038/s41558-018-0236-4

Mutzner, R., Weijs, S.V., Tarolli, P., Calaf, M., Oldroyd, H.J., Parlange, M.B., 2015. Controls on the diurnal streamflow cycles in two subbasins of an alpine headwater catchment. Water Resources Research 51, 3403–3418. https://doi.org/10.1002/2014WR016581

Newson, M., 1980. The geomorphological effectiveness of floods—a contribution stimulated by two recent events in mid-wales. Earth Surface Processes 5, 1–16. https://doi.org/10.1002/esp.3760050102

Nicollier, T., Antoniazza, G., Ammann, L., Rickenmann, D., Kirchner, J.W., 2022a. Toward a general calibration of the Swiss plate geophone system for fractional bedload transport. Earth Surface Dynamics 10, 929–951. https://doi.org/10.5194/esurf-10-929-2022

Nicollier, T., Antoniazza, G., Rickenmann, D., Hartlieb, A., Kirchner, J.W., 2022b. Improving the Calibration of the Swiss Plate Geophone Bedload Monitoring System by Filtering Out Seismic Signals From Extraneous Particle Impacts. Earth and Space Science 9, e2021EA001962. https://doi.org/10.1029/2021EA001962

Nicollier, T., Rickenmann, D., Boss, S., Travaglini, E., Hartlieb, A., 2020. Calibration of the Swiss plate geophone system at the Zinal field site with direct bedload samples and results from controlled flume experiments. Presented at the SEDHYD River Flow 2020 Conference., p. 8.

Nicollier, T., Rickenmann, D., Hartlieb, A., 2021. Field and flume measurements with the impact plate: effect of bedload grain-size distribution on signal response. Earth Surface Processes and Landforms n/a. https://doi.org/10.1002/esp.5117

Nicollier, T., Rickenmann, D., Hartlieb, A., 2019. Calibration of the Swiss plate geophone system at the Albula field site with direct bedload samples and comparison with controlled flume experiments, in: SEDHYD 2019 Conference, Federal Interagency Sedimentation and Hydrologic, Modeling Conference. p. Paper 345, 8 p.

Nitsche, M., Rickenmann, D., Turowski, J.M., Badoux, A., Kirchner, J.W., 2011. Evaluation of bedload transport predictions using flow resistance equations to account for macro-roughness in steep mountain streams. Water Resources Research 47.

Olinde, L., Johnson, J.P.L., 2015. Using RFID and accelerometer-embedded tracers to measure probabilities of bed load transport, step lengths, and rest times in a mountain stream. Water Resources Research 51, 7572–7589. https://doi.org/10.1002/2014WR016120

Parker, G., 2008. Transport of gravel and sediment mixtures, in: Sedimentation Engineering: Processes, Measurements, Modeling, and Practice. pp. 165–251.

Parker, G., 1990. Surface-based bedload transport relation for gravel rivers. Journal of Hydraulic Research 28, 417–436. https://doi.org/10.1080/00221689009499058

Parker, G., Dhamotharan, S., Stefan, H., 1982. Model experiments on mobile, paved gravel bed streams. Water Resources Research 18, 1395–1408.

Parker, G., Klingeman, P.C., 1982. On why gravel bed streams are paved. Water Resources Research 18, 1409–1423.

Parker, G., Toro-Escobar, C.M., 2002. Equal mobility of gravel in streams: The remains of the day. Water Resources Research 38, 46-1-46–8.

Patterson, M.O., McKay, R., Naish, T., Escutia, C., Jimenez-Espejo, F.J., Raymo, M.E., Meyers, S.R., Tauxe, L., Brinkhuis, H., IODP Expedition 318 Scientists, Klaus, A., Fehr, A., Bendle, J. a. P., Bijl, P.K., Bohaty, S.M., Carr, S.A., Dunbar, R.B., Flores, J.A., Gonzalez, J.J., Hayden, T.G., Iwai, M., Katsuki, K., Kong, G.S., Nakai, M., Olney, M.P., Passchier, S., Pekar, S.F., Pross, J., Riesselman, C.R., Röhl, U., Sakai, T., Shrivastava, P.K., Stickley, C.E., Sugasaki, S., Tuo, S., van de Flierdt, T., Welsh, K., Williams, T., Yamane, M., 2014. Orbital forcing of the East Antarctic ice sheet during the Pliocene and Early Pleistocene. Nature Geoscience 7, 841–847. https://doi.org/10.1038/ngeo2273

Perolo, P., Bakker, M., Gabbud, C., Moradi, G., Rennie, C., Lane, S.N., 2019. Subglacial sediment production and snout marginal ice uplift during the late ablation season of a temperate valley glacier. Earth Surface Processes and Landforms.

Phillips, C.B., Martin, R.L., Jerolmack, D.J., 2013. Impulse framework for unsteady flows reveals superdiffusive bed load transport. Geophysical Research Letters 40, 1328–1333. https://doi.org/10.1002/grl.50323

Piantini, M., Gimbert, F., Bakker, M., Recking, A., Nanni, U., 2022. Using a dense seismic array to study fluvial processes in a braided river reach under flood conditions. LHB 0, 2053314. https://doi.org/10.1080/27678490.2022.2053314

Piton, G., Recking, A., 2017. The concept of travelling bedload and its consequences for bedload computation in mountain streams. Earth Surface Processes and Landforms 42, 1505–1519. https://doi.org/10.1002/esp.4105

Pitscheider, F., Comiti, F., Theule, J., Gems, B., Cavalli, M., 2022. DoD applications in small mountain basins: insights from the Gadria basin (Italy). ROL 58/2022. https://doi.org/10.3301/ROL.2022.19

Porter, P.R., Smart, M.J., Irvine-Fynn, T.D.L., 2019. Glacial Sediment Stores and Their Reworking, in: Heckmann, T., Morche, D. (Eds.), Geomorphology of Proglacial Systems: Landform and Sediment Dynamics in Recently Deglaciated Alpine Landscapes, Geography of the Physical Environment. Springer International Publishing, Cham, pp. 157–176. https://doi.org/10.1007/978-3-319-94184-4_10

Portogallo, M., Simoni, S., Vignoli, G., Bertoldi, W., 2022. Analysis of the Vibration Modes of Impact Geoplates and Implications for Bedload Flux and Grain Size Measurements. Water Resources Research 58, e2022WR032116. https://doi.org/10.1029/2022WR032116

Powell, D.M., Reid, I., Laronne, J.B., 2001. Evolution of bed load grain size distribution with increasing flow strength and the effect of flow duration on the caliber of bed load sediment yield in ephemeral gravel bed rivers. Water Resources Research 37, 1463–1474. https://doi.org/10.1029/2000WR900342

Pralong, M.R., Turowski, J.M., Rickenmann, D., Zappa, M., 2015. Climate change impacts on bedload transport in alpine drainage basins with hydropower exploitation. Earth Surface Processes and Landforms 40, 1587–1599. https://doi.org/10.1002/esp.3737

Rainato, R., Mao, L., García-Rama, A., Picco, L., Cesca, M., Vianello, A., Preciso, E., Scussel, G.R., Lenzi, M.A., 2017. Three decades of monitoring in the Rio Cordon instrumented basin: Sediment budget and temporal trend of sediment yield. Geomorphology, SEDIMENT DYNAMICS IN ALPINE BASINS 291, 45–56. https://doi.org/10.1016/j.geomorph.2016.03.012

Rainato, R., Mao, L., Picco, L., 2018. Near-bankfull floods in an Alpine stream: Effects on the sediment mobility and bedload magnitude. International Journal of Sediment Research 33, 27–34. https://doi.org/10.1016/j.ijsrc.2017.03.006

Ravanel, L., Deline, P., 2011. Climate influence on rockfalls in high-Alpine steep rockwalls: The north side of the Aiguilles de Chamonix (Mont Blanc massif) since the end of the ‘Little Ice Age.’ The Holocene 21, 357–365.

Recking, A., 2013. An analysis of nonlinearity effects on bed load transport prediction. Journal of Geophysical Research: Earth Surface 118, 1264–1281. https://doi.org/10.1002/jgrf.20090

Recking, A., 2012. Influence of sediment supply on mountain streams bedload transport. Geomorphology 175–176, 139–150. https://doi.org/10.1016/j.geomorph.2012.07.005

Recking, A., Leduc, P., Liébault, F., Church, M., 2012. A field investigation of the influence of sediment supply on step-pool morphology and stability. Geomorphology 139–140, 53–66. https://doi.org/10.1016/j.geomorph.2011.09.024

Reid, D.A., Hassan, M.A., Bird, S., Hogan, D., 2019. Spatial and temporal patterns of sediment storage over 45 years in Carnation Creek, BC, a previously glaciated mountain catchment. Earth Surface Processes and Landforms 44, 1584–1601. https://doi.org/10.1002/esp.4595

Reid, I., Frostick, L.E., Layman, J.T., 1985. The incidence and nature of bedload transport during flood flows in coarse-grained alluvial channels. Earth Surface Processes and Landforms 10, 33–44.

Reid, I., Laronne, J.B., 1995. Bed Load Sediment Transport in an Ephemeral Stream and a Comparison with Seasonal and Perennial Counterparts. Water Resources Research 31, 773–781. https://doi.org/10.1029/94WR02233

Reid, I., Laronne, J.B., Powell, D.M., 1995. The nahal yatir bedload database: Sediment dynamics in a gravel-bed ephemeral stream. Earth Surface Processes and Landforms 20, 845–857. https://doi.org/10.1002/esp.3290200910

Rennie, C.D., Vericat, D., Williams, R.D., Brasington, J., Hicks, M., 2017. Calibration of Acoustic Doppler Current Profiler Apparent Bedload Velocity to Bedload Transport Rate, in: Gravel-Bed Rivers. John Wiley & Sons, Ltd, pp. 209–233. https://doi.org/10.1002/9781118971437.ch8

Richards, K., 2004. Rivers: Form and Process of Alluvial Channels. The Blackburn Press, Caldwell, N.J.

Rickenmann, D., 2020. Effect of Sediment Supply on Cyclic Fluctuations of the Disequilibrium Ratio and Threshold Transport Discharge, Inferred From Bedload Transport Measurements Over 27 Years at the Swiss Erlenbach Stream. Water Resources Research 56, e2020WR027741. https://doi.org/10.1029/2020WR027741

Rickenmann, D., 2018. Variability of Bed Load Transport During Six Summers of Continuous Measurements in Two Austrian Mountain Streams (Fischbach and Ruetz). Water Resources Research 54, 107–131. https://doi.org/10.1002/2017WR021376

Rickenmann, D., 2017. Bedload transport measurements with geophones, hydrophones and underwater microphones (passive acoustic methods). Gravel Bed Rivers and Disasters, Wiley & Sons, Chichester, UK 185–208.

Rickenmann, D., 2012. Alluvial Steep Channels: Flow Resistance, Bedload Transport Prediction, and Transition to Debris Flows, in: Gravel-Bed Rivers. John Wiley & Sons, Ltd, pp. 386–397. https://doi.org/10.1002/9781119952497.ch28

Rickenmann, D., 2001. Comparison of bed load transport in torrents and gravel bed streams. Water Resources Research 37, 3295–3305. https://doi.org/10.1029/2001WR000319

Rickenmann, D., 1997. Sediment transport in Swiss torrents. Earth Surface Processes and Landforms 22, 937–951. https://doi.org/10.1002/(SICI)1096-9837(199710)22:10<937::AID-ESP786>3.0.CO;2-R

Rickenmann, D., Ammann, L., Nicollier, T., Boss, S., Fritschi, B., Antoniazza, G., Steeb, N., Chen, Z., Wyss, C., Badoux, A., 2022. Comparison of calibration characteristics of different acoustic impact systems for measuring bedload transport in mountain streams. Earth Surface Dynamics Discussions 1–29. https://doi.org/10.5194/esurf-2022-41

Rickenmann, D., Antoniazza, G., Wyss, C.R., Fritschi, B., Boss, S., 2017. Bedload transport monitoring with acoustic sensors in the Swiss Albula mountain river. Proceedings of the International Association of Hydrological Sciences 375, 5.

Rickenmann, D., Badoux, A., Hunzinger, L., 2016. Significance of sediment transport processes during piedmont floods: the 2005 flood events in Switzerland. Earth Surface Processes and Landforms 41, 224–230. https://doi.org/10.1002/esp.3835

Rickenmann, D., Fritschi, B., 2017. Bedload transport measurements with impact plate geophones in two Austrian mountain streams (Fischbach and Ruetz): system calibration, grain size estimation, and environmental signal pick-up. Earth Surface Dynamics 5.

Rickenmann, D., Heimann, F.U.M., Turowski, J.M., Bieler, C., Böckli, M., Badoux, A., 2014a. Simulation of bedload transport in the Hasliaare River with increased sediment input, in: River Flow. pp. 2273–2281.

Rickenmann, D., Koschni, A., 2010. Sediment loads due to fluvial transport and debris flows during the 2005 flood events in Switzerland. Hydrological Processes: An International Journal 24, 993–1007.

Rickenmann, D., McArdell, B.W., 2008. Calibration of piezoelectric bedload impact sensors in the Pitzbach mountain stream. Geodinamica Acta 21, 35–52.

Rickenmann, D., McArdell, B.W., 2007. Continuous measurement of sediment transport in the Erlenbach stream using piezoelectric bedload impact sensors. Earth Surface Processes and Landforms 32, 1362–1378. https://doi.org/10.1002/esp.1478

Rickenmann, D., Nicollier, T., Boss, S., Badoux, A., 2020. Four years of bedload transport measurements in the Swiss Mountain River Albula. River flow 2020. Proceedings of the 10th conference on fluvial hydraulics 1749–1755. https://doi.org/10.1201/b22619-245

Rickenmann, D., Recking, A., 2011. Evaluation of flow resistance in gravel-bed rivers through a large field data set. Water Resources Research 47.

Rickenmann, D., Turowski, J.M., Fritschi, B., Klaiber, A., Ludwig, A., 2012. Bedload transport measurements at the Erlenbach stream with geophones and automated basket samplers. Earth Surface Processes and Landforms 37, 1000–1011.

Rickenmann, D., Turowski, J.M., Fritschi, B., Wyss, C., Laronne, J., Barzilai, R., Reid, I., Kreisler, A., Aigner, J., Seitz, H., Habersack, H., 2014b. Bedload transport measurements with impact plate geophones: comparison of sensor calibration in different gravel-bed streams. Earth Surface Processes and Landforms 39, 928–942. https://doi.org/10.1002/esp.3499

Rigby, J.R., Wren, D.G., Kuhnle, R.A., 2016. Passive Acoustic Monitoring of Bed Load for Fluvial Applications. Journal of Hydraulic Engineering 142, 02516003. https://doi.org/10.1061/(ASCE)HY.1943-7900.0001122

Roth, D.L., Brodsky, E.E., Finnegan, N.J., Rickenmann, D., Turowski, J.M., Badoux, A., 2016. Bed load sediment transport inferred from seismic signals near a river. Journal of Geophysical Research: Earth Surface 121, 725–747. https://doi.org/10.1002/2015JF003782

Roth, D.L., Finnegan, N.J., Brodsky, E.E., Rickenmann, D., Turowski, J.M., Badoux, A., Gimbert, F., 2017. Bed load transport and boundary roughness changes as competing causes of hysteresis in the relationship between river discharge and seismic amplitude recorded near a steep mountain stream. Journal of Geophysical Research: Earth Surface 122, 1182–1200. https://doi.org/10.1002/2016JF004062

Roussel, E., Marren, P.M., Cossart, E., Toumazet, J.-P., Chenet, M., Grancher, D., Jomelli, V., 2018. Incision and aggradation in proglacial rivers: Post-Little Ice Age long-profile adjustments of Southern Iceland outwash plains. Land degradation & development 29, 3753–3771.

Ruiz-Villanueva, V., Díez-Herrero, A., Ballesteros, J.A., Bodoque, J.M., 2014. Potential Large Woody Debris Recruitment Due to Landslides, Bank Erosion and Floods in Mountain Basins: A Quantitative Estimation Approach. River Research and Applications 30, 81–97. https://doi.org/10.1002/rra.2614

Schimmel, A., Coviello, V., Comiti, F., 2022. Debris flow velocity and volume estimations based on seismic data. Natural Hazards and Earth System Sciences 22, 1955–1968. https://doi.org/10.5194/nhess-22-1955-2022

Schleiss, A., De Cesare, G., Jenzer Althaus, J., 2010. Verlandung der Stauseen gefährdet die nachhaltige Nutzung der Wasserkraft. Wasser, Energie, Luft/Eau, énergie, air 102, 31–40.

Schleiss, A.J., Franca, M.J., Juez, C., De Cesare, G., 2016. Reservoir sedimentation. Journal of Hydraulic Research 54, 595–614. https://doi.org/10.1080/00221686.2016.1225320

Schmandt, B., Gaeuman, D., Stewart, R., Hansen, S.M., Tsai, V.C., Smith, J., 2017. Seismic array constraints on reach-scale bedload transport. Geology 45, 299–302.

Schmidt, K.-H., Morche, D., 2006. Sediment output and effective discharge in two small high mountain catchments in the Bavarian Alps, Germany. Geomorphology, Sedimentary Source-to-Sink-Fluxes in Cold Environments 80, 131–145. https://doi.org/10.1016/j.geomorph.2005.09.013

Schneider, J.M., Rickenmann, D., Turowski, J.M., Bunte, K., Kirchner, J.W., 2015. Applicability of bed load transport models for mixed-size sediments in steep streams considering macro-roughness. Water Resources Research 51, 5260–5283. https://doi.org/10.1002/2014WR016417

Schneider, J.M., Turowski, J.M., Rickenmann, D., Hegglin, R., Arrigo, S., Mao, L., Kirchner, J.W., 2014. Scaling relationships between bed load volumes, transport distances, and stream power in steep mountain channels. Journal of Geophysical Research: Earth Surface 119, 533–549. https://doi.org/10.1002/2013JF002874

Schumm, S.A., 1985. Patterns of alluvial rivers. Annual Review of Earth and Planetary Sciences 13, 5–27.

Sharp, M., Richards, K., Willis, I., Arnold, N., Nienow, P., Lawson, W., Tison, J.-L., 1993. Geometry, bed topography and drainage system structure of the haut glacier d’Arolla, Switzerland. Earth Surface Processes and Landforms 18, 557–571. https://doi.org/10.1002/esp.3290180608

Sims, A.J., Rutherfurd, I.D., 2017. Management responses to pulses of bedload sediment in rivers. Geomorphology, Anthropogenic Sedimentation 294, 70–86. https://doi.org/10.1016/j.geomorph.2017.04.010

Singh, A., Fienberg, K., Jerolmack, D.J., Marr, J., Foufoula-Georgiou, E., 2009. Experimental evidence for statistical scaling and intermittency in sediment transport rates. Journal of Geophysical Research: Earth Surface 114.

Smith, M.W., Vericat, D., 2015. From experimental plots to experimental landscapes: topography, erosion and deposition in sub-humid badlands from Structure-from-Motion photogrammetry. Earth Surface Processes and Landforms 40, 1656–1671. https://doi.org/10.1002/esp.3747

Sorg, A., Huss, M., Rohrer, M., Stoffel, M., 2014. The days of plenty might soon be over in glacierized Central Asian catchments. Environmental Research Letters 9, 104018.

Speerli, J., Bachmann, A., Bieler, S., Schumacher, A., Gysin, S., 2020. Auswirkungen des Klimawanderls auf den Sedimenttransport. Hochschule für Technik, Rapperswil.

Spreafico, M., Lehmann, C., 1994. Sediment transport observations in Switzerland. IAHS Publications-Series of Proceedings and Reports-Intern Assoc Hydrological Sciences 224, 259–268.

Stoffel, M., Mendlik, T., Schneuwly-Bollschweiler, M., Gobiet, A., 2014. Possible impacts of climate change on debris-flow activity in the Swiss Alps. Climatic Change 122, 141–155.

Stover, S.C., Montgomery, D.R., 2001. Channel change and flooding, Skokomish River, Washington. Journal of Hydrology 243, 272–286. https://doi.org/10.1016/S0022-1694(00)00421-2

Tamminga, A., Hugenholtz, C., Eaton, B., Lapointe, M., 2015. Hyperspatial Remote Sensing of Channel Reach Morphology and Hydraulic Fish Habitat Using an Unmanned Aerial Vehicle (UAV): A First Assessment in the Context of River Research and Management. River Research and Applications 31, 379–391. https://doi.org/10.1002/rra.2743

Thornton, J.M., Brauchli, T., Mariethoz, G., Brunner, P., 2021. Efficient multi-objective calibration and uncertainty analysis of distributed snow simulations in rugged alpine terrain. Journal of Hydrology 598, 126241. https://doi.org/10.1016/j.jhydrol.2021.126241

Thornton, J.M., Mariethoz, G., Brunner, P., 2018. A 3D geological model of a structurally complex Alpine region as a basis for interdisciplinary research. Sci Data 5, 180238. https://doi.org/10.1038/sdata.2018.238

Thornton, J.M., Therrien, R., Mariéthoz, G., Linde, N., Brunner, P., 2022. Simulating Fully-Integrated Hydrological Dynamics in Complex Alpine Headwaters: Potential and Challenges. Water Resources Research 58, e2020WR029390. https://doi.org/10.1029/2020WR029390

Tockner, K., Malard, F., Uehlinger, U., Ward, J.V., 2002. Nutrients and organic matter in a glacial river—floodplain system (Val Roseg, Switzerland). Limnology and Oceanography 47, 266–277. https://doi.org/10.4319/lo.2002.47.1.0266

Tropeano, D., 1991. High flow events and sediment transport in small streams in the 'tertiary basin' area in piedmont (Northwest Italy). Earth Surface Processes and Landforms 16, 323–339. https://doi.org/10.1002/esp.3290160406

Tsai, V.C., Minchew, B., Lamb, M.P., Ampuero, J.-P., 2012. A physical model for seismic noise generation from sediment transport in rivers. Geophysical Research Letters 39. https://doi.org/10.1029/2011GL050255

Turowski, J.M., 2012. Semi-Alluvial Channels and Sediment-Flux-Driven Bedrock Erosion, in: Gravel-Bed Rivers. John Wiley & Sons, Ltd, pp. 399–418. https://doi.org/10.1002/9781119952497.ch29

Turowski, J.M., Badoux, A., Leuzinger, J., Hegglin, R., 2013a. Large floods, alluvial overprint, and bedrock erosion. Earth Surface Processes and Landforms 38, 947–958. https://doi.org/10.1002/esp.3341

Turowski, J.M., Badoux, A., Rickenmann, D., 2011. Start and end of bedload transport in gravel-bed streams. Geophysical Research Letters 38. https://doi.org/10.1029/2010GL046558

Turowski, J.M., Böckli, M., Rickenmann, D., Beer, A.R., 2013b. Field measurements of the energy delivered to the channel bed by moving bed load and links to bedrock erosion. Journal of Geophysical Research: Earth Surface 118, 2438–2450. https://doi.org/10.1002/2013JF002765

Turowski, J.M., Rickenmann, D., 2009. Tools and cover effects in bedload transport observations in the Pitzbach, Austria. Earth Surface Processes and Landforms 34, 26–37. https://doi.org/10.1002/esp.1686

Turowski, J.M., Rickenmann, D., Dadson, S.J., 2010. The partitioning of the total sediment load of a river into suspended load and bedload: a review of empirical data. Sedimentology 57, 1126–1146. https://doi.org/10.1111/j.1365-3091.2009.01140.x

Turowski, J.M., Yager, E.M., Badoux, A., Rickenmann, D., Molnar, P., 2009. The impact of exceptional events on erosion, bedload transport and channel stability in a step-pool channel. Earth Surface Processes and Landforms 34, 1661–1673. https://doi.org/10.1002/esp.1855

Vanoni, V.A., 2006. Sedimentation Engineering. American Society of Civil Engineers. https://doi.org/10.1061/9780784408230

Vázquez-Tarrío, D., Recking, A., Liébault, F., Tal, M., Menéndez-Duarte, R., 2019. Particle transport in gravel-bed rivers: Revisiting passive tracer data. Earth Surface Processes and Landforms 44, 112–128. https://doi.org/10.1002/esp.4484

Venditti, J.G., Dietrich, W.E., Nelson, P.A., Wydzga, M.A., Fadde, J., Sklar, L., 2010. Mobilization of coarse surface layers in gravel-bedded rivers by finer gravel bed load. Water Resources Research 46.

Vericat, D., Batalla, R.J., Gibbins, C.N., 2008. Sediment entrainment and depletion from patches of fine material in a gravel-bed river. Water Resources Research 44. https://doi.org/10.1029/2008WR007028

Vittoz, P., Gmür, P., 2009. Introduction aux Journées de la biodiversité dans le Vallon de Nant (Bex, Alpes vaudoises). undefined.

Vorndran, G., 1985. Abtrag und Abtragsraten mit Beispielen aus den Alpen und dem Schwäbisch-baierischen Alpenvorland. Regensburger Geographische Schriften 19, 93–118.

Walter, F., Burtin, A., McArdell, B.W., Hovius, N., Weder, B., Turowski, J.M., 2017. Testing seismic amplitude source location for fast debris-flow detection at Illgraben, Switzerland. Natural Hazards and Earth System Sciences 17, 939–955. https://doi.org/10.5194/nhess-17-939-2017

Wang, Z.-Y., Lee, J.H., Melching, C.S., 2014. River dynamics and integrated river management. Springer Science & Business Media.

Welch, P., 1967. The use of fast Fourier transform for the estimation of power spectra: A method based on time averaging over short, modified periodograms. IEEE Transactions on Audio and Electroacoustics 15, 70–73. https://doi.org/10.1109/TAU.1967.1161901

Wheaton, J.M., Brasington, J., Darby, S.E., Sear, D.A., 2010. Accounting for uncertainty in DEMs from repeat topographic surveys: improved sediment budgets. Earth Surface Processes and Landforms 35, 136–156. https://doi.org/10.1002/esp.1886

Wilcock, P.R., Crowe, J.C., 2003. Surface-based transport model for mixed-size sediment. Journal of Hydraulic Engineering 129, 120–128.

Wilcock, P.R., McArdell, B.W., 1993. Surface-based fractional transport rates: Mobilization thresholds and partial transport of a sand-gravel sediment. Water Resources Research 29, 1297–1312.

Williams, R.D., Brasington, J., Vericat, D., Hicks, D.M., 2014. Hyperscale terrain modelling of braided rivers: fusing mobile terrestrial laser scanning and optical bathymetric mapping. Earth Surface Processes and Landforms 39, 167–183.

Wohl, E., 2013. Mountain Rivers Revisited. John Wiley & Sons.

Wohl, E., 2006. Human impacts to mountain streams. Geomorphology, 37th Binghamton Geomorphology Symposium 79, 217–248. https://doi.org/10.1016/j.geomorph.2006.06.020

Wolman, M.G., 1954. A method of sampling coarse river-bed material. EOS, Transactions American Geophysical Union 35, 951–956.

Wu, L., Liu, X., Ma, X., 2018. Research progress on the watershed sediment delivery ratio. International Journal of Environmental Studies 75, 565–579. https://doi.org/10.1080/00207233.2017.1392771

Wyss, C.R., Rickenmann, D., Fritschi, B., Turowski, J.M., Weitbrecht, V., Boes, R.M., 2016a. Laboratory flume experiments with the Swiss plate geophone bed load monitoring system: 1. Impulse counts and particle size identification. Water Resources Research 52, 7744–7759. https://doi.org/10.1002/2015WR018555

Wyss, C.R., Rickenmann, D., Fritschi, B., Turowski, J.M., Weitbrecht, V., Travaglini, E., Bardou, E., Boes, R.M., 2016b. Laboratory flume experiments with the Swiss plate geophone bed load monitoring system: 2. Application to field sites with direct bed load samples. Water Resources Research 52, 7760–7778. https://doi.org/10.1002/2016WR019283

Wyss, C.R., Rickenmann Dieter, Fritschi Bruno, Turowski Jens M., Weitbrecht Volker, Boes Robert M., 2016c. Measuring Bed Load Transport Rates by Grain-Size Fraction Using the Swiss Plate Geophone Signal at the Erlenbach. Journal of Hydraulic Engineering 142, 04016003. https://doi.org/10.1061/(ASCE)HY.1943-7900.0001090

Yager, E.M., Dietrich, W.E., Kirchner, J.W., McArdell, B.W., 2012a. Prediction of sediment transport in step-pool channels. Water Resources Research 48. https://doi.org/10.1029/2011WR010829

Yager, E.M., Kenworthy, M., Monsalve, A., 2015. Taking the river inside: Fundamental advances from laboratory experiments in measuring and understanding bedload transport processes. Geomorphology, Laboratory Experiments in Geomorphology 46th Annual Binghamton Geomorphology Symposium 18-20 September 2015 244, 21–32. https://doi.org/10.1016/j.geomorph.2015.04.002

Yager, E.M., Turowski, J.M., Rickenmann, D., McArdell, B.W., 2012b. Sediment supply, grain protrusion, and bedload transport in mountain streams. Geophysical Research Letters 39.

Zekollari, H., Huss, M., Farinotti, D., 2019. Modelling the future evolution of glaciers in the European Alps under the EURO-CORDEX RCM ensemble. The Cryosphere 13, 1125–1146. https://doi.org/10.5194/tc-13-1125-2019

Zhan, Z., 2019. Distributed Acoustic Sensing Turns Fiber-Optic Cables into Sensitive Seismic Antennas. Seismological Research Letters 91, 1–15. https://doi.org/10.1785/0220190112

Zhang, T., Li, D., East, A.E., Walling, D.E., Lane, S., Overeem, I., Beylich, A.A., Koppes, M., Lu, X., 2022. Warming-driven erosion and sediment transport in cold regions. Nat Rev Earth Environ 1–20. https://doi.org/10.1038/s43017-022-00362-0